The Deformation of an Elastic Cell in an Inviscid Stream

A thesis submitted to the School of Mathematics at the University of East Anglia in partial fulfilment of the requirements for the degree of Doctor of Philosophy

Adam Alexander Yorkston

July 2020

Abstract

In this thesis we study the deformation of an elastic cell in an inviscid fluid flow. We formulate the system of equations which governs the unsteady interaction between a thin-walled two-dimensional elastic cell and an inviscid fluid flow, allowing for fluids both in the exterior and interior of the cell. We present a conformal mapping method to simplify the exterior flow, and discuss numerical methods to evaluate the interior flow.

We focus on two particular flow configurations: a massless cell in a uniform stream, and a massive cell in a stream with circulation where the weight of the cell is balanced by the lift generated by the flow. We present asymptotic methods to obtain equilibria at low flow speeds, and use numerical methods to perform a detailed analysis of the solution space. For the massless cell we also analyse the linear stability of the equilibria, and study the subsequent nonlinear evolution of the unsteady cells.

We also extend the elastic cell formulation to allow for a fixed angle corner and an inextensible internal support, providing a simple model of an inflatable aerofoil. We present numerical methods based on a conformal mapping and a boundary integral equation which we use to analyse the deformed cell shapes in an inviscid flow, and obtain the parameter values for which the cell takes an aerodynamic shape. We compute the viscous flow past these deformed aerofoils and assess their aerodynamic viability.

Contents

List of Figures

List of Tables

Acknowledgements

I would like to thank my supervisors Mark Blyth and Emilian Părău for their invaluable guidance and support. I would also like to thank Bethany and my family for their support throughout my studies.

1

Introduction

1.1 Motivation

The deformation of an elastic body in response to hydrodynamic forces is a problem with applications in many fields. In biomechanics, elastic cells have been used to model the deformation of blood cells as they travel through veins and arteries (Pozrikidis, 2003; Fedosov et al., 2014), as well as elastic capsules used for drug delivery (Chang and Olbricht, 1993). Elastic models can be used to understand the collapse of veins in response to an imposed transmural pressure under laboratory conditions (Moreno et al., 1970), or due to the blood flow itself (Fung, 1997). In the aerospace industry there is increasing interest in the use of inflatable aerofoils which deform elastically in response to the airflow. The most well-known of these inflatable aerofoils is the Goodyear Inflatoplane (Goodyear Aircraft, 1957). Inflatable aerofoils have several advantages over traditional rigid aerofoils. They can be packed into a small volume for ease of transportation, and for this reason they have been suggested for use in extraterrestrial exploration (Smith et al., 2000; Landis et al., 2003). Their design also typically involves some sort of internal support structure, which can be tailored in-flight to optimise the performance in multiple roles with different flight requirements (Lynch and Rogers, 1976; Simpson, 2008). In each of these examples an understanding of the fluid-structure interaction between the elastic body and the flow is of

fundamental importance; it is crucial to be able to predict the fluid flow and subsequent elastic deformation and to assess the stability of the deformed states.

1.2 Background

The deformation of an elastic cell in response to a uniform transmural pressure was first examined by Lévy (1884), who identified a critical pressure above which a circular cell can deform into a buckled shape. Halphen (1888) subsequently identified a set of critical pressures p_n above which the circular cell deforms into a mode-n rotationally symmetric shape, and both Halphen (1888) and Greenhill (1899) obtained analytical solutions for these deformed cells in terms of elliptic integrals. The deformation of an elastic cell in response to a uniform transmural pressure has since been studied extensively, notably by Carrier (1947) and Tadjbakhsh and Odeh (1967).

Several extensions to this problem have subsequently been studied. Flaherty et al. (1972) used a similarity solution to obtain buckled cells with regions of self-contact, significantly expanding the set of physically permissible solutions. These self-contact solutions were further expanded on by Djondjorov et al. (2011). Watson and Wang (1981) studied the deformed shape of a heavy cell supported by a point force, while Blyth and Pozrikidis (2002) examined the bucking of a heavy cell resting on a horizontal or inclined plane. Elgindi et al. (1992) studied the deformation of an elastic tube submerged in a fluid with a variable hydrostatic pressure.

There is extensive literature on the numerical modelling of elastic cells in viscous flows (e.g. Pozrikidis, 2010), as well as semi-analytical studies (e.g. Higley et al., 2012). However, the problem of an elastic cell submerged in an inviscid fluid flow has received comparatively little attention. In this case the

pressure field around the cell is not known in advance, but depends on the flow field past the deformed cell shape. This coupling between the elastic deformation and the fluid flow significantly increases the complexity of the problem.

A closely related problem is that of a bubble in a uniform stream. This problem was notably studied by Vanden-Broeck and Keller (1980), who obtained numerical solutions by formulating the problem as an integrodifferential equation. Shankar (1992) used a conformal mapping method to obtain asymptotic solutions for low flow speeds, while Nie and Tanveer (1995) assessed the linear stability of the bubble in a uniform stream. Exact solutions for the deformation of a bubble in a circulatory flow were obtained by Crowdy (1999), and extended upon by Wegmann and Crowdy (2000).

The deformation of an elastic cell in a fluid flow was notably studied by Blyth and Părău (2013), who used a method based on a conformal mapping to obtain both analytical and numerical results for deformed equilibria shapes for a cell in either a uniform stream or a circulatory flow. Focussing on cell shapes which are both left-right symmetric and top-bottom symmetric, they used a linear expansion for the cell curvature to predict the first order deformation of an initially circular cell in a weak flow. Guided by these results they computed fully nonlinear equilibria using a numerical method based on a conformal mapping that is restricted to cells with a top-bottom cell symmetry. They demonstrated that at low flow speeds a cell will deform into an elliptical-type shape with its major axis oriented either horizontally aligned with the uniform stream or at ninety degrees to it, depending on whether the transmural pressure is above or below the first buckling pressure obtained by Lévy (1884) for a cell in a static fluid.

1.3 Thesis Outline

In Chapter 2 we formulate the system of equations which governs the unsteady interaction between a thin-walled two-dimensional elastic cell and an inviscid, irrotational, and incompressible fluid flow. The fluid flow past the cell is taken to be a uniform stream in the far-field with some circulation around the cell. The cell material is assumed to have some weight, which can be taken to balance the lift force generated by the flow. We also allow for the cell to be filled with an incompressible fluid. We use a conformal mapping method to simplify the flow equations, and derive the steady system for cells in equilibria. We also confirm the conservation of energy of the unsteady system.

In Chapter 3 we study the equilibria, stability and unsteady motion of a massless cell in a uniform flow. This provides a good model for cells consisting of a thin, low-density elastic material, where the inertia of the cell wall is much lower than the elastic and fluid forces acting upon it. We take as our point of departure the work of Blyth and Părău (2013), who used a linear expansion of the curvature at low flow speeds to demonstrate that a circular cell in a static fluid will deform into an elliptical-type shape with its major axis oriented either horizontally aligned with the uniform stream or at ninety degrees to it, depending on whether the transmural pressure is above or below the critical pressure identified by Lévy (1884). We use a conformal mapping method based on that used by Shankar (1992) to obtain asymptotic expansions of the equilibria at low flow speeds, and use numerical methods to explore the full solution space. We find a sequence of critical pressures, corresponding to those identified by Halphen (1888), at which further bifurcations are encountered; notably, we show for the first time that steady cell shapes with left-right asymmetry and cells with top-bottom asymmetry in the presence of a uniform flow are possible. We develop a linear stability method based on that presented by Nie and Tanveer (1995) to study the linear stability of the

deformed cells both for a uniform pressure interior and a fluid filled interior and present maps in parameter space of the regions of stability. We discover that certain solution branches are always stable, while some are stable only for a small region of parameter space, and find that the presence of a fluid in the interior of the cell significantly reduces the region of parameter-space for which the steady solutions are linearly stable. We compute the nonlinear time-evolution of the unstable cells subjected to a small initial perturbation and identify regions in which they fall into one of two distinct regular motions, either a flipping motion or a bulging motion, while travelling downstream with the flow. The presence of an interior fluid is found to increase the frequency of these motions while reducing the mean speed of the motion downstream. Finally, we compute the Lyapunov exponent of one of these unsteady simulations to assess the chaos of the system. Some of the results presented in Chapter 3 have previously been published in Yorkston et al. (2020a).

In Chapter 4 we study the equilibria of an elastic cell in a flow with circulation. We firstly consider a circulatory flow, with no flow in the far-field. This problem was studied in detail by Blyth and Părău (2013), who used a linear analysis to obtain a dispersion relation between the circulation and the fluid pressure at which mode-k buckled cells emerge. Using the conformal mapping method described in Chapter 3 we obtain asymptotic expansions for these buckled cells, and use numerical solutions to verify their accuracy. We then consider a uniform stream flow, with some circulation around the cell to allow for the generation of lift. This lift force is balanced by the weight of the cell material. We use a conformal mapping to obtain asymptotic solutions for low flow speeds and find that, as in the uniform stream problem, distinct solution branches bifurcate from the unit circle at a series of critical pressures. However, in the presence of circulation we find a much more complex

bifurcation structure and uncover solution branches which are distinct from any previously obtained.

In Chapter 5 we study the deformation a simple inflatable aerofoil, modelled as thin two-dimensional elastic sheet whose ends are joined together to form a corner of prescribed angle. We also allow for a straight inextensible support joining two chosen points on the boundary, which constrains the deformation to provide a more realistic model of an inflatable aerofoil. We present two separate numerical methods used to evaluate the aerofoil deformation in response to an inviscid flow; we use a conformal mapping method based on the Kármán-Trefftz transform for the unsupported cell, while an iterative method based on a boundary integral method is required for the supported cell. We present a set of distinct equilibria shapes in the absence of a flow and relate these solutions to the buckled cells described in the previous chapters. We analyse the deformation in response to a fluid flow and uncover a complex interchange of the solution branches as the flow speed is increased. We show that by tuning the internal support a good aerofoil-like shape can be obtained and analyse the physical parameters for which the aerofoil can maintain a good shape in response to the fluid pressures. We use a combination of boundary layer calculations and full DNS using the software package Gerris (Popinet, 2003, 2009) in order to assess the relevance of the inviscid calculations to a real flow, and determine the aerodynamic viability of the deformed aerofoils by computing the lift-to-drag ratio. Some of the results presented in Chapter 5 have been prepared for publication in Yorkston et al. (2020b).

Finally, in Chapter 6 we summarise our results and discuss potential future work.

2

Formulation of the Governing Equations

In this chapter we formulate the system of equations which governs the unsteady interaction between a thin-walled two-dimensional elastic cell and an inviscid, irrotational, incompressible fluid flow. The fluid flow past the cell is taken to be a uniform stream in the far-field with some circulation around the cell. We also allow for the cell to be filled with a volume of incompressible fluid, which provides a model of an air-filled cell in an air flow, for example.

The equations which determine the internal stress of an elastic shell in response to a deformation were notably studied by Pozrikidis (2002a), who justified a linear constitutive relation for the bending moment of the shell. We use this relation, along with an inextensibility condition, to derive an expression for the internal stress of an unsteady elastic cell, and thus derive the equations which govern the unsteady motion of the cell in response to a given transmural pressure. We formulate the equations which govern the fluid flow past the cell as well as the unsteady motion of the fluid in the interior of the cell, and obtain dynamic and kinematic conditions which determine the unsteady interaction between the fluid and the cell. We analyse the energy of this system, and present a conformal mapping method to simplify the exterior flow problem. We present the steady system which governs the equilibrium cell shapes, and obtain some invariants of the steady system.

2.1 Problem Description

We consider the deformation of a smooth, two-dimensional elastic cell submerged in an inviscid, incompressible, irrotational fluid flow. The cell is modelled as a thin elastic shell with uniform thickness h and uniform density ρ_c. The cell material is assumed to deform elastically with flexural rigidity E_B, and in the absence of external forces the cell is assumed to take a circular rest-state with radius ℓ. The cell material is also assumed to be inextensible, with constant perimeter $2\pi\ell$.

The fluid flow past the cell is taken to be a uniform stream of speed U in the positive x direction, with circulation Γ around the cell. The flow is assumed to be inviscid, irrotational, and incompressible with uniform density $\rho^{(e)}$. In the interior of the cell, we allow for an inviscid, irrotational, and incompressible fluid of density $\rho^{(i)}$, where $\rho^{(i)} = 0$ reduces the interior to a uniform pressure. The cell is assumed to be impermeable, with no fluid motion across the cell wall. Note however that, since the flow is inviscid, we cannot enforce a no-slip condition at the cell wall.

The system of equations and subsequent results derived in this chapter provide a basis for the following chapters; in Chapter 3 we analyse the equilibria of this system in the absence of circulation, and assess the linear stability and compute the unsteady evolution of the full nonlinear system, and in Chapter 4 we consider equlibria in the presence of circulation. Note that in Chapters 3 and 4 restrictions are made on the parameters of the system in order to provide a simpler solution space to analyse. The system derived in this chapter is capable of modelling more general cases than those considered in this thesis; these will be discussed in the Future Work section in Chapter 6.

2.2 Elastic Deformation

We start by deriving the equations which govern the deformation and unsteady motion of an elastic cell in response to some transmural pressure. We assume the thickness h of the cell wall is small, which allows us to represent the cell boundary as a one-dimensional curve $\boldsymbol{\eta}(s,t) = x(s,t)\boldsymbol{i} + y(s,t)\boldsymbol{j}$, where $0 \leq s \leq 2\pi\ell$ is the arc-length distance along the boundary in the anticlockwise direction relative to some reference point at $s = 0$. The unit tangent vector in the positive s direction is given by $\hat{\boldsymbol{\tau}} = \boldsymbol{\eta}_s = x_s\boldsymbol{i} + y_s\boldsymbol{j}$, and the unit normal vector in the direction pointing from the interior to the exterior of the cell is given by $\hat{\boldsymbol{n}} = y_s\boldsymbol{i} - x_s\boldsymbol{j}$. The arc-length derivatives of the unit tangent and normal vectors are given by the Frenet-Serret formulae as $\hat{\boldsymbol{\tau}}_s = \kappa\hat{\boldsymbol{n}}$ and $\hat{\boldsymbol{n}}_s = -\kappa\hat{\boldsymbol{\tau}}$, where the signed curvature κ is defined as $\kappa = x_{ss}y_s - x_s y_{ss}$. Note that the sign of the curvature is sometimes taken to be the opposite of that used here; we have chosen the sign such that the unit circle has a curvature of $\kappa = -1$.

Since we are going to model the fluid flow using a complex potential, it will be convenient to deal with vectors using complex notation. A vector $\boldsymbol{a} = a_i\boldsymbol{i} + a_j\boldsymbol{j}$ can be represented as the complex number $a = a_i + \mathrm{i}a_j$, with the dot product $\boldsymbol{a}\cdot\boldsymbol{b}$ given by $\mathrm{Re}(\overline{a}b)$. In complex form, the unit tangent and normal vectors are given by $\hat{\tau} = \eta_s$ and $\hat{n} = -\mathrm{i}\eta_s$ respectively, and the curvature can be written as $\kappa = -\mathrm{Im}\left(\eta_{ss}\overline{\eta}_s\right)$. A vector $\boldsymbol{a}$ and its complex form a thus satisfy $\boldsymbol{a}\cdot\hat{\boldsymbol{\tau}} = \mathrm{Re}\left(a\overline{\eta}_s\right)$ and $\boldsymbol{a}\cdot\hat{\boldsymbol{n}} = -\mathrm{Im}\left(a\overline{\eta}_s\right)$. Throughout this work quantities will be represented in both vector and complex form as appropriate, with bold symbols representing vectors and non-bold symbols representing complex values.

The material properties of the cell wall are modelled using two constitutive relations; an inextensibility condition, which prevents the cell material stretching throughout the cell deformation, and a constitutive relation for the elastic bending moment, which determines the extent to which the cell deforms when subjected to an external force. Considering firstly the

Symbol	Parameter	Units
ℓ	Radius of the undeformed cell	m
h	Cell wall thickness	m
ρ_c	Cell wall density	$\mathrm{kg\,m^{-3}}$
E_B	Flexural rigidity of cell wall	$\mathrm{kg\,m^2\,s^{-2}}$
g	Acceleration due to gravity	$\mathrm{m\,s^{-2}}$
U	Far-field flow speed	$\mathrm{m\,s^{-1}}$
Γ	Circulation	$\mathrm{m^2\,s^{-1}}$
$\rho^{(e)}/\rho^{(i)}$	Exterior/interior fluid density	$\mathrm{kg\,m^{-3}}$
$p^{(e)}/p^{(i)}$	Exterior/interior fluid pressure	$\mathrm{kg\,m^{-1}\,s^{-2}}$

Table 2.1: The dimensional parameters of the system.

inextensibility condition, we require the arc-length distance between any two physical material elements of the elastic material to remain constant throughout the cell deformation. It is important to distinguish between the arc-length parameter s and the position of a physical material element, which will not in general correspond to a fixed value of s throughout the cell deformation. The arc-length parameter s represents some arbitrarily chosen arc-length parametrisation, which in our case will be determined in terms of a conformal mapping from the unit circle, and does not in general correspond to a particular particle of the cell material throughout the cell deformation. However, since the cell material is assumed to be inextensible, the arc-length distance between any two material elements must be constant; the cell material is thus restricted to a tank-treading motion, with each material particle deviating by the same distance from its original arc-length position. The arc-length position of the material element initially located at $s = s_0$ can thus be expressed as $s = s_0 + S_0(t)$, where the function $S_0(t)$ gives the uniform deviation of the cell material from its initial arc-length position and will be determined by the dynamics of the system.

The material derivative of the cell is defined as

$$\frac{\mathrm{D}}{\mathrm{D}t} = \frac{\partial}{\partial t} + S_0' \frac{\partial}{\partial s}, \tag{2.2.1}$$

which gives the rate of change of a quantity from the perspective of a material element. The velocity of the cell material can then be defined as

$$\boldsymbol{v}^{(c)}(s,t) = \frac{\mathrm{D}\boldsymbol{\eta}}{\mathrm{D}t} = \boldsymbol{\eta}_t + S_0' \hat{\boldsymbol{\tau}}. \tag{2.2.2}$$

This is equal to the time derivative of the cell parametrisation for a fixed s plus the rate at which the material element is deviating from that fixed value of s in the tangential direction. The time derivatives of the tangent and normal vectors can be obtained by noting that $\hat{\boldsymbol{\tau}}_t \cdot \hat{\boldsymbol{\tau}} = \frac{1}{2}\frac{\partial}{\partial t}(\hat{\boldsymbol{\tau}} \cdot \hat{\boldsymbol{\tau}}) = 0$ and $\hat{\boldsymbol{n}}_t \cdot \hat{\boldsymbol{n}} = \frac{1}{2}\frac{\partial}{\partial t}(\hat{\boldsymbol{n}} \cdot \hat{\boldsymbol{n}}) = 0$, and so

$$\hat{\boldsymbol{\tau}}_t = (\hat{\boldsymbol{\tau}}_t \cdot \hat{\boldsymbol{n}})\hat{\boldsymbol{n}} = \big(\boldsymbol{\eta}_{st} \cdot \hat{\boldsymbol{n}}\big)\hat{\boldsymbol{n}} = -\mathrm{Im}\big(\eta_{st}\overline{\eta}_s\big)\hat{\boldsymbol{n}} \tag{2.2.3}$$

and

$$\hat{\boldsymbol{n}}_t = (\hat{\boldsymbol{n}}_t \cdot \hat{\boldsymbol{\tau}})\hat{\boldsymbol{\tau}} = \left(\frac{\partial}{\partial t}(\hat{\boldsymbol{n}} \cdot \hat{\boldsymbol{\tau}}) - \hat{\boldsymbol{n}} \cdot \hat{\boldsymbol{\tau}}_t\right)\hat{\boldsymbol{\tau}} = \mathrm{Im}\big(\eta_{st}\overline{\eta}_s\big)\hat{\boldsymbol{\tau}}. \tag{2.2.4}$$

The acceleration of the cell material is thus given by

$$\boldsymbol{a}^{(c)}(s,t) = \frac{\mathrm{D}^2\boldsymbol{\eta}}{\mathrm{D}t^2} = \boldsymbol{\eta}_{tt} + S_0''\hat{\boldsymbol{\tau}} - 2S_0'\mathrm{Im}\big(\eta_{st}\overline{\eta}_s\big)\hat{\boldsymbol{n}} + {S_0'}^2\kappa\hat{\boldsymbol{n}}. \tag{2.2.5}$$

As well as restricting the motion of the cell material, the inextensibility condition requires the cell to have constant perimeter $2\pi\ell$, equal to that of the undeformed rest cell. The cell parametrisation $\eta(s,t)$ must therefore be periodic in s with period $2\pi\ell$.

We then consider the forces acting on the cell wall. Figure 2.2.1 shows the forces acting on a cut-out segment of the cell wall. The cell is subjected to a transmural pressure $\Delta p(s,t)$ acting in the direction $-\hat{\boldsymbol{n}}$ normal to the cell

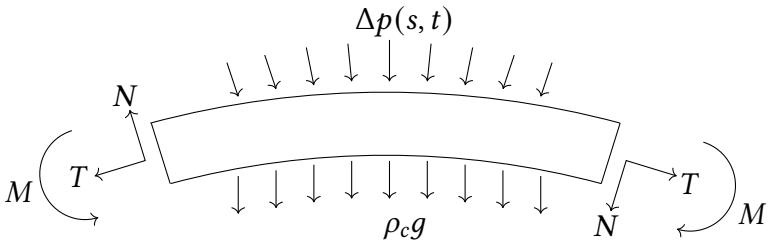

Figure 2.2.1: The forces acting on a segment of the elastic cell.

boundary, and a weight per unit area $\rho_c hg$ acting in the negative vertical direction $-\boldsymbol{j}$. The cell material has some internal stress vector $\boldsymbol{R}(s,t) = N(s,t)\hat{\boldsymbol{n}} + T(s,t)\hat{\boldsymbol{\tau}}$, where $N(s,t)$ and $T(s,t)$ are the normal and tangential components of the stress respectively. By convention we take $\boldsymbol{R}(s,t)$ to be the stress acting on the end of the segment with a higher value of s, and $-\boldsymbol{R}(s,t)$ to be the stress acting on the end of the segment with a lower value of s. There is also bending moment $M(s,t)$ acting at each end of the segment. By convention a positive value of $M(s,t)$ will act anticlockwise on the end of the segment with a higher value of s and clockwise on the end with a lower value of s. This bending moment arises directly from the elasticity of the cell, acting to restore a deformed cell to its rest state.

Following the work of Pozrikidis (2002a), we assume the bending moment at any point is directly proportional to the deviation of the curvature κ of the cell wall from the circular rest-state, which has radius ℓ and curvature $-1/\ell$. This gives the constitutive equation for the bending moment

$$M = -E_B\left(\frac{1}{\ell} + \kappa\right), \tag{2.2.6}$$

where E_B is the flexural rigidity of the cell material; this is the force couple required to bend the cell one unit of curvature from its rest-state. According to thin-shell theory (Pozrikidis, 2002a), the flexural rigidity is given by $E_B = \frac{Eh^3}{12(1-\nu^2)}$, where E is the Young's modulus of the cell material, ν is the Poisson's ratio of the cell material, and h is the thickness of the cell wall.

To obtain a relation between the internal stress $\boldsymbol{R}(s,t)$ and the bending moment $M(s,t)$, we consider a small segment of the cell wall of length $2\delta s$ spanning from $s-\delta s$ to $s+\delta s$. We consider the rotational form of Newton's 2nd law acting on this segment, which states that the rate of change of the angular momentum of a body is equal to the sum of all external moments acting upon it. This can be written as

$$\sum M_i \boldsymbol{k} = \rho_c h \frac{\mathrm{d}}{\mathrm{d}t} \int_{s-\delta s}^{s+\delta s} \left[\boldsymbol{\eta}(s',t) - \boldsymbol{\eta}_0(t)\right] \times \boldsymbol{v}^{(c)}(s',t)\mathrm{d}s' \tag{2.2.7}$$

where $\boldsymbol{k} \equiv \boldsymbol{i} \times \boldsymbol{j}$, $\boldsymbol{\eta}_0(t)$ is the centre of mass of the segment, $\sum M_i$ is the sum of the all moments acting on the segment about the centre of mass, and $\rho_c h \int_{s-\delta s}^{s+\delta s} \left[\boldsymbol{\eta}(s',t) - \boldsymbol{\eta}_0(t)\right] \times \boldsymbol{v}^{(c)}(s',t)\mathrm{d}s'$ is the angular momentum of the elastic material. The moments acting on the segment are the bending moments $M(s+\delta s,t)$ and $-M(s-\delta s,t)$, the moments due to the stress acting at each end of the cell $\left[\boldsymbol{\eta}(s+\delta s,t) - \boldsymbol{\eta}_0(t)\right] \times \boldsymbol{R}(s+\delta s,t)$ and $\left[\boldsymbol{\eta}(s-\delta s,t) - \boldsymbol{\eta}_0(t)\right] \times -\boldsymbol{R}(s-\delta s,t)$, and the moment due to the external forces acting upon the cell

$$\int_{s-\delta s}^{s+\delta s} \left[\boldsymbol{\eta}(s',t) - \boldsymbol{\eta}_0(t)\right] \times \left[-\rho_c h g \boldsymbol{j} - \Delta p(s',t)\hat{\boldsymbol{n}}(s',t)\right]\mathrm{d}s'.$$

Equation (2.2.7) thus gives

$$\begin{aligned}
&M(s+\delta s,t)\boldsymbol{k} - M(s-\delta s,t)\boldsymbol{k} \\
&+ \left[\boldsymbol{\eta}(s+\delta s,t) - \boldsymbol{\eta}_0(t)\right] \times \boldsymbol{R}(s+\delta s,t) - \left[\boldsymbol{\eta}(s-\delta s,t) - \boldsymbol{\eta}_0(t)\right] \times \boldsymbol{R}(s-\delta s,t) \\
&- \int_{s-\delta s}^{s+\delta s} \left[\boldsymbol{\eta}(s',t) - \boldsymbol{\eta}_0(t)\right] \times \left[\rho_c h g \boldsymbol{j} + \Delta p(s')\hat{\boldsymbol{n}}(s',t)\right]\mathrm{d}s' \\
&= \frac{d}{dt} \int_{s-\delta s}^{s+\delta s} \rho_c h \left[\boldsymbol{\eta}(s',t) - \boldsymbol{\eta}_0(t)\right] \times \boldsymbol{v}^{(c)}(s',t)\mathrm{d}s'.
\end{aligned}$$

Dividing this expression by δs and taking the limit as $\delta s \to 0$, we obtain $2M_s\boldsymbol{k} + 2\boldsymbol{\eta}_s \times \boldsymbol{R} = 0$, where $\boldsymbol{\eta}_s \times \boldsymbol{R} = -N\boldsymbol{k}$. Recalling the elastic constitutive relation

(2.2.6), we obtain

$$N = M_s = -E_B \kappa_s. \tag{2.2.8}$$

The normal stress $N(s,t)$ is thus given explicitly in terms of the cell curvature $\kappa(s,t)$ and the flexural rigidity E_B.

Next considering the linear form of Newton's second law on the same segment of the cell material, we require

$$\begin{aligned} &\boldsymbol{R}(s+\delta s,t) - \boldsymbol{R}(s-\delta s,t) \\ &- \int_{s-\delta s}^{s+\delta s} [\rho_c h g \boldsymbol{j} + \Delta p(s',t)\hat{\boldsymbol{n}}(s',t)]\mathrm{d}s' = \int_{s-\delta s}^{s+\delta s} \rho_c h \boldsymbol{a}^{(c)}(s',t)\mathrm{d}s', \end{aligned}$$

where the left-hand side is the net force acting upon the segment and the right-hand side is the mean acceleration of the segment, where $\boldsymbol{a}^{(c)}(s,t)$ is the material acceleration of the cell given by (2.2.5). Dividing this expression by δs and taking the limit as $\delta s \longrightarrow 0$, we obtain

$$\boldsymbol{R}_s - \rho_c h g \boldsymbol{j} - \Delta p \hat{\boldsymbol{n}} = \rho_c \boldsymbol{a}^{(c)}. \tag{2.2.9}$$

Recalling from (2.2.8) that $N = -E_B \kappa_s$, $\boldsymbol{R}_s$ can be written in the form

$$\boldsymbol{R}_s = \frac{\partial}{\partial s}(-E_B \kappa_s \hat{\boldsymbol{n}} + T\hat{\boldsymbol{\tau}}) = (-E_B \kappa_{ss} + \kappa T)\hat{\boldsymbol{n}} + (T_s + E_B \kappa \kappa_s)\hat{\boldsymbol{\tau}},$$

where the derivatives of $\hat{\boldsymbol{\tau}}$ and $\hat{\boldsymbol{n}}$ are given by the Frenet-Serret formulae. This allows us to split (2.2.9) into normal and tangential parts as

$$-E_B \kappa_{ss} + \kappa T + \rho_c h g \mathrm{Re}(\eta_s) - \Delta p = \rho_c h \boldsymbol{a}^{(c)} \cdot \hat{\boldsymbol{n}}, \tag{2.2.10}$$

$$T_s + E_B \kappa \kappa_s - \rho_c h g \mathrm{Im}(\eta_s) = \rho_c h \boldsymbol{a}^{(c)} \cdot \hat{\boldsymbol{\tau}}. \tag{2.2.11}$$

Integrating (2.2.11), we obtain

$$T = -\tfrac{1}{2}E_B\kappa^2 + \frac{E_B\sigma}{\ell^2} + \rho_c hg\mathrm{Im}(\eta) + \rho_c h\int_0^s \boldsymbol{a}^{(c)}\cdot\hat{\boldsymbol{\tau}}\,\mathrm{d}s, \tag{2.2.12}$$

where the term $\frac{E_B\sigma}{\ell^2}$ is an unknown function of integration with dimensionless function of time $\sigma(t)$, which acts as a sort of constraint force which must be chosen to satisfy the inextensibility constraint. The role of this parameter in the dynamics of the system will be explained in more detail in Chapter 3.

Recalling the expression for the material acceleration $\boldsymbol{a}^{(c)}$ given by (2.2.5), we have

$$\boldsymbol{a}^{(c)}\cdot\hat{\boldsymbol{n}} = -\mathrm{Im}\big(\eta_{tt}\overline{\eta}_s\big) - 2S_0'\mathrm{Im}\big(\eta_{st}\overline{\eta}_s\big) + \kappa S_0'^2, \quad \boldsymbol{a}^{(c)}\cdot\hat{\boldsymbol{\tau}} = \mathrm{Re}\big(\eta_{tt}\overline{\eta}_s\big) + S_0'',$$

where $S_0(t)$ is the arc-length position of the material element initially located at $s = 0$. Equation (2.2.12) is thus reduced to

$$T = -\tfrac{1}{2}E_B\kappa^2 + \frac{E_B\sigma}{\ell^2} + \rho_c hg\mathrm{Im}(\eta) + \rho_c h\left(S_0''s + \int_0^s Re\big(\eta_{tt}\overline{\eta}_s\big)\mathrm{d}s\right), \tag{2.2.13}$$

Substituting (2.2.13) into (2.2.10), we obtain

$$\begin{aligned}\Delta p = &-E_B\left(\kappa_{ss} + \tfrac{1}{2}\kappa^3 - \frac{\sigma}{\ell^2}\kappa\right) + \rho_c hg\big(\mathrm{Re}(\eta_s) + \kappa\mathrm{Im}(\eta)\big)\\ &+ \rho_c h\left(\mathrm{Im}\big(\eta_{tt}\overline{\eta}_s\big) + 2S_0'\mathrm{Im}\big(\eta_{st}\overline{\eta}_s\big) - \kappa S_0'^2 + S_0''\kappa s + \kappa\int_0^s \mathrm{Re}\big(\eta_{tt}\overline{\eta}_s\big)\mathrm{d}s\right).\end{aligned} \tag{2.2.14}$$

This equation implicitly determines the unsteady deformation of the cell in response to a given transmural pressure. This transmural pressure will generally depend on the fluid flows in the exterior and interior of the cell, which themselves depend on the deformed shape of the cell. The equations which govern the fluid flow and the coupling between the flow and the cell

deformation will be discussed in the following sections.

Evaluating the difference between (2.2.14) at $s = 2\pi$ and $s = 0$, we obtain

$$2\pi S_0'' + \int_0^{2\pi\ell} \mathrm{Re}\big(\eta_{tt}\overline{\eta}_s\big)\mathrm{d}s = \int_0^{2\pi\ell} \boldsymbol{a}^{(c)} \cdot \hat{\boldsymbol{\tau}}\mathrm{d}s = 0. \tag{2.2.15}$$

The value of S_0'', which determines the tangential acceleration of the cell material, is thus given explicitly in terms of the boundary parametrisation $\eta(s,t)$. We can obtain a more convenient expression for S_0'' by noting that

$$\mathrm{Re}\big(\eta_{tt}\overline{\eta}_s\big) = \frac{\partial}{\partial t}\mathrm{Re}\big(\eta_t\overline{\eta}_s\big) - \frac{1}{2}\frac{\partial}{\partial s}\big(\eta_t\overline{\eta}_t\big),$$

which gives

$$S_0'' = -\frac{1}{2\pi\ell}\frac{\partial}{\partial t}\left(\int_0^{2\pi\ell} \mathrm{Re}\big(\eta_t\overline{\eta}_s\big)\mathrm{d}s\right).$$

We thus obtain

$$S_0'(t) = S_0'(0) + \frac{1}{2\pi\ell}\left[\int_0^{2\pi\ell} \boldsymbol{\eta}_t \cdot \boldsymbol{\eta}_s\mathrm{d}s\right]_{t=0} - \frac{1}{2\pi\ell}\int_0^{2\pi\ell} \boldsymbol{\eta}_t \cdot \boldsymbol{\eta}_s\mathrm{d}s. \tag{2.2.16}$$

This equation can be considered as a conservation of the angular momentum of the cell wall, which determines the speed of the tank-treading of the cell material relative to the arc-length parameter s. Note that the value of $S_0(t)$ does not appear in (2.2.14), which depends only on $S_0'(t)$ and $S_0''(t)$, which are both given explicitly in terms of $\eta(s,t)$ and its derivatives.

2.3 Fluid Flow

We next consider the equations which govern the unsteady fluid flow in the interior and exterior of the cell. Both fluids are assumed to be incompressible, irrotational, and inviscid; these assumptions allow for the use of a complex potential to describe the flows, which will significantly simplify the problem.

The exterior and interior fluids have uniform densities $\rho^{(e)}$ and $\rho^{(i)}$ respectively. In the far-field the exterior fluid takes the form of a uniform stream of speed U in the positive horizontal direction, and the fluid is taken to have some constant circulation Γ around the cell.

Since both fluids are inviscid and incompressible, their flows are governed by the incompressible Euler equations along with the irrotationality condition (Batchelor, 2000)

$$\frac{\partial \boldsymbol{u}}{\partial t} + \frac{1}{2}\nabla \boldsymbol{u}^2 + \frac{1}{\rho}\nabla p - \boldsymbol{g} = 0, \quad \text{(Euler momentum equation)} \tag{2.3.1}$$

$$\nabla \cdot \boldsymbol{u} = 0, \quad \text{(Incompressibility)} \tag{2.3.2}$$

$$\nabla \times \boldsymbol{u} = 0, \quad \text{(Irrotationality)} \tag{2.3.3}$$

where $\boldsymbol{u}(z,t)$ is the flow velocity, ρ is the fluid density, $p(z,t)$ is the fluid pressure, and $\boldsymbol{g}$ is the force of gravity acting on the fluid. These equations are valid for both the exterior flow $\boldsymbol{u}^{(e)}(z,t)$ and the interior flow velocity $\boldsymbol{u}^{(i)}(z,t)$; we use a superscript to distinguish between the two regions only where a distinction is required. The incompressibility and irrotationality conditions along with appropriately chosen boundary conditions determine the flow fields, while the Euler momentum equation simply determines the pressure field throughout the flow.

At the cell boundary $z = \eta(s,t)$ we require a kinematic boundary condition to ensure that no fluid passes through the cell wall, which is assumed to be impermeable. The component of the flow velocity normal to the cell wall must therefore be equal to the normal velocity of the cell wall itself, which can be written in vector form as

$$\boldsymbol{u}\big(\eta(s,t),t\big) \cdot \hat{\boldsymbol{n}}(s,t) = \boldsymbol{\eta}_t(s,t) \cdot \hat{\boldsymbol{n}}(s,t). \tag{2.3.4}$$

Note that since the fluids are inviscid, we do not impose a no-slip condition on the cell wall.

For the interior fluid, (2.3.1)–(2.3.4) fully determine the flow in the interior of a given cell. For the exterior flow however, we also require a boundary condition in the far-field. In the far-field the exterior flow is assumed to be a uniform stream of speed U in the positive horizontal direction, which gives the far-field condition

$$\boldsymbol{u}^{(e)}(z,t) \to U\boldsymbol{i} \quad \text{as} \quad |z| \to \infty. \tag{2.3.5}$$

Finally, we are free to choose the value of the circulation of the exterior flow around cell boundary Γ, defined by

$$\Gamma = \int_0^{2\pi} \boldsymbol{u}^{(e)} \cdot \hat{\boldsymbol{\tau}} \mathrm{d}s. \tag{2.3.6}$$

The fluid flow equations can be simplified by use of a complex potential $w(z)$, defined by $w(x + \mathrm{i}y) = \varphi(x,y) + \psi(x,y)\mathrm{i}$ where $\varphi(x,y)$ is the velocity potential of the flow and $\psi(x,y)$ is the stream function. Note that the exterior and interior flows each have distinct potentials, which are not required to match at the boundary. We use a superscript to distinguish between the potentials in the exterior and interior only where a distinction is required. The flow velocities are given in complex form by the complex potentials as $\overline{u}(z,t) = w_z(z,t)$, where $\overline{u}$ is the complex conjugate of u, or in vector form as $\boldsymbol{u}(z,t) = \nabla \mathrm{Re}(w(z,t))$. The potentials are required to be analytic throughout the region occupied by the fluids, specifically the exterior of the cell for the exterior potential $w^{(e)}(z,t)$ and the interior of the cell for the interior potential $w^{(i)}(z,t)$. Note however that there is no requirement for either of the potentials to be analytic at the cell boundary itself.

The benefits of using a complex potential can be seen by considering the incompressibility condition (2.3.2) and the irrotationality condition (2.3.3).

Since the complex potential is required to be analytic in the region of the flow, it must satisfy Laplace's equation $\nabla^2(\mathrm{Re}(w)) = 0$. The divergence of the flow velocity is thus $\nabla \cdot \boldsymbol{u} = \nabla^2(\mathrm{Re}(w)) = 0$, and so the incompressibility condition (2.3.2) is satisfied automatically. The vorticity of the flow is given by $\nabla \times \boldsymbol{u} = \nabla \times \nabla(\mathrm{Re}(w)) = 0$, and so the irrotationality condition (2.3.3) is also satisfied automatically. Thus by introducing a complex potential we have reduced the fluid flow problem to finding analytic functions $w^{(e)}(z,t)$ and $w^{(i)}(z,t)$ which satisfy the relevant boundary conditions; namely the kinematic condition (2.3.4) for both the interior and exterior potentials, as well as the far-field condition (2.3.5) and circulation (2.3.6) for the exterior potential, with the pressure field determined by Euler's equation (2.3.1).

To write the kinematic condition (2.3.4) in terms of the complex potential $w(z,t)$ we introduce the notation $\Omega(s,t) \equiv w(\eta(s,t),t)$ to denote the complex potential evaluated on the surface of the cell, where the derivatives are given by

$$w_z\big(\eta(s,t),t\big) = \frac{\Omega_s}{\eta_s}, \quad w_t\big(\eta(s,t),t\big) = \Omega_t - \frac{\eta_t}{\eta_s}\Omega_s.$$

The flow velocity evaluated at the cell boundary $z = \eta(s,t)$ is then given by

$$u(\eta(s,t),t) = \overline{w}_z(\eta(s,t),t) = \frac{\overline{\Omega}_s}{\overline{\eta}_s},$$

or in vector form as $\boldsymbol{u}(\eta(s,t),t) = \mathrm{Re}(\Omega_s)\hat{\boldsymbol{\tau}} + \mathrm{Im}(\Omega_s)\hat{\boldsymbol{n}}$, with the flow speed at the cell boundary given by $q(s,t) = |\Omega_s|$. The kinematic condition (2.3.4) is thus given in terms of the complex potentials as

$$\mathrm{Im}\Big(\Omega_s^{(e)}\Big) = \mathrm{Im}\Big(\Omega_s^{(i)}\Big) = -\mathrm{Im}\big(\eta_t\overline{\eta_s}\big). \tag{2.3.7}$$

For the exterior flow we must also satisfy the far-field condition (2.3.5) and the circulation condition (2.3.6). Recalling that the velocity is given in complex

form as $\overline{u^{(e)}} = w_z^{(e)}$, $\overline{u^{(e)}}$ must be analytic in z with a Laurent series of the form

$$\overline{u^{(e)}} = U + \sum_{n=1}^{\infty} a_n(t) z^{-n}, \tag{2.3.8}$$

where $\overline{u} \to U$ as $z \to \infty$ to satisfy the far-field condition. Integrating with respect to z, we obtain a series expansion for $w^{(e)}$ in the form

$$w^{(e)}(z,t) = Uz + a_1(t)\log z + \sum_{n=2}^{\infty} \frac{a_n(t)}{1-n} z^{1-n},$$

where the constant of integration, which plays no role in the flow field $\boldsymbol{u}^{(e)}$, has been taken to be zero. To satisfy the circulation condition (2.3.6), we require

$$\Gamma = \int_0^{2\pi} \mathrm{Re}\left(\eta_s \overline{u^{(e)}}\right) \mathrm{d}s = \mathrm{Re}\left(\oint_\eta \overline{u^{(e)}} \mathrm{d}z\right).$$

This contour integral can be evaluated using the residue theorem, where (2.3.8) gives the residue of $\overline{u^{(e)}}$ as a_{-1}. We thus have $\Gamma = \mathrm{Re}(2\pi \mathrm{i} a_1) = -2\pi \mathrm{Im}(a_1)$, and so $a_1 = \mathrm{Im}(a_1)\mathrm{i} = \frac{\Gamma}{2\pi \mathrm{i}}$. The complex potential thus takes the form

$$w^{(e)}(z,t) = Uz + \frac{\Gamma}{2\pi \mathrm{i}} \log z + \sum_{n=2}^{\infty} \frac{a_n}{1-n} z^{1-n}.$$

Since we have only determined $w^{(e)}$ up to $O(1/z)$ as $z \to \infty$, this can be written as a far-field condition

$$w^{(e)}(z,t) - Uz - \frac{\Gamma}{2\pi \mathrm{i}} \log z \to 0 \quad \text{as} \quad |z| \to \infty, \tag{2.3.9}$$

which contains both the far-field condition for the flow velocity (2.3.5) and the circulation condition (2.3.6).

To obtain the pressure field in the flow, we note that the Euler momentum

equation (2.3.1) is given in terms of the complex potential as

$$\nabla\left(\mathrm{Re}\left(\frac{\partial w}{\partial t}\right)+\tfrac{1}{2}|\nabla w|^2+\frac{1}{\rho}p+gy\right)=0,$$

which we integrate to obtain Bernoulli's equation

$$\mathrm{Re}\left(\frac{\partial w}{\partial t}\right)+\tfrac{1}{2}|\nabla w|^2+\frac{1}{\rho}p+gy=C(t), \tag{2.3.10}$$

where $C(t)$ is some function of time. Evaluating Bernoulli's equation for the interior fluid and comparing to some arbitrary reference point $z=z_0(t)$ located in the interior of the cell to remove the unknown function $C(t)$, we find that the internal fluid pressure evaluated at the cell boundary is given by

$$\begin{aligned}p^{(i)}=p_0-\rho^{(i)}\,\mathrm{Re}&\left(\Omega_t^{(i)}-\frac{\eta_t}{\eta_s}\Omega_s^{(i)}-w_t^{(i)}(z_0,t)\right)\\&-\frac{\rho^{(i)}}{2}\left(\left|\Omega_s^{(i)}\right|^2-\left|w_z^{(i)}(z_0,t)\right|^2\right)-\rho^{(i)}g\mathrm{Im}(\eta-z_0),\end{aligned} \tag{2.3.11}$$

where $p_0(t)$ is the interior fluid pressure evaluated at the interior reference point $z=z_0(t)$. The value of $p_0(t)$ cannot be freely chosen, and will be determined by the dynamics of the system. Note that setting $\rho^{(i)}=0$ reduces the interior to a uniform pressure.

For the exterior fluid pressure, we firstly evaluate Bernoulli's equation in the far-field $|x|\to\infty$ and $y=0$, which gives

$$C(t)=\frac{1}{2}U^2+\frac{p_\infty}{\rho^{(e)}},$$

where p_∞ is the far-field pressure evaluated at $y=0$. The fluid pressure evaluated at the cell boundary is thus given by

$$p^{(e)}=p_\infty-\rho^{(e)}\mathrm{Re}\left(\Omega_t^{(e)}-\frac{\eta_t}{\eta_s}\Omega_s^{(e)}\right)-\frac{\rho^{(e)}}{2}\left(\left|\Omega_s^{(e)}\right|^2-U^2\right)-\rho^{(e)}g\mathrm{Im}(\eta). \tag{2.3.12}$$

2.4 Coupled System

We now seek to combine the equations which govern the cell deformation with those which govern the unsteady fluid flow to form a single coupled system which governs the full dynamics of the problem. Recalling that the cell deformation equation (2.2.14) depends on the transmural pressure difference, we substitute the expressions for the exterior and interior fluid pressures (2.3.12) and (2.3.11) into (2.2.14) to obtain the dynamic condition

$$\begin{aligned}
&p_0 - p_\infty - E_B\left(\kappa_{ss} + \tfrac{1}{2}\kappa^3 - \frac{\sigma}{\ell^2}\kappa\right) \\
&+ \rho^{(e)}\,\mathrm{Re}\left(\Omega_t^{(e)} - \frac{\eta_t}{\eta_s}\Omega_s^{(e)}\right) + \tfrac{1}{2}\rho^{(e)}\left(\left|\Omega_s^{(e)}\right|^2 - U^2\right) \\
&- \rho^{(i)}\,\mathrm{Re}\left(\Omega_t^{(i)} - \frac{\eta_t}{\eta_s}\Omega_s^{(i)} - w_t^{(i)}(z_0,t)\right) - \tfrac{1}{2}\rho^{(i)}\left(\left|\Omega_s^{(i)}\right|^2 - \left|w_z^{(i)}(z_0,t)\right|^2\right) \\
&+ \rho^{(e)} g\,\mathrm{Im}(\eta) - \rho^{(i)} g\,\mathrm{Im}(\eta - z_0) \\
&+ \rho_c h g\big(\mathrm{Re}(\eta_s) + \kappa\,\mathrm{Im}(\eta)\big) \\
&+ \rho_c h\left(\mathrm{Im}\big(\eta_{tt}\overline{\eta}_s\big) + 2S_0'\eta_{st}\overline{\eta}_s - \kappa {S_0'}^2 + S_0''\kappa s + \kappa\int_0^s \mathrm{Re}\big(\eta_{tt}\overline{\eta}_s\big)\mathrm{d}s\right) = 0.
\end{aligned} \tag{2.4.1}$$

Here the terms on first line are the elastic and pressure terms, the terms on the second and third rows relate to the exterior and interior flows respectively, the fourth row relates to the buoyancy of the cell, the fifth row relates to the weight of the cell, and the sixth row relates to the inertia of the cell. The dynamic condition (2.4.1) and the kinematic condition (2.3.4) couple the elastic deformation problem with the fluid flow problem, determining the unsteady interaction between the elastic cell and fluids in the interior and exterior of the cell.

We then nondimensionalise the system, taking the length scale ℓ to be the perimeter of the cell divided by 2π, the velocity scale to be $\sqrt{E_B/\left(\ell^3\rho^{(e)}\right)}$, and the time scale to be $\sqrt{\ell^5\rho^{(e)}/E_B}$. Rescaling all variables and substituting into

Symbol	Meaning
α	Far-field flow speed
β	Circulation
$P(t)$	Pressure difference between the far-field and the interior
ϱ	Ratio between the exterior and interior fluid densities
D	Cell density
G	Strength of gravity
s	Arc-length distance around the cell boundary
z	Position in the complex plane
ζ	Position in the preimage plane
ϕ	Arc-length parameter of the unit circle in the ζ-plane
$\eta(s,t)$	Complex position of the cell boundary
$\hat{\boldsymbol{\tau}}(s,t)$	Unit tangent vector to the cell boundary
$\hat{\boldsymbol{n}}(s,t)$	Unit normal vector to the cell boundary
$\kappa(s,t)$	Curvature of the cell boundary
$\sigma(t)$	Parameter related to the internal stress of the cell
$z_0(t)$	Interior reference point
$w^{(e)}/w^{(i)}(z,t)$	Complex potential of the exterior/interior flow
$\Omega^{(e)}/\Omega^{(i)}(s,t)$	Complex potentials of the exterior/interior flow evaluated at the cell boundary
$u^{(e)}/u^{(i)}(z,t)$	Velocity of the exterior/interior flow
$q^{(e)}/q^{(i)}(s,t)$	Exterior/interior flow speed evaluated at the cell boundary
$v^{(c)}(s,t)$	Velocity of the cell material
$a^{(c)}(s,t)$	Acceleration of the cell material
$S_0(t)$	Arc-length position of the material element initially located at $s = 0$, $t = 0$

Table 2.2: The dimensionless parameters of the system.

(2.4.1), we obtain the dimensionless dynamic condition

$$\begin{aligned}
&\mathrm{Re}\left(\Omega_t^{(e)} - \frac{\eta_t}{\eta_s}\Omega_s^{(e)}\right) + \frac{1}{2}\left(\left|\Omega_s^{(e)}\right|^2 - \alpha^2\right) - P - \left(\kappa_{ss} + \tfrac{1}{2}\kappa^3 - \sigma\kappa\right) \\
&- \varrho\mathrm{Re}\left(\Omega_t^{(i)} - \frac{\eta_t}{\eta_s}\Omega_s^{(i)} - w_t^{(i)}(z_o, t)\right) - \frac{\varrho}{2}\left(\left|\Omega_s^{(i)}\right|^2 - \left|w_z^{(i)}(z_0, t)\right|^2\right) \\
&+ G\,\mathrm{Im}\left(\eta - \varrho\eta + \varrho z_0\right) + GD\left(\mathrm{Re}(\eta_s) + \kappa\mathrm{Im}(\eta)\right) \\
&+ D\left(\mathrm{Im}(\eta_{tt}\overline{\eta}_s) + 2S_0'\eta_{st}\overline{\eta}_s - \kappa S_0'^2 + S_0''\kappa s + \kappa\int_0^s \mathrm{Re}(\eta_{tt}\overline{\eta}_s)\mathrm{d}s\right) = 0,
\end{aligned} \tag{2.4.2}$$

where all variables are henceforth assumed to be dimensionless, and the dimensionless parameters are defined as

$$\alpha = U\sqrt{\frac{\ell^3\rho^{(e)}}{E_B}}, \quad \beta = -\Gamma\sqrt{\frac{\ell\rho^{(e)}}{E_B}}, \quad G = \frac{g\rho^{(e)}\ell^4}{E_B}, \quad D = \frac{\rho_c h}{\rho^{(e)}\ell}, \quad \varrho = \frac{\rho^{(i)}}{\rho^{(e)}}, \tag{2.4.3}$$

where α is proportional to the far-field flow speed, β is proportional to the circulation around the cell, $P(t)$ is proportional to the pressure difference between the far-field and the interior reference point z_0, G is proportional to the strength of gravity, D is proportional to the density of the cell material, and ϱ is the density ratio between the interior and exterior fluids. Note that a positive value of β corresponds to a negative value of Γ, such that a positive value of β corresponds to a positive lift acting upon the cell.

The dimensionless functions of time $P(t) = \left(p_\infty - p_0(t)\right)\ell^3/E_B$ and $\sigma(t)$, which relate to the pressure difference between the far-field and the interior and to the internal stress of the cell respectively, are determined implicitly by equation (2.4.2). The interior reference point $z_0(t)$ can be freely chosen.

For clarity we will restate here all the dimensionless equations and conditions which the dimensionless variables must satisfy to complete the system.

The function $\eta(s, t)$ is the arc-length parametrised cell wall position in the

complex z-plane, which must be periodic in s with period 2π. The curvature of the cell is given by $\kappa = -\mathrm{Im}(\eta_{ss}\overline{\eta}_s)$. The parameter $S_0(t)$, which tracks the arc-length position of the material element initially located at $s = 0$, is given by

$$S_0'(t) = S_0'(0) + \frac{1}{2\pi}\left[\int_0^{2\pi} \boldsymbol{\eta}_t \cdot \boldsymbol{\eta}_s \mathrm{d}s\right]_{t=0} - \frac{1}{2\pi}\int_0^{2\pi} \boldsymbol{\eta}_t \cdot \boldsymbol{\eta}_s \mathrm{d}s, \tag{2.4.4}$$

with $S_0(0) = 0$. The value $S_0'(0)$ can be freely chosen as an initial value.

The exterior complex potential $w^{(e)}(z,t)$, which is required to be analytic in the exterior of the cell, must satisfy the far-field condition

$$w^{(e)}(z,t) - \alpha z + \frac{\beta}{2\pi \mathrm{i}} \log z \to 0 \quad \text{as} \quad |z| \to \infty, \tag{2.4.5}$$

as well as the kinematic boundary condition

$$\mathrm{Im}\left(\Omega_s^{(e)}\right) = -\mathrm{Im}\left(\eta_t \overline{\eta}_s\right), \tag{2.4.6}$$

where here $\Omega^{(e)}(s,t) = w^{(e)}(\eta(s,t),t)$ is the complex potential evaluated at the cell boundary. The flow velocity at the cell boundary is given by

$$u^{(e)}(\eta(s,t),t) = \frac{\overline{\Omega}_s^{(e)}}{\overline{\eta_s}} = \mathrm{Re}\left(\Omega_s^{(e)}\right)\hat{\tau} + \mathrm{Im}\left(\Omega_s^{(e)}\right)\hat{n}, \tag{2.4.7}$$

with flow speed $q^{(e)}(s,t) = \left|\Omega_s^{(e)}\right|$.

The interior complex potential $w^{(i)}(z,t)$, which is required to be analytic in the interior of the cell, must satisfy the kinematic boundary condition

$$\mathrm{Im}\left(\Omega_s^{(i)}\right) = -\mathrm{Im}\left(\eta_t \overline{\eta}_s\right), \tag{2.4.8}$$

where here $\Omega^{(i)}(s,t) = w^{(i)}(\eta(s,t),t)$ is the complex potential evaluated at the

cell boundary. The interior flow velocity at the cell boundary is given by

$$u(\eta(s,t),t)^{(i)} = \frac{\overline{\Omega}_s^{(i)}}{\overline{\eta}_s} = \mathrm{Re}\left(\Omega_s^{(i)}\right)\hat{\tau} + \mathrm{Im}\left(\Omega_s^{(i)}\right)\hat{n}, \tag{2.4.9}$$

with flow speed $q^{(i)}(s,t) = \left|\Omega_s^{(i)}\right|$.

These equations and conditions form a complete system which implicitly determines the unsteady evolution of the cell boundary $\eta(s,t)$, the interior and exterior fluid flow potentials $w^{(i)}(z,t)$ and $w^{(e)}(z,t)$, and the time-dependent values $\sigma(t)$, $S_0(t)$ and $P(t)$, for a given choice of initial conditions. The parameters α, β, G, D and ϱ can be freely chosen, as can the internal reference point $z_0(t)$.

While the above system is complete, in practice it is difficult to solve the two-dimensional flow fields either analytically or numerically. In Section 2.6 we present a conformal mapping technique which can be used to reduce the fluid flow equations to one-dimensional boundary conditions, significantly simplifying the system.

2.5 Energies of the System

In this section we derive expressions for each form of energy in the system. We also obtain expressions for the time-derivatives of each of the energies, and show how these each relate to terms in the dynamic condition (2.4.2).

The system contains seven distinct forms of energy; the interior and exterior fluids each have a kinetic energy and a gravitational potential energy, while the cell wall itself has a kinetic energy, a gravitational potential energy, and an elastic bending energy due to the internal elastic forces of the cell.

2.5.1 Translating Reference Frame

Some care is required in defining the energies of the exterior fluid. Since the exterior fluid occupies an infinite area, with mean dimensionless flow speed α, the kinetic energy of the fluid defined in the standard sense will be infinite. We instead evaluate the kinetic energy in a reference frame moving at speed α in the positive horizontal direction, and show that in this moving reference frame the exterior fluid has a finite kinetic energy. It's important to note that the kinetic energies of both the interior fluid and the cell wall will vary between the two reference frames, and we must therefore evaluate all kinetic energies in this moving reference frame. Since the reference frame is translating horizontally, the bending energy of the cell and the three gravitational potentials are invariant between the two reference frames, and can therefore be evaluated in either reference frame.

Denoting values in the moving reference frame with a tilde, the complex position in the moving reference frame is given by $\tilde{z} \equiv z - \alpha t$, with the cell boundary located at $\tilde{z} = \tilde{\eta}(s,t) \equiv \eta(s,t) - \alpha t$. The complex potentials and corresponding flow velocities for the interior and exterior fluids are then given by $\tilde{w}(\tilde{z},t) \equiv w(\tilde{z}+\alpha t,t) - \alpha(\tilde{z}+\alpha t)$ and $\tilde{\boldsymbol{u}}(\tilde{z},t) \equiv \boldsymbol{u}(\tilde{z}+\alpha t,t) - \alpha \boldsymbol{i}$ respectively, with the complex potential at the cell boundary given by $\tilde{\Omega}(s,t) \equiv \Omega(s,t) - \alpha\eta(s,t)$.

The far-field condition for the exterior fluid in the moving reference frame is

$$\tilde{w}^{(e)}(\tilde{z},t) + \frac{\beta}{2\pi \mathrm{i}} \log \tilde{z} \to 0 \quad \text{as} \quad |\tilde{z}| \to \infty, \tag{2.5.1}$$

and the kinematic condition in the moving reference frame is

$$\left(\tilde{\boldsymbol{\eta}}_t - \tilde{\boldsymbol{u}}\right) \cdot \hat{\boldsymbol{n}} = 0. \tag{2.5.2}$$

Note that $\hat{\boldsymbol{\tau}}(s,t)$, $\hat{\boldsymbol{n}}(s,t)$ and $\kappa(s,t)$ are all invariant under the change of reference frame, as they depend only on the shape of the cell which is

invariant between reference frames.

2.5.2 Kinetic Energy of the Exterior Fluid

We firstly consider the dimensionless kinetic energy of the exterior fluid in the moving reference frame. The dimensionless kinetic energy of the fluid in a given region $\tilde{A}$ in the $\tilde{z}$-plane is given by

$$\mathscr{K}^{(e)} = \frac{1}{2}\iint_{\tilde{A}} \left|\tilde{\boldsymbol{u}}^{(e)}\right|^2 \mathrm{d}\tilde{x}\mathrm{d}\tilde{y}. \tag{2.5.3}$$

We take the region $\tilde{A}$ to be the region between the cell boundary $\tilde{z} = \tilde{\eta}(s,t)$ and the circle $\tilde{z} = re^{\mathrm{i}\theta}$, where the radius r is taken to be sufficiently large to contain the cell entirely within the circle, as depicted in Figure 2.5.1. The total kinetic energy of the exterior fluid is then given as the limit of (2.5.3) as $r \to \infty$. To evaluate the surface integral, we make use of the two-dimensional form of the divergence theorem

$$\iint_{\tilde{A}} \nabla \cdot \boldsymbol{f}\mathrm{d}x\mathrm{d}y = \int_{\partial\tilde{A}} \boldsymbol{f} \cdot \hat{\boldsymbol{n}}\mathrm{d}s, \tag{2.5.4}$$

where $\partial\tilde{A}$ is the boundary of the region $\tilde{A}$ and $\hat{\boldsymbol{n}}$ is the unit normal vector to the boundary pointing outwards from the region $\tilde{A}$. Noting that

$$\left|\tilde{\boldsymbol{u}}^{(e)}\right|^2 = \nabla \cdot \left(\mathrm{Re}\left(\tilde{w}^{(e)}\right)\tilde{\boldsymbol{u}}^{(e)}\right),$$

we apply the divergence theorem to (2.5.3) to obtain

$$\begin{aligned}\mathscr{K}^{(e)} &= \frac{1}{2}\iint_{\tilde{A}} \nabla \cdot \left(\mathrm{Re}\left(\tilde{w}^{(e)}\right)\tilde{\boldsymbol{u}}^{(e)}\right)\mathrm{d}\tilde{x}\mathrm{d}\tilde{y} \\ &= \frac{1}{2}\int_0^{2\pi} \mathrm{Re}\left(\tilde{w}^{(e)}\right)\tilde{\boldsymbol{u}}^{(e)} \cdot \hat{\boldsymbol{r}} r d\theta - \frac{1}{2}\int_0^{2\pi} \mathrm{Re}\left(\tilde{\Omega}^{(e)}\right)\tilde{\boldsymbol{u}}^{(e)} \cdot \hat{\boldsymbol{n}}\mathrm{d}s.\end{aligned} \tag{2.5.5}$$

For large $|\tilde{z}|$ the far-field condition gives

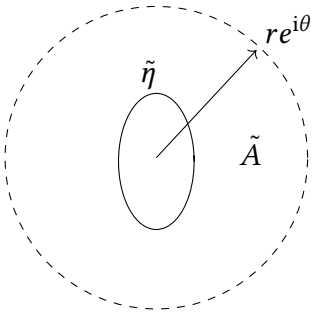

Figure 2.5.1: Sketch of the area $\tilde{A}$ between the cell boundary $\tilde{\eta}$ and the circle $\tilde{z} = re^{i\theta}$ over which the kinetic energy of the fluid is evaluated in (2.5.3).

$$\tilde{w}^{(e)} = -\frac{\beta}{2\pi i}\log\tilde{z} + O\left(\tilde{z}^{-1}\right) \quad \text{as} \quad |\tilde{z}| \to \infty,$$

and so

$$\mathrm{Re}\left(\tilde{w}^{(e)}\right) = -\frac{\beta\theta}{2\pi} + O\left(\frac{1}{r}\right) \quad \text{as} \quad r \to \infty$$

on the outer boundary B. We then have

$$\tilde{\boldsymbol{u}}^{(e)} \cdot \hat{\boldsymbol{r}} = \nabla\mathrm{Re}\left(\tilde{w}^{(e)}\right) \cdot \hat{\boldsymbol{r}} = \mathrm{Re}\left(\frac{\partial\tilde{w}^{(e)}}{\partial r}\right) = O\left(r^{-2}\right) \quad \text{as} \quad r \to \infty,$$

and so

$$\int_0^{2\pi} \tfrac{1}{2}\mathrm{Re}\left(\tilde{w}^{(e)}\right)\tilde{\boldsymbol{u}}^{(e)} \cdot \hat{\boldsymbol{r}} r \mathrm{d}\theta = O\left(\frac{1}{r}\right) \quad \text{as} \quad r \to \infty.$$

The contribution to the kinetic energy from the boundary B in (2.5.5) thus vanishes as $r \to \infty$, giving the total dimensionless kinetic energy of the exterior fluid as

$$\begin{aligned}\mathscr{K}^{(e)} &= -\frac{1}{2}\int_0^{2\pi} \mathrm{Re}\left(\tilde{\Omega}^{(e)}\right)\tilde{\boldsymbol{u}}^{(e)} \cdot \hat{\boldsymbol{n}}\mathrm{d}s \\ &= -\frac{1}{2}\int_0^{2\pi} \mathrm{Re}\left(\Omega^{(e)} - \alpha\eta\right)\mathrm{Im}\left(\Omega_s^{(e)} - \alpha\eta_s\right)\mathrm{d}s.\end{aligned} \tag{2.5.6}$$

We then consider the time derivative of $\mathscr{K}^{(e)}$, which is required to show that the total energy of the system is conserved in time. To obtain the time

derivative we could simply differentiate (2.5.6) directly; however, a more useful form can be obtained by applying Reynolds' transport theorem to (2.5.3). Reynolds' transport theorem states that for a function $f(z,t)$ and a time-dependent area $A(t)$ the time-derivative of the surface integral of f is given by

$$\frac{\mathrm{d}}{\mathrm{d}t}\iint_{A(t)} f\mathrm{d}x\mathrm{d}y = \iint_{A(t)} \frac{\partial f}{\partial t}\mathrm{d}x\mathrm{d}y + \oint_{\partial A(t)} \Big(\boldsymbol{v}^b \cdot \hat{\boldsymbol{n}}^b\Big) f dl, \tag{2.5.7}$$

where $\partial A(t)$ is the boundary curve of the area $A(t)$ and $\boldsymbol{v}^b \cdot \hat{\boldsymbol{n}}^b$ is the normal velocity of the boundary ∂A. Applying Reynolds' transport theorem to (2.5.3), and noting that the outer boundary is independent of time, we have

$$\frac{\mathrm{d}\mathscr{K}^{(e)}}{\mathrm{d}t} = \iint_{\tilde{A}} \tilde{\boldsymbol{u}}^{(e)} \cdot \tilde{\boldsymbol{u}}_t^{(e)}\mathrm{d}x\mathrm{d}y - \frac{1}{2}\int_0^{2\pi} \big|\tilde{\Omega}_s^{(e)}\big|^2 \big[\tilde{\boldsymbol{u}}^{(e)} \cdot \hat{\boldsymbol{n}}\big]\mathrm{d}s.$$

Then writing

$$\tilde{\boldsymbol{u}}^{(e)} \cdot \tilde{\boldsymbol{u}}_t^{(e)} = \nabla \cdot \Big(\mathrm{Re}\Big(\tilde{w}_t^{(e)}\Big)\tilde{\boldsymbol{u}}^{(e)}\Big),$$

we use the divergence theorem (2.5.4) to obtain

$$\begin{aligned}
\frac{\mathrm{d}\mathscr{K}^{(e)}}{\mathrm{d}t} &= \iint_{\tilde{A}} \tilde{\boldsymbol{u}}^{(e)} \cdot \tilde{\boldsymbol{u}}_t^{(e)}\mathrm{d}x\mathrm{d}y - \frac{1}{2}\int_0^{2\pi} \big|\tilde{\Omega}_s^{(e)}\big|^2 \big[\tilde{\boldsymbol{u}}^{(e)} \cdot \hat{\boldsymbol{n}}\big]\mathrm{d}s \\
&= \int_0^{2\pi} \mathrm{Re}\Big(\tilde{w}_t^{(e)}\Big)\tilde{\boldsymbol{u}}^{(e)} \cdot \hat{\boldsymbol{r}} r\mathrm{d}\theta - \int_0^{2\pi}\left[\mathrm{Re}\Big(\tilde{w}_t^{(e)}\Big) + \frac{1}{2}\big|\tilde{\Omega}_s^{(e)}\big|^2\right]\big[\tilde{\boldsymbol{u}}^{(e)} \cdot \hat{\boldsymbol{n}}\big]\mathrm{d}s \\
&= -\int_0^{2\pi}\left[\mathrm{Re}\left(\Omega_t^{(e)} - \frac{\eta_t}{\eta_s}\Omega_s^{(e)}\right) + \frac{1}{2}\big|\Omega_s^{(e)}\big|^2\right]\big[\tilde{\boldsymbol{\eta}}_t \cdot \hat{\boldsymbol{n}}\big]\mathrm{d}s,
\end{aligned} \tag{2.5.8}$$

where the contribution from the boundary B vanishes as $r \to \infty$. We observe that the term $\mathrm{Re}\Big(\Omega_t^{(e)} - \frac{\eta_t}{\eta_s}\Omega_s^{(e)}\Big) + \frac{1}{2}\big|\Omega_s^{(e)}\big|^2$ corresponds to a term in the dynamic condition (2.4.2). We will show that each of the energies of the system contain a corresponding term in (2.4.2).

2.5.3 Kinetic Energy of the Interior Fluid

The dimensionless kinetic energy of the fluid in the interior evaluated in the moving reference frame is given by

$$\mathscr{K}^{(i)} = \frac{\varrho}{2} \iint_{\tilde{A}} \left|\tilde{u}^{(i)}\right|^2 \mathrm{d}\tilde{x}\mathrm{d}\tilde{y}, \tag{2.5.9}$$

where $\tilde{A}$ is the region interior to the cell in the $\tilde{z}$-frame. Using the divergence theorem (2.5.4), we obtain

$$\begin{aligned} \mathscr{K}^{(i)} &= \frac{\varrho}{2} \iint_{\tilde{A}} \nabla \cdot \left(\mathrm{Re}\left(\tilde{w}^{(i)}\right)\tilde{\boldsymbol{u}}^{(i)}\right)\mathrm{d}x\mathrm{d}y = \frac{\varrho}{2} \int_{\partial\tilde{A}} \mathrm{Re}\left(\tilde{\Omega}^{(i)}\right)\left[\tilde{\boldsymbol{u}}^{(i)} \cdot \hat{\boldsymbol{n}}\right]\mathrm{d}s \\ &= \frac{\varrho}{2} \int_0^{2\pi} \mathrm{Re}\left(\Omega^{(i)} - \alpha\eta\right)\mathrm{Im}\left(\Omega_s^{(i)} - \alpha\eta_s\right)\mathrm{d}s. \end{aligned} \tag{2.5.10}$$

To obtain the time derivative of $\mathscr{K}^{(i)}$ we apply Reynolds' transport theorem (2.5.7) to (2.5.9), giving

$$\frac{\mathrm{d}\mathscr{K}^{(i)}}{\mathrm{d}t} = \varrho \iint_{\tilde{A}} \tilde{\boldsymbol{u}}^{(i)} \cdot \tilde{\boldsymbol{u}}_t^{(i)}\mathrm{d}x\mathrm{d}y + \frac{\varrho}{2} \int_{\partial\tilde{A}} \left|\tilde{\Omega}_s^{(i)}\right|^2 \left[\tilde{\boldsymbol{u}}^{(i)} \cdot \hat{\boldsymbol{n}}\right]\mathrm{d}s.$$

Recalling that

$$\tilde{\boldsymbol{u}}^{(i)} \cdot \tilde{\boldsymbol{u}}_t^{(i)} = \nabla \cdot \left(\mathrm{Re}\left(\tilde{w}_t^{(i)}\right)\tilde{\boldsymbol{u}}^{(i)}\right),$$

we use the divergence theorem (2.5.4) to obtain

$$\begin{aligned} \frac{\mathrm{d}\mathscr{K}^{(i)}}{\mathrm{d}t} &= \varrho \iint_{\tilde{A}} \tilde{\boldsymbol{u}}^{(i)} \cdot \tilde{\boldsymbol{u}}_t \mathrm{d}x\mathrm{d}y + \frac{\varrho}{2} \int_{\partial\tilde{A}} \left|\tilde{\Omega}_s^{(i)}\right|^2 \left[\tilde{\boldsymbol{u}}^{(i)} \cdot \hat{\boldsymbol{n}}\right]\mathrm{d}s \\ &= \varrho \int_0^{2\pi} \left[\mathrm{Re}\left(\Omega_t^{(i)} - \frac{\eta_t}{\eta_s}\Omega_s^{(i)}\right) + \frac{1}{2}\left|\Omega_s^{(i)}\right|^2\right]\left[\tilde{\boldsymbol{\eta}}_t \cdot \hat{\boldsymbol{n}}\right]\mathrm{d}s. \end{aligned} \tag{2.5.11}$$

We observe that the term $\varrho\left[\mathrm{Re}\left(\Omega_t^{(i)} - \frac{\eta_t}{\eta_s}\Omega_s^{(i)}\right) + \frac{1}{2}\left|\Omega_s^{(i)}\right|^2\right]$ corresponds to a term in the dynamic condition (2.4.2).

2.5.4 Gravitational Potential Energy of the Fluids

We next consider the dimensionless gravitational potential energies of the exterior and interior fluids. As with the kinetic energy, some care must be taken to ensure that the gravitational potential of the fluid in the exterior is finite. We define the gravitational potential energy of the exterior fluid relative to that of a uniform stream in the absence of an obstacle. The relative dimensionless gravitational potential of the exterior flow is given by

$$\mathscr{V}^{(e)} = -\iint_A Gy \,\mathrm{d}x\mathrm{d}y. \tag{2.5.12}$$

Using the divergence theorem (2.5.4), we obtain

$$\mathscr{V}^{(e)} = -G\int_0^{2\pi} \mathrm{Re}(\eta)\mathrm{Im}(\eta)\boldsymbol{i}\cdot\hat{\boldsymbol{n}}\mathrm{d}s = -G\int_0^{2\pi} \mathrm{Re}(\eta)\mathrm{Im}(\eta)\mathrm{Im}(\eta_s)\mathrm{d}s. \tag{2.5.13}$$

The dimensionless gravitational potential of the interior fluid, which is defined in the standard way, is given by

$$\mathscr{V}^{(i)} = \varrho G\iint_A y\mathrm{d}x\mathrm{d}y = \varrho G\int_0^{2\pi} \mathrm{Re}(\eta)\mathrm{Im}(\eta)\mathrm{Im}(\eta_s)\mathrm{d}s = -\varrho\mathscr{V}^{(e)}. \tag{2.5.14}$$

The time derivative of the gravitational potentials of the two fluids is then given by

$$\begin{aligned}\frac{\mathrm{d}\mathscr{V}^{(e)}}{\mathrm{d}t} + \frac{\mathrm{d}\mathscr{V}^{(i)}}{\mathrm{d}t} &= (\varrho-1)G\int_0^{2\pi} \mathrm{Im}(\eta)\big[\mathrm{Re}(\eta_t)\mathrm{Im}(\eta_s) - \mathrm{Im}(\eta_t)\mathrm{Re}(\eta_s)\big]\mathrm{d}s\\ &= (\varrho-1)G\int_0^{2\pi} \mathrm{Im}(\eta)\big[\boldsymbol{\eta}_t\cdot\hat{\boldsymbol{n}}\big]\mathrm{d}s.\end{aligned}$$

Recalling that $\tilde{\boldsymbol{\eta}}(s,t) = \boldsymbol{\eta}(s,t) - \alpha t\boldsymbol{i}$, we have $\boldsymbol{\eta}_t\cdot\hat{\boldsymbol{n}} = \tilde{\boldsymbol{\eta}}_t\cdot\hat{\boldsymbol{n}} + \alpha\mathrm{Im}(\eta_s)$, and so

$$\begin{aligned}\frac{\mathrm{d}\mathscr{V}^{(e)}}{\mathrm{d}t} + \frac{\mathrm{d}\mathscr{V}^{(i)}}{\mathrm{d}t} &= (\varrho-1)G\int_0^{2\pi} \mathrm{Im}(\eta)\big[\tilde{\boldsymbol{\eta}}_t\cdot\hat{\boldsymbol{n}}\big] + \alpha\mathrm{Im}(\eta)\mathrm{Im}(\eta_s)\mathrm{d}s\\ &= (\varrho-1)G\int_0^{2\pi} \mathrm{Im}(\eta)\big[\tilde{\boldsymbol{\eta}}_t\cdot\hat{\boldsymbol{n}}\big]\mathrm{d}s.\end{aligned} \tag{2.5.15}$$

We observe that the term $(\varrho - 1)G\mathrm{Im}(\eta)$ corresponds to a term in the dynamic condition (2.4.2).

2.5.5 Bending Energy of the Cell

We now consider the dimensionless internal bending energy of the elastic cell. This is the energy stored in the elastic material as it is deformed from its circular rest state. We introduce the bending energy functional $\mathscr{W}(\boldsymbol{\eta})$ which gives the bending energy for a given cell parametrisation $\boldsymbol{\eta}(s,t)$. To obtain an expression for the functional $\mathscr{W}(\boldsymbol{\eta})$, we follow the approach by Pozrikidis (2002) by considering the variation of the internal energy of the cell due to an infinitesimal perturbation $\delta\boldsymbol{\eta}$ to the cell shape $\boldsymbol{\eta}$, given by $\delta\mathscr{W} = \mathscr{W}(\boldsymbol{\eta} + \delta\boldsymbol{\eta}) - \mathscr{W}(\boldsymbol{\eta})$. This can be considered the change in bending energy due to a virtual displacement $\delta\boldsymbol{\eta}$ of the cell wall. The principle of virtual work states that this change in energy is equal to the negative of the work done by the internal stress through the deformation, given by

$$W_{\text{ext}} = \int_0^{2\pi} \boldsymbol{R}_s \cdot \delta\boldsymbol{\eta} \mathrm{d}s.$$

Since the cell perimeter must remain constant throughout the deformation, we use the same arc-length parameter s for both the perturbed and unperturbed cells. We thus require $\left|\frac{\partial}{\partial s}(\boldsymbol{\eta} + \delta\boldsymbol{\eta})\right| = 1$, and so

$$\left(\frac{\partial}{\partial s}(\boldsymbol{\eta} + \delta\boldsymbol{\eta})\right)^2 - \left(\frac{\partial \boldsymbol{\eta}}{\partial s}\right)^2 = 2\hat{\boldsymbol{\tau}} \cdot \frac{\partial \delta\boldsymbol{\eta}}{\partial s} = 0.$$

It thus follows that

$$\int_0^{2\pi} \frac{\partial}{\partial s}\big(f(s,t)\hat{\boldsymbol{\tau}}\big) \cdot \delta\boldsymbol{\eta} \mathrm{d}s = \int_0^{2\pi} f(s,t)\hat{\boldsymbol{\tau}} \cdot \frac{\partial \delta\boldsymbol{\eta}}{\partial s} \mathrm{d}s = 0, \tag{2.5.16}$$

for any function $f(s,t)$. This result will be used throughout this section. The variation of the bending energy is then given by the principle of virtual work as

$$\delta\mathscr{W} = -W_{\text{ext}} = -\int_0^{2\pi} \frac{\partial}{\partial s}(T\hat{\boldsymbol{\tau}} + N\hat{\boldsymbol{n}}) \cdot \delta\boldsymbol{\eta}\mathrm{d}s = \int_0^{2\pi} \frac{\partial}{\partial s}(\kappa_s\hat{\boldsymbol{n}}) \cdot \delta\boldsymbol{\eta}\mathrm{d}s.$$

Integrating by parts and applying (2.5.16), we obtain

$$\begin{aligned}\delta\mathscr{W} &= -\int_0^{2\pi} \kappa_s\hat{\boldsymbol{n}} \cdot \frac{\partial\delta\boldsymbol{\eta}}{\partial s}\mathrm{d}s \\ &= \int_0^{2\pi} (\kappa+1)\left[\hat{\boldsymbol{n}} \cdot \frac{\partial^2\delta\boldsymbol{\eta}}{\partial s^2} - \kappa\hat{\boldsymbol{\tau}} \cdot \frac{\partial\delta\boldsymbol{\eta}}{\partial s}\right]\mathrm{d}s \\ &= \int_0^{2\pi} (\kappa+1)\hat{\boldsymbol{n}} \cdot \frac{\partial^2\delta\boldsymbol{\eta}}{\partial s^2}\mathrm{d}s.\end{aligned}$$

Recalling that $\boldsymbol{\eta}_{ss} = \kappa\hat{\boldsymbol{n}}$ and thus $\kappa^2 = \boldsymbol{\eta}_{ss} \cdot \boldsymbol{\eta}_{ss}$, we have

$$2\kappa\delta\kappa = \delta\left(\kappa^2\right) = 2\frac{\mathrm{d}^2\boldsymbol{\eta}}{\mathrm{d}s^2} \cdot \frac{\mathrm{d}^2\delta\boldsymbol{\eta}}{\mathrm{d}s^2} = 2\kappa\hat{\boldsymbol{n}} \cdot \frac{\mathrm{d}^2\delta\boldsymbol{\eta}}{\mathrm{d}s^2},$$

and so

$$\delta\kappa = \hat{\boldsymbol{n}} \cdot \frac{\mathrm{d}^2\delta\boldsymbol{\eta}}{\mathrm{d}s^2}.$$

We thus obtain

$$\delta\mathscr{W} = \int_0^{2\pi} (\kappa+1)\delta\kappa\mathrm{d}s = \delta\int_0^{2\pi} \tfrac{1}{2}(\kappa+1)^2\mathrm{d}s.$$

The variation of internal energy is thus equal to the variation of the quantity

$$\mathscr{W} = \int_0^{2\pi} \tfrac{1}{2}(\kappa+1)^2\mathrm{d}s, \tag{2.5.17}$$

where $\kappa + 1$ is the deviation of the curvature from its rest state. We call this quantity the dimensionless bending energy of the cell.

To obtain the time derivative of the bending energy, we first note that

$$\kappa_t = \frac{1}{2\kappa}\frac{\partial}{\partial t}\left(\kappa^2\right) = \frac{1}{2\kappa}\frac{\partial}{\partial t}\left(\boldsymbol{\eta}_{ss}\cdot\boldsymbol{\eta}_{ss}\right) = \boldsymbol{\eta}_{sst}\cdot\hat{\boldsymbol{n}}.$$

The time derivative of the bending energy is thus given by

$$\frac{\mathrm{d}\mathscr{W}}{\mathrm{d}t} = \int_0^{2\pi}(\kappa+1)\boldsymbol{\eta}_{sst}\cdot\hat{\boldsymbol{n}}\mathrm{d}s.$$

Integrating by parts, and noting that $\boldsymbol{\eta}_{st}\cdot\hat{\boldsymbol{\tau}} = \frac{\partial}{\partial t}(\hat{\boldsymbol{\tau}}\cdot\hat{\boldsymbol{\tau}}) = 0$, we obtain

$$\begin{aligned}\frac{\mathrm{d}\mathscr{W}}{\mathrm{d}t} = \int_0^{2\pi} -\kappa_s\boldsymbol{\eta}_{st}\cdot\hat{\boldsymbol{n}}\mathrm{d}s &= \int_0^{2\pi}(\kappa_{ss}\hat{\boldsymbol{n}} - \kappa_s\kappa\hat{\boldsymbol{\tau}})\cdot\boldsymbol{\eta}_t\mathrm{d}s\\ &= \int_0^{2\pi}\left(\kappa_{ss}+\tfrac{1}{2}\kappa^3\right)\left[\boldsymbol{\eta}_t\cdot\hat{\boldsymbol{n}}\right]\mathrm{d}s.\end{aligned}$$

In terms of the moving reference frame variables, we have

$$\frac{\mathrm{d}\mathscr{W}}{\mathrm{d}t} = \int_0^{2\pi}\left(\kappa_{ss}+\tfrac{1}{2}\kappa^3\right)\left[\tilde{\boldsymbol{\eta}}_t\cdot\hat{\boldsymbol{n}}\right]\mathrm{d}s + \int_0^{2\pi}\left(\kappa_{ss}+\tfrac{1}{2}\kappa^3\right)\alpha\boldsymbol{i}\cdot\hat{\boldsymbol{n}}\mathrm{d}s$$

where

$$\int_0^{2\pi}\kappa_{ss}\boldsymbol{i}\cdot\hat{\boldsymbol{n}}\mathrm{d}s = \int_0^{2\pi}\kappa\kappa_s\boldsymbol{i}\cdot\hat{\boldsymbol{\tau}}\mathrm{d}s = \int_0^{2\pi}-\tfrac{1}{2}\kappa^3\boldsymbol{i}\cdot\hat{\boldsymbol{n}}\mathrm{d}s,$$

which gives

$$\frac{\mathrm{d}\mathscr{W}}{\mathrm{d}t} = \int_0^{2\pi}\left(\kappa_{ss}+\tfrac{1}{2}\kappa^3\right)\tilde{\boldsymbol{\eta}}_t\cdot\hat{\boldsymbol{n}}\mathrm{d}s. \tag{2.5.18}$$

We observe that the term $\kappa_{ss} + \frac{1}{2}\kappa^3$ corresponds to a term in the dynamic condition (2.4.2).

2.5.6 Kinetic Energy of the Cell

We next evaluate the dimensionless kinetic energy of the cell material. Since the kinetic energy will vary between the stationary and translating reference

frames, it must be evaluated in the translating reference frame introduced in Section 2.5.1 to remain consistent with the kinetic energies of the fluids. In this reference frame, the dimensionless kinetic energy of the cell is given by

$$\mathscr{K}^{(c)} = \int_0^{2\pi} \tfrac{1}{2} D \left| \boldsymbol{v}^{(c)} - \alpha \boldsymbol{i} \right|^2 \mathrm{d}s, \tag{2.5.19}$$

where $\boldsymbol{v}^{(c)} = \boldsymbol{\eta}_t + S_0' \hat{\boldsymbol{\tau}}$ is the material velocity of the cell material.

To obtain the time derivative of the kinetic energy, we recall the expression for the material acceleration (2.2.5), allowing us to write the time derivative of the kinetic energy as

$$\begin{aligned} \frac{\mathrm{d}\mathscr{K}^{(c)}}{\mathrm{d}t} &= D \int_0^{2\pi} \left(\tilde{\boldsymbol{\eta}}_t + S_0' \hat{\boldsymbol{\tau}} \right) \cdot \left(\boldsymbol{a}^{(c)} - S_0' \hat{\boldsymbol{\tau}}_t - S_0'^2 \kappa \hat{\boldsymbol{n}} \right) \mathrm{d}s \\ &= D \int_0^{2\pi} \tilde{\boldsymbol{\eta}}_t \cdot \boldsymbol{a}^{(c)} - S_0'^2 \tilde{\boldsymbol{\eta}}_t \cdot \boldsymbol{\eta}_{ss} + S_0' \hat{\boldsymbol{\tau}} \cdot \boldsymbol{a}^{(c)} \mathrm{d}s. \end{aligned}$$

The term $\hat{\boldsymbol{\tau}} \cdot \boldsymbol{a}$ vanishes due to (2.2.15), and since

$$\tilde{\boldsymbol{\eta}}_t \cdot \tilde{\boldsymbol{\eta}}_{ss} = \frac{\partial}{\partial s} \left(\tilde{\boldsymbol{\eta}}_t \cdot \tilde{\boldsymbol{\eta}}_s \right) - \frac{1}{2} \frac{\partial}{\partial t} \left(\tilde{\boldsymbol{\eta}}_s \cdot \tilde{\boldsymbol{\eta}}_s \right) = \frac{\partial}{\partial s} \left(\tilde{\boldsymbol{\eta}}_t \cdot \tilde{\boldsymbol{\eta}}_s \right)$$

the term $\tilde{\boldsymbol{\eta}}_t \cdot \tilde{\boldsymbol{\eta}}_{ss}$ also vanishes, leaving

$$\begin{aligned} \frac{\mathrm{d}\mathscr{K}^{(c)}}{\mathrm{d}t} &= D \int_0^{2\pi} \tilde{\boldsymbol{\eta}}_t \cdot \boldsymbol{a}^{(c)} \mathrm{d}s \\ &= D \int_0^{2\pi} \left(\tilde{\boldsymbol{\eta}}_t \cdot \hat{\boldsymbol{n}} \right) \left(\boldsymbol{a}^{(c)} \cdot \hat{\boldsymbol{n}} \right) + \left(\tilde{\boldsymbol{\eta}}_t \cdot \hat{\boldsymbol{\tau}} \right) \left(\boldsymbol{a}^{(c)} \cdot \hat{\boldsymbol{\tau}} \right) \mathrm{d}s. \end{aligned}$$

Noting that

$$\frac{\partial}{\partial s} \left(\boldsymbol{\eta}_t \cdot \hat{\boldsymbol{\tau}} \right) = \boldsymbol{\eta}_t \cdot \hat{\boldsymbol{\tau}}_s + \boldsymbol{\eta}_{st} \cdot \boldsymbol{\eta}_s = \kappa \boldsymbol{\eta}_t \cdot \hat{\boldsymbol{n}},$$

we integrate by parts to obtain

$$\frac{\mathrm{d}\mathscr{K}^{(c)}}{\mathrm{d}t} = \int_0^{2\pi} D \left(\boldsymbol{a}^{(c)} \cdot \hat{\boldsymbol{n}} - \kappa \int_0^s \boldsymbol{a}^{(c)} \cdot \hat{\boldsymbol{\tau}} \mathrm{d}s \right) \left[\tilde{\boldsymbol{\eta}}_t \cdot \hat{\boldsymbol{n}} \right] \mathrm{d}s. \tag{2.5.20}$$

Note that the term $D\Big(\boldsymbol{a}^{(c)} \cdot \hat{\boldsymbol{n}} - \kappa \int_0^s \boldsymbol{a}^{(c)} \cdot \hat{\boldsymbol{\tau}} \mathrm{d}s\Big)$ corresponds to a term in the dynamic condition (2.4.2).

2.5.7 Gravitational Potential Energy of the Cell

Finally, we consider the dimensionless gravitational potential of the cell material, which is given by

$$\mathscr{V}_c = \int_0^{2\pi} GD\mathrm{Im}(\eta)\mathrm{d}s. \tag{2.5.21}$$

Noting that $\mathrm{Im}(\eta_t) = \tilde{\boldsymbol{\eta}}_t \cdot \boldsymbol{j} = \tilde{\boldsymbol{\eta}}_t \cdot \big(\mathrm{Im}(\eta_s)\hat{\boldsymbol{\tau}} - \mathrm{Re}(\eta_s)\hat{\boldsymbol{n}}\big)$, the time derivative of the gravitational potential is given by

$$\frac{\mathrm{d}\mathscr{V}_c}{\mathrm{d}t} = -GD \int_0^{2\pi} \big(\mathrm{Re}(\eta_s) + \kappa \mathrm{Im}(\eta)\big)\big[\tilde{\boldsymbol{\eta}}_t \cdot \hat{\boldsymbol{n}}\big]\mathrm{d}s. \tag{2.5.22}$$

Note that the term $-GD\big(\mathrm{Re}(\eta_s) + \kappa \mathrm{Im}(\eta)\big)$ corresponds to a term in the dynamic condition (2.4.2).

2.5.8 Total Energy of the System

Now that we have obtained expressions for each of the seven distinct energies of the system, we can write the total energy of the system as

$$\begin{aligned}\mathscr{E} = \int_0^{2\pi} \Bigg[&\tfrac{1}{2}\mathrm{Re}\Big(\Omega^{(e)} - \alpha\eta\Big)\mathrm{Im}\Big(\Omega_s^{(e)} - \alpha\eta_s\Big) + \tfrac{1}{2}(\kappa+1)^2 \\ &+ \frac{\varrho}{2}\mathrm{Re}\Big(\Omega^{(i)} - \alpha\eta\Big)\mathrm{Im}\Big(\Omega_s^{(i)} - \alpha\eta_s\Big) + \tfrac{1}{2}D|\eta_t + S_t\eta_s - \alpha|^2 \\ &+ G(\varrho-1)\mathrm{Re}(\eta)\mathrm{Im}(\eta)\mathrm{Im}(\eta_s) + GD\mathrm{Im}(\eta)\Bigg]\mathrm{d}s.\end{aligned} \tag{2.5.23}$$

Finally, we verify that the total energy of the system is conserved. While the conservation of energy follows directly from the conservative formulation of the system, it is useful to verify it directly. We sum the time-derivatives of

each of the energies to obtain

$$\begin{aligned}\frac{\mathrm{d}\mathscr{E}}{\mathrm{d}t} = \int_0^{2\pi} \Bigg[&- \mathrm{Re}\left(\Omega_t^{(e)} - \frac{\eta_t}{\eta_s}\Omega_t^{(e)}\right) - \frac{1}{2}\left|\Omega_s^{(e)}\right|^2 \\ &+ \mathrm{Re}\left(\Omega_t^{(i)} - \frac{\eta_t}{\eta_s}\Omega_t^{(i)}\right) + \frac{\varrho}{2}\left|\Omega_s^{(i)}\right|^2 \\ &+ \left(\kappa_{ss} + \tfrac{1}{2}\kappa^2\right) + D\left(\boldsymbol{a}^{(c)} \cdot \hat{\boldsymbol{n}} - \kappa \int_0^s \boldsymbol{a}^{(c)} \cdot \hat{\boldsymbol{\tau}}\mathrm{d}s\right) \\ &- G(1-\varrho)\mathrm{Im}(\eta) - GD\big(\mathrm{Re}(\eta_s) + \kappa\mathrm{Im}(\eta_s)\big)\Bigg]\left[\tilde{\boldsymbol{\eta}}_t \cdot \hat{\boldsymbol{n}}\right]\mathrm{d}s.\end{aligned} \tag{2.5.24}$$

As previously noted, each of the terms in (2.5.24) corresponds to a term in the dynamic condition (2.4.2). Substituting (2.4.2) into (2.5.24), we obtain

$$\begin{aligned}\frac{\mathrm{d}\mathscr{E}}{\mathrm{d}t} = \left(\frac{\alpha^2}{2} + P - \varrho\mathrm{Re}\left(w_t^{(i)}(z_0,t)\right) - \frac{\varrho}{2}\left|w_z^{(i)}(z_0,t)\right|^2 - \varrho G\mathrm{Im}(z_0)\right)\int_0^{2\pi} \tilde{\boldsymbol{\eta}}_t \cdot \hat{\boldsymbol{n}}\mathrm{d}s \\ + \int_0^{2\pi} \sigma\kappa\tilde{\boldsymbol{\eta}}_t \cdot \hat{\boldsymbol{n}}\mathrm{d}s.\end{aligned}$$

The kinematic condition gives

$$\int_0^{2\pi} \tilde{\boldsymbol{\eta}}_t \cdot \hat{\boldsymbol{n}}\mathrm{d}s = \int_0^{2\pi} \mathrm{Im}\left(\Omega_s^{(i)} - \alpha\eta_s\right)\mathrm{d}s = 0,$$

and so

$$\frac{\mathrm{d}\mathscr{E}}{\mathrm{d}t} = \int_0^{2\pi} \sigma\kappa\tilde{\boldsymbol{\eta}}_t \cdot \hat{\boldsymbol{n}}\mathrm{d}s = -\sigma\int_0^{2\pi} \hat{\boldsymbol{\tau}}_t \cdot \hat{\boldsymbol{\tau}}\mathrm{d}s = 0.$$

We have thus confirmed that the total energy of the unsteady system is conserved.

2.6 Conformal Mapping

To obtain the exterior flow potential it is convenient to make use of a conformal mapping. By mapping the exterior of the deformed cell from some simpler domain, in particular the exterior of the unit circle, we will show that the exterior flow problem can be reduced to a one-dimensional Fourier series

at the cell boundary, significantly simplifying the problem.

The Riemann mapping theorem states that there exists a three-parameter family of transformations that map the interior of the unit circle $|\zeta| < 1$ in the complex ζ-plane to any chosen simply connected domain (except the entire complex plane) (Carrier et al., 2005). A unique mapping is obtained by specifying three real restrictions, or one complex restriction and one real restriction. There thus exists a unique mapping $z = f(\zeta)$ from the interior of the unit circle $|\zeta| < 1$ to any simply connected domain containing the point $z = 0$ such that $f(0) = 0$ and $\arg(f'(0)) = 0$. Such a mapping can be expanded as a Taylor series about $\zeta = 0$ as

$$f(\zeta) = f'(0)\zeta + f''(0)\zeta^2 + \ldots, \tag{2.6.1}$$

where $f'(0) > 0$ and higher derivatives are generally complex.

We're interested in obtaining a mapping from the exterior of the unit circle to the exterior of the elastic cell. We firstly note that the transformation $\zeta \rightarrow \frac{1}{\zeta}$ maps the exterior of the unit circle $|\zeta| > 1$ to the interior of the unit circle $|\zeta < 1|$. We also note that the transformation $z \rightarrow \frac{1}{z-a}$ maps the exterior of the elastic cell to the interior of some simply connected domain, where a is a point in the interior of the cell; there thus exists a simply connected domain which is mapped to the exterior of the cell by the mapping $z \rightarrow \frac{1}{z} + a$. Combining these two transformations with that given by (2.6.1), we obtain the conformal mapping

$$z(\zeta) = \frac{1}{f\left(1/\zeta\right)} + a = \frac{1}{f'(0)}\zeta + a - \frac{f''(0)}{f'(0)^2} + \ldots$$

which maps the exterior of the unit circle in the ζ-plane to the exterior of the cell in the z-plane. Since the values of the derivatives $f^{(n)}(0)$ are undetermined

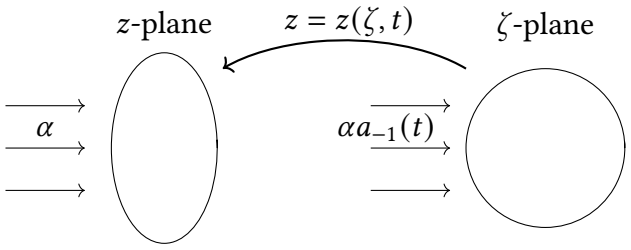

Figure 2.6.1: Definition sketch of the conformal mapping.

at this stage, this mapping can be written as

$$z(\zeta, t) = a_{-1}(t)\zeta + \sum_{n=0}^{\infty} a_n(t)\zeta^{-n}, \tag{2.6.2}$$

where a_{-1} is real and a_n are complex coefficients. Note that since we are mapping to a time-dependent domain the coefficients a_n must be time-dependent. This mapping is the same as that used by Shankar (1992) for the steady flow past a deformed bubble. A sketch of this mapping is shown in Figure 2.6.1. Note that this mapping is only valid for the exterior of the cell; since any conformal mapping from $\mathbb{C}$ to $\mathbb{C}$ must be linear, a mapping from the exterior of the unit circle to the exterior of the cell cannot be conformal throughout the interior of the cell. The interior fluid must therefore be dealt with using a different method.

We denote the complex potential in the ζ-plane as $W^{(e)}(\zeta, t) \equiv w^{(e)}\big(z(\zeta, t), t\big)$, where $w^{(e)}(z, t)$ is the complex potential in the z-plane. Recalling the far-field condition (2.4.5), $W^{(e)}(\zeta, t)$ must satisfy

$$W^{(e)}(\zeta, t) - \alpha z(\zeta, t) + \frac{\beta}{2\pi \mathrm{i}} \log\big(z(\zeta, t)\big) \to 0 \quad \text{as} \quad |\zeta| \to \infty.$$

Noting that $z(\zeta, t) - a_{-1}(t)\zeta - a_0(t) \to 0$ and $\log\big(z(\zeta, t)\big) - \log\zeta - \log a_{-1} \to 0$ as $|\zeta| \to \infty$, the far-field condition is reduced to

$$W^{(e)}(\zeta, t) - \alpha a_{-1}(t)\zeta - \alpha a_0(t) + \frac{\beta}{2\pi \mathrm{i}} \log\zeta + \frac{\beta}{2\pi \mathrm{i}} \log a_{-1} \to 0 \quad \text{as} \quad |\zeta| \to \infty,$$

where the imaginary value $\frac{\beta}{2\pi \mathrm{i}} \log a_{-1}$ can be neglected since the complex potential is only defined up to an arbitrary imaginary function of time. Note however that the real value $\alpha a_0(t)$ plays a role in Bernoulli's equation (2.3.10), and thus cannot be neglected. Since $W^{(e)}(\zeta, t) - \alpha a_{-1}(t)\zeta - \alpha a_0(t) + \frac{\beta}{2\pi \mathrm{i}} \log \zeta$ is analytic in the exterior of the cell, including at $\zeta = \infty$, $W^{(e)}(\zeta, t)$ can be written as a Laurent series of the form

$$W^{(e)}(\zeta, t) = \alpha a_{-1}(t)\zeta - \frac{\beta}{2\pi \mathrm{i}} \log \zeta + \alpha a_0(t) + \sum_{n=1}^{\infty} b_n(t)\zeta^{-n}. \tag{2.6.3}$$

The partial derivatives of $w^{(e)}(z, t)$ are given in terms of $W^{(e)}(\zeta, t)$ and $z(\zeta, t)$ by

$$w_z^{(e)}(z, t) = \frac{W_\zeta^{(e)}(\zeta, t)}{z_\zeta(\zeta, t)}, \quad w_t^{(e)}(z, t) = W_t^{(e)}(\zeta, t) - \frac{W_\zeta^{(e)}(\zeta, t) z_t(\zeta, t)}{z_\zeta(\zeta, t)}.$$

Parametrising the unit circle in the ζ-plane as $\zeta = \mathrm{e}^{\mathrm{i}\phi}$, where $0 \leq \phi < 2\pi$, the cell boundary can then be parametrised in terms of ϕ as

$$\eta(\phi, t) = z\left(\mathrm{e}^{\mathrm{i}\phi}, t\right) = a_{-1}(t)\mathrm{e}^{\mathrm{i}\phi} + a_0(t) + \sum_{n=1}^{\infty} a_n(t) e^{-\mathrm{i}n\phi}, \tag{2.6.4}$$

and the complex potential at the cell boundary $\Omega(\phi, t) \equiv W\left(\mathrm{e}^{\mathrm{i}\phi}, t\right)$ is given by

$$\Omega^{(e)}(\phi, t) = \alpha a_{-1}(t) e^{\mathrm{i}\phi} - \frac{\beta\phi}{2\pi} + \alpha a_0(t) + \sum_{n=1}^{\infty} b_n(t) e^{-\mathrm{i}n\phi}. \tag{2.6.5}$$

Note that $\eta(\phi)$ is not an arc-length parametrisation; the arc-length parameter is given by

$$s = \int_0^{\phi} |\eta_\phi| \mathrm{d}\phi, \tag{2.6.6}$$

where $s = 0$ is taken to correspond to $\phi = 0$. Since we require $\eta(s, t)$ to be

periodic in s with period 2π, we require

$$\int_0^{2\pi} |\eta_\phi| \mathrm{d}\phi = 2\pi. \tag{2.6.7}$$

We then have $s_\phi = |\eta_\phi|$ and

$$s_t = \int_0^\phi \frac{\mathrm{Re}\left(\eta_{\phi t}\overline{\eta}_\phi\right)}{|\eta_\phi|}\mathrm{d}\phi,$$

and derivatives in (s,t) are related to derivatives in (ϕ,t) by

$$\frac{\partial}{\partial s} = \frac{1}{|\eta_\phi|}\frac{\partial}{\partial \phi}, \qquad \left.\frac{\partial}{\partial t}\right|_s = \left.\frac{\partial}{\partial t}\right|_\phi - s_t\frac{\partial}{\partial \phi}$$

We note that $\frac{\partial}{\partial s}$ and $\left.\frac{\partial}{\partial t}\right|_s$ commute as expected. These results can be applied to (2.6.4) and (2.6.5) to obtain algebraic expressions for the variables $q^{(e)}$, κ and κ_{ss} in terms of ϕ and the coefficients a_n and b_n. Thus by using a conformal mapping we have reduced the functions $\eta(s,t)$ and $\Omega^{(e)}(s,t)$ to Fourier series with the far-field condition satisfied automatically, and all other variables given as nonlinear algebraic expressions in terms of the Fourier coefficients.

An advantage of the conformal mapping (2.6.2) is the rate of decay of the mapping coefficients a_n as $n \to \infty$. By Carathéodory's theorem, the mapping can be extended continuously onto the boundary at $|\zeta| = 1$, allowing us to express the cell boundary in the z-plane as $z = \eta\left(e^{\mathrm{i}\phi}\right) = a_{-1}e^{\mathrm{i}\phi} + \sum_{n=0}^{\infty} a_n e^{-\mathrm{i}n\phi}$. Since the cell boundary $z\left(e^{\mathrm{i}\phi}\right)$ is assumed to be smooth, periodic and infinitely differentiable, we can appeal to standard Fourier series results to conclude that coefficients a_n must decay faster than any power of n as $n \to \infty$, although not necessarily exponentially.

A similar mapping could be used to define a conformal mapping from the interior of the unit circle to the interior of the cell, which would also provide a parametrisation of the cell in the z-plane of the form $\eta^{(i)}(\phi,t) = z^{(i)}\left(e^{\mathrm{i}\phi},t\right)$.

However, the point $\zeta = e^{\mathrm{i}\phi}$ will generally not map to the same point on the cell boundary for the interior and exterior mappings; that is, $\eta(\phi, t) \neq \eta^{(i)}(\phi, t)$. While a matching function $\phi^{(i)}(\phi)$ can be used to match the two incompatible parametrisations, we opt to use alternative methods to deal with the interior fluid, which will be discussed in Chapter 3.

We can obtain a useful result for analytic functions in the ζ-plane based on the Hilbert transform, which will be of particular use in dealing with the conformal mapping in the following chapters. Suppose we have a complex function $F(\zeta, t)$ which is analytic in the region $|\zeta| > 1$ with real limit $F_\infty(t)$ as $|\zeta| \to \infty$. The function $F(\zeta, t)$ has a Laurent series of the form

$$F(\zeta) = F_\infty(t) + \sum_{n=1}^{\infty} A_n(t)\zeta^{-n}$$

with only negative powers of ζ. Denoting the function evaluated at the cell boundary $\zeta = e^{\mathrm{i}\phi}$ as $f(\phi, t) = F\left(e^{\mathrm{i}\phi}, t\right)$, we have

$$f(\phi, t) = F_\infty(t) + \sum_{n=1}^{\infty} A_n(t)e^{-\mathrm{i}n\phi}.$$

We thus have

$$\int_0^{2\pi} f(\phi, t)\mathrm{d}\phi = 2\pi F_\infty(t). \tag{2.6.8}$$

Now, suppose we know the value of $\mathrm{Re}\left(f(\phi, t)\right)$ and want to obtain the full complex function $f(\phi, t)$. This can be achieved using a Hilbert transform. The Hilbert transform of a function $f(\phi, t)$ is defined as

$$\mathcal{H}(f(\phi, t)) = \frac{1}{\pi}\int_{-\infty}^{\infty} \frac{f(k, t)}{\phi - k}\mathrm{d}k,$$

where the periodic function $f(\phi, t)$ is taken to be extended periodically over $\mathbb{R}$, and the integral is taken as a Cauchy principal value. The Hilbert transform is

particularly useful due to the well-known result

$$\mathcal{H}\left(e^{\mathrm{i}n\phi}\right) = -\mathrm{i}\,\mathrm{sgn}(n)e^{\mathrm{i}n\phi} \quad \text{for} \quad n \neq 0.$$

Applying this result to

$$\mathrm{Re}(f(\phi,t)) = F_\infty(t) + \frac{1}{2}\sum_{n=1}^{\infty} A_n e^{-\mathrm{i}n\phi} + \overline{A_n}e^{\mathrm{i}n\phi},$$

we obtain

$$\mathcal{H}\Big(\mathrm{Re}\big(f(\phi,t)\big)\Big) = \frac{\mathrm{i}}{2}\sum_{n=1}^{\infty} A_n e^{-\mathrm{i}n\phi} - \overline{A_n}e^{\mathrm{i}n\phi} = -\mathrm{Im}\big(F(\phi)\big),$$

and so

$$f(\phi,t) = \mathrm{Re}\big(f(\phi,t)\big) - \mathrm{i}\mathcal{H}\Big(\mathrm{Re}\big(f(\phi,t)\big)\Big). \tag{2.6.9}$$

We can thus reconstruct any complex function $F(\phi)$ which is analytic in the region $|\zeta| > 1$ from its real part $\mathrm{Re}\big(F(\phi)\big)$ using the Hilbert transform.

2.7 Steady System

We now consider the steady form of the system, which governs the shape of a deformed elastic cell in equilibrium with the fluid flow. We firstly show that for a steady cell the interior fluid must be static. Noting that the dimensionless kinetic energy of the interior fluid is given by the divergence theorem as

$$\frac{1}{2}\iint_A \left|\boldsymbol{u}^{(i)}\right|^2 \mathrm{d}x\mathrm{d}y = \frac{1}{2}\int_0^{2\pi} \mathrm{Re}\Big(w^{(i)}\Big)\boldsymbol{u}^{(i)}\cdot\hat{\boldsymbol{n}}\mathrm{d}s,$$

the kinematic condition for the steady cell requires $\boldsymbol{u}^{(i)}\cdot\hat{\boldsymbol{n}} = 0$, and so the kinetic energy of the internal fluid is zero. The interior fluid is thus static. We henceforth drop the superscript (e) from the external flow variables, with all

flow variables now assumed to relate to the exterior flow.

We make use of the conformal mapping from the exterior of the unit circle in some ζ-plane to the exterior of the cell in the z-plane, as given by (2.6.2). Noting that the choice of the coefficient a_0 simply corresponds to a translation of the cell in the ζ-plane, we are free to choose $a_0 = 0$ without loss of generality. The mapping is then given by

$$z(\zeta) = a_{-1}\left(\zeta + \sum_{n=1}^{\infty} a_n \zeta^{-n}\right), \tag{2.7.1}$$

where the mapping coefficients a_n have now been rescaled by the real coefficient a_{-1}. The cell boundary itself is given by

$$\eta(\phi) = z\left(e^{\mathrm{i}\phi}\right) = a_{-1}\left(\mathrm{e}^{\mathrm{i}\phi} + \sum_{n=1}^{\infty} a_n e^{-\mathrm{i}n\phi}\right), \tag{2.7.2}$$

where $0 \leq \phi \leq 2\pi$. The value of the coefficient a_{-1} can be determined by recalling that the cell must have perimeter 2π, giving

$$2\pi = \int_0^{2\pi} |\eta_\phi| \mathrm{d}\phi = a_{-1} \int_0^{2\pi} \left|\mathrm{e}^{\mathrm{i}\phi} - \sum_{n=1}^{\infty} n a_n e^{-\mathrm{i}n\phi}\right| \mathrm{d}\phi,$$

and thus

$$a_{-1} = \frac{2\pi}{\int_0^{2\pi} \left|\mathrm{e}^{\mathrm{i}\phi} - \sum_{n=1}^{\infty} n a_n e^{-\mathrm{i}n\phi}\right| \mathrm{d}\phi}. \tag{2.7.3}$$

The flow velocity around the cell wall is given in complex form by (2.4.7) as

$$u = \frac{\mathrm{Re}\left(\Omega_\phi\right)}{|\eta_\phi|}\hat{\tau} + \frac{\mathrm{Im}\left(\Omega_\phi\right)}{|\eta_\phi|}\hat{n}.$$

The kinematic condition, which requires no flow normal to the cell boundary, thus requires

$$\mathrm{Im}\left(\Omega_\phi\right) = 0.$$

Applying this condition to the Fourier series of the complex potential given by (2.6.5), we find that $b_1 = \alpha a_{-1}$ and $b_n = 0$ for $n > 1$, giving the complex potential in the ζ-plane as

$$W(\zeta) = \alpha a_{-1}\left(\zeta + \frac{1}{\zeta}\right) - \frac{\beta}{2\pi \mathrm{i}} \log \zeta. \tag{2.7.4}$$

The complex potential evaluated on the cell wall is given by

$$\Omega(\phi) = W\left(e^{\mathrm{i}\phi}\right) = 2\alpha a_{-1} \cos\phi - \frac{\beta\phi}{2\pi},$$

which gives the flow speed at the cell boundary

$$q(\phi) = \left|\frac{\Omega_\phi}{\eta_\phi}\right| = \left|\frac{2\alpha a_{-1}\sin(\phi) + \beta/2\pi}{\eta_\phi}\right|. \tag{2.7.5}$$

The dynamic condition (2.4.2) is thus reduced to

$$\begin{aligned}\frac{1}{2}\left(\left|\frac{2\alpha a_{-1}\sin(\phi) + \beta/2\pi}{\eta_\phi}\right|^2 - \alpha^2\right) - P - \left(\kappa_{ss} + \tfrac{1}{2}\kappa^3 - \sigma\kappa\right) \\ + G(1-\varrho)\mathrm{Im}(\eta) + GD\left(\mathrm{Re}(\eta_s) + \kappa \mathrm{Im}(\eta)\right) = 0,\end{aligned} \tag{2.7.6}$$

with dimensionless parameters

$$\alpha = U\sqrt{\frac{\ell^3 \rho^{(e)}}{E_B}}, \quad \beta = -\Gamma\sqrt{\frac{\ell \rho^{(e)}}{E_B}}, \quad P = \frac{(p_\infty - p_0)\ell^3}{E_B},$$
$$GD = \frac{g\rho_c h \ell^3}{E_B}, \quad \varrho = \frac{\rho^{(i)}}{\rho^{(e)}}.$$

The dimensionless value σ can be considered the constraint force arising in the tangential stress of the cell wall to satisfy the global inextensibility of the cell, and is determined implicitly by (2.7.6).

The values of κ and κ_{ss} can be written explicitly in terms of the parametrisation ϕ and the mapping coefficients a_n by repeated use of the

relation

$$\frac{\partial}{\partial s} = \frac{1}{|\eta_\phi|}\frac{\partial}{\partial \phi}$$

on the Fourier series (2.7.2). The problem is thus reduced to finding σ and the mapping coefficients a_n which satisfy the dynamic condition (2.7.6).

To ensure that equilibrium solutions are possible, the parameters G, D and β must be chosen such that the net force acting upon the cell is zero. There are three net forces acting upon the cell: the lift generated by the circulation around the cell, which is given by the Kutta-Joukowski theorem (Batchelor, 2000) as $\boldsymbol{F}_L = -\rho^{(e)} U\Gamma \boldsymbol{j}$; the weight of the cell material, given by $\boldsymbol{F}_W = -2\pi\ell\rho_c hg\boldsymbol{j}$; and the buoyancy due to the difference in density between the interior and exterior fluids, given by $\boldsymbol{F}_B = \left(\rho^{(e)} - \rho^{(i)}\right) gA\boldsymbol{j}$, where A is the area of the cell. Thus to ensure there is a net balance of forces acting on the cell, we require

$$\boldsymbol{F}_L + \boldsymbol{F}_W + \boldsymbol{F}_B = \left(-2\pi g\ell\rho_c h - \rho^{(e)} U\Gamma + \left(\rho^{(e)} - \rho^{(i)}\right) gA\right)\boldsymbol{j} = 0,$$

which gives the dimensionless relation

$$2\pi GD - \alpha\beta + G(\varrho - 1)A = 0. \tag{2.7.7}$$

We note some of invariances in the dynamic condition (2.7.6). Firstly, we observe an invariance to a reversal of the flow direction, given by $\alpha \longrightarrow -\alpha$, $\beta \longrightarrow -\beta$. We can therefore restrict our studies to $\alpha \geq 0$, with steady solutions for $\alpha < 0, \beta$ equal to those found for $-\alpha > 0, -\beta$. The system is also invariant to the transformation $\eta(\phi) \longrightarrow -\overline{\eta}(-\phi)$, which corresponds to a left-right mirroring of the cell shape. This invariance implies that, for a given set of parameters, an equilibrium cell be reflected horizontally to obtain another, potentially identical, equilibrium cell. Note that this does necessarily imply that the cell must be left-right symmetric; in Chapter 3 we will present equilibrium solutions which lack

this symmetry. Finally, we note that (2.7.6) is invariant to the transformation $\eta(\phi) \rightarrow \overline{\eta}(-\phi)$, $\beta \rightarrow -\beta$, $G \rightarrow -G$, which corresponds to a vertical reflection of the system along with a reversal of the gravitational force acting on the cell. While a negative value of G is not physically permissible, we note that for $G = \beta = 0$ any equilibrium cell shape can be reflected horizontally to obtain another, potentially identical, equilibrium shape.

It will be useful to obtain relations for the mapping coefficients a_n corresponding to transformations of the cell boundary $\eta(\phi)$. We start by considering a rotation of the cell by some angle θ about the origin, given by the transformation $\eta(\phi) \rightarrow e^{\mathrm{i}\theta} z(\phi)$. The rotated cell boundary is thus given by

$$\eta(\phi) = a_{-1} e^{\mathrm{i}\theta} \left(e^{\mathrm{i}\phi} + \sum_{n=1}^{\infty} a_n e^{-\mathrm{i}n\phi} \right) = a_{-1} \left(e^{\mathrm{i}(\phi+\theta)} + \sum_{n=1}^{\infty} a_n e^{(n+1)i\theta} e^{-in(\phi+\theta)} \right).$$

However, this expression is not in the form required by (2.7.2). To obtain the required form we take the transformation $\phi \rightarrow \phi - \theta$, giving

$$\eta(\phi) = a_{-1} \left(e^{\mathrm{i}\phi} + \sum_{n=1}^{\infty} a_n e^{(n+1)i\theta} e^{-\mathrm{i}n\phi} \right)$$

A rotation by angle θ about the origin thus corresponds to the transformation $a_n \rightarrow e^{(n+1)\mathrm{i}\theta} a_n$. For the case where the cell has a mode-m rotational symmetry the coefficients a_n must remain unchanged by this transformation; a mode-m symmetric cell thus requires $a_n = 0$ for $n \notin \{mk - 1 | k \in \mathbb{N}\}$. Next considering a vertical reflection of the cell given by the transformation $\eta(\phi) \rightarrow \overline{\eta}(-\phi)$, the reflected cell is parametrised as

$$\eta(\phi) = a_{-1} \left(e^{\mathrm{i}\phi} + \sum_{n=1}^{\infty} \overline{a_n} e^{-\mathrm{i}n\phi} \right).$$

A vertical reflection thus corresponds to the transformation $a_n \rightarrow \overline{a_n}$. For the case of a top-bottom symmetric cell the coefficients a_n must remain

unchanged by this transformation; a top-bottom symmetric cell thus requires $\mathrm{Im}(a_n) = 0$ for all n. A horizontal reflection of the cell can then be obtained by combining a vertical reflection with a rotation of angle π about the origin, giving the transformation by $a_n \rightarrow (-1)^{n+1}\overline{a_n}$. For the case of a left-right symmetric cell the coefficients a_n must remain unchanged by this transformation; a left-right symmetric cell thus requires a_n to be real for odd n and imaginary for even n. Finally, for the case of a cell which is both left-right symmetric and top-bottom symmetric we conclude that a_n must be real for odd n and zero for even n.

2.8 Summary

We have formulated the system of equations which governs the unsteady deformation of a two-dimensional elastic cell submerged in an inviscid fluid flow. Modelling the cell as a thin elastic shell, we used the elastic constitutive relation justified by Pozrikidis (2002a) to derive an equation which determines the unsteady deformation of the cell in response to a given transmural pressure difference. We have formulated the flow equations for both the uniform stream in the exterior of the cell and the fluid in the interior of the cell in terms of complex potentials and used Bernoulli's equation to obtain the transmural fluid pressure of the potential flow.

We have shown that the elastic deformation equations are coupled with the fluid equations by dynamic and kinematic conditions to form a complete set of equations which governs the unsteady evolution of the system. We have obtained expressions for each of the distinct forms of energy contained in the unsteady system and shown that the total energy is conserved.

We presented a conformal mapping method to reduce the exterior flow problem to a one-dimensional Fourier series at the cell boundary, and

presented some useful results which follow from the conformal mapping.

Finally, we considered the steady form of the system, and showed that by using the conformal mapping the steady system can be reduced to a single equation which governs the deformed equilibrium cell shapes, and presented some of invariants of the steady system.

The steady system presented here forms the basis of the analyses in Chapters 3 and 4, in which steady solutions are analysed extensively both analytically and numerically, and the unsteady system is used in Chapter 3 to analyse the linear stability of the equilibrium cells and to simulate the non-linear evolution of the unstable cells subjected to a small perturbation. We note however that we study only a subset of the parameter space, focussing on cells which have no buoyancy and, in the case of the unsteady problem, no inertia. The system derived in this chapter can therefore be used to study several extensions to the current study; these will be discussed in more detail in the Future Work section in Chapter 6.

3

Deformation and Stability of an Elastic Cell in a Uniform Stream

In this chapter we consider the equilibria, stability and unsteady motion of a massless elastic cell in a uniform stream. A massless cell provides a good model for cells with a thin, low-density material where the inertia of the elastic material is much lower than the elastic and fluid forces acting upon it. The cell deformation and unsteady motion are determined by the governing equations derived in Chapter 2, which we will show can be simplified for a massless cell to obtain explicit expressions for the unsteady evolution of the system.

The study by Blyth and Părău (2013) provided some preliminary insight into the elastic problem. Focusing on cell shapes which are both left-right symmetric and top-bottom symmetric, they used a linear expansion for the cell curvature to predict the first order deformation of an initially circular cell in a weak flow. Guided by these results they computed fully nonlinear equilibria using a numerical method based on a conformal mapping that is restricted to cells with a top-bottom cell symmetry.

We use the conformal mapping technique of Shankar (1992) as presented in Chapter 2 to develop an asymptotic expansion in the flow speed parameter that allows corrections to be determined to any order, and we use this to identify novel solutions, expanding considerably on the previous results of Blyth and

Părău (2013). We then extend these new solution branches to arbitrary flow speed using a numerical method, and present a thorough analysis of the solution space.

Following the approach of Nie and Tanveer (1995) developed for the bubble problem, we determine the linear stability of the cell equilibria by formulating and solving an eigenvalue problem for the linear growth rates under a small amplitude perturbation, with the interior fluid represented using a Schwarz-Christoffel mapping as described by Driscoll and Trefethen (2002). We present analytical and numerical methods to simplify the unsteady system to facilitate an explicit time-stepping method to simulate the nonlinear unsteady evolution of the cell, using Baumgarte stabilisation (Baumgarte, 1972) to preserve the cell perimeter. We use this time-stepping scheme to verify the linear stability results, as well as to follow the evolution of a linearly unstable cell into the fully nonlinear regime. We create a stability map of the parameter space to delineate the regions of dominance of certain linear growth rates, which can be used as a guide to the fully nonlinear unsteady motion. We use the method by Sprott (2003) to compute the maximal Lyapunov exponent of the unsteady motions, allowing us to determine whether the system exhibits chaos.

Some of the results presented in this chapter were previously published in Yorkston et al. (2020a).

3.1 Steady Formulation

We start by considering the steady system which was derived in Section 2.7. We recall that for equilibria to exist we require zero net force acting on the cell. This force balance is given in terms of the dimensionless parameters by (2.7.7)

as

$$2\pi GD - \alpha\beta + G(\varrho - 1)A = 0,$$

where G is proportional to the strength of gravity, D is proportional to the density of the cell wall, α and β are the dimensionless far-field flow speed and circulation respectively, ϱ is the density ratio between the exterior and interior fluids, and A is the area of the cell. For the case of a massless cell we have $D = 0$, and to simplify the analysis of the system we will also assume that $G = 0$; the force balance thus requires $\beta = 0$. These assumptions have been chosen to provide a physically relevant system which is simple enough to thoroughly analyse the solution space. However, other choices of the parameters can easily be considered using similar methods to those presented in this chapter. In Chapter 4 we consider the case where D, G and β are all non-zero, with the weight of the cell balanced by the lift generated by the circulation, and in Chapter 6 we discuss other potential parameter choices which could be considered in future studies.

The equilibrium cell shapes are determined by the steady dynamic condition (2.7.6), which for $D = G = \beta = 0$ is reduced to

$$\frac{\alpha^2}{2}\left(\frac{(2a_{-1}\sin\phi)^2}{|\eta_\phi|^2} - 1\right) - \left(\kappa_{ss} + \tfrac{1}{2}\kappa^3 - \sigma\kappa\right) - P = 0, \tag{3.1.1}$$

with dimensionless parameters

$$\alpha = U\sqrt{\frac{\ell^3\rho_e}{E_B}}, \quad P = \frac{(p_\infty - p_0)\ell^3}{E_B}.$$

Here $\eta(\phi)$ is the parametrisation of the cell boundary in the complex z-plane, $\kappa(\phi)$ is the curvature of the cell, s is the anticlockwise arc-length distance along the cell wall, α is the far-field flow speed parameter, P is the dimensionless pressure difference between the far-field and the interior of the

cell, σ is a dimensionless value related to the internal tension of the cell, and a_{-1} is a scaling coefficient defined in (3.1.3). The cell boundary parametrisation $\eta(\phi)$ is given by (2.7.2) as

$$\eta(\phi) = a_{-1}\left(e^{\mathrm{i}\phi} + \sum_{n=1}^{\infty} a_n e^{-\mathrm{i}n\phi}\right) \tag{3.1.2}$$

where $0 \le \phi \le 2\pi$, with the coefficient a_{-1} taken to be

$$a_{-1} = \frac{2\pi}{\int_0^{2\pi} \left|e^{\mathrm{i}\phi} - \sum_{n=1}^{\infty} n a_n e^{-\mathrm{i}n\phi}\right| \mathrm{d}\phi} \tag{3.1.3}$$

to ensure the perimeter of the cell is equal to 2π. The curvature κ and its second arc-length derivative κ_{ss} are given by

$$\kappa(\phi) = -\mathrm{Im}(\eta_{ss}\overline{\eta}_s), \quad \kappa_{ss}(\phi) = -\mathrm{Im}(\eta_{ssss}\overline{\eta}_s + \eta_{sss}\overline{\eta}_{ss})$$

where the derivatives are evaluated using the relation

$$\frac{\mathrm{d}}{\mathrm{d}s} = \frac{1}{|\eta_\phi|}\frac{\mathrm{d}}{\mathrm{d}\phi}.$$

We note that in the limit $E_B \to 0$ the elastic problem is reduced to that of a bubble in a uniform stream, which has been studied notably by Vanden-Broeck and Keller (1980), Shankar (1992), and Nie and Tanveer (1995). In terms of the dimensional parameters this corresponds to $P \to -\infty$ with $\alpha^2 \approx -P$ and $\sigma \approx -P$.

The numerical method used to compute steady solutions is based on that presented by Tanveer (1996), which was used to compute the deformation of a bubble with surface tension submerged in a uniform flow. We truncate the Fourier series (3.1.2) at some N terms by taking $a_n = 0$ for $n > N$, and split the coefficients into the $2N$ real variables $\mathrm{Re}(a_n)$ and $\mathrm{Im}(a_n)$ for $1 \le n \le N$, with

a_{-1} given in terms of a_n by (3.1.3). The parameters α and P can be freely chosen, while σ is to be found along with the mapping coefficients a_n by satisfying (3.1.1). We then evaluate (3.1.1) at $2N+1$ equally spaced collocation points $\phi_j = \frac{2\pi(j-1)}{2N+1}$ for $j = 1, \ldots, 2N+1$, giving $2N+1$ equations to solve for the $2N+1$ variables $\mathrm{Re}(a_n)$, $\mathrm{Im}(a_n)$ and σ. We use Newton's method to obtain a numerical solution, with the Jacobian of the truncated system obtained analytically to optimise the computations. For the results shown in this section, we generally take $N = 200$, although for certain parameter values we require up to $N = 2000$ to obtain accurate results.

To confirm the accuracy of the numerical results, we note that for any given mapping function we can obtain the absolute value of the left-hand side of (3.1.1) analytically along the entire cell, not just at the $2N+1$ collocation points used in Newton's method. We can therefore verify the validity of our results by sampling (3.1.1) at a much larger number of points, say $1000N$, and confirm the maximum value remains below some tolerance level. All steady results in this chapter have a maximum absolute error less than 10^{-10}. We use the small flow speed asymptotic results presented below as an initial guess for Newton's method and use numerical continuation to increase the flow speed to explore the full nonlinear solution space.

3.2 Unsteady Formulation

We next consider the system that governs the unsteady motion and interaction between the cell and the fluids in the interior and exterior which was derived in Section 2.4. As in the steady problem we take the parameters $D = G = \beta = 0$,

which reduces the unsteady dynamic condition (2.4.2) to

$$\begin{aligned}&\operatorname{Re}\left(\Omega_t^{(e)} - \frac{\eta_t}{\eta_\phi}\Omega_\phi^{(e)}\right) + \frac{1}{2}\left(\frac{\left|\Omega_\phi^{(e)}\right|^2}{\left|\eta_\phi\right|^2} - \alpha^2\right) - P - \left(\kappa_{ss} + \tfrac{1}{2}\kappa^3 - \sigma\kappa\right)\\ &- \varrho\operatorname{Re}\left(\Omega_t^{(e)} - \frac{\eta_t}{\eta_\phi}\Omega_\phi^{(e)} - w_t^{(i)}(z_0,t)\right) - \frac{\varrho}{2}\left(\frac{\left|\Omega_\phi^{(i)}\right|^2}{|\eta_\phi|} - \left|w_z^{(i)}(z_0,t)\right|^2\right) = 0,\end{aligned} \tag{3.2.1}$$

where $\eta(\phi,t)$ is the complex cell parametrisation with parameter $0 \le \phi \le 2\pi$, $\Omega^{(e)}(\phi,t) \equiv w^{(e)}\big(\eta(\phi,t),t\big)$ and $\Omega^{(i)}(\phi,t) \equiv w^{(i)}\big(\eta(\phi,t),t\big)$ are the exterior and interior complex potentials respectively evaluated at the cell boundary, and $z_0(t)$ is some reference point in the interior of the cell. The dimensionless parameters are defined as

$$\alpha = U\sqrt{\frac{\ell^3\rho_e}{E_B}}, \quad P(t) = \frac{(p_\infty - p_0(t))\ell^3}{E_B}, \quad \varrho = \frac{\rho^{(i)}}{\rho^{(e)}},$$

where α is the far-field flow speed parameter, $P(t)$ is the dimensionless pressure difference between the far-field and the interior of the cell at the reference point $z_0(t)$, ϱ is the density ratio between the exterior and the interior fluids, and $\sigma(t)$ is a dimensionless value related to the internal tension of the cell.

Using the conformal mapping method presented in Section 2.6, the parametrisation of the cell boundary $\eta(\phi,t)$ is given by (2.6.4) as

$$\eta(\phi,t) = a_{-1}(t)\mathrm{e}^{\mathrm{i}\phi} + a_0(t) + \sum_{n=1}^{\infty} a_n(t)e^{-\mathrm{i}n\phi}, \tag{3.2.2}$$

and exterior complex potential evaluated at the cell boundary $\Omega^{(e)}(\phi,t)$ is given by (2.6.5) as

$$\Omega^{(e)}(\phi,t) = \alpha a_{-1}(t)e^{\mathrm{i}\phi} + \alpha a_0(t) + \sum_{n=1}^{\infty} b_n(t)e^{-\mathrm{i}n\phi}. \tag{3.2.3}$$

Both the exterior and interior potentials must satisfy the kinematic condition

$$\mathrm{Im}\Big(\Omega_\phi^{(e)}\Big) = \mathrm{Im}\Big(\Omega_\phi^{(i)}\Big) = -\mathrm{Im}\Big(\eta_t\overline{\eta}_\phi\Big), \tag{3.2.4}$$

and the cell is assumed to be inextensible with perimeter given by

$$\int_0^{2\pi} |\eta_\phi| \mathrm{d}\phi = 2\pi. \tag{3.2.5}$$

This system contains three types of energy, as derived in Section 2.5; the dimensionless kinetic energy of the internal fluid

$$\mathscr{K}^{(i)} = \frac{\varrho}{2}\int_0^{2\pi} \mathrm{Re}\Big(\Omega^{(i)} - \alpha\eta\Big)\mathrm{Im}\Big(\Omega_\phi^{(i)} - \alpha\eta_\phi\Big)\mathrm{d}\phi,$$

the dimensionless kinetic energy of the external fluid

$$\mathscr{K}^{(e)} = -\tfrac{1}{2}\int_0^{2\pi} \mathrm{Re}\Big(\Omega^{(e)} - \alpha\eta\Big)\mathrm{Im}\Big(\Omega_\phi^{(e)} - \alpha\eta_\phi\Big)\mathrm{d}\phi,$$

and the dimensionless bending energy of the cell

$$\mathscr{W} = \int_0^{2\pi} \tfrac{1}{2}(\kappa+1)^2|\eta_\phi|\mathrm{d}\phi, \tag{3.2.6}$$

where the kinetic energies are defined in terms of a reference frame translating at speed α with the uniform stream. The total energy of the system $\mathscr{E} = \mathscr{K}^{(i)} + \mathscr{K}^{(e)} + \mathscr{W}$ is an invariant of the motion, with a minimum energy of $\mathscr{E} = 0$ corresponding to a circular cell moving at constant speed α with the flow.

The kinematic condition (3.2.4) implicitly determines the motion of the cell boundary for a given exterior or interior flow. To obtain an explicit expression for the cell boundary velocity $\eta_t(\phi, t)$, we make use of the result (2.6.9) derived in Section 2.6. We start by noting that the kinematic condition can be written

as

$$-\operatorname{Re}\left(\frac{\mathrm{i}\Omega_{\phi}^{(e)}}{|\eta_{\phi}|^{2}}\right)=\operatorname{Re}\left(\frac{\mathrm{i}\eta_{t}}{\eta_{\phi}}\right)=\operatorname{Re}\left(\frac{z_{t}}{\zeta z_{\zeta}}\right)\Bigg|_{\zeta=e^{\mathrm{i}\phi}}, \tag{3.2.7}$$

where $z(\zeta,t)$ is the conformal mapping from the exterior of the unit circle in the ζ-plane to the exterior of the cell. Since $z(\zeta,t)$ is conformal in the exterior we must have $|z_{\zeta}|>0$ for $|\zeta|>1$, and so $\frac{z_t}{\zeta z_\zeta}$ must be analytic in the exterior $|\zeta|>1$. In the far-field we have $z=a_{-1}(t)\zeta+a_0(t)+O\left(\zeta^{-1}\right)$, and so $z_t=a'_{-1}(t)\zeta+a'_0(t)+O\left(\zeta^{-1}\right)$ and $z_\zeta=a_{-1}(t)+O\left(\zeta^{-2}\right)$. We thus have

$$\frac{z_t}{\zeta z_\zeta}\to\frac{a'_{-1}}{a_{-1}}\quad\text{as}\quad|\zeta|\to\infty,$$

where a_{-1} is real. We can therefore apply the relation (2.6.9) to obtain

$$\frac{\mathrm{i}\eta_t}{\eta_\phi}=\operatorname{Re}\left(\frac{\mathrm{i}\eta_t}{\eta_\phi}\right)-\mathrm{i}\mathcal{H}\left(\operatorname{Re}\left(\frac{\mathrm{i}\eta_t}{\eta_\phi}\right)\right),$$

where $\mathcal{H}$ is the Hilbert transform defined as

$$\mathcal{H}(f(\phi,t))=\frac{1}{\pi}\int_{-\infty}^{\infty}\frac{f(k,t)}{\phi-k}\mathrm{d}k,$$

with the integral taken as a Cauchy principal value. We can thus rewrite the kinematic condition (3.2.7) as

$$\eta_t=-\mathrm{i}\eta_\phi\operatorname{Im}\left(\frac{\Omega_\phi^{(e)}}{|\eta_\phi|^2}\right)-\eta_\phi\mathcal{H}\left(\operatorname{Im}\left(\frac{\Omega_\phi^{(e)}}{|\eta_\phi|^2}\right)\right), \tag{3.2.8}$$

an explicit expression for the time derivative $\eta_t(\phi,t)$ in terms of the exterior potential $\Omega^{(e)}(\phi,t)$.

In obtaining (3.2.8) we have not enforced the inextensibility condition, which requires

$$L(t)=\int_0^{2\pi}\left|\eta_\phi\right|\mathrm{d}\phi=2\pi, \tag{3.2.9}$$

where $L(t)$ is the perimeter of the cell. Since (3.2.8) explicitly determines the value of η_t for a given exterior potential, the inextensibility condition must be satisfied implicitly by some restraint on $\Omega^{(e)}$ via (3.2.1) by an appropriate choice of the unknown σ. Recalling the vector relations $\boldsymbol{\eta}_\phi = |\eta_\phi|\boldsymbol{\tau}$ and $\boldsymbol{\tau}_\phi = \kappa|\eta_\phi|\boldsymbol{n}$, as well as the kinematic condition on the boundary $\boldsymbol{\eta}_t \cdot \boldsymbol{n} = \mathrm{Im}\left(\Omega^{(e)}_\phi\right)/|\eta_\phi|$, we have

$$\frac{\partial}{\partial t}\left|\frac{\partial \eta}{\partial \phi}\right| = \boldsymbol{\eta}_{\phi t} \cdot \boldsymbol{\tau} = \frac{\partial}{\partial \phi}\left(\boldsymbol{\eta}_t \cdot \boldsymbol{\tau}\right) - \kappa|\eta_\phi|\boldsymbol{\eta}_t \cdot \boldsymbol{n} = \frac{\partial}{\partial \phi}\left(\boldsymbol{\eta}_t \cdot \boldsymbol{\tau}\right) - \kappa \mathrm{Im}\left(\Omega^{(e)}_\phi\right),$$

and so we obtain

$$L'(t) = \frac{\partial}{\partial t}\int_0^{2\pi} |\eta_\phi| \mathrm{d}\phi = \int_0^{2\pi} \kappa_\phi \mathrm{Im}\left(\Omega^{(e)}\right) \mathrm{d}\phi, \tag{3.2.10}$$

and

$$L''(t) = \int_0^{2\pi} \left[\kappa_\phi \mathrm{Im}\left(\Omega^{(e)}_t\right) - \kappa_t \mathrm{Im}\left(\Omega^{(e)}_\phi\right)\right] \mathrm{d}\phi. \tag{3.2.11}$$

The second time derivative of the perimeter of the cell therefore depends directly on $\Omega^{(e)}_t$, which can be seen in (3.2.1) to depend linearly on the value of $\sigma(t)$. The inextensibility condition (3.2.9) must therefore be satisfied indirectly by choosing $\sigma(t)$ such that $L''(t)$ takes an appropriate value to ensure the condition $L(t) = 2\pi$ is satisfied. The simplest choice would be simply to set $L''(t) = 0$, which along with the initial conditions $L(0) = 2\pi$ and $L'(0) = 0$ is enough to ensure that $L(t) = 2\pi$ for all t. However, such a condition is not numerically stable; if due to numerical error we can only satisfy $L''(t) = \epsilon$ for some small constant ϵ, the cell perimeter will instead be given by $L(t) = 2\pi + \frac{1}{2}\epsilon t^2$, resulting in an error which grows quadratically in time.

To avoid this numerical instability we utilise the Baumgarte stabilisation method (Baumgarte, 1972) by satisfying

$$L''(t) = -2\gamma L'(t) - \gamma^2(L(t) - 2\pi), \tag{3.2.12}$$

where γ is a freely chosen large positive constant. Note that with the initial conditions $L(0) = 2\pi$ and $L'(0) = 0$ this condition is analytically equivalent to the condition $L''(t) = 0$. However, if the perimeter $L(t)$ deviates from 2π due to numerical error, the Baumgarte stabilisation acts to return $L(t)$ back to 2π. Supposing again that we can only set $L''(t)$ up to some small numerical error ϵ such that $L''(t) = -2\gamma L'(t) - \gamma^2(L(t) - 2\pi) + \epsilon$, $L(t)$ will be given by

$$L(t) = 2\pi + \frac{\epsilon}{\gamma^2}\big(1 - (1 + \gamma t)e^{-\gamma t}\big),$$

where $L(t) \to 2\pi + \epsilon/\gamma^2$ as $t \to \infty$. The Baumgarte stabilisation (3.2.12) thus ensures that there is no unbounded numerical drift of the perimeter from 2π. A larger value of the parameter γ will generally reduce the numerical error, although taking γ too high will increase the stiffness of the equation and make the system harder to solve numerically. We find that a value of $\gamma = 10^4$ is sufficient to ensure the drift in the perimeter remains sufficiently small; this will be discussed in Section 3.2.3.

To obtain the time derivatives of the complex potentials, we note that (3.2.1) gives an explicit value for $\mathrm{Re}\Big(\Omega_t^{(e)} - \varrho\Omega_t^{(i)}\Big)$, while differentiating the kinematic condition (3.2.4) with respect to time and integrating with respect to ϕ gives

$$\mathrm{Im}\Big(\Omega_t^{(e)} - \Omega_t^{(i)}\Big) = C(t), \tag{3.2.13}$$

where $C(t)$ is some function of integration. Equations (3.2.1) and (3.2.13) provide two conditions which the time derivatives $\Omega_t^{(e)}$ and $\Omega_t^{(i)}$ must satisfy. Two more conditions are obtained by requiring the potentials $w^{(e)}(z,t)$ and $w^{(i)}(z,t)$ to be analytic in the exterior and interior respectively. For the exterior potential $w^{(e)}(z,t)$, the analyticity in the exterior can be satisfied by use of the conformal mapping, which restricts the form of the Fourier series (3.2.3) to contain only negative frequencies. However, the analyticity of the

interior potential $w^{(i)}(z,t)$ is much harder to satisfy explicitly.

To evaluate the flow in the interior of the cell, we focus on two physically relevant values for the density ratio ϱ, namely $\varrho = 0$ and $\varrho = 1$. The case where $\varrho = 0$ corresponds to an interior fluid with zero density, which reduces the interior fluid to a uniform pressure field in the interior, effectively removing the interior fluid from the problem. This is a suitable assumption for cells where the interior fluid has a much lower density than the exterior fluid; for example, a gas-filled cell submerged in a liquid. The case where $\varrho = 1$ corresponds to an interior fluid with the same density as that of the exterior fluid. This provides a model for cells which are filled with the same fluid as that in which they are submerged; for example, an air-filled cell surrounded by air. We present two methods which can be used to satisfy the analyticity condition for the interior flow for $\varrho = 1$, allowing us to evaluate $\Omega_t^{(e)}$ and $\Omega_t^{(i)}$ numerically.

3.2.1 Uniform Pressure Interior

For the case of $\varrho = 0$ the interior of the cell attains a uniform pressure, with the interior potential $\Omega^{(i)}$ no longer playing a role in the system. To obtain the time derivative of the exterior potential $\Omega^{(e)}$, we note that

$$\Omega_t^{(e)} - \frac{\eta_t}{\eta_\phi}\Omega_\phi^{(e)} = \left(W_t - \frac{z_t}{z_\zeta}W_\zeta\right)\bigg|_{\zeta=e^{\mathrm{i}\phi}},$$

where $W(\zeta,t)$ is the complex potential in the ζ-plane given by (2.6.3). Since $W_t - W_\zeta z_t/z_\zeta$ is analytic in $|\zeta| > 1$ with $W_t - W_\zeta z_t/z_\zeta \to 0$ as $|\zeta| \to \infty$, we can apply the result (2.6.9) to obtain

$$\Omega_t^{(e)} - \frac{\eta_t}{\eta_\phi}\Omega_\phi^{(e)} = \mathrm{Re}\left(\Omega_t^{(e)} - \frac{\eta_t}{\eta_\phi}\Omega_\phi^{(e)}\right) + \mathcal{H}\left(\mathrm{Re}\left(\Omega_t^{(e)} - \frac{\eta_t}{\eta_\phi}\Omega_\phi^{(e)}\right)\right)$$

where the dynamic condition (3.2.1) gives

$$\mathrm{Re}\left(\Omega_t^{(e)} - \frac{\eta_t}{\eta_\phi}\Omega^{(e)}\right) = -\frac{1}{2}\left(\frac{\left|\Omega_\phi^{(e)}\right|^2}{|\eta_\phi|^2} - \alpha^2\right) + \left(\kappa_{ss} + \tfrac{1}{2}\kappa^3 - \sigma\kappa\right) + P. \tag{3.2.14}$$

The time derivative of the exterior potential is therefore given by

$$\begin{aligned}\Omega_t^{(e)} = \frac{\Omega_\phi^{(e)}}{\eta_\phi}\eta_t - \frac{1}{2}\left(\frac{\left|\Omega_\phi^{(e)}\right|^2}{|\eta_\phi|^2} - \alpha^2\right) + \left(\kappa_{ss} + \frac{1}{2}\kappa^3\right) + P \\ + \mathrm{i}\mathcal{H}\left(\frac{1}{2}\frac{\left|\Omega_\phi^{(e)}\right|^2}{|\eta_\phi|^2} - \kappa_{ss} - \frac{1}{2}\kappa^3\right) - \sigma\big(\kappa - \mathrm{i}\mathcal{H}(\kappa)\big).\end{aligned} \tag{3.2.15}$$

To obtain the value of $\sigma(t)$ we substitute (3.2.15) into (3.2.11), which gives the second derivative of the cell perimeter L as

$$\begin{aligned}L''(t) = \int_0^{2\pi}\left[\kappa_\phi \mathrm{Im}\left(\frac{\eta_t}{\eta_\phi}\Omega_\phi^{(e)}\right) + \kappa_\phi\mathcal{H}\left(\frac{1}{2}\frac{\left|\Omega_\phi^{(e)}\right|^2}{|\eta_\phi|^2} - \kappa_{ss} - \tfrac{1}{2}\kappa^3\right) - \kappa_t \mathrm{Im}\left(\Omega_\phi^{(e)}\right)\right]\mathrm{d}\phi \\ - \sigma\int_0^{2\pi}\kappa_\phi\mathcal{H}(\kappa)\mathrm{d}\phi,\end{aligned}$$

which depends linearly on σ. The value of σ can then be chosen directly to ensure that the value of $L''(t)$ satisfies the Baumgarte stabilisation (3.2.12). To determine the value of $P(t)$ we note that (2.6.8) gives

$$\int_0^{2\pi}\mathrm{Re}\left(\Omega_t^{(e)} - \frac{\eta_t}{\eta_\phi}\Omega_\phi^{(e)}\right)\mathrm{d}\phi = 0,$$

so integrating (3.2.14) we obtain

$$P(t) = \frac{1}{2\pi}\int_0^{2\pi}\left[\frac{1}{2}\left(\frac{\left|\Omega_\phi^{(e)}\right|^2}{|\eta_\phi|^2} - \alpha^2\right) - \kappa_{ss} - \frac{1}{2}\kappa^3 + \sigma\kappa\right]\mathrm{d}\phi. \tag{3.2.16}$$

We have thus obtained explicit expressions for both $\sigma(t)$ and $P(t)$ as well as the time derivatives of both $\eta(\phi,t)$ and $\Omega(\phi,t)$. To compute the time evolution

of unsteady solutions, we truncate the Fourier series (3.2.2) and (3.2.3) by setting $a_n = b_n = 0$ for $n > N$, where N is a chosen truncation value, and evaluate equations (3.2.8) and (3.2.15) to obtain values of η_t and $\Omega_t^{(e)}$ at some M equally spaced collocation points $\phi_i = \frac{2\pi(i-1)}{M}$ for $i = 1, \ldots, M$. The values of $a_n'(t)$ and $b_n'(t)$ can then be obtained from the Fourier series expansions (3.2.2) and (3.2.3) by a discrete Fourier transform. The Hilbert transform in (3.2.8) and (3.2.15) is computed in Fourier space using the known result

$$\mathcal{H}\left(e^{in\phi}\right) = -\mathrm{i}\,\mathrm{sgn}(n)e^{in\phi} \text{ for } n \neq 0.$$

The system can then be solved by use of an explicit time-stepping method, the details of which will be discussed in Section 3.2.3.

3.2.2 Interior Fluid

We next consider the case where $\varrho = 1$, corresponding to an interior fluid with equal density to that of the exterior fluid. The presence of an interior fluid increases the complexity of the problem; unlike the exterior flow, we don't have a conformal mapping to the interior, and so the analyticity of the interior potential must be satisfied by an alternative method. Recalling that the interior potential is only defined up to some arbitrary complex function of time, we take the real part of this arbitrary function such that $w^{(i)}(z_0, t) = 0$, and take the imaginary part to set $C(t) = 0$ in (3.2.13), giving

$$\mathrm{Im}\left(\Omega_t^{(e)} - \Omega_t^{(i)}\right) = 0. \tag{3.2.17}$$

and thus

$$\Omega_t^{(e)} - \Omega_t^{(i)} = \mathrm{Re}\left(\Omega_t^{(e)} - \Omega_t^{(i)}\right) \tag{3.2.18}$$

where $\mathrm{Re}\left(\Omega_t^{(e)} - \Omega_t^{(i)}\right)$ is given explicitly by (3.2.1). While (3.2.18) gives an explicit expression for the difference $\Omega_t^{(e)} - \Omega_t^{(i)}$, the interior potential must still be restricted by an analyticity condition to uniquely determine $\Omega_t^{(e)}$ and $\Omega_t^{(i)}$.

Since we require $w^{(i)}(z,t)$ to be analytic in the interior, it can be written as a Taylor series in z about the interior reference point z_0. The Taylor coefficients can then be obtained by satisfying the kinematic condition (3.2.4) on the boundary, and their derivatives can be obtained by satisfying (3.2.18) on the boundary. This method is effective for cells which are close to the circular rest state, but for more severely deformed cells we will see that this method becomes numerically unsuitable.

Alternatively, we can use a boundary integral method. For $w_t^{(i)}(z,t)$ to be analytic in the interior, we require $\mathrm{Re}\left(w_t^{(i)}(z,t)\right)$ to be harmonic in the interior, and thus satisfy a boundary integral equation, which along with (3.2.1) and (3.2.4) implicitly determines the time derivatives of both potentials. These equations can then be solved numerically to obtain values for the time derivatives. While this method is more complex than the Taylor series method, it remains accurate for severely deformed cell shapes, and is therefore a more reliable method.

In practice, we compute the time derivatives using both methods and compare the results to confirm their validity. The details of both methods are presented below.

Taylor Series Method

We represent the interior complex potential as a Taylor series about the interior reference point $z = z_0(t)$ as

$$w^{(i)}(z,t) = \sum_{n=0}^{\infty} c_n(t)(z - z_0(t))^n, \tag{3.2.19}$$

where the coefficients c_n are to be found and c_0 must be imaginary due to the restriction $\mathrm{Re}\Big(w^{(i)}(z_0,t)\Big) = 0$. At the cell boundary we have

$$\Omega^{(i)}(\phi,t) = \sum_{n=0}^{\infty} c_n(t)\big(\eta(\phi,t) - z_0(t)\big)^n, \tag{3.2.20}$$

and so the kinematic condition (3.2.17) requires

$$\mathrm{Im}\left(\sum_{n=0}^{\infty} c_n(t)(\eta(\phi,t) - z_0(t))^n\right) = \mathrm{Im}\Big(\Omega^{(e)}(\phi,t)\Big), \tag{3.2.21}$$

which depends linearly on the unknown coefficients c_n. If the exterior potential is known, the interior potential can be obtained numerically by truncating the coefficients c_n after N terms and sampling (3.2.21) at $2N+1$ evenly spaced values of $\phi_j = \frac{2\pi(j-1)}{2N+1}$ for $j = 1,\ldots,2N+1$ around the cell boundary, giving $2N+1$ real equations for the N complex variables c_n for $1 \le n \le N$ and the imaginary variable c_0.

To obtain the time derivatives of the coefficients $b_n'(t)$ and $c_n'(t)$ of the exterior and interior potentials, we note that (3.2.18) can be written as

$$\Omega_t^{(e)} - \Omega_t^{(i)} - P(t) = F(\phi,t) + \sigma G(\phi,t) \tag{3.2.22}$$

where $F(\phi,t)$ and $G(\phi,t)$ are known functions corresponding to terms in the dynamic condition (3.2.1). The time derivatives $\Omega_t^{(e)}$ and $\Omega_t^{(i)}$ can be obtained in terms of the coefficients b_n' and c_n' by differentiating the series expansions (3.2.3) and (3.2.20) respectively. Substituting these series into (3.2.22), we obtain

$$\begin{aligned}&\sum_{n=1}^{\infty}\Big[b_n' e^{-\mathrm{i}n\phi} - c_n'(\eta - z_0)^n\Big] + c_0' - P(t) - \sigma G(\phi,t)\\ &= F(\phi,t) - \alpha a_{-1}'(t)e^{\mathrm{i}\phi} - \alpha a_0'(t) + \sum_{n=1}^{\infty}\Big[n(\eta_t - z_0')c_n(\eta - z_0)^{n-1}\Big],\end{aligned} \tag{3.2.23}$$

which depends linearly on the unknowns b_n', c_n', $P(t)$ and $\sigma(t)$. Truncating

the series (3.2.3) and (3.2.20) after N terms, we have $2N$ complex unknowns, namely b'_n and c'_n for $1 \leq n \leq N$, and three real unknowns c'_0, P and σ. We then sample equation (3.2.23) at $2N+1$ evenly spaced values of $\phi_j = \frac{2\pi(j-1)}{2N+1}$ for $j = 1, \ldots, 2N+1$ around the cell boundary, giving $2N+1$ complex equations to be satisfied. To complete the system, we satisfy the inextensibility condition using the Baumgarte stabilisation (3.2.12), where $L''(t)$ is given in terms of $\Omega_t^{(e)}$ by (3.2.11). To ensure the results are accurate, we increase the truncation level N and confirm that the values of $b'_n(t)$ and $c'_n(t)$ converge to within an acceptable tolerance.

This method works well for cells which are not deformed too severely from the unit circle. For cells with significant deformation however, we find that for large values of n the term $c_n(\eta - z_0)^n$ in (3.2.20) will be very sensitive to changes in η on sections of the cell wall with $|\eta - z_0| > 1$, while for sections of the cell wall with $|\eta - z_0| < 1$ a large change in η will result in only a small change in the term $c_n(\eta - z_0)^n$. This leads to significant numerical error when satisfying the boundary condition in the regions where $|\eta - z_0| < 1$, resulting in poor convergence of the values of $b'_n(t)$ and $c'_n(t)$.

Boundary Integral Method

An alternative method for obtaining the interior flow is based on the boundary integral method. The boundary integral method is a numerical method used to solve Laplace's equation in the interior of a boundary curve by satisfying a discretised boundary integral equation. Noting that the real and imaginary parts of an analytic function must be harmonic, the boundary integral method can be used to reduce the analyticity of the potential $w^{(i)}(z,t)$ and its time derivative $w_t^{(i)}(z,t)$ to an integral equation at the cell boundary, which along with (3.2.1) and (3.2.17) can be used to uniquely determine their values numerically. The numerical method presented below is based on that

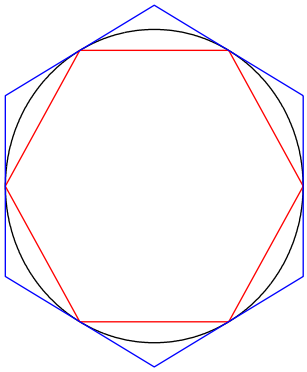

Figure 3.2.1: Sketch showing two polygonal approximations to a closed curve (black). The red polygon is obtained by taking the vertices at evenly spaced points around the curve, while the blue polygon is obtained by taking the polygon to be tangent to the curve at evenly spaced points around the curve.

detailed by Pozrikidis (2002b).

The boundary integral equation for a non-singular harmonic function $f(z)$ in the interior of some boundary curve C is given by Pozrikidis (2002b) as

$$\frac{1}{2}f(z') = \int_C G(z,z')\big[\hat{\boldsymbol{n}}(z)\cdot\nabla f(z)\big]\mathrm{d}s(z) - \int_C^{PV} f(z)\big[\hat{\boldsymbol{n}}(z)\cdot\nabla G(z,z')\big]\mathrm{d}s(z), \tag{3.2.24}$$

where z' is some point on the boundary C, $\hat{\boldsymbol{n}}$ is the unit normal vector pointing from the interior towards the exterior of the cell, and PV denotes the principal value integral. Here $G(z,z')$ is the free-space Green's function defined as

$$G(z,z') = -\frac{1}{2\pi}\log|z-z'|,$$

with

$$\nabla G(z,z') = -\frac{1}{2\pi}\frac{(x-x')\boldsymbol{i}+(y-y')\boldsymbol{j}}{|z-z'|^2}.$$

To solve (3.2.24) numerically, we discretise the cell boundary into N straight boundary elements denoted by E_j for $j = 1,\ldots,N$. Some care must be taken in choosing the discretisation of the cell; if we simply take the vertices to be at N sample points around cell boundary, we obtain a polygon whose normal and

tangent vectors are discontinuous at the sample points. Instead, we construct a polygon which is tangent to the boundary curve at N chosen sample points $\eta_j = \eta(\phi_j, t)$ where $\phi_j = \frac{2\pi(j-1)}{N}$ for $j = 1, \ldots, N$, which allows us to obtain an accurate normal derivative of $f(z)$ at the sample points. A sketch of this polygon is shown in blue in Figure 3.2.1. The boundary element E_j can then be parametrised by

$$E_j = \eta_j^v + \left(\eta_{j+1}^v - \eta_i^v\right)t \quad \text{for} \quad 0 \leq t \leq 1, \tag{3.2.25}$$

where η_j^v are the numerically obtained vertices of the polygon, with the element E_j taken to contain the jth sample point η_j. The complex tangent and normal vectors $\hat{\tau}_j$ and $\hat{n}_j$, which are both constant on each boundary element, are given by

$$\hat{\tau}_j = \frac{\eta_{j+1}^v - \eta_j^v}{\left|\eta_{j+1}^v - \eta_j^v\right|} = \hat{\tau}(\phi_j), \qquad \hat{n}_j = -\mathrm{i}\frac{\eta_{j+1}^v - \eta_j^v}{\left|\eta_{j+1}^v \eta -_j^v\right|} = \hat{n}(\phi_j)$$

respectively. We approximate the functions f and $\nabla f \cdot \hat{\boldsymbol{n}}$ as constant values f_j and $(\nabla f \cdot \hat{\boldsymbol{n}})_j$ over the boundary element E_j equal to their values at the sample points η_j. The boundary integral equation (3.2.24) can thus be discretised as

$$\frac{1}{2}f(z') = \sum_{j=1}^{N}(\nabla f \cdot \hat{\boldsymbol{n}})_j \int_{E_j} G(z, z')\mathrm{d}s(z) - \sum_{j=1}^{N} f_j \int_{E_j}^{PV} \left[\hat{\boldsymbol{n}}_j \cdot \nabla G(z, z')\right]\mathrm{d}s(z). \tag{3.2.26}$$

Evaluating (3.2.26) at each of the sample points $z' = \eta_k$ for $k = 1, \ldots, N$, we obtain the N equations

$$\frac{1}{2}f_k = \sum_{j=1}^{N}(\nabla f \cdot \hat{\boldsymbol{n}})_j \int_{E_j} G(z, \eta_k)\mathrm{d}s(z) - \sum_{j=1}^{N} f_j \int_{E_j}^{PV} \left[\hat{\boldsymbol{n}}_j \cdot \nabla G(z, \eta_k)\right]\mathrm{d}s(z) \tag{3.2.27}$$

for $k = 1, \ldots, N$, which depend linearly on the $2N$ unknowns f_j and $(\nabla f \cdot \hat{\boldsymbol{n}})_j$

and N. If the normal derivative $(\nabla f \cdot \hat{\boldsymbol{n}})_j$ is known the system of equations (3.2.27) can easily be solved numerically. Note however that this system will be rank-deficient; since f_j is a potential, the boundary integral method will only determine its value to an arbitrary constant, this constant can be fixed by enforcing an additional restraint on f. If however the normal derivative is not known, (3.2.27) simply provides a restriction which must be satisfied alongside any other boundary conditions to complete the problem.

The integrals in (3.2.27) are evaluated numerically using Gauss-Legendre Quadrature, which gives the integral of a function $g(z)$ along a boundary element as

$$\begin{aligned}\int_{E_j} g(z)\mathrm{d}s(z) &= \int_0^1 g\Big(\eta_j^v + \big(\eta_{j+1}^v - \eta_j^v\big)t\Big)\big|\eta_{j+1}^v - \eta_j^v\big|\mathrm{d}t \\ &= \frac{1}{2}\sum_{j=1}^{n} g\left(\eta_j^v + \frac{\big(\eta_{j+1}^v - \eta_j^v\big)\big(t_j+1\big)}{2}\right)\big|\eta_{j+1}^v - \eta_j^v\big|W_j,\end{aligned}$$

where $g(z)$ is the function being integrated and t_j and W_j are the nodes and weights of the Gauss-Legendre Quadrature. Note the rescaling of the argument of g, which changes the integral from $[0,1]$ to the standard $[-1,1]$.

Applying the boundary integral method to the interior velocity potential $\mathrm{Re}\Big(w^{(i)}(z,t)\Big)$, we note that the normal derivative to the boundary is given by the kinematic condition as

$$\hat{\boldsymbol{n}} \cdot \nabla \mathrm{Re}\Big(w^{(i)}(z,t)\Big)\Big|_{z=\eta(\phi,t)} = \mathbf{u}^{(i)}(\eta,t)\cdot\hat{\boldsymbol{n}} = \mathbf{u}^{(e)}(\eta,t)\cdot\hat{\boldsymbol{n}} = \mathrm{Im}\Big(\Omega_s^{(e)}(\phi,t)\Big).$$

The discretised boundary integral equation (3.2.27) thus gives

$$\begin{aligned}\frac{1}{2}\mathrm{Re}\Big(\Omega_k^{(i)}\Big) = &\sum_{j=1}^{N}\mathrm{Im}\Big(\Omega_s^{(e)}(\phi_j,t)\Big)\int_{E_j} G(z,\eta_k)\mathrm{d}s(z) \\ &- \sum_{j=1}^{N}\mathrm{Re}\Big(\Omega_j^{(i)}\Big)\int_{E_j}^{PV}\big[\hat{\boldsymbol{n}}_j\cdot\nabla G(z,\eta_k)\big]\mathrm{d}s(z),\end{aligned} \tag{3.2.28}$$

where $\Omega_j^{(i)}$ is the approximated value of $\Omega^{(i)}(\phi_j, t)$. To uniquely determine the arbitrary constant in $\mathrm{Re}\left(w^{(i)}(z,t)\right)$, we take $\mathrm{Re}\left(w^{(i)}(z_0,t)\right) = 0$ at the interior reference point, given by a boundary integral equation as

$$\sum_{j=1}^{N} \mathrm{Im}\left(\Omega_s^{(e)}(\phi_j,t)\right) \int_{E_j} G(z,z_0)\mathrm{d}s(z) - \sum_{j=1}^{N} \Omega_j^{(i)} \int_{E_j}^{PV} \left[\hat{\boldsymbol{n}}_j \cdot \nabla G(z,z_0)\right]\mathrm{d}s(z) = 0. \tag{3.2.29}$$

Equations (3.2.28) and (3.2.29) form a complete linear system which can be solved numerically for a given exterior flow potential $\Omega^{(e)}$ to obtain values of $\mathrm{Re}\left(\Omega_k^{(i)}\right)$. The complex values $\Omega_k^{(i)}$ can then be obtained by recalling that the Kinematic condition requires $\mathrm{Im}\left(\Omega^{(i)}(\phi,t)\right) = \mathrm{Im}\left(\Omega^{(e)}(\phi,t)\right)$, giving $\Omega^{(i)}(\phi_k,t) \approx \mathrm{Re}\left(\Omega_k^{(i)}\right) + \mathrm{Im}\left(\Omega^{(e)}(\phi_k,t)\right)\mathrm{i}$ at the N sample points ϕ_k.

The boundary integral method can also be used to obtain values for the time-derivative of the interior potential $\mathrm{Re}\left(w_t^{(i)}(z,t)\right)$. The derivative normal to the cell wall is given in complex form as

$$\hat{\boldsymbol{n}} \cdot \nabla \mathrm{Re}\left(w_t^{(i)}(z,t)\right) = \mathrm{Im}\left(w_{zt}^{(i)}\eta_s\right) = \mathrm{Im}\left(\Omega_{st}^{(i)} - \frac{\eta_{st}}{\eta_s}\Omega_s^{(i)} + \frac{\eta_t\eta_{ss}}{\eta_s^2}\Omega_s^{(i)} - \frac{\eta_t}{\eta_s}\Omega_{ss}^{(i)}\right),$$

where $\Omega_s^{(i)}$ and $\Omega_{ss}^{(i)}$ are assumed to have already been obtained numerically using the boundary integral method presented above, and $\mathrm{Im}\left(\Omega_{st}^{(i)}\right)$ is given in terms of the exterior potential by the kinematic condition as

$$\mathrm{Im}\left(\Omega_{st}^{(i)}\right) = \mathrm{Im}\left(\Omega_{st}^{(e)}\right).$$

The discretised boundary integral equation (3.2.27) thus gives

$$\frac{1}{2}\mathrm{Re}\left(\Omega_t^{(i)}(\phi_k,t)\right) = -\sum_{j=1}^{N}\mathrm{Re}\left(\Omega_t^{(i)}(\phi_j,t)\right)\int_{E_j}^{PV}\left[\hat{\boldsymbol{n}}_j\cdot\nabla G(z,\eta_k)\right]\mathrm{d}s(z) + \sum_{j=1}^{N}\mathrm{Im}\left(\Omega_{st}^{(e)} - \frac{\eta_{st}}{\eta_s}\Omega_s^{(i)} + \frac{\eta_t\eta_{ss}}{\eta_s^2}\Omega_s^{(i)} - \frac{\eta_t}{\eta_s}\Omega_{ss}^{(i)}\right)\Bigg|_{\phi=\phi_j}\int_{E_j} G(z,\eta_k)\mathrm{d}s(z). \tag{3.2.30}$$

Note however that the value of $\mathrm{Im}\left(\Omega_{st}^{(e)}\right)$ cannot generally be determined in advance; the unsteady evolution of both $\Omega^{(e)}$ and $\Omega^{(i)}$ are determined implicitly by the dynamic condition (3.2.1), which must be satisfied alongside the boundary integral equation to obtain values of both the interior and exterior potentials.

Recalling that $\Omega^{(e)}(\phi,t)$ is given by (3.2.3) as a Fourier series, we can obtain an expression for $\mathrm{Im}\left(\Omega_{st}^{(e)}\right)$ which depends linearly on the time-derivative of the Fourier coefficients $b_n'(t)$. Truncating the Fourier series after $\frac{N-1}{2}$ terms by setting $b_n'(t) = 0$ for $n \geq \frac{N-1}{2}$, we have $N-1$ real unknowns corresponding to the real and imaginary parts of b_n. Note that this requires N to be odd. We then sample the dynamic condition (3.2.1) at the N sample points ϕ_j, giving N equations which depend linearly on $\mathrm{Re}\left(\Omega_t^{(i)}(\phi_k,t)\right)$ and $b_n'(t)$ as well as the unknowns $P(t)$ and $\sigma(t)$. Along with the boundary integral equation (3.2.30), this gives a total of $2N$ equations with $2N+1$ unknowns. However, recalling that the discretised boundary integral equation is rank-deficient, we only have $2N-1$ linearly independent equations. To fix the arbitrary constant in $\Omega_t^{(i)}$, we set $\frac{\partial}{\partial t}\left(w^{(i)}(z_0,t)\right) = 0$, and to complete the system we enforce the inextensibility of the cell by satisfying the Baumgarte stabilisation condition (3.2.12). The problem is thus reduced to a linear system of $2N+2$ equations with rank $2N+1$, which can be solved numerically to obtain values for the $2N+1$ unknowns $b_n'(t)$, $\mathrm{Re}\left(\Omega_t^{(i)}(\phi_k,t)\right)$, σ, and P.

3.2.3 Numerical Method

We have presented methods to obtain the time derivatives of the truncated Fourier coefficients $a_n'(t)$ and $b_n'(t)$ numerically for both $\varrho = 0$ and $\varrho = 1$. Note that while the time derivative of the interior potential can also be obtained numerically, we opt to compute the interior potential directly from the kinematic condition by solving either equation (3.2.21) or (3.2.28) wherever the interior flow is required. The variables $a_n'(t)$ and $b_n'(t)$ can then be integrated in time numerically using the MATLAB function `ode113`, which uses an Adams-Bashforth-Moulton method. Due to the chaotic nature of the system, which will be discussed in Section 3.5, the system is very sensitive to variations in the initial state, so the computations are only accurate for small values of t. To ensure the validity of the results over the time frames considered, the truncation levels for the results presented in this chapter were taken at $N = 51$, $N = 61$ and $N = 71$ and it was confirmed that the results converge as N is increased. Recalling that the perimeter of the cell, the area inside the cell and the total energy $\mathscr{E}$ are all conserved quantities of the system, we can use the numerical drift of these quantities to give an indication of the scale of the numerical error. The stabilisation factor γ is taken to be 10^4 for all computations, which keeps the absolute difference between the perimeter and 2π below 10^{-6}, and the drift in the cell area and total energy of the system are both confirmed to also remain below 10^{-6}.

3.3 Linear Stability Method

The linear stability of an equilibrium state describes the growth rate of a small perturbation to the system. By linearising the unsteady system, we can decompose a small perturbation into a series of eigenvectors, with corresponding eigenvalues determining their growth in time. The spectrum of

eigenvalues determines whether a small random perturbation will grow in time, with the corresponding eigenvectors indicating how the perturbation growth affects the system.

To linearise the unsteady system we introduce small perturbations to each of the unknowns: the cell boundary and the exterior complex potential are perturbed from some steady state as $\eta(\phi) + \varepsilon\hat{\eta}(\phi, t)$ and $\Omega^{(e)}(\phi) + \varepsilon\hat{\Omega}^{(e)}(\phi, t)$ respectively; the interior potential, which is zero for an equilibrium state, is perturbed as $\varepsilon\hat{\Omega}^{(i)}(\phi, t)$; and the time-dependent parameters are perturbed as $\sigma + \varepsilon\hat{\sigma}(t)$ and $P + \varepsilon\hat{P}(t)$. Here hats indicate time-dependent perturbations to the steady solution, and ε is taken to be a small positive constant. Substituting these perturbed variables into the dynamic condition (3.2.1) and comparing $O(\varepsilon)$ terms, we obtain

$$\begin{aligned}\mathrm{Re}\left(\hat{\Omega}^{(e)}_t - \frac{\Omega^{(e)}_\phi}{\eta_\phi}\hat{\eta}_t - \varrho\hat{\Omega}^{(i)}_t\right) + \mathrm{Re}\left(\frac{\overline{\Omega}_\phi}{|\eta_\phi|^2}\hat{\Omega}^{(e)}_\phi - \frac{\left|\Omega^{(e)}_\phi\right|^2}{\eta_\phi|\eta_\phi|^2}\hat{\eta}_\phi\right) \\ - \hat{\kappa}_{ss} - \tfrac{3}{2}\kappa^2\hat{\kappa} + \sigma\hat{\kappa} + \hat{\sigma}\kappa - \hat{P} = 0,\end{aligned} \tag{3.3.1}$$

where $\hat{\kappa} = \mathrm{Im}\left(\overline{\eta}_{ss}\hat{\eta}_s - \overline{\eta}_s\hat{\eta}_{ss}\right)$. The kinematic condition (3.2.4) is linearised in the same way, giving

$$\mathrm{Im}\left(\hat{\eta}_t\,\overline{\eta}_\phi\right) = -\mathrm{Im}\left(\hat{\Omega}^{(e)}_\phi\right) = -\mathrm{Im}\left(\hat{\Omega}^{(i)}_\phi\right), \tag{3.3.2}$$

and the perimeter condition (3.2.9) gives

$$\int_0^{2\pi} \kappa\mathrm{Im}\left(\hat{\Omega}^{(e)}_{\phi t}\right)\mathrm{d}\phi = 0. \tag{3.3.3}$$

The functions $\hat{\eta}(\phi, t)$ and $\hat{\Omega}^{(e)}(\phi, t)$ are given by (3.2.2) and (3.2.3) as

$$\hat{\eta}(\phi, t) = \hat{a}_{-1}(t)\mathrm{e}^{\mathrm{i}\phi} + \hat{a}_0(t) + \sum_{n=1}^{\infty}\hat{a}_n(t)e^{-\mathrm{i}n\phi}$$

and

$$\hat{\Omega}^{(e)}(\phi, t) = \alpha \hat{a}_{-1}(t) e^{\mathrm{i}\phi} + \alpha \hat{a}_0(t) + \sum_{n=1}^{\infty} \hat{b}_n(t) e^{-\mathrm{i}n\phi},$$

where $\hat{a}_n$ and $\hat{b}_n$ are the perturbed Fourier coefficients.

As noted in Section 3.2.2, it is difficult to enforce the analyticity of the interior potential $\hat{w}^{(i)}(z, t)$. We have already seen two methods which can be used to enforce the analyticity condition, using either a Taylor series expansion of the interior potential or the boundary integral method. For the linearised system however, we can make use of a conformal mapping technique for the interior fluid, which allows us to take a more analytic approach in constructing the full linear system.

The interior of the cell can be mapped from the interior of some convenient domain in some ζ-plane by use of a Schwarz-Christoffel mapping, which maps to the interior of a chosen polygon from some simple domain in the ζ-plane. By discretising the cell boundary $\eta(s, t)$ as an N-sided polygon, we can obtain an accurate approximation of a mapping to the interior of the cell. The Schwarz-Christoffel mapping is obtained numerically using the MATLAB package `Schwarz-Christoffel Toolbox` presented by Driscoll and Trefethen (2002). There are two key advantages to using a Schwarz-Christoffel mapping for the interior; the Schwarz-Christoffel mapping explicitly maps known points on the boundary of the domain in the preimage ζ-plane to the vertices of the polygon in the z-plane, which allows us to satisfy the governing equations at evenly spaced values of ϕ without having to interpolate the mapping to locate these points in the preimage ζ-plane. The Schwarz-Christoffel mapping also allows us to choose an appropriate preimage domain for the problem; we will show that when the cell becomes significantly deformed from its circular rest state, a mapping from the unit

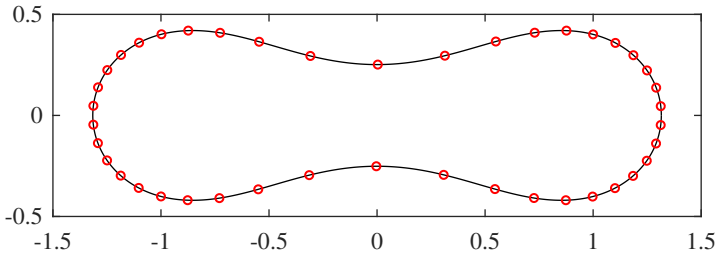

(a) The preimage of the cell with evenly spaced markers

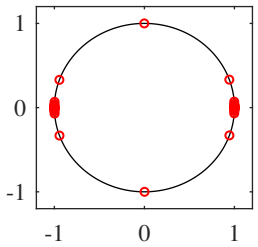

(b) Marker distribution on a circular mapping

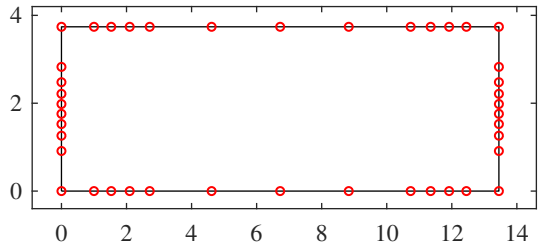

(c) Marker distribution on a rectangular mapping

Figure 3.3.1: Sketch of the points on (b) a circular domain and (c) a rectangular domain which are mapped to evenly spaced points along the boundary of an elongated cell (a) by a Schwarz-Christoffel mapping.

circle becomes inappropriate, but by choosing a rectangular domain the mapping can remain accurate even for severely deformed cells. The Schwarz-Christoffel mapping is ill-suited for the nonlinear time-stepping method, since it is computationally demanding to compute the Schwarz-Christoffel mapping at every time-step. For the linear stability problem however, since the unperturbed interior fluid is static the perturbed cell boundary $\hat{\eta}(\phi, t)$ only contributes to the interior flow at $O(\varepsilon^2)$, and so we only require a conformal mapping to the steady cell shape $\eta(\phi)$. The Schwarz-Christoffel mapping therefore only needs to be computed once to evaluate the stability of an equilibrium solution.

The simplest choice of preimage domain is the interior of the unit circle. This works well for cell shapes close to the unit circle, but for more severely deformed shapes we encounter the problem of crowding, where a conformal mapping from the interior of the shape to the interior of the unit disk tends to map evenly distributed points in the z-plane to bunched up points in the ζ-

plane (DeLillo, 1994), causing difficulties in solving the equations numerically. An example of this crowding effect can be seen in Figure 3.3.1. To reduce the crowding effect, we instead choose the preimage domain to be the interior of a rectangle, with the aspect ratio chosen automatically to minimise the effects of crowding.

Once a mapping has been obtained from the interior of a rectangle in the ζ-plane, we require a velocity potential $\varphi(x, y, t)$ that satisfies Laplace's equation on the interior of the rectangle $0 \leq x \leq L, 0 \leq y \leq H$. By separation of variables it can be shown that the general solution is given by

$$\begin{aligned}\varphi(x,y) = &\sum_{n=1}^{\infty} A_n \cosh\left(\tfrac{\pi n}{L} y\right) \cos\left(\tfrac{\pi n}{L} x\right) + \sum_{n=1}^{\infty} B_n \cosh\left(\tfrac{\pi n}{L}(y-H)\right) \cos\left(\tfrac{\pi n}{L} x\right) \\ &+ \sum_{n=1}^{\infty} C_n \cosh\left(\tfrac{\pi n}{H} x\right) \cos\left(\tfrac{\pi n}{H} y\right) + \sum_{n=1}^{\infty} D_n \cosh\left(\tfrac{\pi n}{H}(x-L)\right) \cos\left(\tfrac{\pi n}{H} y\right) \\ &+ a + bx + cy + d(x^2 - y^2),\end{aligned} \tag{3.3.4}$$

where the coefficients A_n, B_n, C_n, D_n, a, b, c and d are to be found in terms of the perturbed external flow coefficients $\hat{b}_n$ by satisfying the kinematic condition. We write the kinematic condition in terms of the potential $\varphi(x, y, t)$ as

$$\frac{\partial \varphi}{\partial n} = \mathrm{Im}\left(\hat{\Omega}_s^{(e)}\right) |F'(\zeta)|, \tag{3.3.5}$$

where $|F'(\zeta)|$ is the first derivative of the interior conformal mapping function and $\frac{\partial \varphi}{\partial n}$ is the normal derivative of the potential $\varphi(x, y, t)$ on the rectangular boundary. The normal derivative is given on each of the four edges of the

rectangle as

$$
\begin{aligned}
-\varphi_x(0,y) &= -a - \sum_{n=1}^{\infty} D_n \frac{\pi n}{H} \sinh\left(-\tfrac{\pi n}{H} L\right) \cos\left(\tfrac{\pi n}{H} y\right), \\
\varphi_x(L,y) &= a + 2cL + \sum_{n=1}^{\infty} C_n \frac{\pi n}{H} \sinh\left(\tfrac{\pi n}{H} L\right) \cos\left(\tfrac{\pi n}{H} y\right), \\
-\varphi_y(x,0) &= -b - \sum_{n=1}^{\infty} B_n \frac{\pi n}{L} \sinh\left(-\tfrac{\pi n}{L} H\right) \cos\left(\tfrac{\pi n}{L} x\right), \\
\varphi_y(x,H) &= b - 2cH + \sum_{n=1}^{\infty} A_n \frac{\pi n}{L} \sinh\left(\tfrac{\pi n}{L} H\right) \cos\left(\tfrac{\pi n}{L} x\right).
\end{aligned}
$$

We truncate the series solution (3.3.4) after some M terms, setting $A_n = B_n = C_n = D_n = 0$ for $n > M$. (3.3.5) can then be satisfied numerically at $4M+3$ evenly spaced points around the rectangle in the ζ-plane to obtain expressions for A_n, B_n, C_n, D_n, a, b and c which depend linearly on the exterior flow coefficients $\hat{b}_n$, with the value of d obtained by setting $\hat{w}^{(i)}(z_0, t) = 0$. The contribution of the interior flow to the dynamic condition (3.3.1) $\mathrm{Re}\left(\Omega_t^{(i)}\right)$ is then given as a linear expression depending on the coefficients $\hat{b}_n'(t)$.

We truncate the coefficients $\hat{a}$ and $\hat{b}$ after some K terms and split them into real and imaginary parts, giving a total of $4K + 5$, corresponding to $\hat{a}_{-1}$, $\hat{P}$, $\hat{\sigma}$, and the real and imaginary parts of $\hat{a}_n$ and $\hat{b}_n$ for $0 \le n \le K$. We evaluate (3.3.2) and (3.3.1) at $2K + 2$ equally spaced collocation points ϕ_i, which together with (3.3.3) gives $4K + 5$ equations for the $4K + 5$ unknowns. These equations can then be written as the linear system

$$
\boldsymbol{A}\boldsymbol{X}' = \boldsymbol{B}\boldsymbol{X}, \tag{3.3.6}
$$

where $\boldsymbol{X}(t)$ contains the $4K + 5$ unknowns, and $\boldsymbol{A}$ and $\boldsymbol{B}$ are $(4K + 5) \times (4K + 5)$ matrices whose elements are known explicitly in terms of a_n, b_n, $\hat{a}_{-1}$, $\hat{P}$ and $\hat{\sigma}$. Seeking normal mode solutions of the form $\boldsymbol{X}(t) = \boldsymbol{X}_0 e^{\lambda t}$, we obtain the generalised eigenvalue problem $\lambda \boldsymbol{A}\boldsymbol{X}_0 = \boldsymbol{B}\boldsymbol{X}_0$, which we solve

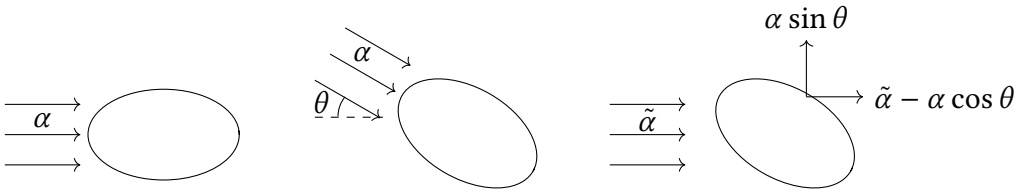

Figure 3.3.2: Illustration to show how the rotation of a solution for a given α may be used to construct a new steadily translating solution for $\tilde{\alpha}$.

numerically using the in-built MATLAB function `eig`. Since the matrices $\boldsymbol{A}$ and $\boldsymbol{B}$ are real, the eigenvalues λ must come in complex conjugate pairs $\{\lambda, \overline{\lambda}\}$, with corresponding eigenvectors $\{\boldsymbol{v}, \overline{\boldsymbol{v}}\}$. These eigenvectors are in general complex, but real solutions to (3.3.6) can be constructed by taking $\boldsymbol{X} = r\left(\boldsymbol{v}e^{\lambda t+\mathrm{i}k} + \overline{\boldsymbol{v}}e^{\overline{\lambda}t-\mathrm{i}k}\right)$, where r and k are freely chosen real numbers corresponding to the magnitude and phase-shift of the perturbation respectively. A steady solution is said to be spectrally stable if the magnitude of the perturbed parameters remains bounded as the $t \longrightarrow \infty$. The solution is thus spectrally stable if $\mathrm{Re}(\lambda) \leq 0$ for all eigenvalues λ, and unstable otherwise.

Note that given a solution to the unsteady system for a chosen far-field flow speed α we can construct another unsteady solution for a different $\tilde{\alpha}$ by rotating the system clockwise through an arbitrary angle θ and taking a reference frame moving with velocity $\boldsymbol{V} = (\alpha\cos\theta - \tilde{\alpha}, -\alpha\sin\theta)$, as illustrated in Figure 3.3.2. The new solution corresponds to the original cell motion with a superimposed steady translation of velocity $-\boldsymbol{V}$. This reflects the Galilean invariance of the physical system. The steady solution at $(\alpha + \hat{\alpha}, P)$ can therefore be considered a perturbation of the steady solution at (α, P), which has a different cell shape and correspondingly a different flow. Hence for a steady solution at (α, P) there always exist perturbations of the form $\hat{\eta}(\phi, t) = (a+b\mathrm{i})t+C_1(\phi)$, $\hat{\Omega}(\phi, t) = C_2(\phi)$ which satisfy the linear system, where a and b are freely chosen constants and $C_1(\phi)$ and $C_2(\phi)$ are associated with the change in shape and the corresponding flow change respectively. With reference to (3.3.6), these perturbations can be

expressed as a linear combination of the two linearly independent perturbations $\boldsymbol{X}_1 = \boldsymbol{v}_1 t + \boldsymbol{w}_1$ and $\boldsymbol{X}_2 = \boldsymbol{v}_2 t + \boldsymbol{w}_2$, where $\boldsymbol{v}_1$ corresponds to a perturbation of $\mathrm{Re}(a_0)$ only and is a horizontal translation, and $\boldsymbol{v}_2$ corresponds to a perturbation of $\mathrm{Im}(a_0)$ only and is a vertical translation. Substituting these expressions into the linear system (3.3.6), we obtain $\boldsymbol{B}\boldsymbol{v}_n = 0$, $\boldsymbol{B}\boldsymbol{w}_n = \boldsymbol{A}\boldsymbol{v}_n$ for $n = 1, 2$. The two linearly independent $\boldsymbol{v}_n$ are thus eigenvectors with generalised eigenvectors $\boldsymbol{w}_n$ of rank 2 corresponding to a zero eigenvalue. The steady solution at $(\alpha, P + \hat{P})$ can also be considered a perturbation of the steady solution at (α, P), which has a different shape and correspondingly a different flow. Since this perturbation is time-independent, it also corresponds to an eigenvector with zero eigenvalue. We conclude that (3.3.6) has a zero eigenvalue with three linearly independent eigenvectors and two linearly independent generalised eigenvectors of rank 2, which implies algebraic multiplicity five and geometric multiplicity three. This agrees with the results obtained numerically.

Since the unsteady system (3.2.1)–(3.2.4) is invariant under the transform $\eta(\phi, t) \to -\overline{\eta}(\pi - \phi, -t)$, $\Omega^{(e)}(\phi, t) \to -\overline{\Omega}^{(e)}(\pi - \phi, -t)$, $\Omega^{(i)}(\phi, t) \to -\overline{\Omega}^{(i)}(\pi - \phi, -t)$, if a steady solution has eigenvalue λ then its reflection about a vertical axis is another steady solution with eigenvalue $-\lambda$. Furthermore, recalling that the eigenvalues λ appear in complex conjugate pairs, if the steady solution is left-right symmetric the eigenvalues will appear as quadruples $\{\lambda, \overline{\lambda}, -\lambda, -\overline{\lambda}\}$, and in this case stability can only occur if $\mathrm{Re}(\lambda) = 0$ for all eigenvalues λ.

3.4 Steady State Analysis

In this section we consider the steady equilibrium states of the system, which are governed by (3.1.1). We derive asymptotic solutions for low flow speeds, and analyse the full solution-space numerically.

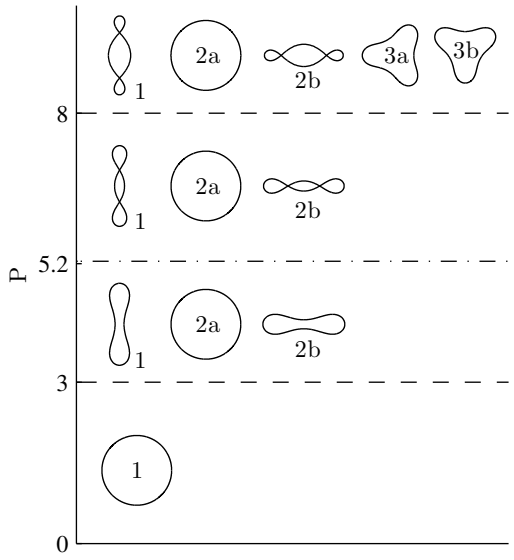

Figure 3.4.1: Illustration of the distinct cell shapes which exist for $\alpha = 0$. The critical pressures $P = 3$ and $P = 8$ correspond to the bifurcation points of mode-2 and mode-3 buckled cells respectively. The pressure $P = 5.2$ indicates a point of self-contact of a mode-2 cell; such cells self-intersect above this pressure.

3.4.1 Static Fluid Results

We start by considering the case where the exterior fluid is static, which corresponds to setting $\alpha = 0$. In the absence of a flow the exterior fluid takes a uniform pressure, and the governing equation (3.1.1) is reduced to

$$\kappa_{ss} + \tfrac{1}{2}\kappa^3 - \sigma\kappa + P = 0. \tag{3.4.1}$$

There clearly exists a trivial circular solution $\kappa = -1$, $\sigma = \frac{1}{2} - P$ which is valid for all P. However, it is well known that in addition to this trivial solution there exists a set of mode-n symmetric buckled solutions which emerge as the transmural pressure P increased beyond a series of critical values (Halphen, 1888). These buckled solutions have been studied extensively, notably by Lévy (1884) and later Flaherty et al. (1972), but finding analytical expressions in terms of our mapping coefficients will prove useful in providing a starting point for the computational analysis, allowing us to explore solutions branches for $\alpha > 0$ that stem from these buckled solutions.

Since buckled solutions are known to bifurcate from the circular solution as P is raised past a series of critical values P_{crit}, we define the small parameter ε such that $P = P_{\text{crit}} + \varepsilon^2$ and expand σ, a_{-1}, and the mapping coefficients a_n as asymptotic series in ε as

$$\begin{aligned} a_n &= a_{n,1}\varepsilon + a_{n,2}\varepsilon + O\left(\varepsilon^3\right), \\ a_{-1} &= 1 + a_{-1,1}\varepsilon + a_{-1,2}\varepsilon^2 + O\left(\varepsilon^3\right), \\ \sigma &= \tfrac{1}{2} - P_{\text{crit}} + \sigma_1\varepsilon + \sigma_2\varepsilon^2 + O\left(\varepsilon^3\right), \end{aligned}$$

where $\varepsilon = 0$ gives the circular solution with $a_n = 0$, $a_{-1} = 1$ and $\sigma = \frac{1}{2} - P$. Substituting these values into (3.1.2), we obtain an asymptotic expansion for $\eta(\phi)$, and can thus obtain analytic expressions for both κ and κ_{ss} in terms of the coefficients a_n. To satisfy (3.1.3) at $O\left(\varepsilon\right)$, we require $a_{-1,1} = 0$. Equation (3.4.1) at $O\left(\varepsilon\right)$ then gives

$$-\sigma_1 + \sum_{n=2}^{\infty}(n^2-1)(P_{\text{crit}} - n^2 + 1)\left[\text{Re}(a_{n-1,1})\cos(n\phi) + \text{Im}(a_{n-1,1})\sin(n\phi)\right] = 0.$$

Comparing the coefficients of $\cos(n\phi)$ and $\sin(n\phi)$ we obtain

$$(P_{\text{crit}} - n^2 + 1)a_{n-1,1} = 0 \quad \text{for} \quad n \geq 2.$$

Since we are looking for non-circular solutions, we require at least one of the coefficients $a_{n-1,1}$ to be non-zero. We thus require $P_{\text{crit}} = k^2 - 1$ for some integer $k \geq 2$, which gives $a_{n-1,1} = 0$ for $n \neq k$ with $a_{k-1,1}$ unknown. These critical transmural pressures agree with those obtained by Halphen (1888). To obtain the value of $a_{k-1,1}$, (3.4.1) must be satisfied at higher powers of ε.

Since the cell is in a static fluid with no gravity, a given solution can be freely rotated to obtain another solution. To obtain a unique solution, we fix the rotation of the cell by taking $a_{k-1,1}$ to be real and positive. We then satisfy (3.4.1)

at $O(\varepsilon^2)$, $O(\varepsilon^3)$ and $O(\varepsilon^4)$ in the same way as at $O(\varepsilon)$ to determine the value of $a_{k-1,1}$ along with the other mapping coefficients up to $O(\varepsilon^3)$. This method can however be continued to arbitrary powers of ε to obtain more accurate results. The expansions of the coefficients up to $O(\varepsilon^3)$ are found to be

$$\begin{aligned}
\sigma &= \frac{3}{2} - k^2 + \frac{k^2+1}{k^2-1}\varepsilon^2 + O(\varepsilon^3),\\
a_{-1} &= 1 - \frac{2k^2}{3(k+1)^2(k-1)}\varepsilon^2 + O(\varepsilon^3),\\
a_{k-1} &= \frac{2\sqrt{6}k}{3(k^2-1)^{3/2}}\varepsilon + O(\varepsilon^3),\\
a_{2k-1} &= -\frac{2(2k+1)}{3(k+1)^3(k-1)}\varepsilon^2 + O(\varepsilon^3),\\
a_n &= O(\varepsilon^3) \quad \text{for} \quad n \notin \{k-1, 2k-1\},
\end{aligned}$$

which gives the cell shape at leading order

$$\eta(\phi) = e^{\mathrm{i}\phi} + \frac{2\sqrt{6}k}{3(k^2-1)^{3/2}}\varepsilon e^{-(k-1)\mathrm{i}\phi} + O(\varepsilon^2). \tag{3.4.2}$$

Note that these results give different solutions for $\varepsilon > 0$ and $\varepsilon < 0$, which correspond to the two possible ways a mode-m shape can be top-bottom symmetric, one being a $\frac{\pi}{m}$ rotation of the other. Figure 3.4.1 shows some of these buckled cells, and the parameters for which they occur, up to the mode-3 buckled cell. The labels used to classify the cells will be explained in the following section. We observe from (3.4.2) that the buckled cell bifurcating from $P = k^2 - 1$ has a mode-k rotational symmetry as expected. As ε, and thus the pressure P, is increased, these buckled cells become more deformed, until they eventually self-intersect, at which point the solutions become physically invalid.

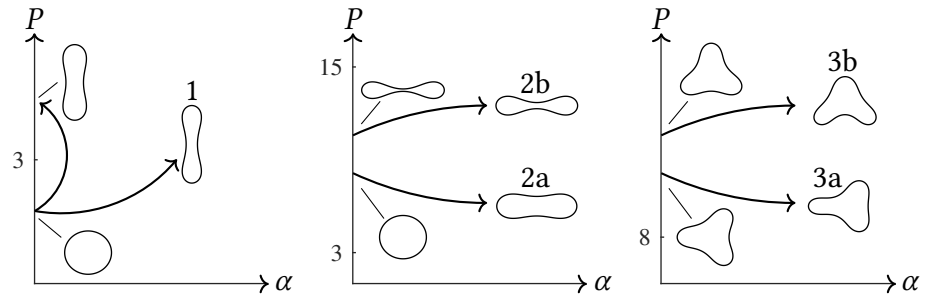

(a) Type 1 (b) Types 2a and 2b (c) Types 3a and 3b

Figure 3.4.2: Sketch showing the classification of the steady solutions in relation to those at $\alpha = 0$. The arrows illustrate a continuous path taken to reach a particular cell type. The cells in a static fluid at $\alpha = 0$ are also shown.

3.4.2 Cell Classification

To describe the behaviour of the steady solutions as the parameters α and P are varied, it is useful to label the solutions in terms of those found at $\alpha = 0$. The labels of the cells at $\alpha = 0$ are shown in Figure 3.4.1. We use the terms horizontally aligned and vertically aligned to refer to cells whose longest axis is parallel and perpendicular to the flow direction, respectively, as seen for example in Figure 3.4.3a (vertically aligned) and Figure 3.4.3b (horizontally aligned).

For $\alpha = 0$ and $P < 3$, there only exists the circular solution. We label as type 1 those solutions that can be obtained by continuously varying P and α from the circular state at $\alpha = 0, P < 3$. This is illustrated in Figure 3.4.2a by following one of the arrows from $\alpha = 0$. Note that since $(\alpha, P) = (0, 3)$ is a bifurcation point, we exclude the possibility of passing through this point in this definition. By numerically following a particular type 1 branch to $\alpha = 0$ and $P > 3$ we obtain the vertically aligned buckled mode-2 solution, which must therefore also be of type 1.

For $\alpha = 0$ and $3 < P < 8$, there exist both a buckled mode-2 solution and a circular solution. In the absence of a flow, these mode-2 solutions can take any orientation. However, as α is increased from zero only the horizontally

and vertically aligned cells persist. We have already seen that the vertically aligned mode-2 cells are of type 1. We label as type 2a or type 2b any solution which has both top-bottom and left-right symmetry and which, on following a continuous path in the $\alpha - P$ plane to a point $\alpha = 0$ with $3 < P < 15$, arrives at the circular state or the horizontal mode-2 solution respectively, as shown in Figure 3.4.2b. By numerically following a particular type 2a branch to $\alpha = 0$ and $P > 15$ we obtain the buckled mode-4 solution, which must therefore also be of type 2a. The other orientation of the buckled mode-4 solution, as well as the circular solution at $P > 15$, form solution branches separate from those previously defined, and will not be considered in the present work.

For $\alpha = 0$ and $8 < P < 15$, as well as the circular and mode-2 solutions there also exists a buckled mode-3 solution. As α is increased, we find that four orientations of this mode-3 solution persist: the two left-right symmetric orientations, and the two top-bottom symmetric orientations. Due to the symmetry of the problem, the two left-right symmetric orientations are top-bottom reflections of each other, and the two top-bottom symmetric orientations are left-right reflections of each other. We label as type 3a any solution with top-bottom symmetry and left-right asymmetry which, on following a continuous path in the $\alpha - P$ plane to a point $\alpha = 0$ with $P > 8$, arrives at a buckled mode-3 solution, as shown in Figure 3.4.2c. Similarly, we label as type 3b any solution which has left-right symmetry and top-bottom asymmetry which, on following a continuous path in the $\alpha - P$ plane to a point $\alpha = 0$ with $P > 8$, arrives at a buckled mode-3 solution.

For $\alpha = 0$ and $P > 15$ there exist mode-4 buckled solutions, and in general for $P > k^2 - 1$ there exist mode-n solutions for all $n \leq k$. In this work we focus on the type 1, 2a, 2b, 3a and 3b cases as defined above, but higher mode buckled solutions can be studied using the same techniques as presented here for the lower mode solutions.

3.4.3 Asymptotic Results for Low Flow Speeds

We seek asymptotic expansions for low flow speeds $\alpha \ll 1$ for solution branches stemming from the unit circle at $\alpha = 0$. Since (3.1.1) is invariant under the transformation $\alpha \mapsto -\alpha$, we expand the unknowns in powers of α^2 as

$$\begin{aligned} a_{-1} &= 1 + \alpha^2 a_{-1,1} + \alpha^4 a_{-1,2} + \ldots, \\ a_n &= \alpha^2 a_{n,1} + \alpha^4 a_{n,2} + \ldots \quad (n \geq 1), \\ \sigma &= \tfrac{1}{2} - P + \alpha^2 \sigma_1 + \alpha^4 \sigma_2 + \ldots. \end{aligned}$$

We substitute these expressions into (3.1.1)–(3.1.3), which can be solved at each order $O(\alpha^{2m})$ to obtain the values of $a_{-1,m}$, $a_{n,m}$ and σ_m. Note that although most of the results in this section are only shown to $O(\alpha^2)$, this method can be used to obtain results to arbitrary powers of α. We use the symbolic computing environment Maple to obtain the results presented in this section. These results can then be compared to numerical results to confirm their accuracy.

At $O(\alpha^2)$, (3.1.3) gives $a_{-1,1} = 0$, and (3.1.1) gives

$$\begin{aligned} &\tfrac{1}{2} - \sigma_1 - \cos 2\phi \\ &\quad + \sum_{n=2}^{\infty} (n^2 - 1)(P - n^2 + 1)\left\{ \mathrm{Re}(a_{n-1,1}) \cos n\phi + \mathrm{Im}(a_{n-1,1}) \sin n\phi \right\} = 0. \end{aligned} \tag{3.4.3}$$

So $\sigma_1 = \frac{1}{2}$, and comparing coefficients of $\cos 2\phi$ and $\sin 2\phi$ in (3.4.3) we find that $a_{1,1}$ is real and satisfies

$$3(P - 3)a_{1,1} = 1. \tag{3.4.4}$$

For $P = 3$, (3.4.4) clearly has no solutions. However, Blyth and Părău (2013) found that solutions can be found by taking an expansion in $\alpha^{2/3}$. Following this approach here we find that

$$\eta(\phi) = e^{\mathrm{i}\phi} - \frac{2}{9}\sqrt[3]{12}\alpha^{2/3} e^{-\mathrm{i}\phi} + O(\alpha^{4/3}) \tag{3.4.5}$$

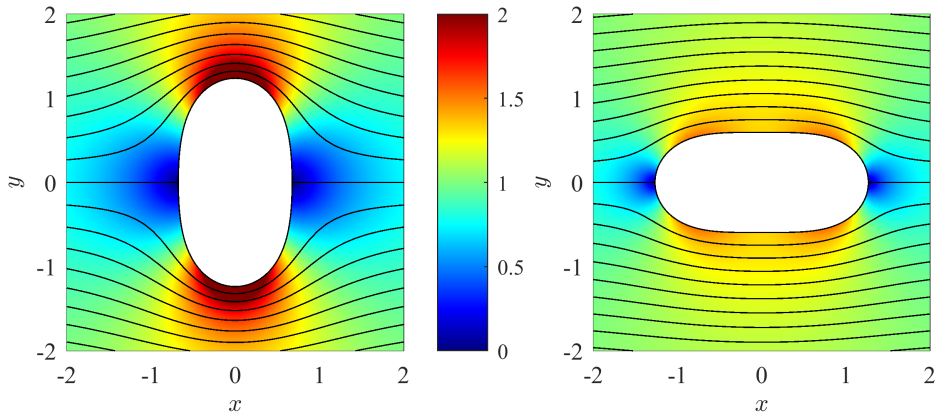

Figure 3.4.3: Streamline plots for solutions at $\alpha = 1$ for the type 1 (left) and type 2a (right) solutions at $P = 2$ and $P = 4$ respectively.

so that, ignoring the $O(\alpha^{4/3})$ correction, the cell is an ellipse with its major axis aligned perpendicular to the flow. This corresponds to a type 1 solution described in Section 3.4.2 and agrees with that found by Blyth and Părău (2013). Note that $P = 3$ is the first of the critical pressure at which buckled cells bifurcate for the static fluid problem.

Henceforth we assume that $P \neq 3$, with $a_{1,1}$ given by (3.4.4) as $a_{1,1} = \frac{1}{3(P-3)}$. Comparing coefficients of $\cos n\phi$ and $\sin n\phi$ in (3.4.3), we have

$$(P - n^2 + 1)a_{n-1,1} = 0 \quad \text{for} \quad n \geq 3. \tag{3.4.6}$$

If $P \neq k^2 - 1$ for all $k \geq 3$, (3.4.6) clearly requires $a_{n,1} = 0$ for $n \geq 2$. However, if $P = k^2 - 1$ for some $k \geq 3$ the coefficient $a_{k-1,1}$ remains undetermined, and must instead be obtained at higher powers of α. Note that these values of P correspond to the critical pressures at which buckled cells bifurcate in the static fluid problem.

First considering the case where $P \neq k^2 - 1$ for all $k \geq 3$, we have $a_{n,1} = 0$ for $n \geq 2$, giving the cell shape as

$$\eta(\phi) = e^{\mathrm{i}\phi} + \frac{\alpha^2}{3(P-3)}e^{-\mathrm{i}\phi} + O(\alpha^4), \tag{3.4.7}$$

which is approximately an ellipse. For $P < 3$, the cell is aligned perpendicular to the flow, which corresponds to a type 1 solution. For $P > 3$, the cell is aligned parallel with the flow, corresponding to a type 2a solution. Figure 3.4.3 shows the cell shape and flow field for both cell orientations obtained numerically by solving the full problem using the method described in Section 3.4.4. Considering higher order terms we obtain

$$\begin{aligned}
\sigma &= \frac{1}{2} - P + \tfrac{1}{2}\alpha^2 - \frac{2P-15}{12(P-3)^2}\alpha^4 + \frac{P-12}{36(P-3)^3}\alpha^6 + O(\alpha^8),\\
a_1 &= \frac{1}{3(P-3)}\alpha^2 - \frac{1}{18(P-3)^2}\alpha^4 - \frac{14P^2-684P+3141}{1080(P-3)^4(P-15)}\alpha^6 + O(\alpha^8),\\
a_3 &= \frac{P-78}{180(P-3)^2(P-15)}\alpha^4 + \frac{22P^2-957P+11673}{5400(P-3)^3(P-15)^2}\alpha^6 + O(\alpha^8),\\
a_5 &= -\alpha^6\frac{2P^2-694P-16311}{7560(P-3)^3(P-15)(P-35)} + O(\alpha^8),\\
a_n &= O(\alpha^8) \quad \text{for} \quad n \notin \{1,3,5\}.
\end{aligned}$$

At $O(\alpha^4)$, this solution has a singularity at $P = 15$, and in general we find that at $O(\alpha^{2m})$ a singularity occurs at $P = 4m^2 - 1$ for integer $m \geq 2$. However, unlike those for $P = 3$, expansions at these critical pressures can be constructed involving only even integer powers.

Next considering the case where $P = k^2 - 1$ for some $k \geq 3$, (3.4.6) requires $a_{n-1,1} = 0$ for $n \geq 3$, $n \neq k$ with $a_{k-1,1}$ is as yet unknown. While the value of $a_{k-1,1}$ can be obtained by satisfying the governing equations at higher orders of α in the same vein as before it is more informative to note that the expansion for the curvature takes the form

$$\kappa = -1 - \left((k^2-1)\left(C_{r1}\cos k\phi + C_{i1}\sin k\phi\right) + \frac{\cos 2\phi}{k^2-4}\right)\alpha^2 + \kappa_2(\phi)\alpha^4 + O(\alpha^6),$$

where $C_{r1} = \mathrm{Re}(a_{k-1,1})$, $C_{i1} = \mathrm{Im}(a_{k-1,1})$, and $\kappa_2(\phi)$ is as yet unknown.

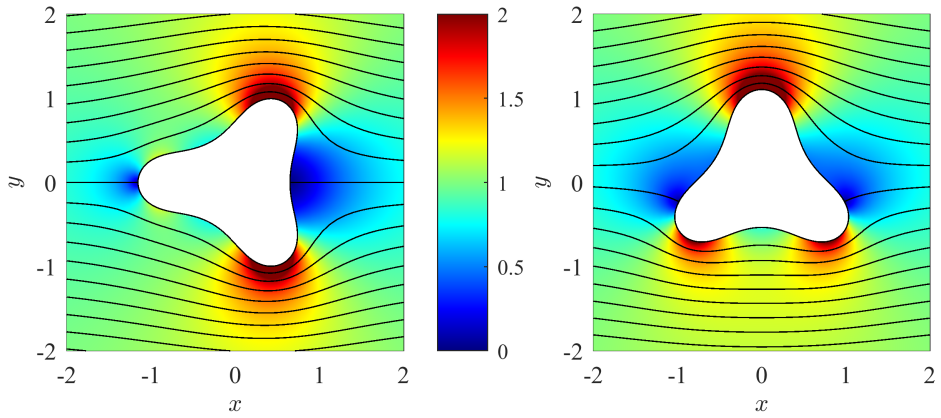

Figure 3.4.4: Streamline plots for the type 3a (left) and type 3b (right) solutions at $\alpha = 1$, $P = 10$.

Substituting into (3.1.1) and considering the $O(\alpha^4)$ terms we obtain

$$\kappa_2'' + k^2\kappa_2 = -\frac{(4k^2-1)\cos 4\phi}{12(k^2-4)^2} - \tfrac{1}{2}(k-1)(k-3)(C_{r1}\cos k\phi + C_{i1}\sin k\phi) + \ldots, \tag{3.4.8}$$

where a prime indicates a derivative in ϕ and all terms on the right-hand side which do not cause a resonance in the ODE on the left-hand side have been omitted for brevity. Since the curvature $\kappa(\phi)$ is required to be periodic, the values of C_{r1} and C_{i1} must be taken to remove the resonant terms. For $k \geq 5$ the resonant terms in (3.4.8) are removed by setting $C_{r1} = C_{i1} = 0$, which gives a cell shape equal to that given by (3.4.7) for $P \neq k^2 - 1$. Note however that these solutions will differ at higher orders of α.

For $k = 4$, which corresponds to the critical pressure $P = 15$, the resonant terms in (3.4.8) are removed by taking $C_{r1} = -7/288$ and $C_{i1} = 0$, giving the cell shape as

$$\eta(\phi) = e^{\mathrm{i}\phi} + \frac{\alpha^2}{36}\left(e^{-\mathrm{i}\phi} - \frac{7}{8}e^{-3\mathrm{i}\phi}\right) + O(\alpha^4). \tag{3.4.9}$$

For $k = 3$, which corresponds to the critical pressure $P = 8$, the resonant terms in (3.4.8) vanish and C_{r1} and C_{i1} remain undetermined. Proceeding to

higher powers of α, we find that to remove the resonances at $O(\alpha^6)$ we require

$$C_{r1}\left(C_{r1}^2 + C_{i1}^2 - \frac{201}{102400}\right) = 0, \qquad C_{i1}\left(C_{r1}^2 + C_{i1}^2 - \frac{201}{102400}\right) = 0,$$

and to remove the resonances at $O(\alpha^8)$ we require

$$\frac{201C_{r2}}{102400} - \frac{2319C_{r1}}{16384000} - 2C_{r1}\left(C_{i1}C_{i2} + C_{r1}C_{r2}\right) - \left(C_{r1}^2 + C_{i1}^2\right)\left(C_{r2} + \frac{29C_{r1}}{1152}\right) = \frac{C_{r1}}{6400},$$
$$\frac{201C_{i2}}{102400} - \frac{2319C_{i1}}{16384000} - 2C_{i1}\left(C_{r1}C_{r2} + C_{i1}C_{i2}\right) - \left(C_{r1}^2 + C_{i1}^2\right)\left(C_{i2} + \frac{29C_{i1}}{1152}\right) = \frac{-C_{i1}}{6400},$$

where $a_{2,1} = C_{r1} + C_{i1}\mathrm{i}$ and $a_{2,2} = C_{r2} + C_{i2}\mathrm{i}$. This gives a set of four simultaneous equations for the four variables $\{\mathrm{Re}(a_{2,1}), \mathrm{Im}(a_{2,1}), \mathrm{Re}(a_{2,2}), \mathrm{Im}(a_{2,2})\}$, which has five solutions. The first of these solutions, $\{0, 0, 0, 0\}$, is the same as that predicted for the general case of $P \neq k^2 - 1$, which is classified as a type 2a solution. The second and third solutions,

$$\{\pm\tfrac{\sqrt{201}}{320}, 0, \mp\tfrac{68263}{246988800}, \mathrm{Im}(a_{2,2})\},$$

represent top-bottom symmetric, left-right asymmetric solutions, with one being a left-right reflection of the other. This is classified as a type 3a solution. Note that $\mathrm{Im}(a_{2,2})$ is left undetermined here. The cell-shape is given by

$$\eta(\phi) = e^{\mathrm{i}\phi} + \frac{\alpha^2}{15}e^{-\mathrm{i}\phi} \pm \frac{\sqrt{201}}{320}\alpha^2 e^{-2\mathrm{i}\phi} + O(\alpha^4).$$

The fourth and fifth solutions,

$$\{0, \pm\tfrac{\sqrt{201}}{320}, \mathrm{Re}(a_{2,2}), \mp\tfrac{6823}{246988800}\},$$

represent left-right symmetric, top-bottom asymmetric solutions, with one being a top-bottom reflection of the other. Here $\mathrm{Re}(a_{2,2})$ is undetermined. This

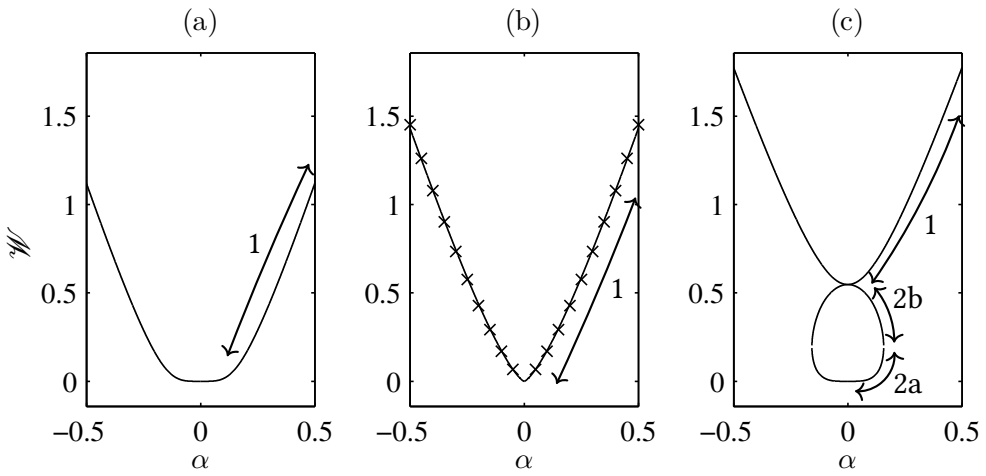

Figure 3.4.5: The bending energy $\mathscr{W}$ against α for (a) $P = 2.9$, (b) $P = 3$ and (c) $P = 3.1$. Panels (a) and (b) show type 1 solutions, and (c) shows type 1, 2a and 2b solutions. The crosses in panel (b) correspond to the asymptotic solution (3.4.5).

is classified as a type 3b solution. The cell-shape is given by

$$\eta(\phi) = e^{\mathrm{i}\phi} + \frac{\alpha^2}{15}e^{-\mathrm{i}\phi} \pm \mathrm{i}\frac{\sqrt{201}}{320}\alpha^2 e^{-2\mathrm{i}\phi} + O\left(\alpha^4\right).$$

Figure 3.4.4 shows the streamlines for these solutions computed using the numerical method discussed in Section 3.4.4. Both type 3 cells have the same shape to $O\left(\alpha^2\right)$ but with different orientations. However, since $\mathrm{Re}(a_{2,2})$ for the top-bottom symmetric solution is different to $\mathrm{Im}(a_{2,2})$ for the left-right symmetric solution, the type 3 cells will take distinct shapes at $O\left(\alpha^4\right)$.

3.4.4 Numerical Results

We then consider numerically computed solutions to the steady problem. We use these numerical solutions to verify the accuracy of the asymptotic results obtained in the previous section, and to explore the solution space for large values of the flow speed α where the asymptotic results are no longer valid. The solutions are computed using the numerical method described in Section 3.2.3.

A useful measure for characterising a cell is the dimensionless bending

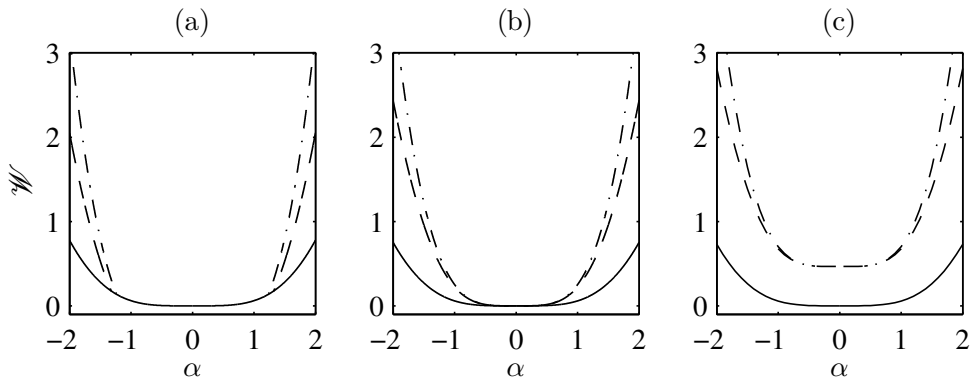

Figure 3.4.6: The bending energy $\mathscr{W}$ against α for (a) $P = 7.9$, (b) $P = 8$ and (c) $P = 8.1$. The solid line indicates type 2a solutions, the dashed line indicates type 3a solutions, and the dash-dot line indicates type 3b solutions.

energy $\mathscr{W}$ defined by (3.2.6). Figure 3.4.5 shows the numerically computed bending energy against α for P near 3, as well as the analytical results from Section 3.4.3 for $P = 3$. These solutions were described by Blyth and Părău (2013) but are included here for completeness. For $P < 3$, we find only type 1 solutions, which are horizontally elongated top-bottom and left-right symmetric cell shapes. These solution branches have $\mathscr{W} = 0$ at $\alpha = 0$, which corresponds to the circular solution. As P is increased to 3 the energy curve develops a cusp, as predicted by the asymptotic expansion (3.4.5). We find excellent agreement between the analytical results and the numerical results. As P is increased above 3, a loop appears in the energy curve underneath the type 1 solution branch, with the lower and upper portions of the loop corresponding to the type 2a and 2b solutions respectively. At $\alpha = 0$, the type 2a solution has $\mathscr{W} = 0$ corresponding to the circular solution, while the type 1 and type 2b solutions have some $\mathscr{W} > 0$ corresponding to the buckled mode-2 solution.

Figure 3.4.6 shows the numerically computed bending energy against α for P near 8. As predicted by the analytic results we find that for $P = 8$ there are three solution branches: the type 2a symmetric solution and the asymmetric type 3a and type 3b solutions. There also exist type 1 and type 2b solutions at

$P = 8$, but these have self-intersecting cell profiles, which are non-physical and hence are not shown. The numerically computed values of the bending energy were compared to those obtained analytically and were found to have excellent agreement for all three solution branches. As P is increased, the type 3a and type 3b branches have $\mathscr{W} > 0$ at $\alpha = 0$, corresponding to the mode-3 buckled cell. But for $P < 8$, the type 3a and type 3b branches do not cross $\alpha = 0$ and instead bifurcate nonlinearly from the type 2a branch at some critical values of $\alpha \neq 0$ which in general are different.

The bifurcation structure can be seen in more detail in Figure 3.4.7, which shows the numerically computed bending energies against P for steady solutions with $\alpha = 0$ and $\alpha = 2$. The solid lines represent both the circular and buckled solutions for $\alpha = 0$. For $\alpha = 0$ the steady problem given by (3.1.1) and (3.1.2) is rotationally invariant around the origin, and hence the solid lines can be rotated around the P-axis to obtain surfaces of revolution. When $\alpha \neq 0$ the rotational invariance is broken by the flow direction and this creates the imperfections in the bifurcation structure seen in Figure 3.4.7. The local structure of the bifurcation branches seen near to $P = 3$ and $P = 15$ bears the hallmarks of a typical imperfect bifurcation. The broken curves either side of the solid branch emanating from $P = 3$ correspond to different orientations of the buckled cell, with the branch on the left corresponding to type 1 cells and the branch on the right corresponding to either type 2a (lower part of the branch) or 2b cells (upper part of the branch). The local structure of the solution branches around $P = 8$ is different; in this case the branch that emanates from $P = 8$ for $\alpha = 0$ divides into two and each of these new branches appear as nonlinear bifurcations from a separate branch. In general the local bifurcation structure at the critical points $P = n^2 - 1$ depends on the parity of n: for n odd the behaviour is qualitatively similar to that seen at $P = 8$ in Figure 3.4.7, while for n even the behaviour is similar to that seen

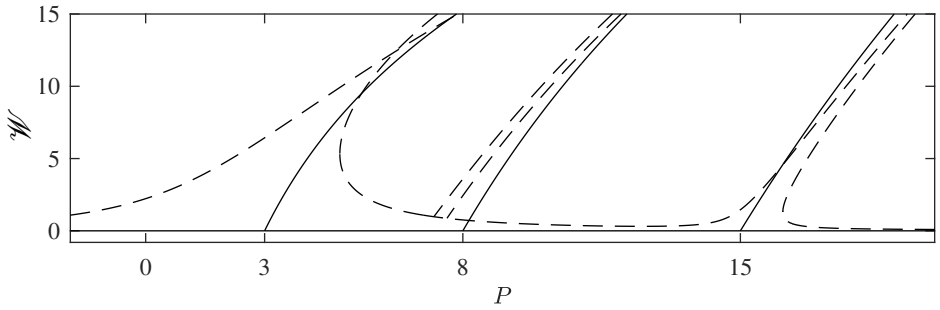

Figure 3.4.7: The bending energy $\mathscr{W}$ against P for $\alpha = 0$ and $\alpha = 2$. The solid line indicates the solutions for $\alpha = 0$, and the dashed line indicates the solutions for $\alpha = 2$.

near $P = 3$ and $P = 15$.

Figure 3.4.8a shows the regions of the $\alpha - P$ plane for which the type 1 solutions exist, and the regions in which they are stable for $\varrho = 0$. The linear stability of the solutions is evaluated using the method described in Section 3.3. These solutions are both top-bottom and left-right symmetric and aligned perpendicular to the flow, as predicted by the linear theory. For $P < 3$, the solutions tend to the circular solution as $\alpha \to 0$, while for $P > 3$ they tend to the vertically aligned buckled mode-2 solution. As α is increased, the cell pinches together until it self-intersects at some critical value α_c, beyond which the system ceases to be valid. The critical value α_c decreases to $\alpha_c = 0$ as P is increased to $P = 5.247$, with no physically acceptable type 1 solutions beyond this point. These physically meaningful type 1 cells are linearly stable over the region shown in the figure; we have not found any cases for which they are unstable.

As noted in Section 3.1, by taking $P \to -\infty$ with $\alpha^2 \sim P$ we obtain the problem for a bubble with constant surface tension in a uniform flow. In terms of our cell classifications the bubbles are considered type 1 solutions, which are the only solutions to exist for $P < 0$. The type 1 solutions deform such that they are aligned perpendicular to the flow, which agrees with the results of Shankar (1992) for equilibria of bubbles in a uniform stream. Nie and Tanveer (1995)

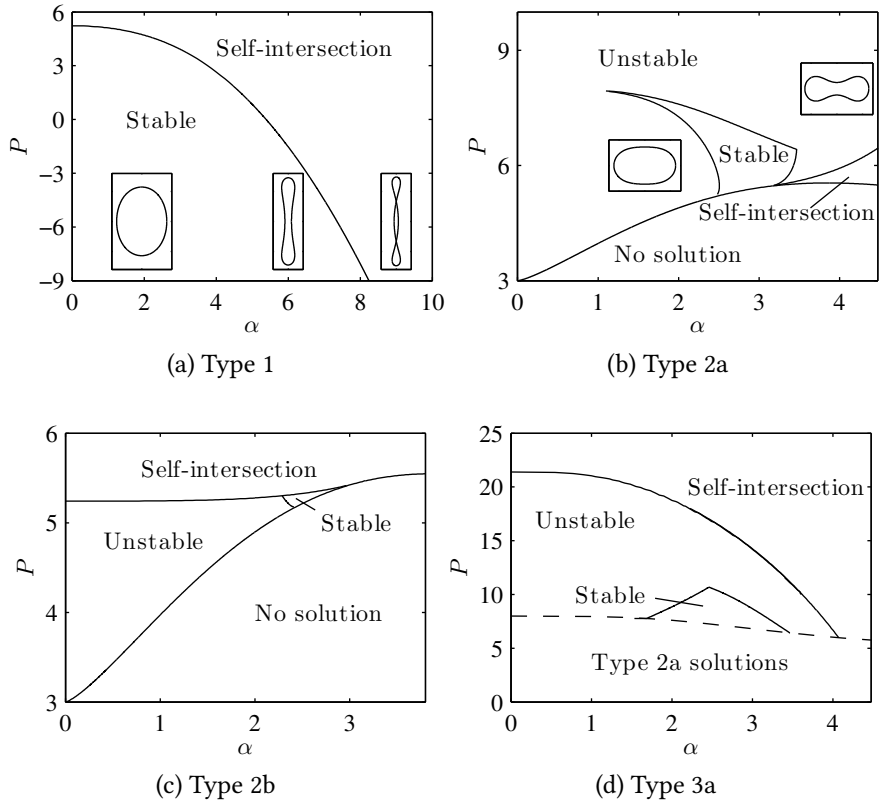

(a) Type 1 (b) Type 2a

(c) Type 2b (d) Type 3a

Figure 3.4.8: Map of the regions in the α-P plane in which each type of solution exists, and the regions in which they are stable for $\varrho = 0$. The cell shapes shown in panel (a) from left to right correspond to $(\alpha, P) = (2, -6)$, $(6, -6)$ and $(9, -6)$ and in panel (b) from left to right correspond to $(\alpha, P) = (1.5, 6)$ and $(4, 8)$.

showed that such solutions are stable for all values of $P/\alpha^2 = (p_\infty - P_{\text{crit}})/(\rho U^2)$. The bubble self-intersects at $P/\alpha_c^2 = -0.273$, so $\alpha_c^2 \sim -3.66P$ as $P \to -\infty$.

Figure 3.4.8b shows the regions of the $\alpha - P$ plane for which the type 2a solutions exist, and the regions in which they are stable for $\varrho = 0$. These solutions are both top-bottom and left-right symmetric and aligned parallel to the flow. As predicted by the analytical results, these solutions only exist for $P > 3$. At $\alpha = 0$ the type 2a cells are circular for $P < 15$ and buckled mode-4 shapes for $P > 15$. Physically acceptable solutions only exist if P exceeds a certain value which depends on α. The type 2a solutions are generally unstable, although there is a large region of stability around $\alpha = 2.8$, $P = 6$.

Figure 3.4.8c shows the regions of the $\alpha - P$ plane for which the type 2b

solutions exist, and the regions in which they are stable for $\varrho = 0$. These solutions are both top-bottom and left-right symmetric, are aligned parallel to the flow, and only exist for $P > 3$. The boundary between the region where solutions exist and the region where solutions do not exist is identical to the one for type 2a solutions, and on this boundary the type 2a and 2b solutions are identical. The type 2b solutions are unstable except within a small region of the $\alpha - P$ plane.

Figure 3.4.8d shows the regions of the $\alpha - P$ plane for which the type 3a solutions exist, and the regions in which they are stable for $\varrho = 0$. These solutions exist above the broken line in the figure. Below this line the cells are type 2a solutions which are left-right, top-bottom symmetric, as shown in Figure 3.4.8b. The type 3a solutions are stable only in a limited region of the $\alpha - P$ plane.

For type 3b solutions we find that, even for cases where the cells are only moderately deformed, the decay rate of the mapping coefficients a_n is very slow, and consequently a large truncation level N is required. This makes the computations for both the equilibrium cells and their stability infeasible for even relatively small values of α and P. Alternative methods such as one based on a boundary integral method can be used to obtain these solutions but this will not be considered here.

The linear stability results presented above are for the case where $\varrho = 0$, which corresponds to a uniform interior pressure. In general, we find that the presence of an interior fluid reduces the stability of the equilibria, reducing the magnitude of each imaginary eigenvalue and increasing the magnitude of each unstable eigenvalue. For the type 1 solutions, the equilibria remain stable for $\varrho = 1$, although the magnitude of the imaginary eigenvalues is reduced. Figure 3.4.9 shows the regions of stability of the type 2a cells in the $\alpha - P$ plane for both $\varrho = 1$ and $\varrho = 0$. By introducing an interior fluid the region of

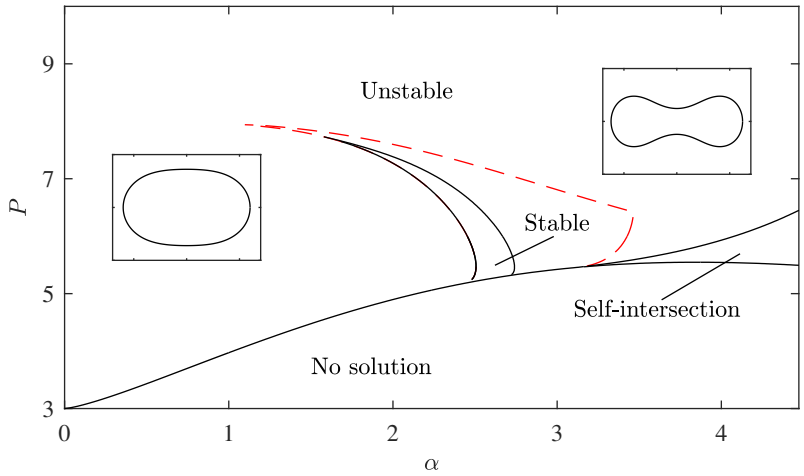

Figure 3.4.9: Map of the regions in which the type 2b equilibrium cells are stable or unstable for $\varrho = 1$. The red dashed line indicates the corresponding boundary between stability and instability for $\varrho = 0$.

instability is significantly increased, leaving only a narrow region in which the cells remain stable. For the type 2b and 3a cells, we find that in the presence of an interior fluid the cell becomes unstable for all values of P and α.

3.5 Unsteady Results

In this section we perform time-dependent simulations of the full unsteady nonlinear system derived in Section 3.2 to validate the linear stability results presented in Section 3.4.4, and analyse the nonlinear unsteady motion of the unstable steady cells perturbed by an initially small perturbation.

We firstly consider the unsteady results for cells with a uniform interior pressure with $\varrho = 0$. Figure 3.5.1 shows the value of the mapping coefficient $\mathrm{Im}(a_1)$ against time for the steady type 1 solution at $\alpha = 0$, $P = 0$ perturbed by a stable eigenvector, with results shown for both the linear theory and the nonlinear numerical simulations. We observe that the linear results agree very well with the simulated results. Figure 3.5.2 shows the value of the mapping coefficient $\mathrm{Im}(a_1)$ against time for the steady type 1 solution at $\alpha = 2$, $P = 5$ perturbed by an unstable eigenvector, with results shown for both the linear

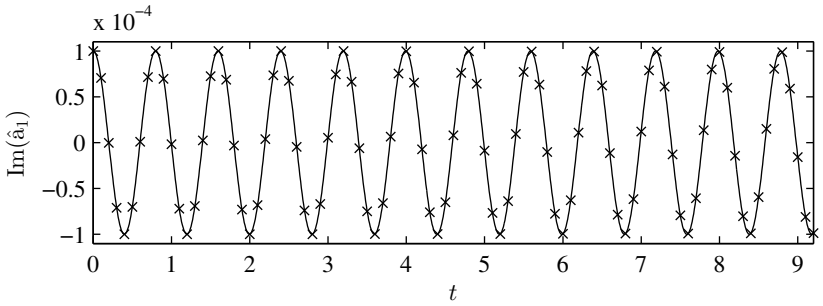

Figure 3.5.1: Results of a time-dependent simulation for a stable steady type 1 solution at $\alpha = 2$, $P = 0$ perturbed at $t = 0$ by the stable eigenvector with eigenvalue $\lambda = 7.87\mathrm{i}$, scaled by setting $\mathrm{Im}(\hat{a}_1) = 10^{-4}$ and $\mathrm{Im}(\hat{a}_1') = 0$. The solid line shows the numerical calculation and the crosses show the eigenvector.

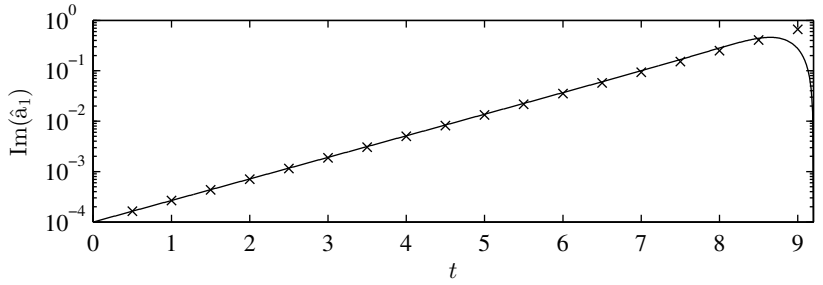

Figure 3.5.2: Results of a time-dependent simulation for an unstable steady type 2b solution at $\alpha = 2$, $P = 5$ perturbed at $t = 0$ by the unstable eigenvector with eigenvalue $\lambda = 0.978$, scaled by setting $\mathrm{Im}(\hat{b}_1) = -10^{-6}$. The solid line shows the numerical calculation and the crosses show the eigenvector.

theory and the nonlinear numerical simulations. The linear theory agrees well with the nonlinear results until the perturbation grows too large, at which point the linear theory ceases to be valid. The linear theory thus accurately predicts the growth rates of small perturbations for both stable and unstable eigenvectors, confirming the validity of the linear stability method.

The nonlinear unsteady simulations can also be used to study the behaviour of the unstable cells as the perturbations become large and nonlinear effects become significant. Recalling that both the area and perimeter of the cell are conserved throughout the unsteady evolution of the system, for near-circular cells whose area is close to π the deformation of the cell is severely restricted, with the cell motion consisting of small oscillations of the cell wall while maintaining its near-circular shape. For initial conditions

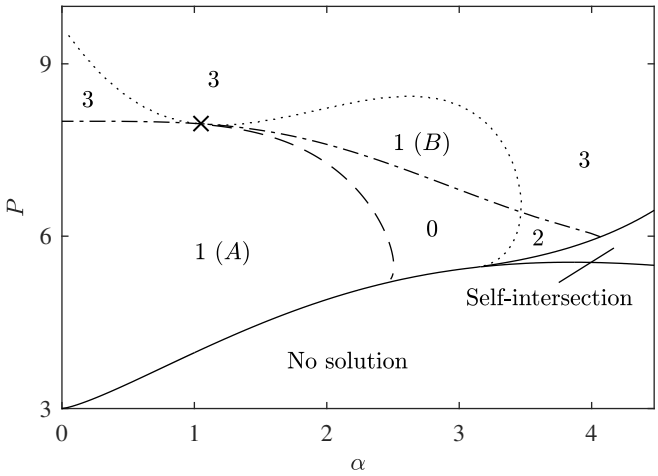

Figure 3.5.3: Map showing the number of unstable eigenvalues for the type 2a steady solutions in the $\alpha - P$ plane. On the dashed and dot-dashed lines there is a repeated zero eigenvalue, corresponding to bifurcations of type 3b and type 3a cells from the type 2a cells. On the dotted line there is a pair of repeated real eigenvalues for $\alpha < 1.05$ and a pair of repeated imaginary eigenvalues for $\alpha > 1.05$. The dotted line meets the dashed line at $\alpha = 1.05$, $P = 7.95$, marked by a cross in the map. (A) and (B) mark the two distinct regions with a single unstable eigenvalue.

corresponding to more deformed steady solutions, the unsteady evolution of the cell is found to depend on the number of unstable eigenvectors obtained from the linear stability analysis from Section 3.3; if there is a single unstable eigenvector, a random small perturbation will grow in the direction of the unstable eigenvector, which causes the cell to exhibit qualitatively similar unsteady motions for all initial perturbations. If however there are multiple unstable eigenvectors, the unsteady motion of the cell subjected to a random initial perturbation cannot be predicted, with each of the unstable eigenvectors interacting nonlinearly as the perturbation grows.

Figure 3.5.3 shows the number of unstable eigenvalues for the type 2a cells. There are two regions in which the type 2a cell has a single unstable eigenvalue, labelled region A and region B. In region A, the unstable eigenvector rotates the cell, with the direction of rotation determined by the sign of the perturbation. The typical motion of a cell in this region subjected to a small initial perturbation is sketched in Figure 3.5.4a. As the motion

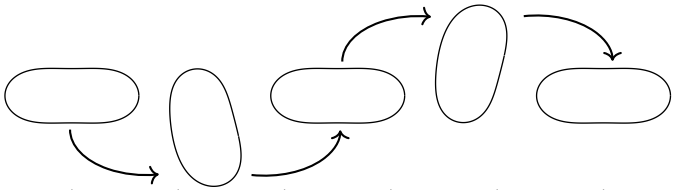

(a) Typical cell motion in region A

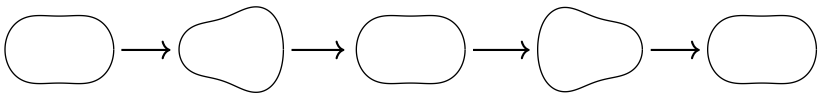

(b) Typical cell motion in region B

Figure 3.5.4: Sketch demonstrating the nonlinear unsteady motions typical of cells in (a) region A and (b) region B identified in Figure 3.5.3 subjected to a small initial perturbation., with the leftmost cells depicting initial conditions.

becomes dominated by the unstable eigenvector, the cell rapidly flips over, moving downstream as it does so before holding its position in a near-steady state. It then flips in the opposite direction, again being carried downstream before returning to a near-steady state. The whole cycle is then essentially repeated. However, this motion is not periodic, and there are irregular small amplitude oscillations superimposed on the cell wall. We ran several simulations in region A and confirmed this general behaviour. This motion is found to also be typical of the unstable type 2b cells, which only ever have a single unstable eigenvalue. Figure 3.5.5 shows the horizontal and vertical components of the velocity of the centroid of the cell for a simulation of a specific type 2a cell at $\alpha = 2$, $P = 6$ perturbed by its single unstable eigenvector at $t = 0$. The crosses in the figure show where each frame in the cell cycle in Figure 3.5.4a occurs. The recurring pattern of cell motion is clearly visible, with the small amplitude oscillations appearing as small irregular bumps in the curve. The alternating direction in which the cell flips can be seen in the vertical component of the centroid velocity, while the horizontal component shows the downstream motion while the cell is flipping.

The typical motion of a cell in region B from Figure 3.5.3 subjected to a small perturbation is shown in Figure 3.5.4b. As the motion becomes

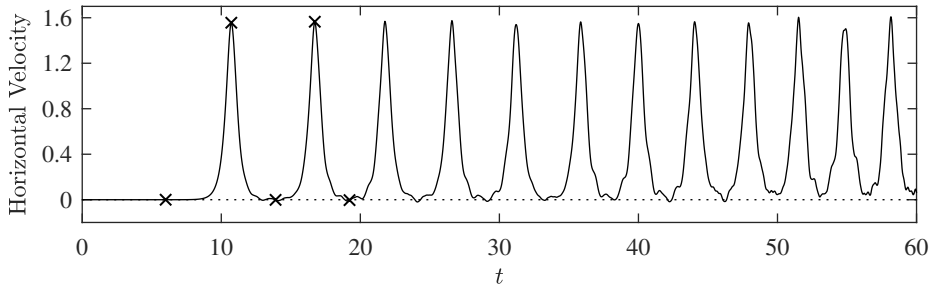

(a) Horizontal centroid velocity of the cell

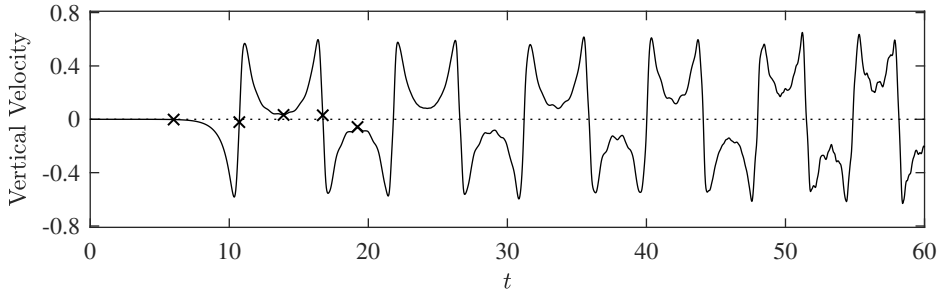

(b) Vertical centroid velocity of the cell

Figure 3.5.5: Simulation of the unsteady evolution of the unstable type 2a steady solution at $\alpha = 2$, $P = 6$ perturbed at $t = 0$ by the unstable eigenvector with eigenvalue $\lambda = 1.3048$, scaled by setting $\mathrm{Im}(\hat{b}_1) = -10^{-6}$. The dotted lines correspond to the unperturbed steady solution, and the crosses indicate the first five points at which the cell resembles each of the five cells shown in Figure 3.5.4a.

dominated by the unstable eigenvector, the cell bulges out to resemble a type 3a shape before returning to a near-steady state. During this bulging motion, the cell undergoes intermittent bursts of downstream acceleration, while in between holding its position in a near-steady state. The cell repeats this motion, switching the side to which it bulges in an unpredictable way, with irregular small-amplitude oscillations occurring along the cell wall. We carried out several simulations in region B and confirmed this general behaviour. The resemblance to type 3a cells can be explained by noting that the unstable eigenvector corresponds to the eigenvalue associated with the bifurcation from type 2a cells to type 3a cells on the dot-dashed line in Figure 3.5.3. The downstream motion of the unsteady cells can be explained by use of an energy argument. The bending energy and centroid velocity for a simulation of the type 2a cell at $\alpha = 2.5$, $P = 8$ perturbed by its single unstable

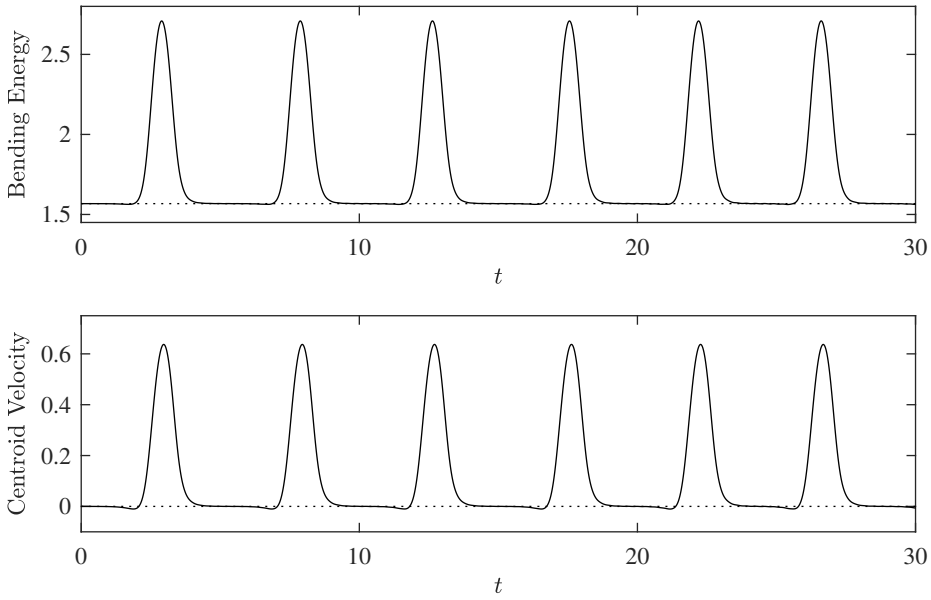

Figure 3.5.6: The bending energy and horizontal centroid velocity during the evolution of the unstable type 2a steady solution at $\alpha = 2.5$, $P = 8$ perturbed at $t = 0$ by the unstable eigenvector with eigenvalue $\lambda = 3.7155$, scaled by setting $\mathrm{Im}(\hat{b}_1) = -10^{-4}$. The dotted line corresponds to the steady solution. This motion is top-bottom symmetric, so the centroid velocity has no vertical component.

eigenvector at $t = 0$, are shown in Figure 3.5.6. Since this initial perturbation is top-bottom symmetric, the cell retains this symmetry throughout the motion, and therefore the centroid velocity is always in the horizontal direction. During the bursts of downstream motion the bending energy of the cell increases, with a corresponding decrease in the kinetic energy of the flow. When the bending energy dips below its initial value, there is a corresponding negative centroid velocity. Since the minimum kinetic energy of the flow corresponds to a cell rigidly translating downstream at speed α, a decrease of kinetic energy will generally correspond to a downstream cell motion.

Figure 3.5.7 shows the horizontal and vertical components of the centroid velocity for a simulation of the type 2a cell at $\alpha = 1, P = 6$ perturbed by its single unstable eigenvector at $t = 0$. The cell initially falls into a similar unstable motion to that seen in Figure 3.5.5. As t is increased however, these regular motions collapse into an unpredictable, seemingly chaotic motion. This chaos

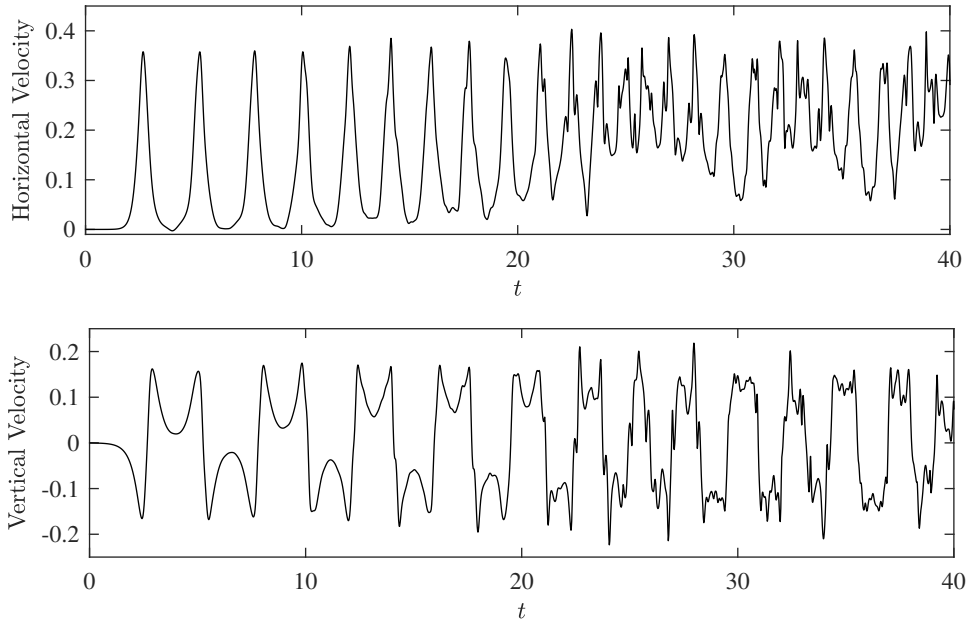

Figure 3.5.7: The horizontal and vertical components of the centroid velocity during the evolution of the unstable type 2a steady solution at $\alpha = 1$, $P = 6$ perturbed at $t = 0$ by the unstable eigenvector with eigenvalue $\lambda = 3.0132$, scaled by setting $\mathrm{Im}(\hat{b}_1) = -10^{-6}$.

will be analysed in Section 3.5.1.

We then consider the unsteady results for a cell with a fluid in the interior with $\varrho = 1$. Figure 3.5.8 shows the nonlinear evolution of a cell initially perturbed from equilibrium by an unstable eigenvector, along with the corresponding unsteady motion for $\varrho = 0$. We find that, as in the $\varrho = 0$ case, the cell still falls into a regular oscillatory motion superimposed with small-scale chaotic oscillations. However, for $\varrho = 1$ the large-scale oscillatory motion occurs at a higher frequency than the $\varrho = 0$ case. We also observe from Figure 3.5.8 that despite achieving the same vertical velocity as for $\varrho = 0$, the downstream velocity of the cell throughout the flipping is much slower for $\varrho = 1$. However, the cell does achieve a higher average downstream speed due to the more frequent bursts of downstream motion.

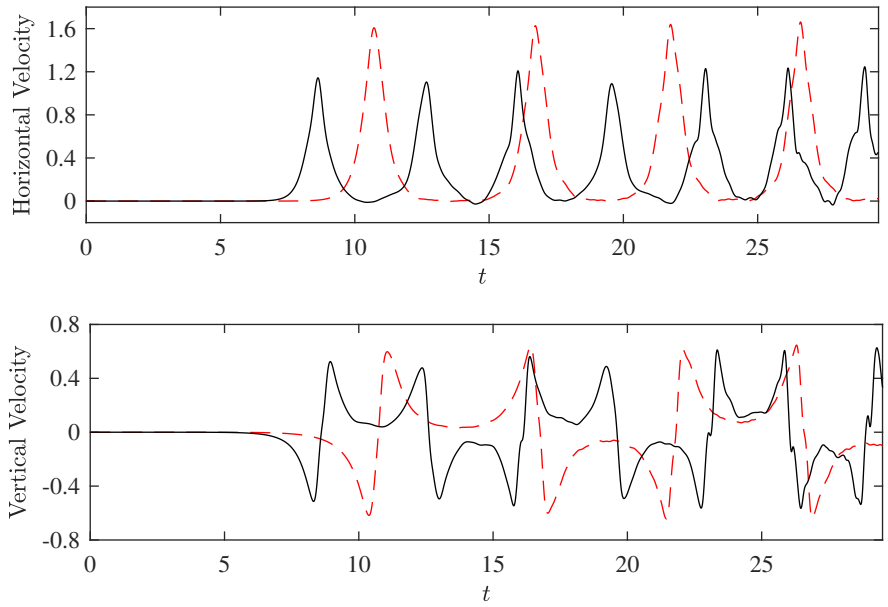

Figure 3.5.8: The horizontal and vertical components of the centroid velocity during the evolution of the unstable type 2a steady solution at $\alpha = 2$, $P = 6$ perturbed at $t = 0$ by the unstable eigenvector with eigenvalue $\lambda = 1.7192$, scaled by setting $\mathrm{Im}(\hat{b}_1) = -10^{-6}$. The dashed red line indicates the corresponding evolution in the absence of an interior fluid, as shown in Figure 3.5.5.

3.5.1 Chaos

In Section 3.5 we observed that while an unstable cell can fall into a regular large-scale motion, there are also small irregular oscillations are superimposed on top of this regular motion. We also found that for certain parameter values the unsteady cells wall into an entirely irregular motion, which suggests that the system may be chaotic. In this section we analyse this chaotic behaviour.

Figure 3.5.9 shows the divergence of the centroid velocities of two trajectories perturbed from some fiducial reference trajectory at $t = 0$ by a small random perturbation, normalised by setting the initial difference in centroid speeds to be 10^{-6} and 10^{-8} respectively. We find that the trajectories rapidly diverge, with the magnitude of the perturbations reaching an upper limit of $O(10^{-1})$. The magnitude of the difference in centroid speeds is independent of the initial difference, which indicates chaos.

The chaotic nature of a particular trajectory $\mathbf{x}(t)$ in phase-space can be

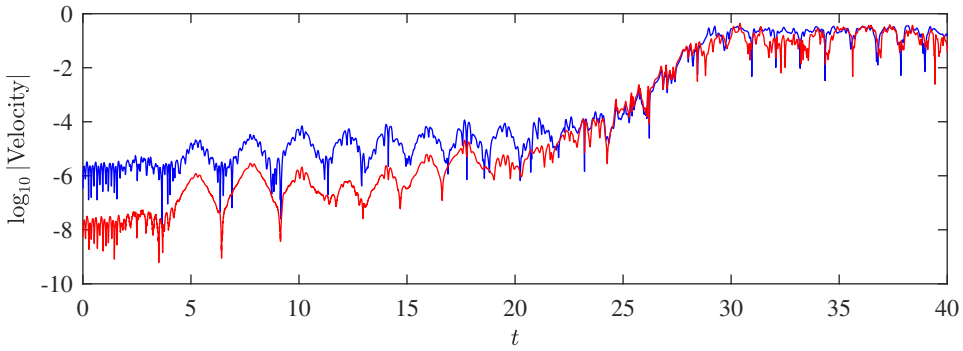

Figure 3.5.9: Plot of the deviation of the centroid velocity from that of the fiducial trajectory for two perturbed trajectories. The fiducial trajectory is that shown in Figure 3.5.7. The blue curve has an initial perturbation of 10^{-6}, and red curve has an initial perturbation of 10^{-8}.

determined by considering the Lyapunov exponents. These describe the rate at which a perturbed trajectory $\mathbf{x}(t) + \varepsilon\delta\mathbf{x}(t)$ deviates from the fiducial trajectory, where $\mathbf{x}$ is some vector denoting position in phase-space and $\varepsilon\delta\mathbf{x}(t)$ is an unsteady perturbation to $\mathbf{x}$ for a small constant ε. We take $\mathbf{x}$ to be the vector containing the mapping coefficients a_n and b_n, although as noted by Peitgen et al. (2004) the Lyapunov exponents are independent of the choice of $\mathbf{x}$. While $|\varepsilon\delta\mathbf{x}(t)| \ll 1$ this deviation is expected to grow linearly, with a spectrum of eigenvalues λ_n and corresponding eigenvectors $\delta\mathbf{x}_n$ such that

$$\frac{\partial_t|\delta\mathbf{x}_n|}{|\delta\mathbf{x}_n|} \to \lambda_n \quad \text{as} \quad \varepsilon \to 0. \tag{3.5.1}$$

These eigenvalues $\lambda_n(t)$ are called the local Lyapunov exponents, which are in general time-dependent. For a conservative system, the Lyapunov exponents will also generally depend in the initial condition $\mathbf{x}_0$, since trajectories with different values of the conserved quantities cannot meet.

The chaos of the fiducial trajectory is determined by the largest Lyapunov exponent λ_1. In general, a perturbation $\delta\mathbf{x}(t)$ will grow fastest in the direction of the eigenvector $\delta\mathbf{x}_1(t)$, with the relative magnitude of the other eigenvectors

becoming arbitrarily small for large t. For large t we thus have

$$\lim_{\varepsilon \to 0} \frac{\partial_t |\delta \mathbf{x}|}{|\delta \mathbf{x}|} \approx \lambda_1(t) \quad \text{as} \quad t \to \infty. \tag{3.5.2}$$

The average maximal Lyapunov exponent is then defined as the average value of the local Lyapunov exponent in time. Integrating (3.5.2) in time, we obtain

$$\lambda_{\max} = \lim_{t \to \infty} \frac{1}{t} \lim_{\varepsilon \to 0} \log\left(\frac{|\delta \mathbf{x}(t)|}{|\delta \mathbf{x}_0|} \right). \tag{3.5.3}$$

The average maximal Lyapunov exponent quantifies the average rate at which small perturbations of the fiducial trajectory grow in time. We say that a trajectory is chaotic if $\lambda_{\max} > 0$.

While for some simple systems the Lyapunov exponent can be found analytically, for more complicated systems numerical simulations must be used. To deal with the limit $|\delta \mathbf{x}_0| \to 0$ in (3.5.3) numerically we must take $|\delta \mathbf{x}_0|$ to be some small finite number. By taking $|\delta \mathbf{x}_0| \ll 0$, $\delta \mathbf{x}(t)$ will grow linearly for small t, but as $\delta \mathbf{x}(t)$ grows the nonlinear terms will become significant and the numerical approximation to (3.5.3) will become invalid. To overcome this problem, we use the method described by Sprott (2003). We start by taking an initial perturbation $\varepsilon \delta \mathbf{x}_0$, where $|\delta \mathbf{x}_0| = 1$ and ε is typically taken to be 10^{-8}. The two trajectories $\mathbf{x}(t)$ and $\mathbf{x}(t) + \varepsilon \delta \mathbf{x}(t)$ are then evolved in time until $|\delta \mathbf{x}|$ is larger than some chosen value, which in our computations is taken to be 100. The value $\log\left(|\delta \mathbf{x}(t)|\right)$ is then stored, and $\delta \mathbf{x}(t)$ is rescaled to have magnitude 1. This process is then repeated, with an approximation for the maximal Lyapunov exponent at any moment in time given as the sum of the stored values of $\log\left(|\delta \mathbf{x}(t)|\right)$ divided by the time t, until the approximation converges to within a required tolerance. To ensure that the choice of initial perturbation $\delta \mathbf{x}_0$ does not affect approximation of the maximal Lyapunov exponent, we run concurrent simulations for various initial perturbations and

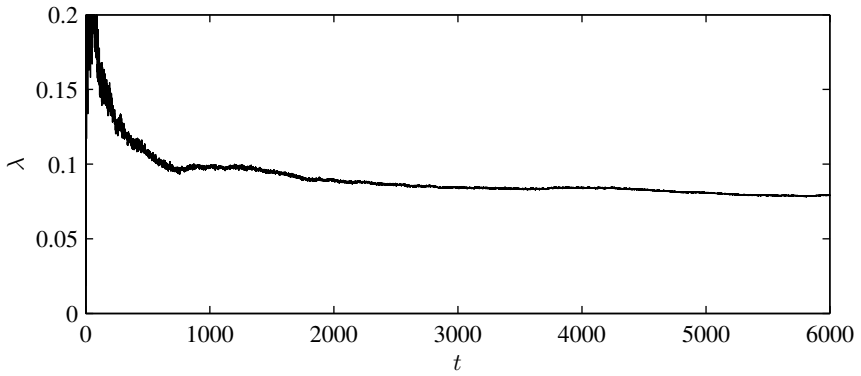

Figure 3.5.10: The approximate value of the maximum Lyapunov exponent λ against time for $\alpha = 0.1$, $P = 6$ for various initial perturbations of the fiducial trajectory. The fiducial trajectory is given by a small perturbation of the unstable type 2a cell at $t = 0$.

confirm that the values are consistent. In practice, it takes a very long time for the approximate Lyapunov exponent to converge to a precise value, but since we are only interested in confirming that a trajectory is chaotic it is sufficient to confirm that the approximate Lyapunov exponent is converging to some positive value, which is indicative of chaos. Note that this process has a high computational cost, requiring multiple simulations of the unsteady system for large values of t, which prohibits a full analysis of the chaos of the system.

Figure 3.5.10 depicts the approximation of the maximal Lyapunov exponent computed for a simulation with the fiducial trajectory given by perturbing the unstable steady solution at $\alpha = 0.1$, $P = 6$. The exponent appears to converge very slowly towards the positive value 0.08 indicating a chaotic motion.

3.6 Summary

We have studied a massless two-dimensional elastic cell in a uniform stream, with a focus on determining equilibrium states and their stability. Using a conformal mapping approach we have constructed asymptotic approximations valid in the presence of weak flow and computed fully nonlinear equilibria numerically to explore the full solution space. We presented numerical

methods to determine the linear stability of the equilibria for both a uniform pressure interior and a fluid-filled interior, and used numerical methods to obtain the fully nonlinear time-evolution of the unsteady cells, allowing us to identify both regular and chaotic behaviours in the cell motion.

In a study devoted to steady equilibrium solutions, Blyth and Părău (2013) used a linear analysis for low flow speed to demonstrate that a circular cell in a static fluid will deform into an elliptical-type shape with its major axis oriented either horizontally aligned with the uniform stream or at ninety degrees to it, depending on whether the transmural exceeds or is below the buckling pressure identified by Lévy (1884) for a cell in a static fluid. The analysis of Blyth and Părău (2013) was based on a curvature expansion that required knowledge only of the leading order flow around the undeformed cell, and cannot provide details of the first order correction to the flow-field. In the present work we have taken a more natural approach and used a conformal mapping method to enable an expansion in α to be taken to arbitrary order. In doing so we have uncovered parts of the solution space that were missed by Blyth and Părău (2013), notably a sequence of critical pressures $P = k^2 - 1$ for integer $k \geq 2$ at which further bifurcations are encountered. For example, we have shown for the first time that steady cell shapes with left-right asymmetry and cells with top-bottom asymmetry in the presence of a uniform flow are possible.

We have focused on solutions bifurcating from the first two critical transmural pressures, namely $P = 3$ and $P = 8$, and mapped the steady solution space in each case. We also carried out a linear stability analysis of the steady solutions and compared the results favourably with time-dependent numerical computations of the full nonlinear system. We found that the horizontally aligned symmetric cells which exist for $P < 5.247$ are linearly stable for all parameter values that we considered. The vertically aligned symmetric cells which exist for $P > 3$ were found to be generally unstable,

although we identified some values of the parameters for which these cells were stable. The solutions with a left-right asymmetry were also found to be stable only in a limited region of the parameter space. We found that the presence of a fluid in the interior of the cell significantly reduces the region of parameter-space for which the steady solutions are linearly stable.

We computed the nonlinear time-evolution of the unstable cells subjected to a small initial perturbation and identified regions in which they fall into one of two distinct regular motions, either a flipping motion or a bulging motion, with small irregular oscillations superimposed on the larger scale regular motions. In the flipping motion, the cell flips between near-steady states, with the direction of rotation alternating, but the cell always travelling downstream while flipping. In the bulging motion the cell bulges out to one side to resemble a top-bottom symmetric mode-3 shape before returning to a near-steady solution, again travelling downstream during the deformation. In this case the side to which the cell bulges switches in an unpredictable manner. When a fluid is introduced to the interior of the cell we found that the regular motions occur at a higher frequency, although the downstream velocity of the cell during these motions is reduced. We computed an approximate maximum Lyapunov exponent of the unsteady motions and found it to tend to a positive value, which is indicative of chaos.

4

Equilibria of an Elastic Cell in a Flow with Circulation

In this chapter we study the equilibria of an elastic cell in a fluid flow with circulation. This problem can be considered an extension of the equilibria problem considered in Chapter 3, with the addition of a circulation around the cell.

We consider the problem in two parts. First we consider the deformation of a cell in a circulatory flow with no flow in the far-field. This problem was studied in detail by Blyth and Părău (2013), who used a linear analysis to obtain a dispersion relation between the circulation and the fluid pressure at which mode-k buckled cells emerge, and used a numerical method to analyse the subsequent non-linear deformation. Using the conformal mapping method described in Chapter 3 we obtain asymptotic expansions for the buckled cells, and use numerical solutions to verify their accuracy.

We then consider the deformation of a cell in a uniform stream with some circulation around the cell. By the Kutta-Joukowski theorem, the circulation will generate a net lift force acting upon the cell. Since we're interested in equilibrium states, we take the cell material to have some non-zero density chosen such that the weight of the cell balances the lift force. We use the conformal mapping and asymptotic methods described in Chapter 3 to obtain equilibrium solutions analytically for low flow speeds, and use numerical

methods to confirm the analytic solutions and explore the full solution space.

While the equilibrium problem can easily be studied using the same techniques as were used in Chapter 3 for the non-circulatory problem, the unsteady problem becomes significantly more complex when circulation is introduced to the flow. Since the cell wall is taken to have some non-zero density, the inertial term in the governing equation (2.4.2) no longer vanishes and the time-derivatives of the unknowns can no longer be obtained explicitly. These time-derivatives must instead be found numerically as solutions to the integro-differential equation (2.4.2), which significantly increases the computational complexity in solving the unsteady evolution of the system. The unsteady problem is thus left for future work, and will not be considered here.

4.1 Formulation

We formulate the problem based on the general steady formulation derived in Chapter 2. We start by considering the balance of net forces acting on the cell, which is given by (2.7.7) as

$$2\pi GD - \alpha\beta + G(\varrho - 1)A = 0,$$

where A is the area of the cell, and the three terms correspond to the dimensionless weight, lift and buoyancy forces respectively. We're interested in the case where the lift force balances the weight of the cell, with zero buoyancy force. We thus take $\varrho = 1$, which is equivalent to taking the interior and exterior fluids to have equal densities. The net force balance thus requires $GD = \alpha\beta/2\pi$, or in dimensional terms

$$\rho_c = -\frac{\rho^{(e)} U\Gamma}{2\pi g h \ell}.$$

Since the term $\beta/2\pi$ appears throughout the problem, we introduce the notation $\hat{\beta} = \beta/2\pi$ to simplify the expressions; both β and $\hat{\beta}$ will be used throughout this chapter as convenient.

The equilibrium cells must satisfy the dynamic condition (2.7.6), which for $\varrho = 1$ and $GD = \alpha\beta/2\pi$ is reduced to

$$\begin{aligned}\frac{1}{2}\left(\left|\frac{2\alpha a_{-1}\sin(\phi) + \beta/2\pi}{\eta_\phi}\right|^2 - \alpha^2\right) - P - \left(\kappa_{ss} + \tfrac{1}{2}\kappa^3 - \sigma\kappa\right) \\ + \frac{\alpha\beta}{2\pi}\big(\mathrm{Re}(\eta_s) + \kappa\mathrm{Im}(\eta)\big) = 0,\end{aligned} \tag{4.1.1}$$

which depends on the three dimensionless parameters

$$\alpha = U\sqrt{\frac{\ell^3\rho^{(e)}}{E_B}}, \quad \beta = -\Gamma\sqrt{\frac{\ell\rho^{(e)}}{E_B}}, \quad P = \frac{(p_\infty - p_0)\ell^3}{E_B},$$

which correspond to the far-field flow speed, the clockwise circulation, and the pressure difference between the exterior and interior of the cell respectively. Here $\eta(\phi)$ is the parametrisation of the cell boundary in the complex z-plane, $\kappa(\phi)$ is the curvature of the cell, s is the anticlockwise arc-length distance along the cell wall, σ is a dimensionless value related to the internal tension of the cell, and a_{-1} is a scaling coefficient.

The cell boundary parametrisation $\eta(\phi)$ is given by (2.7.2) as

$$\eta(\phi) = a_{-1}\left(e^{\mathrm{i}\phi} + \sum_{n=1}^{\infty} a_n e^{-\mathrm{i}n\phi}\right), \tag{4.1.2}$$

where $0 \le \phi \le 2\pi$ is the argument of the unit circle in the complex ζ-plane, and

$$a_{-1} = \frac{2\pi}{\int_0^{2\pi}\left|\mathrm{e}^{\mathrm{i}\phi} - \sum_{n=1}^{\infty} n a_n e^{-\mathrm{i}n\phi}\right|\mathrm{d}\phi} \tag{4.1.3}$$

is a normalisation factor to ensure the cell perimeter is equal to 2π. The

curvature κ and its second arc-length derivative κ_{ss} are given by

$$\kappa(\phi) = -\mathrm{Im}(\eta_{ss}\overline{\eta}_s), \quad \kappa_{ss}(\phi) = -\mathrm{Im}(\eta_{ssss}\overline{\eta}_s + \eta_{sss}\overline{\eta}_{ss})$$

where the derivatives are evaluated using the relation

$$\frac{\mathrm{d}}{\mathrm{d}s} = \frac{1}{|\eta_\phi|}\frac{\mathrm{d}}{\mathrm{d}\phi}.$$

The problem is thus reduced to obtaining values of the mapping coefficients a_n such that the parametrised cell shape given by (4.1.2) satisfies (4.1.1).

The numerical method used to compute nonlinear equilibria is the same as in Chapter 3, based on that presented by Tanveer (1996). We truncate the Fourier series (4.1.2) at N terms, taking $a_n = 0$ for $n > N$. We then split up the coefficients into the $2N$ real variables $\mathrm{Re}(a_n)$ and $\mathrm{Im}(a_n)$ for $1 \leq n \leq N$, with a_{-1} given in terms of a_n by (4.1.3). The parameters α and P are freely chosen, while σ is to be found along with the mapping coefficients a_n by satisfying (4.1.1). We obtain explicit expressions for κ and κ_{ss} for the truncated mapping in terms of the mapping coefficients a_n and evaluate (4.1.1) at $2N + 1$ equally spaced collocation points $\phi_i = 2\pi(i-1)/(2N+1)$ for $i = 1, \ldots, 2N + 1$, giving $2N + 1$ equations to solve for the $2N + 1$ variables. We obtain the Jacobian of the truncated system analytically, and Newton's method can be used to obtain a numerical solution. For the results shown in this section we generally take $N = 200$, although values as high as $N = 2000$ are required for certain solutions. To confirm the accuracy of the numerical results we note that, for any given mapping function, the absolute value of the left-hand side of (4.1.1) can be obtained analytically along the entire cell, not just at the $2N + 1$ collocation points used in Newton's method. We can therefore verify the validity of our results by sampling (4.1.1) at a much larger number of points, say $1000N$, and confirm that the maximum value remains below some

tolerance level; all results in this chapter have a maximum absolute error less than 10^{-10}. We use the small α asymptotic results presented below as an initial guess for Newton's method. The full nonlinear solution space can then be explored by continuation in the parameters α and P.

4.2 Results for a Circulatory Flow

We first consider the deformation of a cell in a circulatory flow, with zero far-field flow speed α. Setting $\alpha = 0$ in (4.1.1), we obtain

$$\frac{1}{2}\frac{\hat{\beta}^2}{|\eta_\phi|^2} - P - \left(\kappa_{ss} + \tfrac{1}{2}\kappa^3 - \sigma\kappa\right) = 0. \tag{4.2.1}$$

There clearly exists a trivial circular solution of the form

$$\eta(\phi) = e^{\mathrm{i}\phi}, \quad \sigma = \tfrac{1}{2} - P + \tfrac{1}{2}\hat{\beta}^2, \tag{4.2.2}$$

valid for all $\hat{\beta}$ and P. In addition to this circular solution, Blyth and Părău (2013) used a linear analysis to show that a mode-k buckled cell bifurcates from the unit circle as the pressure difference P is raised above one of a series of critical values P_k.

We also note that, in the limit as $P \to -\infty$ with $\sigma \sim -P$ and $\hat{\beta}^2 \sim -P$, the problem is reduced to that of a bubble in a circulatory flow, for which exact solutions were obtained by Crowdy (1999). While the results presented in this section are based on asymptotic expansions from the circular rest-state, the exact solutions for the bubble solution could be used to obtain asymptotic results for weakly elastic cells. However, such an approach is left for future work.

We will use an asymptotic expansion of the mapping coefficients a_n to obtain analytic expressions for the buckled cell shapes as the pressure P is increased

past these critical pressures. Since we expect the buckled cells to bifurcate as P is increased past some critical pressure P_k, we introduce the small parameter ϵ such that $P = P_k + \epsilon^2$, where the critical value P_k is to be found. We expand the mapping coefficients a_n in (4.1.2) and the parameter σ as asymptotic expansions for $|\epsilon| \ll 1$ of the form

$$a_n = a_{n,1}\epsilon + a_{n,2}\epsilon^2 + O\left(\epsilon^3\right) \quad \text{for} \quad n \geq 1,$$
$$\sigma = \tfrac{1}{2} - P_k + \tfrac{1}{2}\hat{\beta}^2 + \sigma_1\epsilon + \sigma_2\epsilon^2 + O\left(\epsilon^3\right),$$

where $\epsilon = 0$ corresponds to the circular solution (4.2.2). Substituting these expansions into (4.2.1) and evaluating at $O(\epsilon)$, we obtain

$$-\sigma_1 + \sum_{n=2}^{\infty}\left(n^2 - 1\right)\left(P_k - n^2 + 1 - \frac{\hat{\beta}^2}{2}\frac{n-1}{n+1}\right)\mathrm{Re}\left(a_{n-1,1}e^{-\mathrm{i}n\phi}\right) = 0. \tag{4.2.3}$$

For non-trivial solutions to exist, we require $a_{k-1,1} \neq 0$ for some $k \geq 2$. Equation (4.2.3) thus gives the set of critical pressures

$$P_k(\beta) = k^2 - 1 + \frac{k-1}{k+1}\frac{\beta^2}{8\pi^2}, \quad k \geq 2, \tag{4.2.4}$$

at which nontrivial solutions emerge. These critical pressures are exactly those obtained by Blyth and Părău (2013). Equation (4.2.3) then gives $\sigma_1 = 0$ and $a_{n,1} = 0$ for $n \neq k-1$, while $a_{k-1,1}$ remains undetermined. The cell shape at $O(\epsilon)$ is thus a mode-k buckled shape given by

$$\eta(\phi) = e^{\mathrm{i}\phi} + \epsilon a_{k-1,1}e^{-\mathrm{i}(k-1)\phi}, \tag{4.2.5}$$

where the coefficient $a_{k-1,1}$ must be determined by satisfying (4.2.1) at higher orders of ϵ.

At higher powers of ϵ (4.2.1) becomes difficult to solve by hand; we thus use

the symbolic computing environment Maple to obtain the following results. Satisfying (4.2.1) at $O(\epsilon^2)$ we obtain

$$a_{2k-1,2} = -\frac{(k-1)^2}{4k}\left(1 + \frac{(k+1)^2(2k+1)}{3k(k+1)(2k+1)+\hat{\beta}^2}\right)a_{k-1,1}^2,$$
$$a_{n,2} = 0 \quad \text{for} \quad n \notin \{k-1, 2k-1\},$$
$$\sigma_2 = \tfrac{1}{4}a_{k-1,1}^2(k-1)^2\left(3(k+1)^2+\hat{\beta}^2\right) - 1,$$

and both $a_{k-1,1}$ and $a_{k-1,2}$ remain unknown. Next satisfying (4.2.1) at $O(\epsilon^3)$, we obtain

$$a_{k-1,1}\left(A - |a_{k-1,1}|^2\right) = 0,$$

where

$$A = \frac{24k^3(k+1)^2(2k+1) + 8k(k+1)\hat{\beta}^2}{\left[(2k+1)\left(9(k+1)^5+\hat{\beta}^4\right) + 3(k+1)(4k^3+9k^2+8k+2)\hat{\beta}^2\right](k-1)^3}.$$

We thus obtain the nontrivial solution

$$a_{k-1,1} = \sqrt{A}e^{\mathrm{i}\theta},$$

where the value of θ can be freely chosen due to the rotational invariance in (4.2.1). The cell shape is given to first order by

$$\eta(\phi) = e^{\mathrm{i}\phi} + \sqrt{A}\sqrt{P - P_k(\beta)}\, e^{\mathrm{i}\theta - \mathrm{i}(k-1)\phi} + O(\epsilon^2). \tag{4.2.6}$$

The cell has a mode-k rotational symmetry, with the magnitude of the deformation from the unit circle proportional to the magnitude of $\sqrt{\left(P - P_k(\beta)\right)A}$, which decreases monotonically with β. As β is increased the deformation thus becomes less severe, until $P_k(\beta)$ surpasses P and the cell

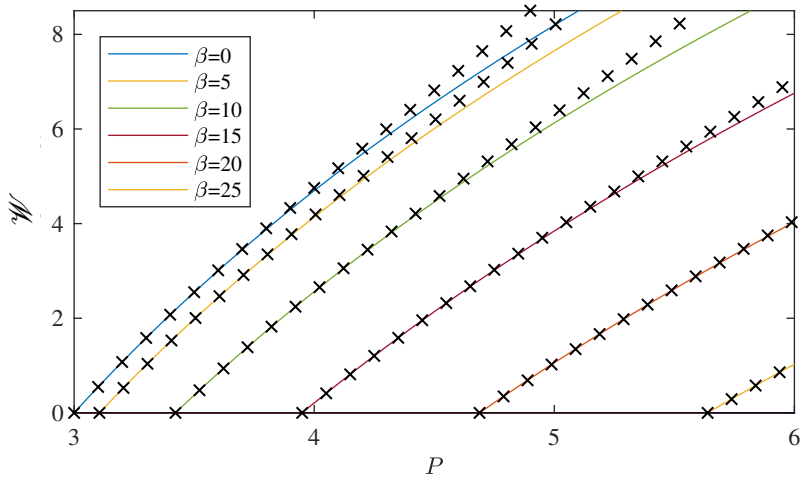

Figure 4.2.1: Numerically computed bending energies of the mode-2 buckled cells against P for various values of β. The black crosses correspond to the $O(\epsilon^6)$ analytical solutions for $k = 2$, where $\epsilon = \sqrt{P - P_2}$.

becomes circular. Setting $\beta = 0$ we obtain $P_k(0) = k^2 - 1$ and

$$\eta(\phi) = e^{i\phi} + \frac{2\sqrt{6}k}{3(k^2-1)^{3/2}}\sqrt{P - k^2 + 1}\, e^{i\theta - i(k-1)\phi} + O(\epsilon^2), \tag{4.2.7}$$

which agrees with the results obtained in Chapter 3 for a cell in a static fluid. This method can easily be continued to higher powers of ϵ to obtain more accurate expansions; however, the algebraic expressions quickly become very complex. We find in general that the value of the coefficient $a_{k-1,n}$ is obtained by satisfying (4.2.1) at $O(\epsilon^{n+2})$.

To confirm the validity of the asymptotic results, we compare the elastic bending energies of the analytic and numerically obtained cells, given by (2.5.17) as

$$\mathscr{W} = \int_0^{2\pi} \tfrac{1}{2}(\kappa + 1)^2 ds. \tag{4.2.8}$$

We compare the numerical results to the asymptotic solutions at $O(\epsilon^6)$, obtained using the symbolic computing environment Maple; the algebraic expressions for these solutions are too large to present here, and the results will thus only be presented graphically.

Figure 4.2.1 shows the bending energies of the mode-2 buckled cells

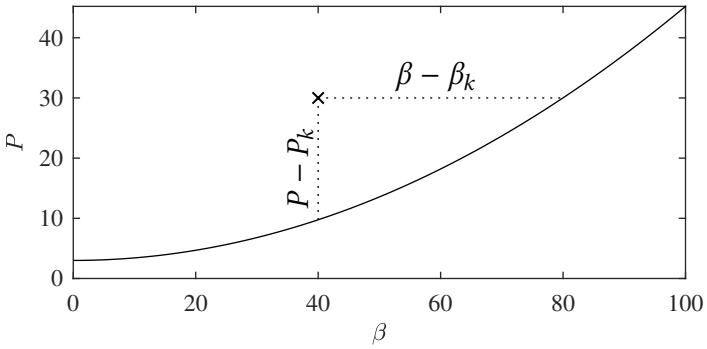

Figure 4.2.2: Sketch of the curve $P = P_2(\beta)$ illustrating how a point in the $\beta - P$ plane can be taken as a perturbation from either $\big(\beta, P_2(\beta)\big)$ or $\big(\beta_2(P), P\big)$.

obtained from the $O\big(\epsilon^6\big)$ asymptotic expansion, as well as those for the numerically computed solutions. For $P < P_2$ the cell is circular with zero bending energy. As P is increased past the critical value P_2 buckled solutions appear, with higher values of the circulation β corresponding to higher critical pressures P_2. For a given pressure P an increased circulation reduces the bending energy of the cell, resulting in a more circular cell shape. For low values of $P - P_2$ the asymptotic results agree very well with the numerical results and remain accurate until approximately $P - P_2 \approx 1$.

In the asymptotic results above we considered the buckled cell at (β, P) to be a perturbation from the circular solution at the critical point $\big(\beta, P_k(\beta)\big)$. However, as shown in Figure 4.2.2, the buckled cell at (β, P) can also be considered a perturbation from the circular cell at the point $\big(\beta_k(P), P\big)$, where the value of $\beta_k(P)$ can be obtained by rearranging (4.2.4) to give

$$\beta_k^2(P) = 8\pi^2\big(P - k^2 + 1\big)\frac{k+1}{k-1}, \quad k \geq 2, \tag{4.2.9}$$

where buckled cells bifurcate from the circular solution as β is reduced past $\beta_k(P)$ for a fixed value of $P > k^2 - 1$. We also define the function $\hat{\beta}_k(P) = \beta_k/2\pi$, which gives the value of $\hat{\beta}$ at which the buckled cells bifurcate.

Since (4.2.1) depends directly on $\hat{\beta}^2$, it is natural to define the small parameter δ such that $\hat{\beta}^2 = \hat{\beta}_k^2(P) - \delta^2$, where $\hat{\beta}$ is used to simplify the results.

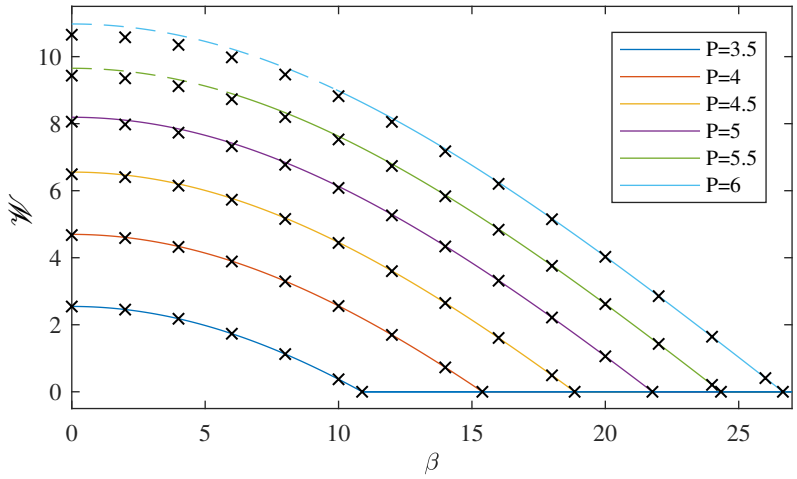

Figure 4.2.3: Numerically computed bending energies of the mode-2 buckled cells against β for various values of P. The black crosses correspond to the $O(\delta^6)$ analytical result, where $\delta = \sqrt{\hat{\beta}_2^2 - \hat{\beta}^2}$.

We expand the unknowns as asymptotic expansions in δ as

$$\begin{aligned} a_n &= a_{n,1}\delta + a_{n,2}\delta^2 + O(\delta^3) \quad n \geq 1, \\ \sigma &= P - \tfrac{1}{2} + (P - k^2 + 1)\frac{k+1}{k-1} + \sigma_1\delta + \sigma_2\delta^2 + O(\delta^3), \end{aligned}$$

where $\delta = 0$ gives the trivial circular solution. Substituting these values into (4.2.1) and evaluating at $O(\delta)$, we find that $\sigma_1 = 0$ and $a_{n,1} = 0$ for $n \neq k-1$, while $a_{k-1,1}$ remains undetermined. Satisfying (4.2.1) at $O(\delta^2)$, we find

$$\begin{aligned} a_{2k-1,2} &= -\frac{(k-1)^2(12k^3 - 2k^2 + 2P - 9k - 1)}{4k(6k^3 - 5k^2 + 2P - 3k + 2)} a_{k-1,1}^2, \\ a_{n,2} &= 0 \quad \text{for} \quad n \notin \{k-1, 2k-1\}, \\ \sigma_2 &= -\frac{1}{2} + \frac{(k^2 + P - 1)^2 - P^2}{4} a_{k-1,1}^2, \end{aligned}$$

where both $a_{k-1,1}$ and $a_{k-1,2}$ remain undetermined. Finally, satisfying (4.2.1) at $O(\delta^3)$ we find that $a_{k-1,1}$ must satisfy

$$a_{k-1,1}(A - |a_{k-1,1}|^2 B) = 0,$$

where

$$A = \frac{4k(2k-1)(3k+2)}{k+1} + \frac{8Pk}{k^2-1}$$

and

$$B = 4(2k+1)P^2 + 2(k-1)(4k+1)\big(3k^2+4k+2\big)P \\ - (2k-1)\big(k^2-1\big)(k-1)\big(3k^2+2k+1\big).$$

Note that $P \geq k^2-1$, and so $B \geq 9(k-1)^2(k+1)^3(2k+1) > 0$ for all $k \geq 2$. We thus obtain the nontrivial solution

$$a_{k-1,1} = \sqrt{\frac{A}{B}}e^{\mathrm{i}\theta},$$

where the angle θ can be freely chosen due to the rotational invariance in (4.2.1). The cell shape is given to first order as

$$\eta(\phi) = e^{\mathrm{i}\phi} + \sqrt{\frac{A}{B}}e^{\mathrm{i}\theta-\mathrm{i}(k-1)\phi}\sqrt{\hat{\beta}_k^2 - \hat{\beta}^2} + O\big(\delta^2\big), \tag{4.2.10}$$

a mode-k buckled cell.

Figure 4.2.3 shows the bending energies of the mode-2 buckled cells obtained from the $O\big(\delta^6\big)$ asymptotic expansion, as well as those for the numerically computed solutions. As β passes below the critical value β_2 the buckled solution branches bifurcate from the circular solution, with the critical value β_2 increasing as the pressure P is increased. Since buckled solution branches only appear for $0 \leq \beta < \beta_2$, the curves in the figure display the whole solution branch for a given value of P. For β close to the critical values β_2 the asymptotic results agree very well with the numerical results. As β is decreased, the asymptotic solutions begin to diverge from the numerical solutions, with the maximum error occurring at $\beta = 0$.

Figures 4.2.4, 4.2.5 and 4.2.6 show the mode-2, mode-3 and mode-4 buckled

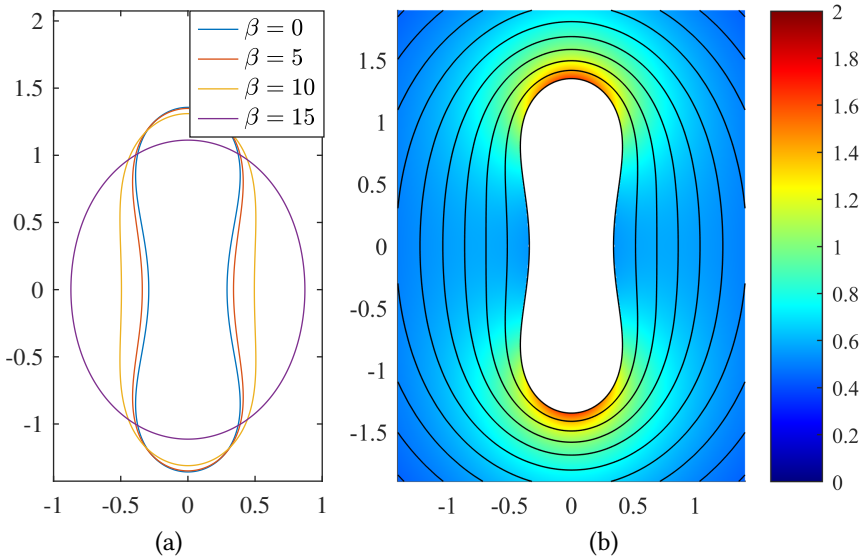

Figure 4.2.4: Numerically computed cell shapes for the mode-2 buckled cell for $P = 4$. (a) shows the cell shape for increasing values of β, with the cell circular for $\beta > 15.3906$. (b) shows a contour plot of the flow around the cell for $\beta = 5$, with the colour scale corresponding to the flow speed divided by $\hat{\beta}$, the flow speed around a unit circle with the same circulation. The black lines are the streamlines of the flow.

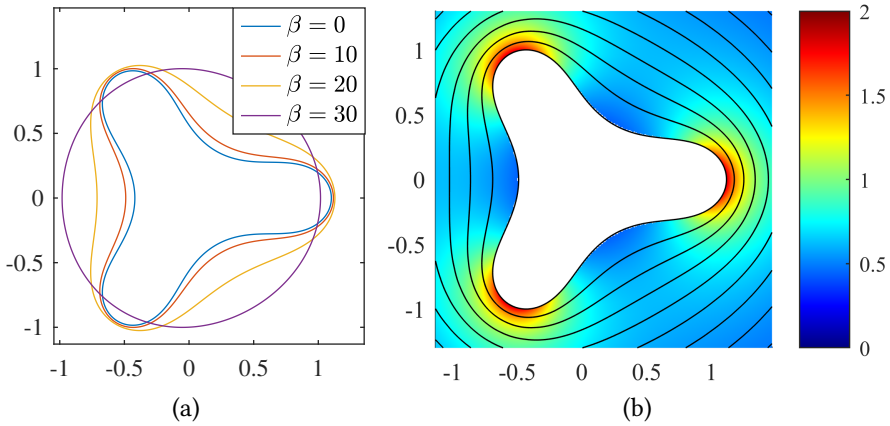

Figure 4.2.5: Numerically computed cell shapes for the mode-3 buckled cell for $P = 12$. (a) shows the cell shape for increasing values of β, with the cell circular for $\beta > 25.1327$. (b) shows a contour plot of the flow around the cell for $\beta = 5$, with the colour scale corresponding to the flow speed divided by $\hat{\beta}$, the flow speed around a unit circle with the same circulation. The black lines are the streamlines of the flow.

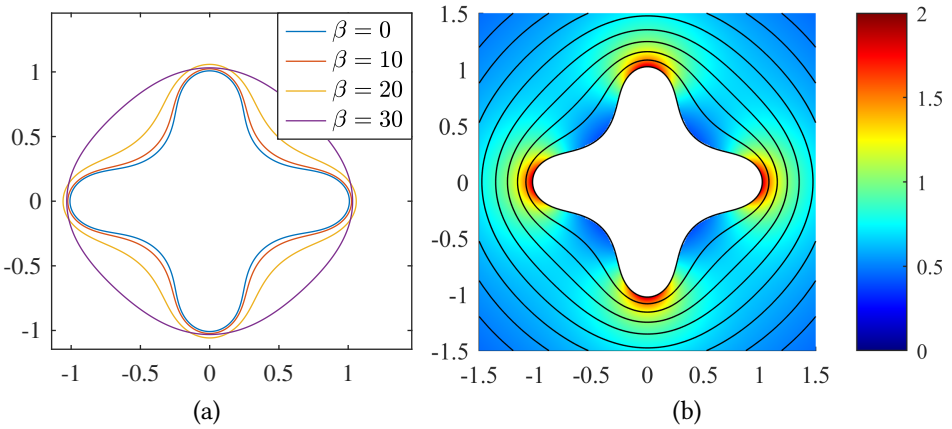

Figure 4.2.6: Numerically computed cell shapes for the mode-4 buckled cell for $P = 22$. (a) shows the cell shape for increasing values of β, with the cell circular for $\beta > 30.3507$. (b) shows a contour plot of the flow around the cell for $\beta = 5$, with the colour scale corresponding to the flow speed divided by $\hat{\beta}$, the flow speed around a unit circle with the same circulation. The black lines are the streamlines of the flow.

cells respectively for varying values of β, along with contour plots and streamlines of the fluid flow. We find that as β is increased from zero the cells become more circular while retaining their rotational symmetry. The maximum flow speed occurs at the tips of the buckled cell with the low fluid pressure increasing the cell deformation in this region.

4.3 Results for a Uniform Stream with Circulation

We now consider equilibrium solutions for a cell in a circulatory uniform stream with both $\alpha \neq 0$ and $\beta \neq 0$. We seek asymptotic solutions for small flow speed α using the same method as in Chapter 3; we assume the buckled cells bifurcate from the trivial circular solution at $\alpha = 0$, and expand the unknowns a_n and σ

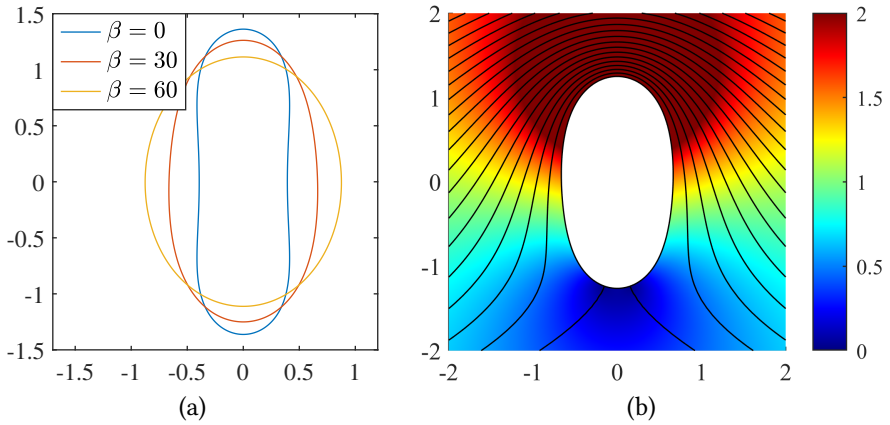

Figure 4.3.1: Numerically computed cell shapes for $\alpha = 2.5$, $P = 0$. (a) shows the cell shape for various values of the circulation β. (b) shows a contour plot of the flow past the cell for $\beta = 30$, with the colour scale corresponding to the flow speed divided by the far-field flow speed α. The black lines are the streamlines of the flow.

as asymptotic series in α of the form

$$a_n = a_{n,1}\alpha + a_{n,2}\alpha^2 + O(\alpha^3) \quad n \geq 1, \tag{4.3.1}$$

$$\sigma = \tfrac{1}{2} - P + \tfrac{1}{2}\hat{\beta}^2 + \sigma_1\alpha + \sigma_2\alpha^2 + O(\alpha^3). \tag{4.3.2}$$

Substituting these expansions into (4.1.1) and evaluating at $O(\alpha)$, we obtain

$$-\sigma_1 + \sum_{n=2}^{\infty} (n^2 - 1)\big(P - P_n(\beta)\big)\mathrm{Re}\Big(a_{n-1,1}e^{-in\phi}\Big) = 0, \tag{4.3.3}$$

where $P_n(\beta)$ is the nth critical pressure given by (4.2.4). We thus require $\sigma_1 = 0$, and for each $n \geq 2$ we require either $a_{n-1,1} = 0$ or $P = P_n(\beta)$. We split the problem into two distinct cases; we start by looking for a solution which is valid for general values of P, where $P \neq P_k(\beta)$ for all $k \geq 2$. We then look for solutions which are valid at each of the critical pressures $P = P_k(\beta)$ for $k \geq 2$.

First seeking a solution valid for general values of P, we assume $P \neq P_k$ for all $k \geq 2$. Equation (4.3.3) thus gives $\sigma_1 = 0$ and $a_{n,1} = 0$ for all $n \geq 1$. Next

satisfying (4.1.1) at $O(\alpha^2)$, we obtain

$$\tfrac{1}{2} - \sigma_2 - \cos(2\phi) + \sum_{n=2}^{\infty} (n^2 - 1)\,(P - P_n(\beta))\mathrm{Re}\left(a_{n-1,2}e^{-\mathrm{i}n\phi}\right) = 0. \tag{4.3.4}$$

Noting that

$$\mathrm{Re}\left(a_{n-1,2}e^{-\mathrm{i}n\phi}\right) = \mathrm{Re}\left(a_{n-1,2}\right)\cos(n\phi) + \mathrm{Im}\left(a_{n-1,2}\right)\sin(n\phi),$$

we compare coefficients of $\cos(n\phi)$ and $\sin(n\phi)$ in (4.3.4) to obtain

$$a_{1,2} = \frac{1}{3(P - P_2)}$$

and $a_{n,2} = 0$ for $n \geq 2$, with $\sigma_2 = \frac{1}{2}$. We then proceed in the same way to higher powers of α using the symbolic computing environment Maple to obtain the $O(\alpha^5)$ solution

$$\begin{aligned}
a_1 &= \frac{1}{3(P - P_2)}\alpha^2 - \frac{1}{18(P - P_2)^2}\alpha^4 + O(\alpha^6),\\
a_2 &= \frac{\left(24P - 297 - 7\hat{\beta}^2\right)\hat{\beta}\mathrm{i}}{1440(P - P_2)^2(P - P_3)(P - P_4)}\alpha^5 + O(\alpha^6),\\
a_3 &= \frac{2P - 156 - \hat{\beta}^2}{360(P - P_2)^2(P - P_4)}\alpha^4 + O(\alpha^6),\\
a_4 &= -\frac{(2P + 159)\hat{\beta}\mathrm{i}}{4320(P - P_2)^2(P - P_4)(P - P_5)}\alpha^5 + O(\alpha^6),\\
a_n &= O(\alpha^6) \quad \text{for} \quad n \geq 5,\\
\sigma &= \frac{1}{2} - P + \frac{\hat{\beta}^2}{2} + \frac{1}{2}\alpha^2 - \frac{1}{4}\frac{6P - 45 - 2\hat{\beta}^2}{9(P - P_2)^2}\alpha^4 + O(\alpha^6),
\end{aligned}$$

which is valid for all $P \neq P_k(\beta)$. The cell shape is given to $O(\alpha^2)$ as

$$\eta(\phi) = e^{\mathrm{i}\phi} + \frac{1}{3(P - P_2)}\alpha^2 e^{-\mathrm{i}\phi} + O(\alpha^4), \tag{4.3.5}$$

an ellipse which is elongated vertically for $P < P_2$ and horizontally for $P > P_2$.

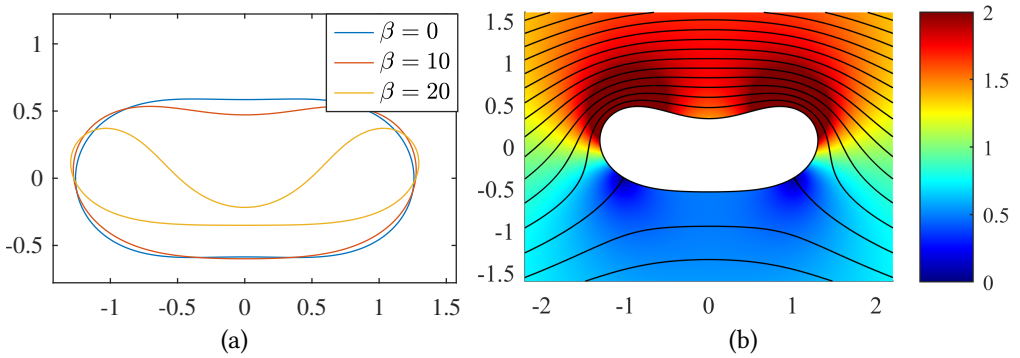

Figure 4.3.2: Numerically computed cell shapes for $\alpha = 2.5$, $P = 6$. (a) shows the cell shape for various values of the circulation β. (b) shows a contour plot of the flow past the cell for $\beta = 15$, with the colour scale corresponding to the flow speed divided by the far-field flow speed α. The black lines are the streamlines of the flow.

Note that setting $\beta = 0$ reduces this solution to that obtained in Chapter 3. However, unlike the $\beta = 0$ solution, the coefficients a_2 and a_4 are imaginary for $\beta \neq 0$, causing the cell to lose its top-bottom symmetry, although the cell remains left-right symmetric. This solution becomes invalid when the pressure P is equal to any of the critical pressures $P_k(\beta)$. This contrasts with the $\beta = 0$ solutions, which are only invalid for $P = P_{2k}$ while remaining valid for $P = P_{2k+1}$. This suggests that the general solution branch valid for $\beta = 0$ and $P = P_{2k+1}$ detaches from $\alpha = 0$ as circulation is introduced; the exact nature of this behaviour will be discussed further on.

Figures 4.3.1 and 4.3.2 show numerically computed cell shapes for $P = 0$ and $P = 6$ respectively for various values of β, along with a plot of the flow field for $\beta = 30$. For $P = 0$ the cell is elongated vertically, as predicted by (4.3.5). As β is increased the cell deformation decreases and the cell becomes more circular. This agrees with (4.3.5); as β is increased the critical pressure $P_2(\beta)$ increases, and so the magnitude of the factor $\frac{1}{3(P-P_2)}$ decreases, resulting in a more circular cell shape. For $P = 6$ the cell is oriented horizontally, which also agrees with (4.3.5). As β is increased, the magnitude of the factor $\frac{1}{3(P-P_2)}$ in (4.3.5) increases,

resulting in a more elongated cell shape. This deformation increases with β until the cell eventually self-intersects, at which point the solution becomes physically invalid.

We then seek asymptotic solutions which are valid at the critical pressures $P = P_k(\beta)$, focussing in particular on the first two critical pressure $P_2(\beta)$ and $P_3(\beta)$. We start by considering the case where $P = P_2(\beta) = 3 + \hat{\beta}^2/6$. As in the case of $\beta = 0$ discussed in Chapter 3, we find that (4.1.1) cannot be satisfied by an expansion in integer powers of α. We instead take an expansion in powers of $\alpha^{1/3}$ and satisfy (4.1.1) at each power of $\alpha^{1/3}$, which gives the unique solution

$$\begin{aligned}
a_1 &= a_{1,1}\alpha^{2/3} + \frac{8\left(\hat{\beta}^2+90\right)}{3\left(5\hat{\beta}^4+774\hat{\beta}^2+10935\right)a_{1,1}}\alpha^{4/3} + O\left(\alpha^2\right),\\
a_3 &= -\frac{\hat{\beta}^2+225}{8\left(\hat{\beta}^2+90\right)}a_{1,1}^2\alpha^{4/3} + O\left(\alpha^2\right),\\
a_n &= O\left(\alpha^2\right) \quad \text{for} \quad n \notin \{1,3\},\\
\sigma &= \tfrac{5}{2} + \tfrac{1}{3}\hat{\beta}^2 + \tfrac{1}{4}\left(\hat{\beta}^2+27\right)a_{1,1}^2\alpha^{4/3} + O\left(\alpha^2\right),
\end{aligned}$$

where

$$a_{1,1} = -\sqrt[3]{\frac{16\left(\hat{\beta}^2+90\right)}{5\hat{\beta}^4+774\hat{\beta}^2+10935}}.$$

The cell shape is given to first order as

$$\eta(\phi) = e^{\mathrm{i}\phi} - \sqrt[3]{\frac{16\left(\hat{\beta}^2+90\right)}{5\hat{\beta}^4+774\hat{\beta}^2+10935}}e^{-\mathrm{i}\phi}\alpha^{2/3} + O\left(\alpha^{4/3}\right), \tag{4.3.6}$$

an ellipse elongated vertically perpendicular to the flow. Note that at higher orders of α the circulation will induce a top-bottom asymmetry. Taking $\beta = 0$ we obtain $a_{1,1} = -\frac{2}{9}\sqrt[3]{12}$, which agrees with the result (3.4.5) obtained in Chapter 3. As β is increased, the magnitude of the coefficient of $e^{-\mathrm{i}\phi}$ in (4.3.6) decreases and the cell becomes more circular.

Figure 4.3.3 shows the numerically computed bending energy against α for

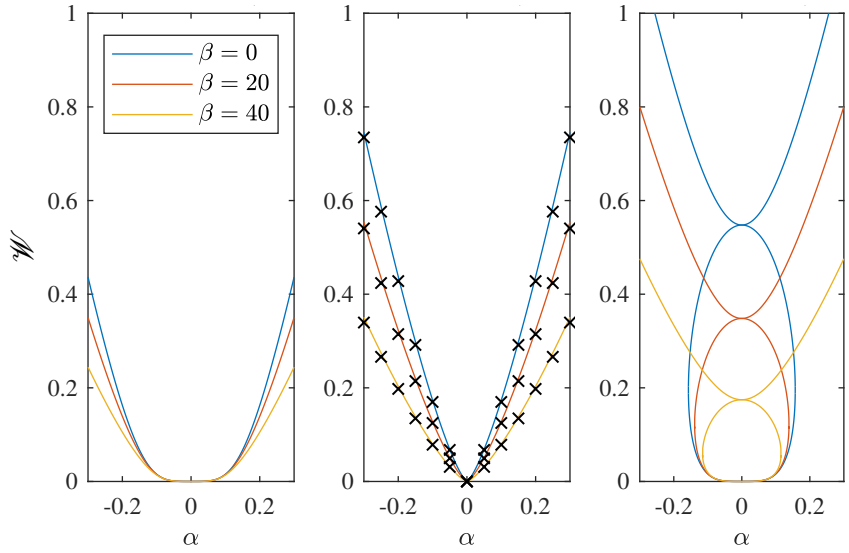

(a) $P = P_2(\beta) - 0.1$ (b) $P = P_2(\beta)$ (c) $P = P_2(\beta) + 0.1$

Figure 4.3.3: Numerically computed bending energy against α for solution branches near $P_2(\beta)$. The black crosses in (b) correspond to the $O(\alpha^6)$ analytical result.

P near $P_2(\beta)$, along with the analytical results for $P = P_2(\beta)$. For $P < P_2(\beta)$ we find a single solution branch, with horizontally elongated cell shapes which are left-right symmetric. As the circulation is increased the bending energy of these cells decreases. These solution branches have $\mathscr{W} = 0$ at $\alpha = 0$, which corresponds to the circular solution. As P is increased to $P_2(\beta)$ the energy curve develops a cusp, as predicted by the expansion (4.3.6). We find excellent agreement between the analytical results and the numerical results for all values of β. As P is increased above $P_2(\beta)$ a loop appears in the energy curve underneath the previous solution branch, corresponding to cells which are vertically elongated. The solution branch containing the horizontally elongated cells no longer bifurcates from the unit circle at $\alpha = 0$, instead corresponding to the buckled mode-2 cell in a static fluid at $\alpha = 0$ with $\mathscr{W} > 0$. This change in orientation of the cells bifurcating from the unit circle at $\alpha = 0$ agrees with that predicted by (4.3.5).

We next consider the case where $P = P_3(\beta) = 8 + \hat{\beta}^2/4$. Using an integer

power expansion of the form (4.3.1), we satisfy (4.1.1) at $O(\alpha)$ to obtain $\sigma_1 = 0$ and $a_{n,1} = 0$ for $n \neq 2$, with $a_{2,1}$ undetermined. At $O(\alpha^2)$, we find that $a_{2,1}$ satisfies

$$\left[(\hat{\beta}^2+140)(7\hat{\beta}^4+2580\hat{\beta}^2+64512)|a_{2,1}|^2 - 2\hat{\beta}^2(\hat{\beta}^2+252)\right]a_{2,1} = 0.$$

We thus have two distinct cases; either $a_{2,1} = 0$, or

$$|a_{2,1}| = \sqrt{\frac{2\hat{\beta}^2(\hat{\beta}^2+252)}{(\hat{\beta}^2+140)(7\hat{\beta}^4+2580\hat{\beta}^2+64512)}},$$

with the argument of the complex coefficient $a_{2,1}$ undetermined at this stage. Each of these cases will correspond to a distinct branch of solutions.

Considering first the case where $a_{2,1} = 0$, we proceed to satisfy (4.1.1) at each power of α up to $O(\alpha^5)$, at which point we obtain

$$\begin{aligned}
a_1 =& \frac{4}{\hat{\beta}^2+60}\alpha^2 - \frac{8}{(\hat{\beta}^2+60)^2}\alpha^4 + O(\alpha^6),\\
a_2 =& -\frac{12(\hat{\beta}^2+105)}{\hat{\beta}(\hat{\beta}^2+60)^2}\mathrm{i}\alpha^3\\
&-\frac{144(3\hat{\beta}^8+1116\hat{\beta}^6+114238\hat{\beta}^4+1260960\hat{\beta}^2-212738400)}{\hat{\beta}^3(\hat{\beta}^2+60)^4(\hat{\beta}^2+192)}\mathrm{i}\alpha^5 + O(\alpha^6),\\
a_3 =& -\frac{20}{(\hat{\beta}^2+60)^2}\alpha^4 + O(\alpha^6),\\
a_4 =& \frac{4(13\hat{\beta}^4+3570\hat{\beta}^2+264600)}{\hat{\beta}(\hat{\beta}^2+60)^3(\hat{\beta}^2+192)}\mathrm{i}\alpha^5 + O(\alpha^6),\\
a_n =& O(\alpha^6) \quad \text{for} \quad n \geq 5,\\
\sigma =& -\tfrac{15}{2} + \tfrac{1}{4}\hat{\beta}^2 + \tfrac{1}{2}\alpha^2 + \frac{2\hat{\beta}^2-12}{(\hat{\beta}^2+60)^2}\alpha^4 + O(\alpha^6).
\end{aligned}$$

The cell shape is given to $O(\alpha^3)$ by

$$\eta(\phi) = e^{\mathrm{i}\phi} + \frac{4}{\hat{\beta}^2 + 60}\alpha^2 e^{-\mathrm{i}\phi} - \frac{12\left(\hat{\beta}^2 + 105\right)}{\hat{\beta}\left(\hat{\beta}^2 + 60\right)^2}\mathrm{i}\alpha^3 e^{-2\mathrm{i}\phi} + O(\alpha^4) \tag{4.3.7}$$

At $O(\alpha^2)$ the cell shape is elliptical with its major axis oriented horizontally in line with the uniform stream, with larger values of β corresponding to a more elongated shape. However, at $O(\alpha^3)$ the cell becomes top-bottom asymmetric, although it retains a left-right symmetry. The $O(\alpha^3)$ term has a singularity at $\beta = 0$; this solution is thus distinct from any obtained in Chapter 3.

We then consider the case where

$$|a_{2,1}| = \sqrt{\frac{2\hat{\beta}^2\left(\hat{\beta}^2 + 252\right)}{7\hat{\beta}^6 + 3560\hat{\beta}^4 + 425712\hat{\beta}^2 + 9031680}}.$$

Satisfying (4.1.1) at $O(\alpha^3)$, we find that $\mathrm{Re}\left(a_{2,1}\overline{a_{2,2}}\right) = 0$ while both $a_{2,1}$ and $a_{2,2}$ remain undetermined. At $O(\alpha^4)$ we obtain $\mathrm{Re}\left(a_{2,1}\right) = 0$ and $\mathrm{Im}\left(a_{2,2}\right) = 0$, with $\mathrm{Re}\left(a_{2,2}\right)$ undetermined. We thus have

$$a_{2,1} = \pm\sqrt{\frac{2\hat{\beta}^2\left(\hat{\beta}^2 + 252\right)}{7\hat{\beta}^6 + 3560\hat{\beta}^4 + 425712\hat{\beta}^2 + 9031680}}\mathrm{i},$$

which gives two distinct solutions depending on the sign of $a_{2,1}$. Finally, at $O(\alpha^6)$ we find that $a_{2,2} = 0$, and obtain the value of $a_{2,3}$, which we omit for

brevity. The solution is then given to $O(\alpha^2)$ as

$$\begin{aligned}
a_1 &= \frac{4}{\hat{\beta}^2 + 60}\alpha^2 + O(\alpha^3),\\
a_2 &= \pm|a_{2,1}|\alpha \mathrm{i} + O(\alpha^3),\\
a_3 &= \pm\frac{4\hat{\beta}|a_{2,1}|}{3\hat{\beta}^2 + 420}\alpha^2 + O(\alpha^3),\\
a_5 &= \frac{\hat{\beta}^2 + 588}{3\hat{\beta}^2 + 756}|a_{2,1}|^2\alpha^2 + O(\alpha^3),\\
a_n &= O(\alpha^3) \quad \text{for} \quad n \notin \{1, 2, 3, 5\},\\
\sigma &= -\tfrac{15}{2} + \tfrac{1}{4}\hat{\beta}^2 + \left(\tfrac{1}{2} + (\hat{\beta}^2 + 48)|a_{2,1}|^2\right)\alpha^2 + O(\alpha^3),
\end{aligned}$$

with the cell shape given by

$$\begin{aligned}
\eta(\phi) = \left(1 - |a_{2,1}|^2\alpha^2\right)e^{\mathrm{i}\phi} + \frac{4\alpha^2}{\hat{\beta}^2 + 60}e^{-\mathrm{i}\phi} \pm |a_{2,1}\alpha|\mathrm{i}e^{-2\mathrm{i}\phi}\\
\pm \frac{4|ai2|\hat{\beta}\alpha^2}{3\beta^2 + \hat{} 420}e^{-3\mathrm{i}\phi} + \frac{\hat{\beta}^2 + 588}{3\hat{\beta}^2 + 756}|a_{2,1}|^2\alpha^2 e^{-5\mathrm{i}\phi} + O(\alpha^3).
\end{aligned} \tag{4.3.8}$$

This cell is left-right symmetric but top-bottom asymmetric. At $O(\alpha)$, the choice of sign of $\mathrm{Im}(a_{2,1})$ simply corresponds to a reflection of the cell shape about the x-axis. At higher orders of α however, the cell shapes differ at $O(\alpha^2)$ depending on the sign of $\mathrm{Im}(a_{2,1})$.

To validate the asymptotic results, we compare the bending energies of the asymptotic results to numerically computed values. The bending energies of the three solution branches which bifurcate from the circular solution at $\alpha = 0$ for $P = P_3$ are shown in Figure 4.3.4. The lowest energy curve corresponds to the case where $a_{2,1} = 0$, while the higher energy curves correspond to the two $a_{2,1} \neq 0$ cases. We find that the analytic results agree very well with the numerical results.

The numerically obtained bending energies of the three solution curves bifurcating from the circular solution at $\alpha = 0$ for $P = P_3(\beta)$ for varying values

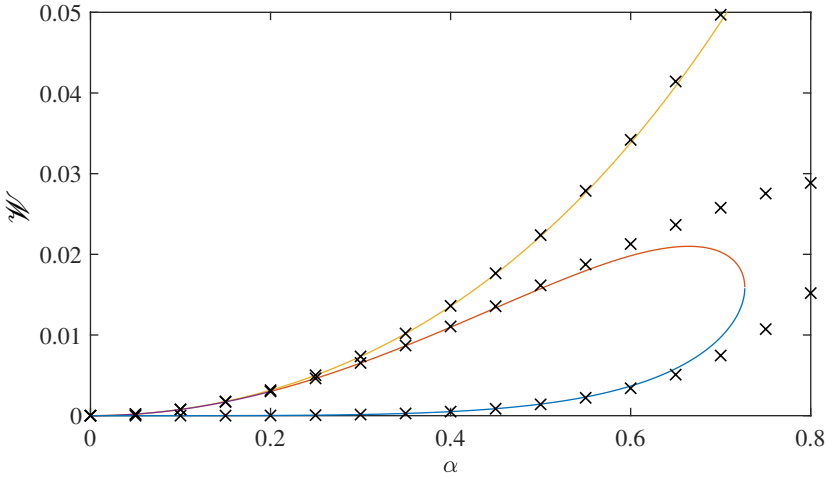

Figure 4.3.4: Bending energies of the three solution branches which bifurcate from the unit circle for $\beta = 50$ and $P = P_3$. The solid lines are numerical solutions to the full nonlinear equations, and the crosses are the $O(\alpha^4)$ analytic results.

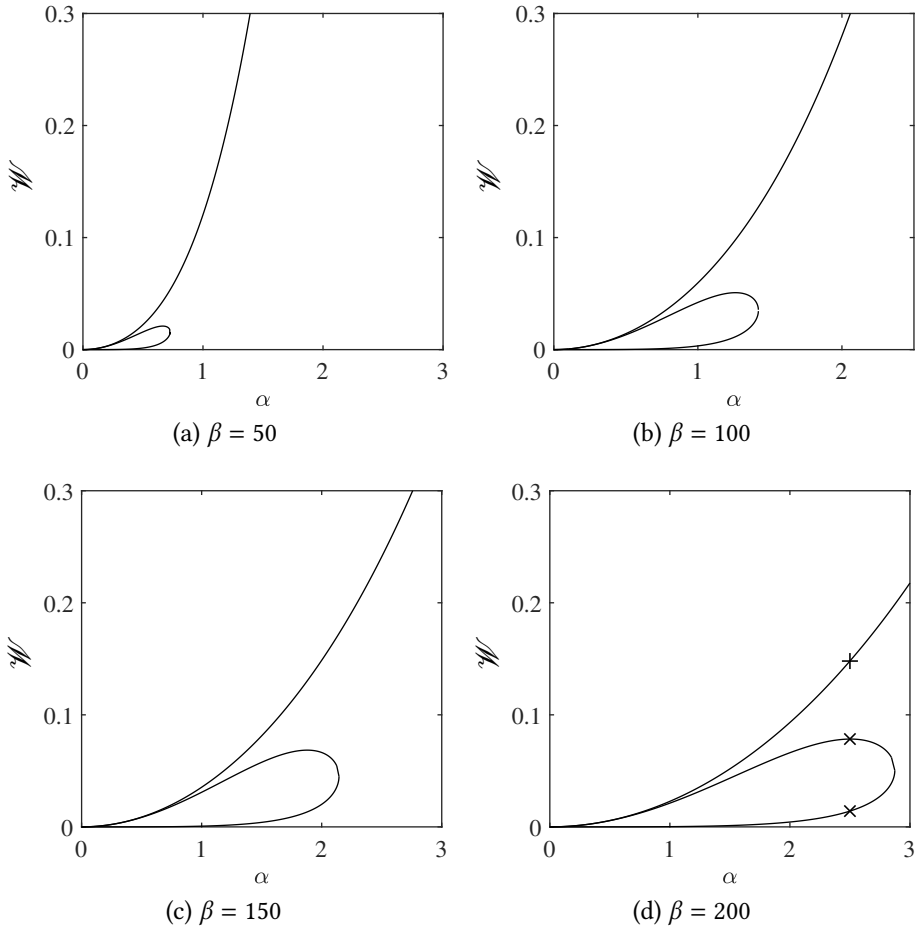

(a) $\beta = 50$ (b) $\beta = 100$

(c) $\beta = 150$ (d) $\beta = 200$

Figure 4.3.5: Bending energies of the solution branches at $P = P_3(\beta)$ against α for large β. The crosses in (d) correspond to the cell shapes depicted in Figure 4.3.6.

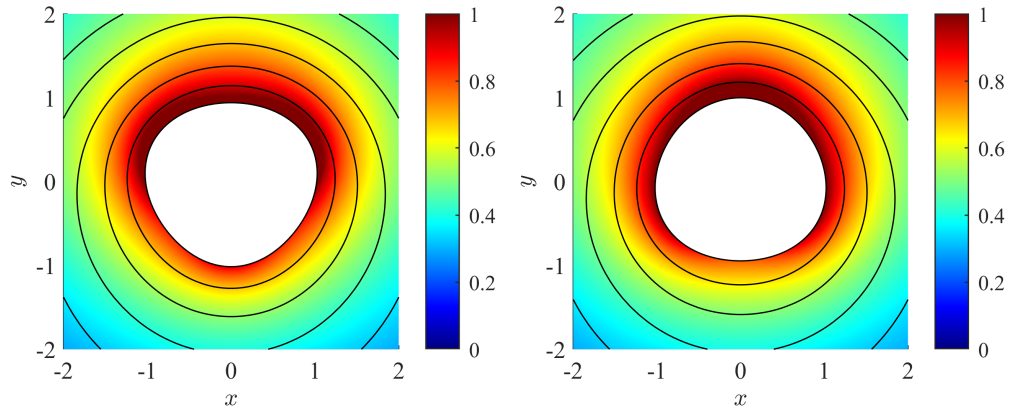

(a) $\mathscr{W} = 0.1480$ (b) $\mathscr{W} = 0.0784$

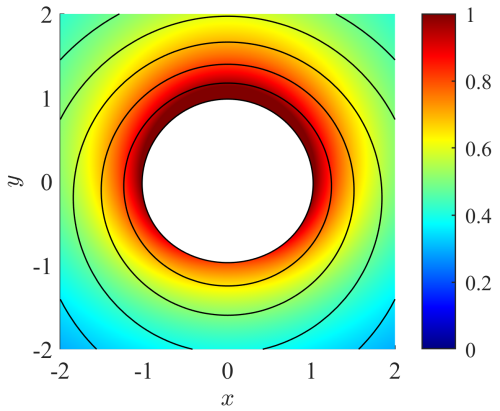

(c) $\mathscr{W} = 0.0141$

Figure 4.3.6: Contour plots of the flow past the three cells which exist for $\alpha = 2.5$, $\beta = 200$, $P = P_3(\beta)$, as shown in Figure 4.3.5d. The colour scale corresponds to the flow speed divided $\hat{\beta}$. The black lines are the streamlines of the flow.

of β are shown in Figure 4.3.5. We find that while solutions exist on the uppermost branch for all values of α, the lower two solution branches exist only for α below some maximum value. This maximum value of α increases as the circulation β is increased; however, the circulation β is always much greater than the maximum uniform flow speed α. Figure 4.3.6 shows the corresponding cell shapes and flow fields for $\alpha = 2.5$ and $\beta = 200$. The high circulation results in a near-circular cell, with the flow field resembling a circulatory flow.

Figure 4.3.7 shows the bending energy of the solution branches for $P = P_3(\beta)$ for low values of β. For $\beta = 0$, we have the three solution branches described

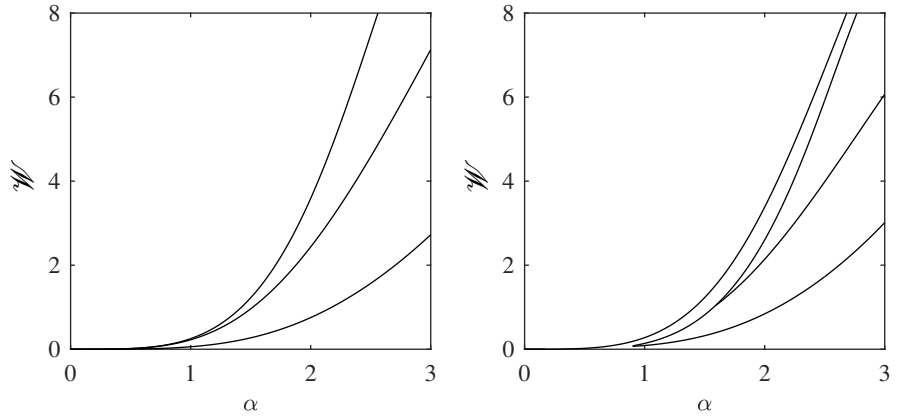

(a) $\beta = 0$ (b) $\beta = 9$

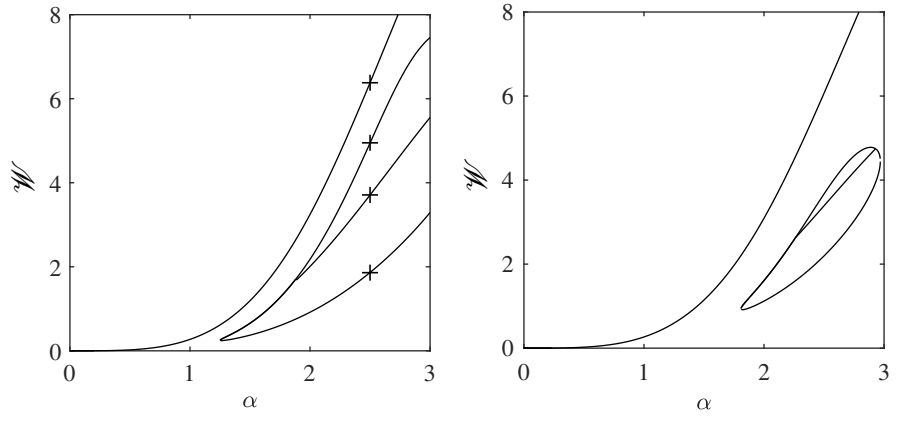

(c) $\beta = 11$ (d) $\beta = 13$

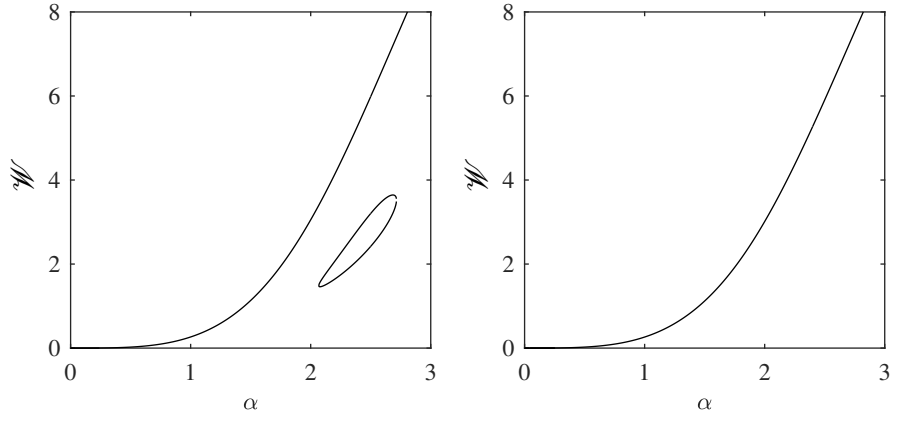

(e) $\beta = 13.5$ (f) $\beta = 14$

Figure 4.3.7: Bending energies of the solution branches at $P = P_3(\beta)$ against α for small β. The crosses in (c) correspond to the cell shapes depicted in Figure 4.3.8.

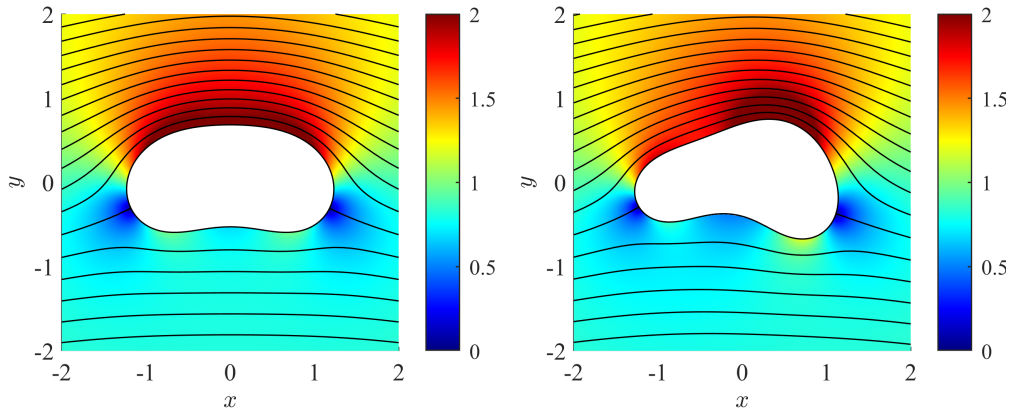

(a) Type 2a ($\mathscr{W} = 1.86$)

(b) Type 3a ($\mathscr{W} = 3.71$)

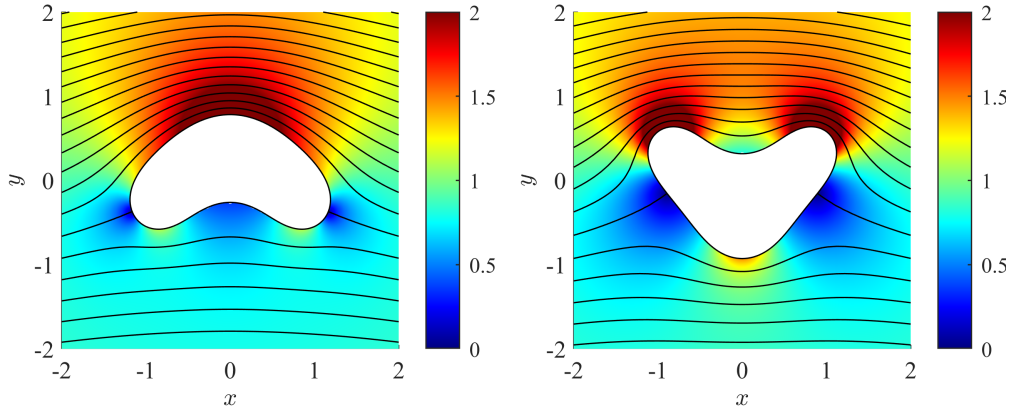

(c) Type $3b_1$ ($\mathscr{W} = 4.95$)

(d) Type $3b_2$ ($\mathscr{W} = 6.38$)

Figure 4.3.8: Contour plots of the flow past the four cells which exist for $\alpha = 2.5$, $\beta = 11$, $P = P_3(\beta)$, as shown in Figure 4.3.7c. The colour scale corresponds to the flow speed divided by the far-field flow speed α. The black lines are the streamlines of the flow.

in Chapter 2. To describe the behaviour of the solution branches, we use the classifications defined in Chapter 2; the lower branch corresponds to type 2a cells, the middle branch corresponds to type 3a cells, and the upper branch corresponds to type 3b cells. Note that while the type 2a cells are left-right and top-bottom symmetric, the type 3a cells are left-right asymmetric and the type 3b cells are top-bottom asymmetric. Since the system for $\beta = 0$ is both left-right and top-bottom symmetric, the type 3a cells can be reflected horizontally to obtain another type 3a solution, and the type 3b cells can be reflected vertically to obtain another type 3b solution. As the circulation is then introduced the system loses its top-bottom symmetry; the type 3b solution branch thus splits

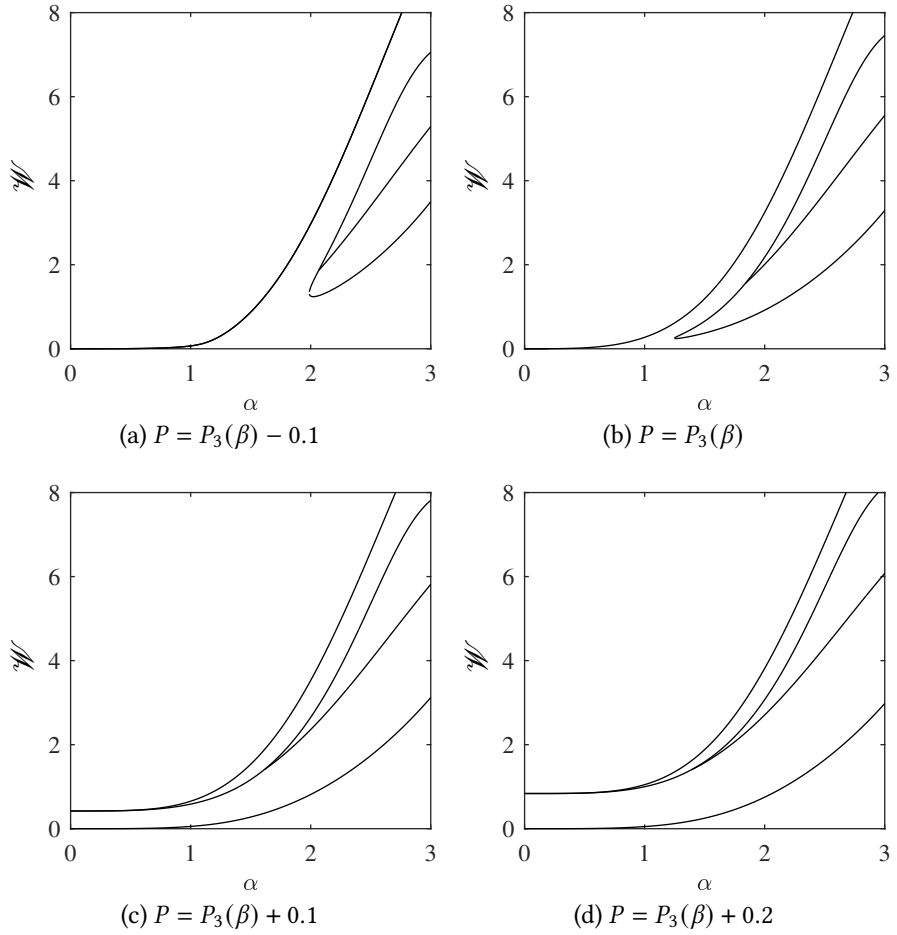

(a) $P = P_3(\beta) - 0.1$ (b) $P = P_3(\beta)$

(c) $P = P_3(\beta) + 0.1$ (d) $P = P_3(\beta) + 0.2$

Figure 4.3.9: Bending energies of the solution branches which exist near $P = P_3(\beta)$ against α for $\beta = 11$.

into two separate branches, depending on the orientation of the cell. We classify the lower energy cell as type $3b_1$ and the higher energy cell as type $3b_2$. Plots of the cell shapes for each of these solution branches are shown in Figure 4.3.8.

For $\beta > 0$ the type 2a, 3a and $3b_1$ branches disconnect from $\alpha = 0$, remaining valid only for α above some minimum value. The type 2a and $3b_1$ branches, which both correspond to left-right symmetric cells, form a continuous loop in the $\alpha - \mathscr{W}$ plane, while the left-right asymmetric type 3a cells bifurcate from the type 2a–$3b_1$ loop. The solution branches shown in Figure 4.3.5 are also present for $\beta > 0$, but for low values of β these branches are too small to be seen. As the circulation β is increased further we find that the type 2a–$3b_1$ branch forms a closed loop, with the solutions existing only for α between two critical values.

The type 3a solution branch is bounded by this closed loop, bifurcating from the 2a–3b$_1$ branch at both ends. This loop becomes smaller as β is increased, until approximately $\beta = 14$ where the loop disappears entirely, leaving only the type 3b$_2$ branch and those shown in Figure 4.3.5.

Figure 4.3.9 shows the bending energies of the solution branches for varying values of P near $P_3(\beta)$. As P is decreased below the critical value $P_3(\beta)$, the minimum value of α at which the types 2a, 3b and 3b$_1$ solution branches exist increases, with only the type 3b$_1$ branch remaining for lower values of α. As P is increased above $P_3(\beta)$, the types 2a, 3b and 3b$_1$ solution branches approach $\alpha = 0$, eventually merging at $\alpha = 0$ with some $\mathscr{W} > 0$, at which point the cell shapes correspond to the mode-3 buckled cell in a static fluid.

4.4 Summary

We have studied the equilibria of an elastic cell in a flow with circulation. Using the conformal mapping approach suggested by Shankar (1992) and Tanveer (1996), we have constructed asymptotic approximations for buckled cells in both a circulatory flow and a uniform stream with circulation. We have computed nonlinear equilibria numerically and confirmed excellent agreement with the asymptotic approximations, and presented a detailed analysis of the nonlinear solutions.

Blyth and Părău (2013) studied the deformation of an elastic cell in a circulatory flow, identifying a set of critical pressures at which buckled cells emerge. We have used a conformal mapping approach to obtain the pressures at which the circular cell buckles into a shape with a mode-k symmetry and obtained two different asymptotic expansions for these buckled cells. We computed nonlinear equilibria numerically and confirmed excellent agreement with the asymptotic approximations. We found that the circulation

reduces the severity of the deformation, with a greater pressure required for the cells to buckle.

We also studied the deformation of an elastic cell in a uniform stream with circulation. This problem can be considered an extension to the uniform stream problem considered in Chapter 3. We used asymptotic expansions for low flow speeds to obtain solutions which bifurcate from the unit circle. We obtained a general solution valid for general values of the pressure P and identified critical pressures at which distinct solution branches emerge. The general solution was found to be elliptical to first order, with the orientation depending on the pressure P; for P below the first critical pressure the cell is oriented vertically with its major axis perpendicular to the flow, while for P above the first critical value the cell is oriented horizontally with its major axis parallel to the flow. We found that as the circulation is increased the vertically oriented cells become more circular, while the horizontally oriented cells become more deformed. We found that the solution space near the second critical pressure becomes significantly more complex when the circulation is introduced, and presented a detailed analysis of the various solution branches which emerge.

5

Deformation and Aerodynamics of an Elastic Aerofoil

Inflatable aerofoils are of increasing interest in the aerospace industry, and have several advantages over traditional rigid aerofoils. They can be packed into a small volume for ease of transportation, and for this reason they have been suggested for use in extraterrestrial exploration (Smith et al., 2000; Landis et al., 2003; Reasor et al., 2012). Their design typically involves some internal support structure which can be tailored in-flight to attain optimal performance in multiple roles with different flight requirements (Lynch and Rogers, 1976; Simpson, 2008). Brown et al. (2001) and Jacob and Smith (2009) provide an overview of the various designs that have been used for inflatable aerofoils. Of particular note is the Goodyear Inflatoplane (Goodyear Aircraft, 1957), which was the first successful example of an inflatable aircraft. Various designs have been considered for the construction of inflatable aerofoils. Of particular relevance to the present study is the inflatable aerofoil by Bain et al. (1963), which is constructed using flexible pressurised panels with an internal support panel to help maintain the aerofoil shape. Murray et al. (2002) considers an aerofoil constructed using a several inflatable cylindrical spars surrounded by open-cell foam with a nylon outer skin. More recently the experimental study of Simpson (2008) considered aerofoils formed by inflating a flexible chamber with internal cables used to maintain the aerofoil structure.

In this chapter we study the deformation of a thin two-dimensional elastic sheet whose ends are joined together to form a corner of prescribed angle, providing a simple model of an inflatable aerofoil. We allow for a straight fixed-length support joining two chosen points on the aerofoil boundary, which constrains the deformation to provide a more realistic aerofoil model. The aerofoil is assumed to maintain a constant altitude with its weight balanced by the lift force due to a circulation which is fixed according to the Kutta condition. We first evaluate the aerofoil deformation in response to an inviscid fluid flow. We present two separate numerical methods used to obtain the deformed equilibrium shapes: we use conformal mapping method based on the Kármán-Trefftz transform for unsupported aerofoils, while an iterative method based on a boundary integral method is required for aerofoils with an internal support. We present a detailed analysis of the numerically computed equilibrium shapes, and uncover a set of distinct solution branches which bifurcate from the smooth cell solutions presented in Chapter 3. We also determine the flow parameters for which the aerofoil can maintain a good aerodynamic shape. We then compute the viscous flow past these aerofoil shapes using a combination of boundary layer calculations and full DNS using the software package Gerris (Popinet, 2003, 2009). This allows us to assess the relevance of the inviscid calculations to a real flow and to determine the aerodynamic viability of the shape by computing the lift-to-drag ratio.

Some of the results presented in this chapter have prepared for publication in Yorkston et al. (2020b).

5.1 Inviscid Formulation

We consider an inflatable aerofoil in a uniform fluid flow, as depicted in Figure 5.1.1. The aerofoil is modelled as a thin two-dimensional elastic cell

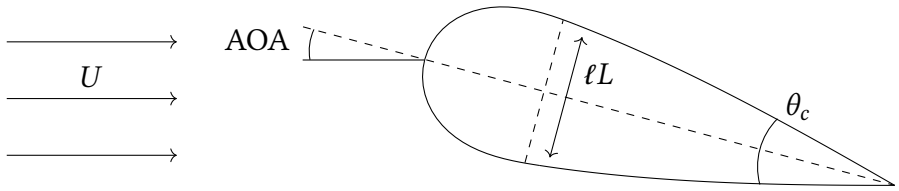

Figure 5.1.1: A sketch of the aerofoil with corner angle θ_c in a uniform stream of speed U. The straight internal support of length $L\ell$, where ℓ is the perimeter of the aerofoil divided by 2π and L is a dimensionless parameter, is shown with a dashed line. The chord of the aerofoil is depicted as a dashed line from the trailing edge to the leading edge, with the angle of attack AOA defined as the angle between the chord and the horizontal.

with a rigid corner of fixed angle θ_c at the trailing edge, where $\theta_c = 0$ corresponds to a cusp and $\theta_c = \pi$ corresponds to a smooth cell. We allow for a straight fixed-length internal support attached to the aerofoil boundary at two chosen points which restricts the deformation of the aerofoil. By adjusting the length and position of the support the extent of the elastic deformation can be controlled, allowing the aerofoil to attain a more aerodynamic shape. The support is attached to the elastic material such that it can pivot freely, and the elastic material is assumed to pass smoothly over the support points as in the design by Bain et al. (1963), which helps maintain a smooth aerofoil shape. In contrast, Simpson (2008) considers an aerofoil consisting of multiple elastic components which can pivot freely at the support point, resulting in a bumpy aerofoil shape; this case is not considered here.

The fluid flow is taken to be a uniform stream of speed U in the far-field, with circulation Γ chosen to satisfy the Kutta condition at the trailing edge. The flow is assumed to be incompressible, irrotational and inviscid; these assumptions allow us to formulate the fluid flow both in terms of a conformal mapping and a boundary integral equation, facilitating the numerical methods used to determine the deformation of the aerofoil in response to the flow. The effects of viscosity, which are important in determining the aerodynamic characteristics of the deformed aerofoils, will be considered in Section 5.4.

The elastic aerofoil problem can be treated as an extension to the smooth elastic cell problem considered in the previous chapters. We base the formulation on the steady system derived in Chapter 2 for the smooth cell, which we modify to account for both the trailing edge corner and the internal support. We nondimensionalise the problem in the same way as before, taking the length scale ℓ to be the perimeter of the aerofoil divided by 2π and the velocity scale to be $\sqrt{E_B/(\ell^3\rho^{(i)})}$, where E_B is the bending modulus of the elastic material and ρ is the fluid density. We denote the dimensionless complex position of the aerofoil boundary as $\eta(s) = x(s) + y(s)\mathrm{i}$, where $0 \leq s \leq 2\pi$ is the arc-length in the anticlockwise direction from the trailing edge corner. We also use the vector notation $\boldsymbol{\eta}(s) = x(s)\boldsymbol{i} + y(s)\boldsymbol{j}$ where convenient. We define the leading-edge of the aerofoil as the point on the curve which maximises the distance $|\eta(s) - \eta(0)|$ from the trailing edge. The chord of the aerofoil is then defined as the line between the leading and trailing edges, with the angle of attack defined as the angle the chord makes to the horizontal, as depicted in Figure 5.1.1.

We assume that the interior of the aerofoil contains a static fluid of equal density to that of the exterior fluid. The density of the elastic material is taken such that the that the weight of the elastic material is balanced by the lift generated by the aerofoil. This is given by the Kutta-Joukowski theorem as $\rho_c = -\frac{\rho^{(e)}U\Gamma}{2\pi gh\ell}$. Under these assumptions, the dynamic condition (2.7.6) which governs the elastic deformation of the aerofoil away from the trailing edge and support points is reduced to

$$\tfrac{1}{2}\left(q^2 - \alpha^2\right) - P - \left(\kappa_{ss} + \tfrac{1}{2}\kappa^3 - \sigma\kappa\right) + \frac{\alpha\beta}{2\pi}\left(\mathrm{Re}(\eta_s) + \kappa\mathrm{Im}(\eta_s)\right) = 0. \qquad (5.1.1)$$

Here $q(s)$ is the flow speed at the aerofoil boundary, $\kappa(s)$ is the curvature of the aerofoil boundary, and $\sigma(s)$ is a piecewise constant function related to the

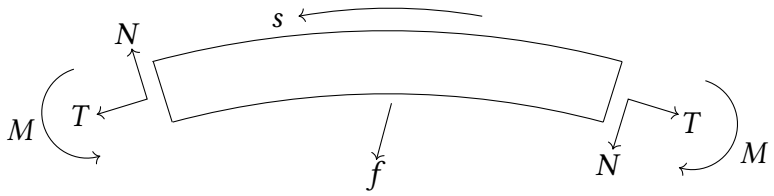

Figure 5.1.2: The internal forces acting on a section of the elastic material centred about the support point $s = S_i$. The internal support exerts a point force of strength f at $s = S_i$.

internal tension of the elastic material which generally takes different values across the support points $s = S_1$ and $s = S_2$, and the dimensionless parameters

$$\alpha = U\sqrt{\frac{\ell^3\rho^{(e)}}{E_B}}, \quad \beta = -\Gamma\sqrt{\frac{\ell\rho^{(e)}}{E_B}}, \quad P = \frac{(p_\infty - p_0)\ell^3}{E_B}$$

correspond to the far-field flow speed, the circulation around the aerofoil, and the pressure difference between the far-field and the interior of the aerofoil respectively. Note that the sign of β has been chosen such that a positive value of β will generate a positive lift acting upon on the aerofoil.

The internal support is assumed to have a uniform tension f and is attached to the aerofoil boundary such that it can pivot freely at two points $0 < S_1 < S_2 < 2\pi$. At $s = S_1$ the support applies a point force $f\hat{\boldsymbol{r}}$ on the aerofoil boundary and at $s = S_2$ it applies a point force $-f\hat{\boldsymbol{r}}$, where $\hat{\boldsymbol{r}}$ is the unit vector defined as

$$\hat{\boldsymbol{r}} = \frac{\boldsymbol{\eta}(S_2) - \boldsymbol{\eta}(S_1)}{|\boldsymbol{\eta}(S_2) - \boldsymbol{\eta}(S_1)|}.$$

The value of f will be determined implicitly to satisfy the constraint

$$\left|\boldsymbol{\eta}(S_2) - \boldsymbol{\eta}(S_1)\right| = L,$$

which fixes the length of the support for a chosen value of the dimensionless parameter L. Figure 5.1.2 depicts the dimensionless internal forces acting on a small segment of the aerofoil centred about the support points $s = S_i$. Here

$T(s)$ and $N(s)$ are the tangential and normal components respectively of the dimensionless internal tension $\boldsymbol{R}(s) = T\hat{\boldsymbol{\tau}} + N\hat{\boldsymbol{n}}$ and $M(s)$ is the elastic bending moment. The values of $T(s)$, $N(s)$ and $M(s)$ are given explicitly by (2.2.12), (2.2.8) and (2.2.6) respectively, which we nondimensionalise to obtain

$$T = \sigma - \tfrac{1}{2}\kappa^2 + \frac{\alpha\beta}{2\pi}y, \quad N = -\kappa_s, \quad M = \kappa^R - \kappa, \tag{5.1.2}$$

where κ^R is the rest curvature of the elastic material which is assumed to be constant. Since the internal support is allowed to pivot freely at the points S_1 and S_2 it exerts no moment on the elastic material; we thus we require the bending moment $M(S)$ to be continuous at the support points $s = S_1$ and $s = S_2$, and so $\kappa(s)$ must also be continuous at these points.

The net force acting upon an infinitesimal segment of the elastic material centred about the support points is given by

$$\left[T\left(S_i^+\right) - T\left(S_i^-\right)\right]\hat{\boldsymbol{\tau}} + \left[N\left(S_i^+\right) - N\left(S_i^-\right)\right]\hat{\boldsymbol{n}} + (-1)^{i+1}f\hat{\boldsymbol{r}}, \quad i = 1, 2.$$

Recalling the explicit expressions for the internal forces (5.1.2), a balance of forces requires the two jump conditions

$$\sigma\left(S_i^+\right) - \sigma\left(S_i^-\right) = (-1)^i f\hat{\boldsymbol{r}} \cdot \hat{\boldsymbol{\tau}}(S_i), \quad i = 1, 2, \tag{5.1.3}$$

$$\kappa_s\left(S_i^+\right) - \kappa_s\left(S_i^-\right) = (-1)^{i+1} f\hat{\boldsymbol{r}} \cdot \hat{\boldsymbol{n}}(S_i), \quad i = 1, 2. \tag{5.1.4}$$

We next consider the internal forces acting at the trailing edge, as shown in Figure 5.1.3. We find that a balance of bending moments about the cusp requires $M(0) = M(2\pi)$ and thus $\kappa(2\pi) = \kappa(0)$. Balancing the internal forces at the trailing edge, we have

$$N(2\pi) = -N(0)\cos\theta_c - T(0)\sin\theta_c, \quad T(2\pi) = -T(0)\cos\theta_c + N(0)\sin\theta_c,$$

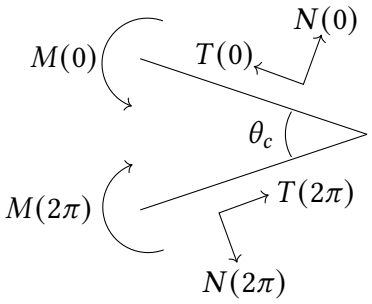

Figure 5.1.3: The internal forces acting on the elastic material at the trailing edge located at $s = 0, 2\pi$.

which gives the two jump conditions

$$\kappa_s(2\pi) = -\kappa_s(0)\cos\theta_c + \left(\sigma(0) - \tfrac{1}{2}\kappa^2(0)\right)\sin\theta_c, \tag{5.1.5}$$

$$\sigma(2\pi) = \tfrac{1}{2}\kappa^2(0) - \left(\sigma(0) - \tfrac{1}{2}\kappa^2(0)\right)\cos\theta_c - \kappa_s(0)\sin\theta_c. \tag{5.1.6}$$

However, we note that unlike the jump conditions given by (5.1.3) and (5.1.4), the force balance at the trailing edge does not need to be satisfied directly; the dynamic condition (5.1.1) ensures that the internal forces of the elastic material are balanced with the external forces acting upon it, and since there is no net external force acting upon the aerofoil the forces at the trailing edge will automatically be balanced.

The inviscid fluid flow past the aerofoil is given in terms of a complex potential $w(z)$, where the complex flow velocity is given by $u(z) = \overline{w_z}(z)$. The complex potential evaluated on the aerofoil boundary is denoted as $\Omega(s) \equiv w\big(\eta(s)\big)$, with the flow speed on the aerofoil boundary given by $q(s) = |\Omega_s|$. The potential must satisfy the kinematic condition

$$\mathrm{Im}(\Omega) = 0, \tag{5.1.7}$$

which ensures there is no flow normal to the impermeable aerofoil boundary,

and the far-field condition

$$w(z) - \alpha z + \frac{\beta}{2\pi \mathrm{i}} \log z \to 0 \quad \text{as} \quad |z| \to \infty, \tag{5.1.8}$$

which ensures that the flow in the far-field is a uniform stream of speed α with circulation β in the anticlockwise direction around the aerofoil. To ensure the flow leaves the aerofoil smoothly at the trailing edge we apply a Kutta condition, which requires a finite flow speed at the trailing edge corner. For a trailing edge corner of angle $\theta_c > 0$ the Kutta condition will result in a stagnation point at the trailing edge, while for a cusp of $\theta_c = 0$ non-zero flow speeds are permissible. The Kutta condition is enforced by requiring the complex potential $\Omega(s)$ to be continuous at the trailing edge, and so

$$\Omega(0) = \Omega(2\pi). \tag{5.1.9}$$

For the smooth cell problem considered in Chapter 3 and Chapter 4 we used a conformal mapping to obtain the fluid flow around the deformed cell in terms of the flow past a unit circle. However, for the aerofoil problem the discontinuities at the trailing edge and the support points cause difficulties in the conformal mapping method. At the trailing edge the boundary curve $\eta(s)$ must have a fixed corner of angle θ_c at which point the mapping cannot be conformal, and at the support points $s = S_1$ and $s = S_2$ the jump condition (5.1.4) requires a discontinuity in the first derivative of the curvature $\kappa_s(s)$ which cannot easily be satisfied using the conformal mapping method. In Section 5.1.1 we will show that the Kármán-Trefftz transform can be used to modify the mapping to allow for a fixed angle corner in the absence of an internal support. However, we find that the conformal mapping cannot easily be modified to deal with the internal support. In Section 5.1.2 we use a boundary integral method to determine the potential flow past the supported

aerofoil and construct an iterative method which can be used to obtain the deformed equilibria for aerofoils which have an internal support.

5.1.1 Conformal Mapping Method

We use a conformal mapping method based on the Kármán-Trefftz transform (von Kármán and Trefftz, 1918)

$$z(\chi) = Ap\frac{(\chi+1)^p + (\chi-1)^p}{(\chi+1)^p - (\chi-1)^p} + B, \quad p = 2 - \frac{\theta_c}{\pi}, \tag{5.1.10}$$

which maps a circle in the χ-plane to an aerofoil-like shape with a corner of angle θ_c at the trailing edge in the z-plane The circle in the χ-plane must intercept the point $\chi = 1$ and contain the point $\chi = -1$, with the radius and centre of the circle determining the shape of the aerofoil in the z-plane. This mapping is conformal everywhere except at the points $\chi = \pm 1$, with the point $\chi = 1$ mapped to the trailing edge corner at $z = Ap + B$ and the point $\chi = -1$ mapped to the point $z = Ap - B$ in the interior of the aerofoil in the z-plane. In the far-field we have $z - A\chi \to B$ as $|\chi| \to \infty$.

The aerofoil shape given by the Kármán-Trefftz mapping depends on the choice of the parameters A and B as well as the complex position of the centre of the circle in the χ-plane, with the radius determined by the requirement that the circle passes through $\chi = 1$. However, a fully deformable aerofoil shape requires a mapping with infinite degrees of freedom. The Kármán-Trefftz mapping alone is thus insufficient to model a fully deformable aerofoil shape. To attain the required degrees of freedom for a fully deformable aerofoil we replace the circle in the χ-plane with an arbitrary smooth closed curve which passes through the point $\chi = 1$ and contains the point $\chi = -1$. The mapped shape in the z-plane will have a corner of angle θ_c at $z = Ap - B$, and by altering the shape of the smooth curve in the preimage χ-plane the aerofoil shape in the

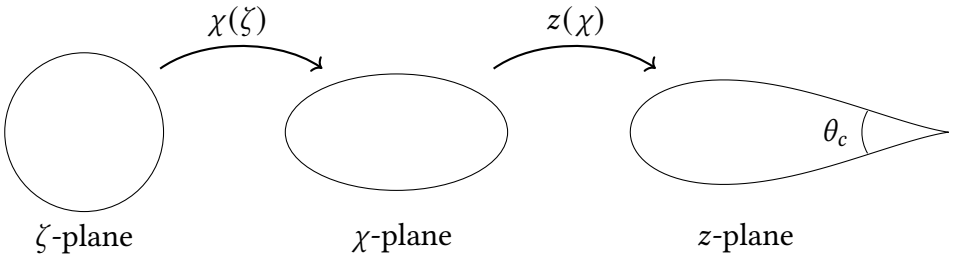

Figure 5.1.4: Sketch of the composite mapping defined by (5.1.12).

z-plane can be deformed with infinite degrees of freedom.

To obtain the potential flow in the preimage χ-plane, we make use of a second conformal mapping

$$\chi(\zeta) = a_{-1}\zeta + a_0 + \sum_{n=1}^{\infty} a_n \zeta^{-n}, \tag{5.1.11}$$

which maps the unit circle in the ζ-plane $\zeta = e^{\mathrm{i}\phi}$ to an arbitrary smooth closed curve in the χ-plane. The coefficients a_n are freely chosen with the constraint that the curve $\chi(e^{\mathrm{i}\phi})$ must pass through the point $\chi = 1$.

We combine the conformal mappings given by (5.1.10) and (5.1.11) to obtain the composite mapping

$$z(\zeta) = Ap\left(\frac{\big(\chi(\zeta)+1\big)^p + \big(\chi(\zeta)-1\big)^p}{\big(\chi(\zeta)+1\big)^p - \big(\chi(\zeta)-1\big)^p} - 1\right), \quad p = 2 - \frac{\theta_c}{\pi}, \tag{5.1.12}$$

where the parameter B in (5.1.10) has been chosen such that the trailing edge corner is located at $z = 0$, and $z - a_{-1}A\zeta \to A(a_0 - p)$ as $|\zeta| \to \infty$. A sketch of this mapping shown in Figure 5.1.4. The aerofoil boundary is given by $\eta(\phi) = z\big(e^{\mathrm{i}\phi}\big)$, with the parameter A chosen such that the boundary curve $\eta(\phi)$ has perimeter 2π. The complex potential is then given in the ζ-plane as

$$w(\zeta) = \alpha a_{-1} A\left(\zeta + \frac{1}{\zeta}\right) - \frac{\beta}{2\pi\mathrm{i}} \log\zeta, \tag{5.1.13}$$

which satisfies both the kinematic condition at the aerofoil boundary (5.1.7) and

the far-field condition (5.1.8). The Kutta condition (5.1.9) must be satisfied by choosing the circulation β such that the stagnation point occurs at the trailing edge.

While the mapping (5.1.12) is capable of mapping to aerofoils whose curvature remains finite as the corner at $s = 0$ is approached, for a general choice of the mapping coefficients a_n the curvature $\kappa(s)$ will have singularities as $s \to 0$ and $s \to \pi$. Since mapping function $\chi(\zeta)$ is conformal on the curve $\zeta = e^{\mathrm{i}\phi}$, we can take a Taylor series of the function $\chi\big(e^{\mathrm{i}\phi}\big)$ about the point ϕ_0, where the point $\zeta = e^{\mathrm{i}\phi_0}$ maps to the trailing edge in the z-plane. We thus have

$$\chi(e^{\mathrm{i}\phi}) = 1 + b_1(\phi - \phi_0) + \frac{b_2}{2}(\phi - \phi_0)^2 + O\big((\phi - \phi_0)^3\big),$$

where the coefficients are given by

$$b_1 = \mathrm{i}a_{-1}e^{\mathrm{i}\phi_0} - \sum_{n=0}^{\infty} \mathrm{i}na_n e^{-n\mathrm{i}\phi_0}, \quad b_2 = -a_{-1}e^{\mathrm{i}\phi_0} - \sum_{n=0}^{\infty} n^2 a_n e^{-n\mathrm{i}\phi_0}.$$

Substituting into (5.1.12) we obtain

$$\begin{aligned}\eta(\phi) =& 2^{1-p}Ap\big(b_1(\phi - \phi_0)\big)^p + \frac{Ap^2}{b_1^2 2^p}\big(b_2 - b_1^2\big)\big(b_1(\phi - \phi_0)\big)^{p+1} \\ &+ 2^{1-2p}Ap\big(b_1(\phi - \phi_0)\big)^{2p} + O\big((\phi - \phi_0)^{p+2}\big),\end{aligned}$$

where the trailing edge corner is located at $\eta(\phi_0) = 0$. The curvature near the trailing edge is then given by

$$\kappa = -\frac{2^{p-2}(p+1)\mathrm{Im}\Big(\overline{b}_1\big(b_2 - b_1^2\big)\Big)}{n|b_1|^3|b_1(\phi - \phi_0)|^{p-1}} - \frac{\mathrm{Im}\big(b_1(b_1(\phi - \phi_0))^{p-1}\big)}{|b_1||b_1(\phi - \phi_0)|^{p-1}} + o(1).$$

For $p \neq 1$ the curvature will have a singularity of $O\big((\phi - \phi_0)^{1-p}\big)$, which must be removed by setting $\mathrm{Im}\big(\overline{b}_1\big(b_2 - b_1^2\big)\big) = 0$. The curvature at the trailing edge

is thus given by

$$\kappa \to -\frac{\mathrm{Im}\big(b_1(b_1(\phi-\phi_0))^{p-1}\big)}{|b_1||b_1(\phi-\phi_0)|^{p-1}} \quad \text{as} \quad \phi \to \phi_0.$$

This limit is generally different depending on whether ϕ approaches ϕ_0 from above or below. For the case where $\theta_c = 0$, corresponding a cusp at the trailing edge, the curvature at the trailing edge is reduced to

$$\kappa\big(\phi_0^+\big) = -\frac{\mathrm{Im}\big(b_1^2\big)}{|b_1|^2} = -\kappa\big(\phi_0^-\big).$$

Recalling that a balance of moments requires the curvature κ to be continuous at the trailing edge, (5.1.12) is thus only capable of mapping to aerofoils with a cusp if the curvature is zero at the trailing edge. Since in general the curvature is non-zero at the trailing edge, this method is therefore only valid for $\theta_c > 0$.

For $\theta_c > 0$ we find that κ_{ss} will in general have a singularity of $O\big((\phi-\phi_0)^{1-3p}\big)$ at $\phi = \phi_0$, which results in a singularity of the same order in the dynamic condition (5.1.1). We deal with this singularity numerically by multiplying (5.1.1) by $\sin(\phi/2)^{3p-1}$ and solving the resulting equation. Since $\sin(\phi/2) > 0$ for $0 < \phi < 2\pi$, a solution of this modified equation must also be a solution of (5.1.1), but at ϕ_0 the singularity is removed. To solve the modified dynamic condition numerically we truncate the mapping coefficients a_n in (5.1.11) after some N terms, setting $a_n = 0$ for $n > N$, and sample the modified dynamic condition at $N + 2$ evenly spaced values of ϕ. This can then be solved numerically using Newton's method to obtain values of the $N + 2$ mapping coefficients a_n for $-1 \le n \le N$. We thus obtain the equilibrium aerofoil shape $\eta(\phi)$ along with the complex potential $w(\zeta)$ for the flow past the deformed aerofoil in terms of the mapping $z(\eta)$ given by (5.1.12).

It is important to note that this method is only valid for an aerofoil without an internal support structure. The conformal mapping (5.1.12) maps

to an aerofoil shape $\eta(\phi)$ which is smooth everywhere but at the trailing edge, and is therefore incapable of satisfying the jump condition (5.1.4). The deformation of the supported aerofoils must instead be obtained using an alternative method.

5.1.2 Iterative Boundary Integral Method

To obtain the deformed equilibrium shapes for aerofoils with an internal support we use an iterative method based on the boundary integral method. The aim of the numerical method is to obtain the aerofoil shape $\eta(s)$ along with the potential flow past the aerofoil which satisfy the dynamic condition (5.1.1), the jump conditions (5.1.3) and (5.1.4), the kinematic condition (5.1.7), the far-field condition (5.1.8), and the Kutta condition (5.1.9). We obtain solutions numerically using an iterative method, first computing the aerofoil shape $\eta(s)$ which satisfies (5.1.1)–(5.1.4) for a chosen flow speed $q(s)$ at the aerofoil boundary, and then finding the fluid potential $w(z)$ which satisfies (5.1.7)–(5.1.9) for the computed value of $\boldsymbol{\eta}(s)$. We then use Newton's method to choose the value of $q(s)$ which satisfies $q(s) = \left|w_z\big(\eta(s)\big)\right|$.

To obtain the aerofoil shape for a chosen flow speed $q(s)$ at the aerofoil boundary we first recall the Frenet-Serret equations $\hat{\tau}_s = \kappa\hat{n}$ and $\hat{n}_s = -\kappa\hat{\tau}$, where $\hat{\tau}(s)$ and $\hat{n}(s)$ are the unit tangent and normal vectors in complex form respectively. Since $\hat{n}$ is normal to $\hat{\tau}$ we have $\hat{n} = -\mathrm{i}\hat{\tau}$, and so $\hat{\tau}_s = -\mathrm{i}\kappa\hat{\tau}$. Denoting the tangent vector in complex form as

$$\hat{\tau} = -e^{\mathrm{i}\theta(s)}, \tag{5.1.14}$$

where $\theta(s)$ is the angle between the tangent vector and the negative horizontal, we have $-\mathrm{i}\kappa\hat{\tau} = \hat{\tau}_s = \mathrm{i}\theta_s\hat{\tau}$, and so $\theta_s = -\kappa$. These expressions allow us to reduce

the dynamic condition (5.1.1) to an explicit system of six first order ODEs

$$\frac{\mathrm{d}}{\mathrm{d}s}\begin{pmatrix} x(s) \\ y(s) \\ \theta(s) \\ \kappa(s) \\ K(s) \\ \sigma(s) \end{pmatrix} = \begin{pmatrix} -\cos\theta \\ -\sin\theta \\ -\kappa \\ K \\ -\frac{1}{2}\kappa^3 + \sigma\kappa - P + \frac{1}{2}\left(q^2 - \alpha^2\right) + \frac{\alpha\beta}{2\pi}(\kappa y - \cos\theta) \\ 0 \end{pmatrix}, \tag{5.1.15}$$

where $K \equiv \kappa_s$, σ is piecewise constant, and the variables can be discontinuous at the points $s = S_1$ and $s = S_2$. To ensure the aerofoil is closed at the trailing edge with angle θ_c, we require

$$x(0) = x(2\pi) = y(0) = y(2\pi) = 0, \quad \theta(2\pi) - \theta(0) = 2\pi - \theta_c. \tag{5.1.16}$$

The value of $\theta(0)$ can be freely chosen to determine the angle of attack of the aerofoil, which will indirectly determine the parameter β via the Kutta condition. At the support points $s = S_i$ we require continuity conditions

$$x\left(S_i^+\right) - x\left(S_i^-\right) = y\left(S_i^+\right) - y\left(S_i^-\right) = \theta\left(S_i^+\right) - \theta\left(S_i^-\right) = \kappa\left(S_i^+\right) - \kappa\left(S_i^-\right) = 0, \tag{5.1.17}$$

along with the jump conditions

$$\sigma\left(S_i^+\right) - \sigma\left(S_i^-\right) = (-1)^i f\hat{\boldsymbol{r}} \cdot \hat{\boldsymbol{\tau}}(S_i), \tag{5.1.18}$$

$$\kappa_s\left(S_i^+\right) - \kappa_s\left(S_i^-\right) = (-1)^{i+1} f\hat{\boldsymbol{r}} \cdot \hat{\boldsymbol{n}}(S_i), \tag{5.1.19}$$

and the internal support length restriction

$$\left|\eta(S_2) - \eta(S_1)\right| = L, \tag{5.1.20}$$

where L is the length of the support. We have five trailing edge conditions, four continuity conditions on each of the two support points, two jump conditions on each of the support points, and the internal support length restriction, giving 18 total conditions to be satisfied. The unknowns are the six variables x, y, θ, κ, K and σ, which are treated as separate continuous variables on each of the three sections of the aerofoil boundary, as well as the unknown support force f for a total of 18 unknowns. The system can then be integrated numerically for a known flow speed $q(s)$ using a Runge-Kutta method to obtain the equilibrium aerofoil shape $\boldsymbol{\eta}(s) = x(s)\boldsymbol{i} + y(s)\boldsymbol{j}$.

Since the aerofoil boundary is not smooth at the support points S_i, the flow speed $q(s)$ cannot in general be assumed to be smooth at these points. We approximate the flow speed as a piecewise Chebyshev series

$$q(s) \approx q_c(s) \equiv \begin{cases} \sum_{n=0}^{N} a_n T_n\left(2\frac{s}{S_1} - 1\right) & \text{for } 0 \le s < S_1, \\ \sum_{n=0}^{N} b_n T_n\left(2\frac{s-S_1}{S_2-S_1} - 1\right) & \text{for } S_1 \le s \le S_2, \\ \sum_{n=0}^{N} c_n T_n\left(2\frac{s-S_2}{2\pi-S_2} - 1\right) & \text{for } S_2 < s \le 2\pi, \end{cases} \tag{5.1.21}$$

where $T_n(s) = \cos\left(n\cos^{-1}(s)\right)$ is the degree n Chebyshev polynomial, N is some truncation value, and the $3N + 3$ coefficients a_n, b_n and c_n are to be found. To ensure $q_c(s)$ is continuous at S_1 and S_2 we take

$$a_0 = b_0 + \sum_{n=1}^{N} b_n \cos\left(\frac{n\pi}{2}\right) - a_n, \quad c_0 = b_0 + \sum_{n=1}^{N} b_n - c_n \cos\left(\frac{n\pi}{2}\right). \tag{5.1.22}$$

The $3N + 1$ remaining coefficients will be found by enforcing the interpolation condition $q_c(s_i) = q(s_i)$ at the $3N + 1$ sample points

$$s_i = \tfrac{1}{2}(1+C_i)S_1, \quad s_{i+N} = \tfrac{1}{2}(1-C_i)S_1 + \tfrac{1}{2}(1+C_i)S_2, \quad s_{i+2N} = \tfrac{1}{2}(1-C_i)S_2 + (1+C_i)\pi \tag{5.1.23}$$

for $i = 1, \ldots, N+1$, where C_i are the Chebyshev nodes

$$C_i = -\cos\left(\frac{(i-1)\pi}{N}\right) \tag{5.1.24}$$

which correspond to the extrema of the Nth Chebyshev polynomial $T_N(s)$. By choosing coefficients a_n, b_n and c_n such that $q_c(s_i) = q(s_i)$ on the rescaled Chebyshev nodes s_i, the Chebyshev series $q_c(s)$ provides a near-best interpolation of the function $q(s)$ (Battles and Trefethen, 2004).

Having obtained an aerofoil shape $\eta(s)$ which satisfies the dynamic condition (5.1.1) for a chosen flow speed $q_c(s)$, we seek to obtain the potential flow past this shape which satisfies the flow conditions (5.1.7)–(5.1.9); this can be achieved using a boundary integral method. Following Pozrikidis (2002b), we decompose the velocity potential $\phi(z) = \mathrm{Re}\big(w(z)\big)$ into two components: the far-field potential $\phi^\infty = \alpha\mathrm{Re}(z) - \frac{\beta}{2\pi}\mathrm{Im}\big(\log(z - z_0)\big)$ which satisfies the far-field condition (5.1.8), where z_0 is a point in the interior of the aerofoil, and an unknown disturbance potential $\phi^D(z)$ which remains bounded in the far-field. The flow velocity is then given in vector form as $\boldsymbol{u} = \nabla\phi = \boldsymbol{u}^\infty + \nabla\phi^D$, where

$$\mathbf{u}^\infty = \alpha\boldsymbol{i} - \frac{\beta}{2\pi}\left[\mathrm{Im}\left(\frac{1}{z - z_0}\right)\boldsymbol{i} + \mathrm{Re}\left(\frac{1}{z - z_0}\right)\boldsymbol{j}\right] \tag{5.1.25}$$

is the flow velocity due to the far-field potential.

The disturbance potential ϕ^D must satisfy the boundary integral equation

$$\begin{aligned}\tfrac{1}{2}\phi^D(z^*) = &-\int_{\eta(s)} G(z, z^*)\big[\hat{\boldsymbol{n}}(z)\cdot\nabla\phi^D(z)\big]\mathrm{d}s(z) \\ &+ \int_{\eta(s)}^{PV} \phi^D(z)[\hat{\boldsymbol{n}}(z)\cdot\nabla G(z, z^*)]\mathrm{d}s(z)\end{aligned} \tag{5.1.26}$$

(Pozrikidis, 2002b), where $\hat{\boldsymbol{n}}$ is the outwards normal vector of the aerofoil boundary, z^* is a point on the aerofoil boundary, $G(z, z^*)$ is the free-space

Green's function

$$G(z, z^*) = -\frac{1}{2\pi}\log|z - z^*|,$$

where

$$\nabla G(z, z^*) = -\frac{1}{2\pi}\frac{(x - x^*)\boldsymbol{i} + (y - y^*)\boldsymbol{j}}{|z - z^*|^2},$$

and the Cauchy principal value (PV) is taken of the second integral in (5.1.26) across the singularity at $z = z^*$. To solve the boundary integral equation (5.1.26) numerically, we discretise the aerofoil boundary as $3N$ straight lines

$$E_i = \eta_i + (\eta_{i+1} - \eta_i)t \quad \text{for} \quad 0 \le t \le 1, \quad i = 1, \ldots, 3N \tag{5.1.27}$$

between the $3N+1$ sample points $\eta_i = \eta(s_i)$ given by (5.1.23). The unit outwards normal vector to the boundary element E_i is constant on each boundary element and is given by

$$\hat{\boldsymbol{n}}_i = \frac{(y_{i+1} - y_i)\boldsymbol{i} - (x_{i+1} - x_i)\boldsymbol{j}}{|\eta_{i+1} - \eta_i|}.$$

We approximate ϕ^D and $\nabla\phi^D$ as constants ϕ_i^D and $(\nabla\phi^D)_i$ on each boundary element, which are assumed to be equal to the values of ϕ^D and $\nabla\phi^D$ at the midpoints $\boldsymbol{\eta}_i^M = \frac{1}{2}(\boldsymbol{\eta}_{i+1} + \boldsymbol{\eta}_i)$. Evaluating the kinematic condition (5.1.7) on the ith boundary element, we obtain

$$\hat{\boldsymbol{n}}_i \cdot \left(\nabla\phi^D\right)_i = -\hat{\boldsymbol{n}}_i \cdot \mathbf{u}^\infty\left(\eta_i^M\right) = -\alpha\mathrm{Re}(\hat{n}_i) + \frac{\beta}{2\pi}\mathrm{Im}\left(\frac{\hat{n}_i}{\eta_i^M - z_0}\right).$$

The boundary integral equation (5.1.26) is then discretised as

$$\begin{aligned}\tfrac{1}{2}\phi^D(z^*) = \alpha\sum_{i=1}^{3N}\mathrm{Re}(\hat{n}_i)\int_{E_i}G(z, z_0)\mathrm{d}s - \frac{\beta}{2\pi}\sum_{i=1}^{3N}\mathrm{Im}\left(\frac{\hat{n}_i}{\eta_i^M - z_0}\right)\int_{E_i}G(z, z^*)\mathrm{d}s \\ + \sum_{i=1}^{3N}\phi_i^D\int_{E_i}^{PV}\hat{\boldsymbol{n}}_i \cdot \nabla G(z, z^*)\mathrm{d}s,\end{aligned} \tag{5.1.28}$$

where the integrals are taken along the boundary elements. Evaluating (5.1.28) at the boundary element midpoints $z^* = \eta_j^M$ for $j = 1, \ldots, 3N$, we obtain the $3N$ equations

$$\frac{1}{2}\phi_j^D - \sum_{i=1}^{3N} \phi_i^D \int_{E_i}^{PV} \hat{\boldsymbol{n}}_i(z) \cdot \nabla G\left(z, \eta_j^M\right) \mathrm{d}s + \frac{\beta}{2\pi} \sum_{i=1}^{3N} \mathrm{Im}\left(\frac{\hat{n}_i}{\eta_i^M - z_0}\right) \int_{E_i} G\left(z, \eta_j^M\right) \mathrm{d}s = \alpha \sum_{i=1}^{3N} \mathrm{Re}(n_i) \int_{E_i} G\left(z, \eta_j^M\right) \mathrm{d}s, \tag{5.1.29}$$

which depend linearly on the unknowns ϕ_i^D and β.

The integrals in (5.1.29) can be evaluated explicitly along the boundary elements $z = E_i$. Recalling that

$$\nabla G\left(z, \eta_j^M\right) = -\frac{1}{2\pi} \frac{\left(x - x_j^M\right)\boldsymbol{i} + \left(y - y_j^M\right)\boldsymbol{j}}{\left|z - \eta_j^M\right|^2}$$

and

$$\hat{\boldsymbol{n}}_i = \frac{(y_{i+1} - y_i)\boldsymbol{i} - (x_{i+1} - x_i)\boldsymbol{j}}{|\eta_{i+1} - \eta_i|},$$

we have

$$\hat{\boldsymbol{n}}_i \cdot \nabla G\left(z, \eta_j^M\right) = -\frac{1}{2\pi|\eta_{i+1} - \eta_i|} \mathrm{Im}\left(\frac{\eta_{i+1} - \eta_i}{z - \eta_j^M}\right).$$

Along the ith boundary element we thus have

$$\int_{E_i}^{PV} \hat{\boldsymbol{n}}_i(z) \cdot \nabla G\left(z, \eta_j^M\right) \mathrm{d}s = -\frac{1}{2\pi} \int_0^1 \mathrm{Im}\left(\frac{\eta_{i+1} - \eta_i}{\eta_i - \eta_j^M + (\eta_{i+1} - \eta_i)t}\right) \mathrm{d}t,$$

For $i \neq j$ the integral is well defined, while for $i = j$ the Cauchy principal value

is taken. We thus obtain

$$\int_{E_i}^{PV} \hat{\boldsymbol{n}}_i \cdot \nabla G\big(z, \eta_j^M\big)\mathrm{d}s = \begin{cases} -\dfrac{1}{2\pi}\mathrm{Im}\left(\log\left(\dfrac{\eta_{i+1}-\eta_j^M}{\eta_i-\eta_j^M}\right)\right) & \text{for } i \neq j, \\ 0 & \text{for } i = j. \end{cases} \tag{5.1.30}$$

To evaluate the integral of $G\left(z, \eta_j^M\right)$ we note that on the boundary element E_i we have $G\left(z, \eta_j^M\right) = -\frac{1}{2\pi}\log\left|z-\eta_j^M\right| = \mathrm{Re}\left[\log\left(\eta_i - \eta_j^M + (\eta_{i+1}-\eta_i)t\right)\right]$. The integral is thus given by

$$\int_{E_i} G\left(z, \eta_j^M\right)\mathrm{d}s = -\frac{|\eta_{i+1}-\eta_i|}{2\pi}\int_0^1 \mathrm{Re}\left[\log\left(\eta_i - \eta_j^M + (\eta_{i+1}-\eta_i)t\right)\right]\mathrm{d}t,$$

which can be integrated directly to obtain

$$\begin{aligned} &\int_{E_i} G\left(z, \eta_j^M\right)\mathrm{d}s \\ &= -\frac{|\eta_{i+1}-\eta_i|}{2\pi}\,\mathrm{Re}\left(\frac{\left(\eta_{i+1}-\eta_j^M\right)\log\left(\eta_{i+1}-\eta_j^M\right) - \left(\eta_i-\eta_j^M\right)\log\left(\eta_i-\eta_j^M\right)}{\eta_{i+1}-\eta_i} - 1\right). \end{aligned}$$

Equation (5.1.29) gives a system of $3N$ linear equations for $j = 1, \ldots, 3N$ to be solved for the $3N + 1$ unknowns ϕ_i^D and β. To complete the system we enforce the Kutta condition (5.1.9) at the trailing edge, which can be written in terms of the velocity potential $\phi = \phi^D + \phi^\infty$ as

$$\phi\big(\boldsymbol{\eta}(0)\big) = \phi\big(\boldsymbol{\eta}(2\pi)\big).$$

This condition is satisfied approximately using the finite-difference equation

$$\phi_1^D - \phi_{3N}^D = \phi^\infty\big(\eta_{3N}^M\big) - \phi^\infty\big(\eta_1^M\big). \tag{5.1.31}$$

The linear system given by (5.1.29) and (5.1.31) can be solved numerically to

obtain values for the unknowns ϕ_i and β. The boundary integral approximation of the flow speed at the aerofoil boundary is then given using the central difference formula

$$q(s_i) \approx q_b(s_i) \equiv \frac{|\phi_i - \phi_{i-1}|}{|\boldsymbol{\eta}_i - \boldsymbol{\eta}_{i-1}|}, \quad i = 2, \ldots, 3N, \tag{5.1.32}$$

with $q_b(0) = q_b(2\pi) = 0$.

We thus have two distinct approximations for the flow speed $q(s)$: $q_c(s)$, which is given by (5.1.21) and satisfies the dynamic condition (5.1.1) and the two jump conditions (5.1.3) and (5.1.4), and $q_b(s)$, which is given by (5.1.32) and satisfies the kinematic condition (5.1.7), the far-field condition (5.1.8), and the Kutta condition (5.1.9). To obtain an approximate solution to the full problem we must obtain values of the Chebyshev coefficients a_n, b_n and c_n such that $q_b(s_i) = q_c(s_i)$ for $i = 1, \ldots, 3N + 1$. We use Newton's method to solve this problem numerically, with the truncation value taken to be both $N = 50$ and $N = 100$ and it was confirmed that the variation of the aerofoil shape $\left|\boldsymbol{\eta}_{(N=100)}(s) - \boldsymbol{\eta}_{(N=50)}(s)\right|$ remained below 10^{-6} for all $0 \leq s \leq 2\pi$.

5.2 Unsupported Aerofoil Results

We start by analysing the deformation of an unsupported aerofoil for both a static fluid and a uniform stream. The results presented in this section were obtained numerically using both the conformal mapping method described in Section 5.1.1 and the iterative boundary integral method described in Section 5.1.2 and it was confirmed that the deformed aerofoil shapes computed by the two methods did not deviate by more than 10^{-6}. Note the conformal mapping technique cannot be used for the case of $\theta_c = 0$; the results for this case are thus obtained solely using the iterative boundary integral method. Similarly, the iterative boundary integral method becomes invalid in the case

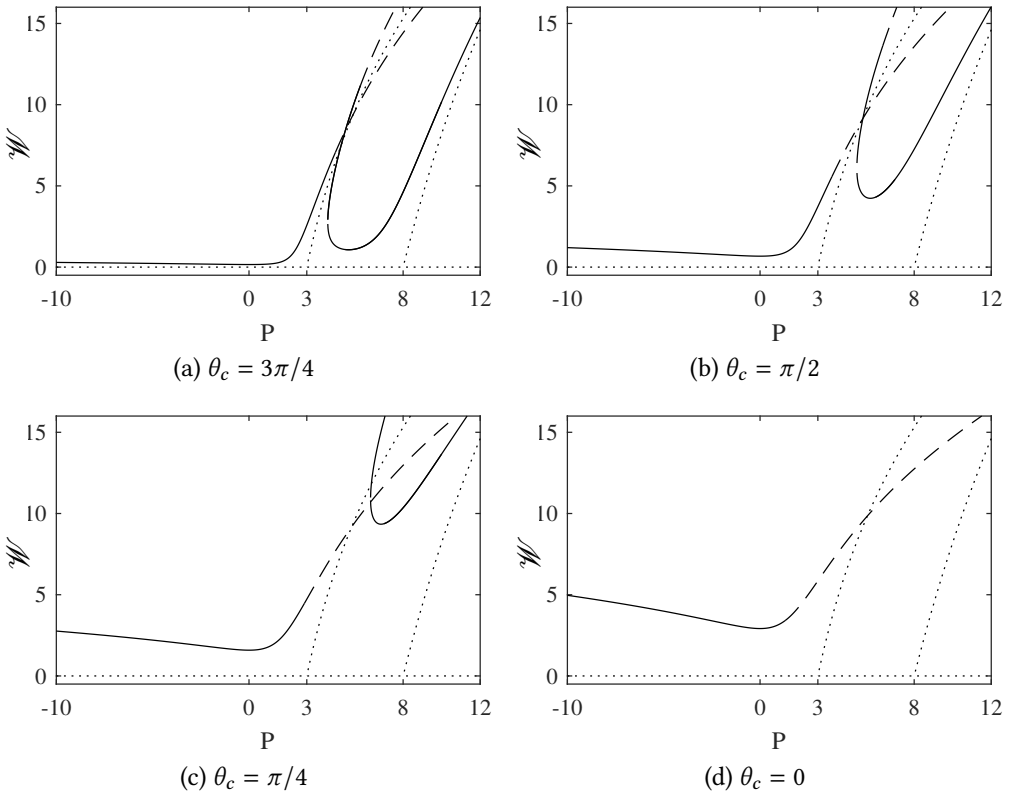

Figure 5.2.1: Bending energy of the unsupported aerofoils in a static fluid. Dashed lines indicate self-intersection. Dotted lines indicate the corresponding smooth $\theta_c = \pi$ solutions.

of self-intersecting aerofoils, which are obtained solely using the conformal mapping method. However, for the static fluid problem the iterative boundary integral method is reduced to solving the system of ODEs (5.1.15), and is thus capable of obtaining self-intersecting aerofoil shapes.

We start by analysing the deformation of an unsupported aerofoil in a static fluid in response to a uniform transmural pressure P. Note that since there is no fluid flow, and thus no lift acting upon the aerofoil, the net force balance requires the elastic material to be weightless. The system thus has a rotational invariance; any equilibrium shape can be freely rotated and remain in equilibrium. In describing the deformation of the aerofoils, we assume that the aerofoil is oriented such that the trailing edge corner points in the positive x direction.

Figure 5.2.1 shows elastic bending energy $\mathscr{W}$ against P for the deformed aerofoil shapes for various values of the corner angle θ_c. The dotted lines in the figure correspond to the solutions obtained in Chapter 3 for a smooth cell with $\theta_c = \pi$; the line at $\mathscr{W} = 0$ corresponds to the circular cell, while the curves bifurcating at $P = 3$ and $P = 8$ correspond to the mode-2 and mode-3 buckled cells respectively. Since the solutions at $\theta_c = \pi$ have a rotational invariance we expect to obtain differing solutions as the corner angle θ_c is reduced from 2π depending on the orientation of the smooth cell. However, we find that solutions only exist for $\theta_c < \pi$ where the aerofoil has a symmetry $\kappa(s) = \kappa(2\pi - s)$ about the trailing edge. The solution branch corresponding to the smooth mode-2 buckled smooth cells thus splits into two distinct branches, corresponding to the two distinct points on the cell where a corner can be introduced while satisfying the symmetry $\kappa(s) = \kappa(2\pi - s)$.

The aerofoil shapes corresponding to the leftmost branch of Figure 5.2.1 are depicted in Figure 5.2.2. These solutions bifurcate at $\theta_c = \pi$ from the unit circle for $P < 3$ and the horizontally aligned mode-2 buckled smooth cell for $P > 3$. As the corner angle is decreased the aerofoil becomes elongated horizontally away from the trailing edge corner, forming a bulbous shape. As the pressure P is increased the deformation becomes more severe, until the aerofoil self-intersects and becomes physically invalid. As P is decreased towards $-\infty$ the aerofoil swells up to a circular shape; however, as seen in Figure 5.2.1 this does not correspond to zero bending energy. As $P \to \infty$ a region of high curvature forms in a small region around the trailing edge, causing an increase in the bending energy.

The aerofoil shapes which occur on the lower right branch of Figure 5.2.1 are depicted in Figure 5.2.3. This branch bifurcates from three distinct solution branches at $\theta_c = \pi$: the vertically aligned mode-2 buckled smooth cell for $P > 3$, the unit circle for $3 < P < 8$, and the top-bottom symmetric mode-3

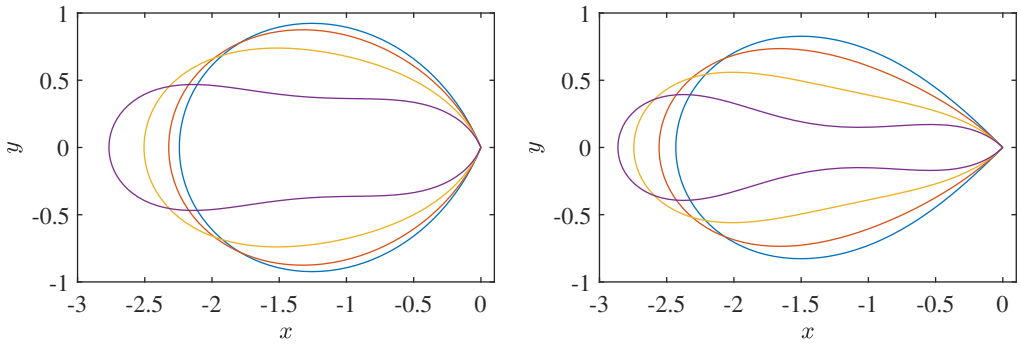

(a) $\theta_c = 3\pi/4$ (b) $\theta_c = \pi/2$

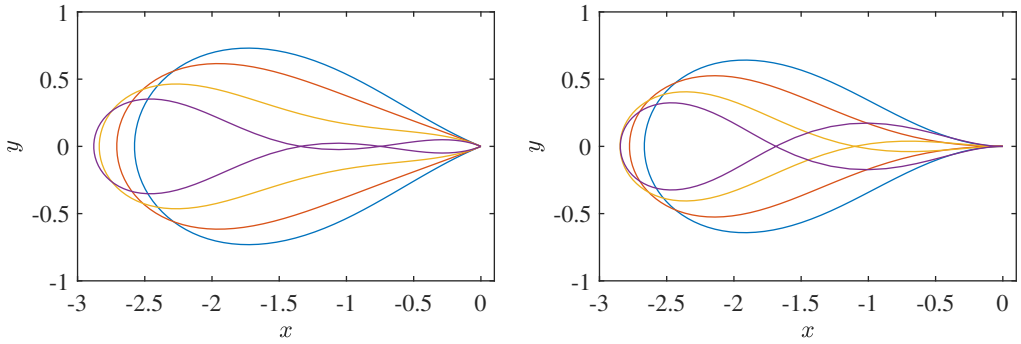

(c) $\theta_c = \pi/4$ (d) $\theta_c = 0$

Figure 5.2.2: Aerofoil shapes for $P = 0$, $P = 2$, $P = 3$ and $P = 4$ corresponding to the leftmost branch in Figure 5.2.1.

buckled smooth cell for $P > 8$. As the corner angle θ_c is decreased from π the left-right symmetry is broken, although the aerofoil still resembles vertically elongated cell. As P is increased the left-right asymmetry becomes more pronounced, and the aerofoil starts to resemble the buckled mode-3 shape. These solutions exist only for P greater than some minimum value; this minimum value of P increases as the corner angle θ_c is decreased. Unlike the leftmost solution branch in Figure 5.2.1, the aerofoils on this branch do not resemble a traditional aerodynamic aerofoil shape.

Figure 5.2.4 shows the solutions which occur on the upper right branch of Figure 5.2.1. This is a continuation of the lower solution branch, and so the solutions again resemble the vertically aligned mode-3 buckled smooth cells. This branch however corresponds to more severely deformed aerofoil shapes, with a higher bending energy than the lower branch.

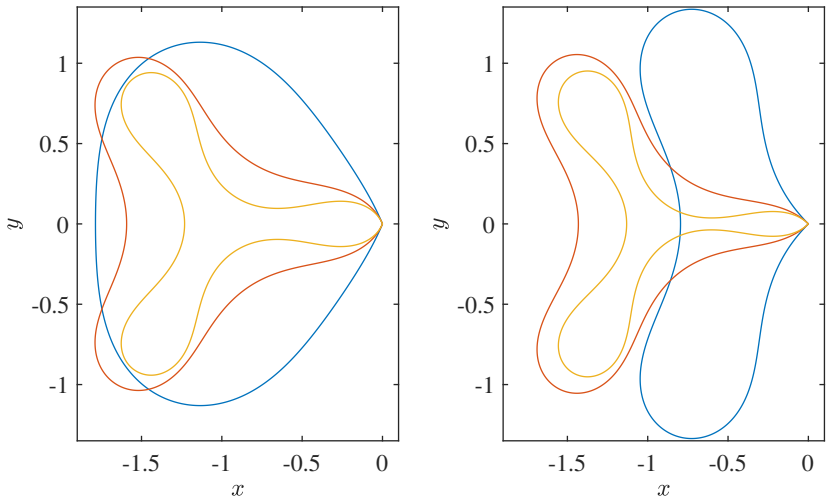

(a) $\theta_c = 3\pi/4$ (b) $\theta_c = \pi/2$

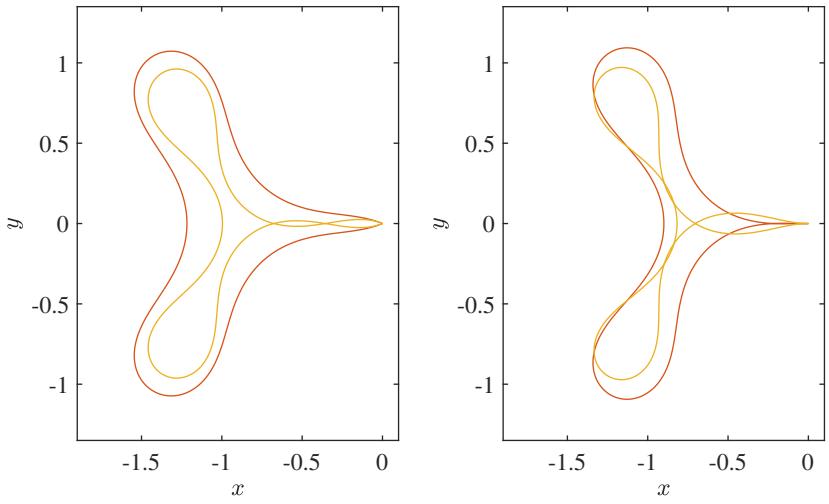

(c) $\theta_c = \pi/4$ (d) $\theta_c = 0$

Figure 5.2.3: Aerofoil shapes for $P = 5$, $P = 10$ and $P = 15$ corresponding to the lower-right branch in Figure 5.2.1.

We next analyse the deformation of an unsupported aerofoil in response to a fluid flow for $\alpha > 0$. The bending energies of the solutions which exist for $-2 \leq P \leq 6$ are shown in Figure 5.2.5 for various values of the far-field flow speed α. The solutions in panel (a) correspond to the static fluid solutions depicted in depicted in Figure 5.2.1c. As the flow speed is increased up to $\alpha = 1.5$, as shown in panel (b), the branch of vertically elongated aerofoils descends in the P-$\mathscr{W}$ plane, with the flow acting to decrease the aerofoil deformation. On the leftmost branch, which corresponds to horizontally elongated aerofoils,

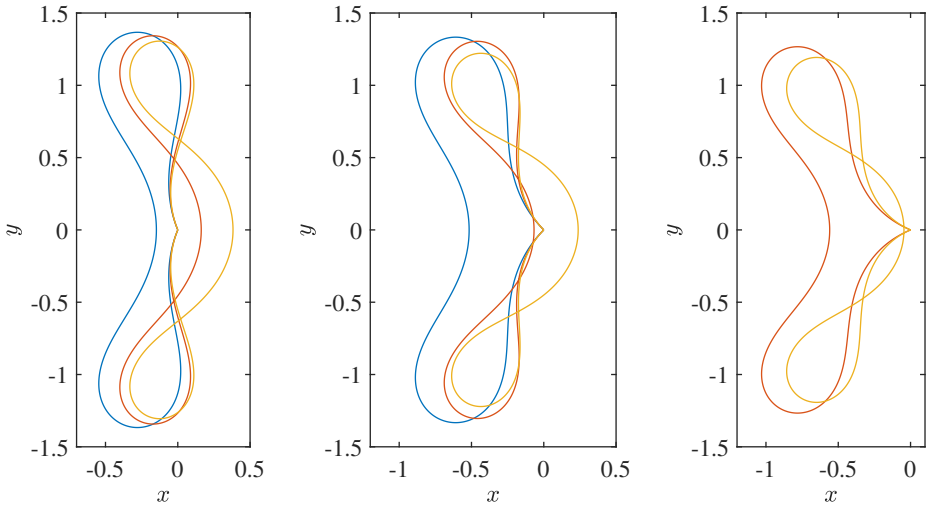

(a) $\theta_c = 3\pi/4$ (b) $\theta_c = \pi/2$ (c) $\theta_c = \pi/4$

Figure 5.2.4: Aerofoil shapes $P = 5.5$, $P = 6.5$ and $P = 7.5$ corresponding to the upper-right branch in Figure 5.2.1.

the fluid flow increases the deformation of the aerofoil, increasing the bending energy. At $\alpha \approx 1.53$ a cusp forms in the leftmost solution branch, from which a loop emerges in the P-$\mathscr{W}$ plane for $\alpha > 1.53$. This loop grows as α is increased until at $\alpha \approx 1.5505$ the loop meets the rightmost solution branch. The solution branches then interchange, with the upper and lower portions of the leftmost branch separating and merging with the upper and lower portions respectively of the right branch, forming two new solution branches. The deformed aerofoil shapes which correspond to these solution branches are presented below.

Figure 5.2.6 depicts the flow past the deformed aerofoils on the lower-left branch of Figure 5.2.5. Note that the values of P shown are chosen such that the solutions remain to the left of the loop in the solution branch. For $\alpha = 1$ the aerofoil takes a bulbous shape. As the pressure P is increased the aerofoil is elongated horizontally, resulting in a more streamlined profile. For $\alpha = 2$ however, the aerofoil deformation is more severe, bulging vertically towards the regions of high flow speed. For $\alpha = 2$ an increase in P increases the severity of the deformation.

Figure 5.2.7 depicts the flow past the deformed aerofoils on the lower-right

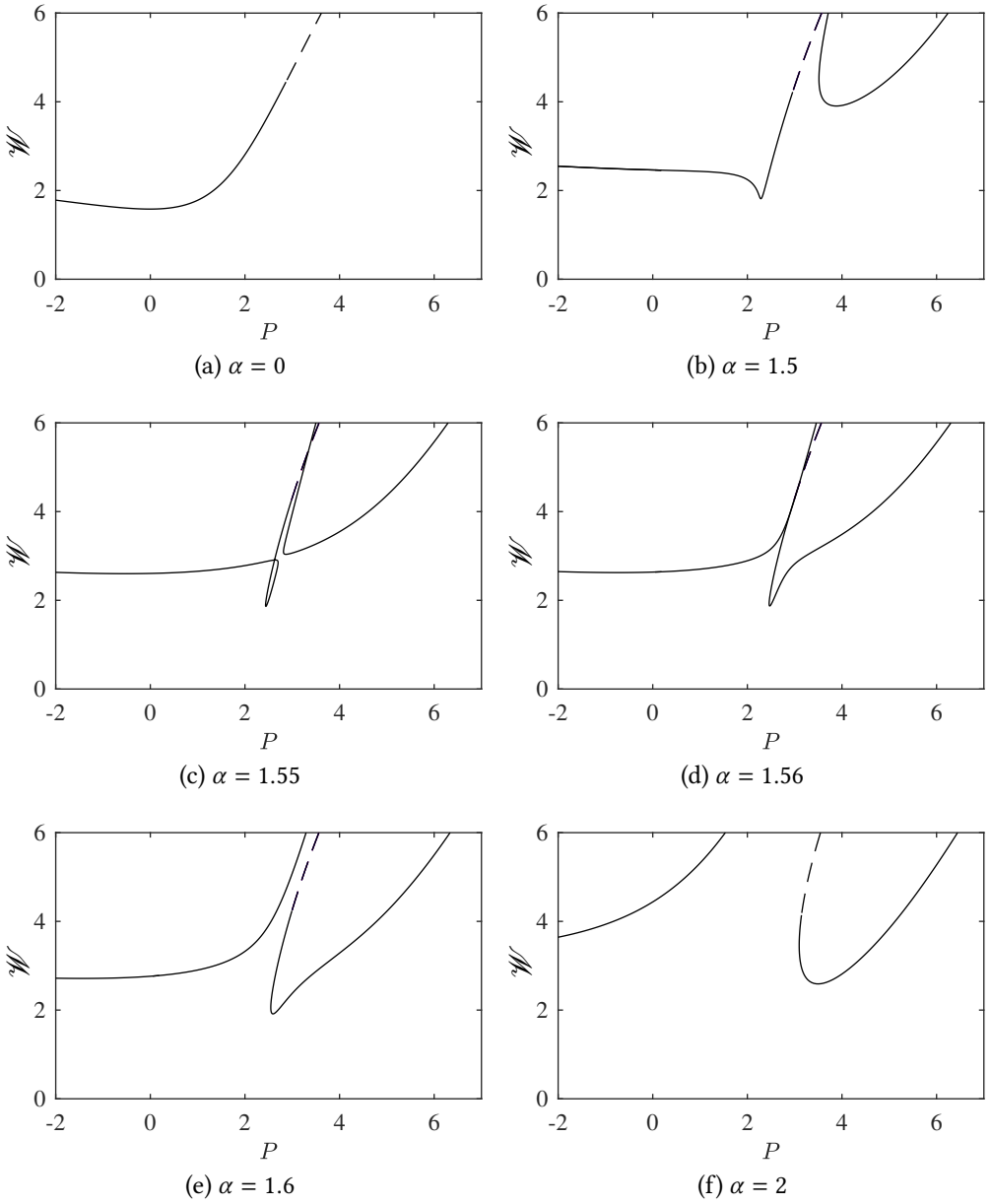

(a) $\alpha = 0$ (b) $\alpha = 1.5$

(c) $\alpha = 1.55$ (d) $\alpha = 1.56$

(e) $\alpha = 1.6$ (f) $\alpha = 2$

Figure 5.2.5: Bending energy of the first two solution branches against P for $\theta_c = \pi/4$ and $\beta = 0$ for various values of α. The dashed line indicates self-intersecting aerofoil shapes.

branch of Figure 5.2.5. These aerofoils are generally more deformed than those shown in Figure 5.2.6, forming a blunt profile while swells perpendicular to the flow. The deformation decreases as the flow speed α is increased, resulting in a thinner although still bulbous aerofoil profile.

Figure 5.2.8 and Figure 5.2.9 depict the flow past the deformed aerofoils with circulation $\beta > 0$ for $P = 2$ and $P = 0$ respectively. First considering the

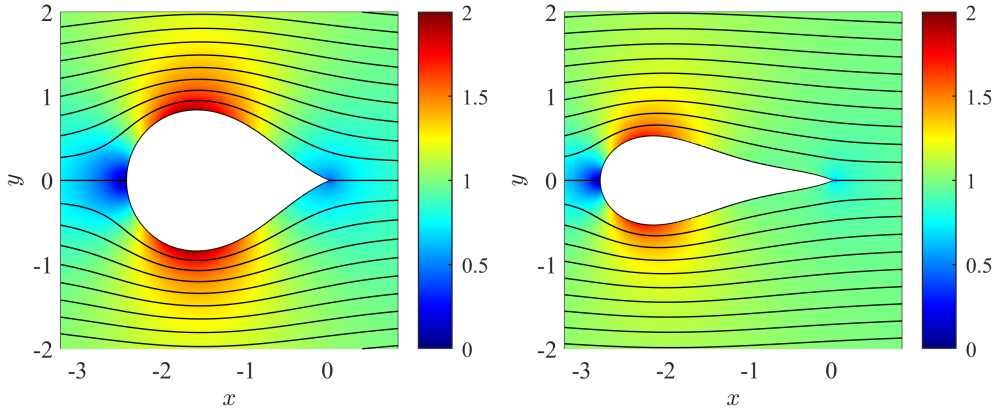

(a) $\alpha = 1$, $P = 0$ (b) $\alpha = 1$, $P = 2$

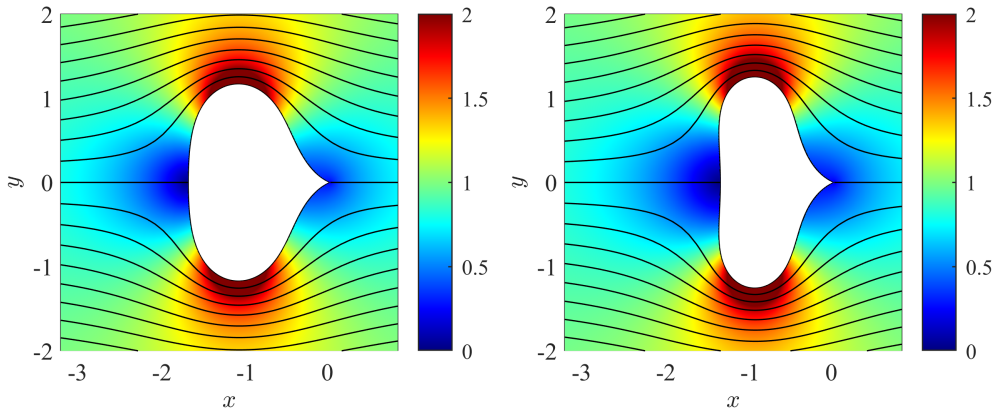

(c) $\alpha = 2$, $P = 0$ (d) $\alpha = 2$, $P = 2$

Figure 5.2.6: Contour plot of the normalised flow speed $|\boldsymbol{u}|/\alpha$ and streamlines for $\beta = 0$ and $\theta_c = \pi/4$ for various values of α and P, corresponding to the solutions on the leftmost solution branch of Figure 5.2.5.

case of $P = 2$, we find that for $\beta = 0$ the aerofoil takes on a fairly aerodynamic shape for both $\alpha = 0.5$ and $\alpha = 1$. As the circulation β is increased the aerofoil deformation differs significantly between the values of α. For $\alpha = 0.5$ the aerofoil twists in the clockwise direction while broadly maintaining its overall shape. Since the flow speed is relatively low, the elastic forces of the elastic material dominate over the fluid forces and the aerofoil acts rigidly in response to the changing flow field. For $\alpha = 1$ however, we find that the aerofoil deformation is move severe; at the trailing edge the aerofoil twists in the clockwise direction as before, but towards the leading edge the aerofoil curves in the negative y direction resulting in a significantly deformed aerofoil

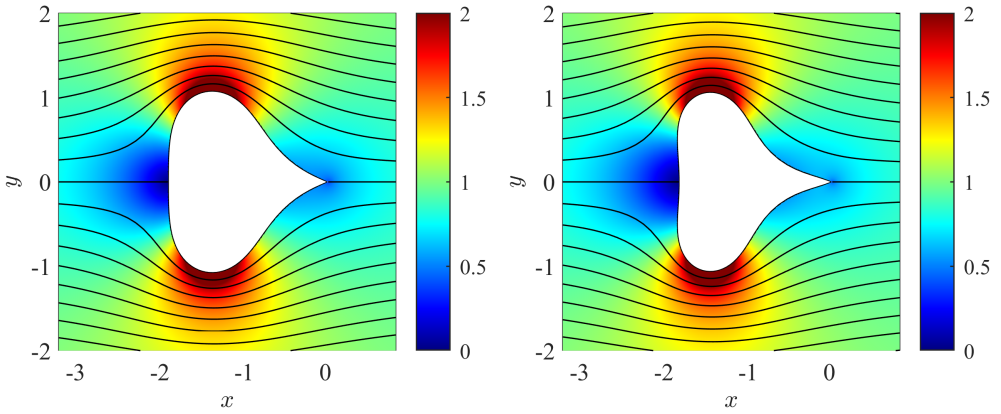

(a) $\alpha = 1.5$, $P = 4$ (b) $\alpha = 1.5$, $P = 6$

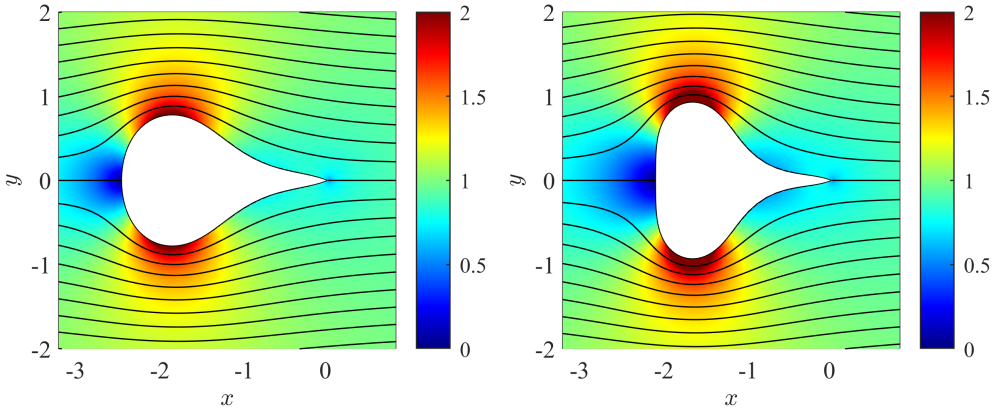

(c) $\alpha = 2$, $P = 4$ (d) $\alpha = 2$, $P = 6$

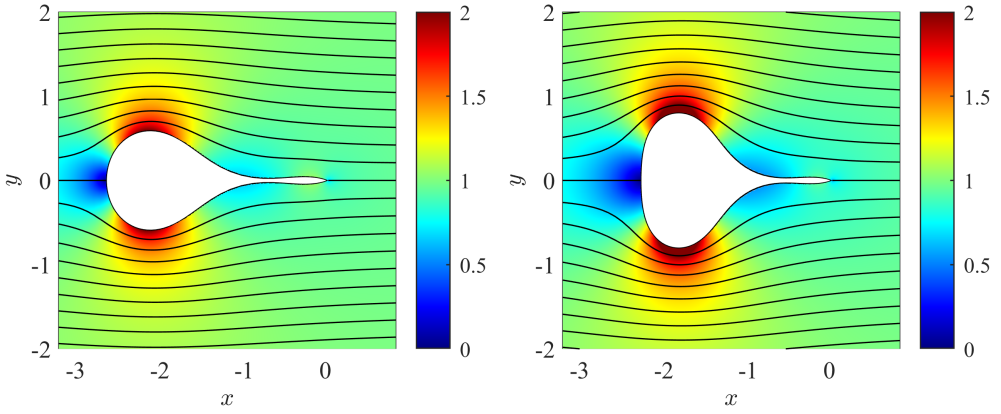

(e) $\alpha = 2.5$, $P = 4$ (f) $\alpha = 2.5$, $P = 6$

Figure 5.2.7: Contour plot of the normalised flow speed $|\boldsymbol{u}|/\alpha$ and streamlines for $\beta = 0$ and $\theta_c = \pi/4$ for various values of α and P, corresponding to the solutions on the lower-right branch of Figure 5.2.5.

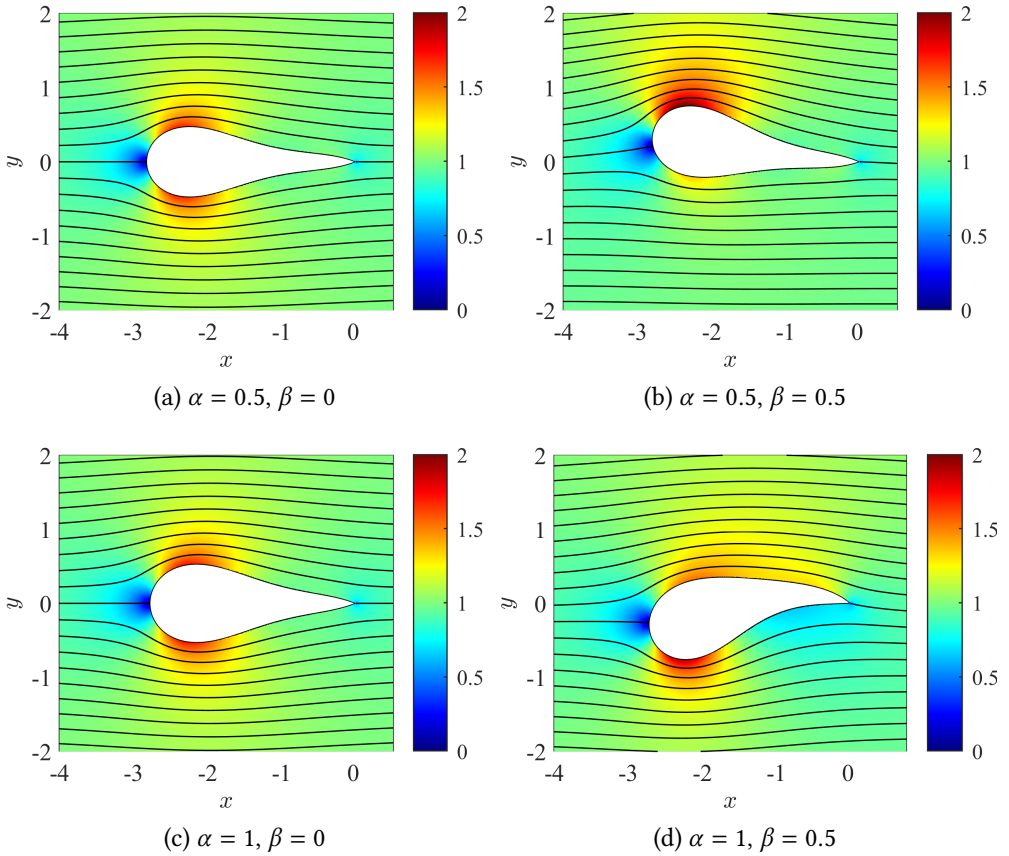

(a) $\alpha = 0.5$, $\beta = 0$

(b) $\alpha = 0.5$, $\beta = 0.5$

(c) $\alpha = 1$, $\beta = 0$

(d) $\alpha = 1$, $\beta = 0.5$

Figure 5.2.8: Contour plot of the normalised flow speed $|\boldsymbol{u}|/\alpha$ and streamlines for $P = 2$ and $\theta_c = \pi/4$ for various values of α and β.

shape. For $P = 0$ the circulation has a similar effect on the aerofoil deformation; for low values of α the circulation causes the aerofoil to twist in the clockwise direction while maintaining its general shape, while for larger values of α a more severe deformation occurs, with significant deformation in the negative y direction.

5.3 Supported Aerofoil Results

We next consider the case of an aerofoil with an internal support. All results in this section were obtained numerically using the iterative boundary integral method presented in Section 5.1.2. To analyse the aerodynamic characteristics

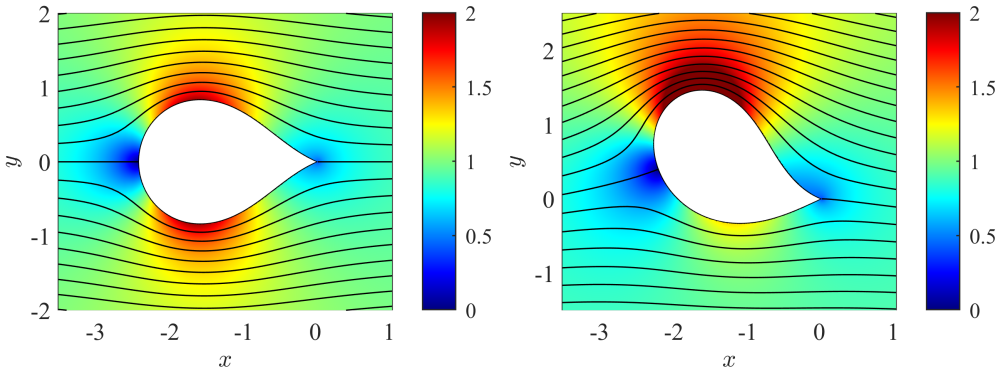

(a) $\alpha = 1$, $\beta = 0$ (b) $\alpha = 1$, $\beta = 3$

(c) $\alpha = 2$, $\beta = 0$ (d) $\alpha = 2$, $\beta = 3$

Figure 5.2.9: Contour plot of the normalised flow speed $|\boldsymbol{u}|/\alpha$ and streamlines for $P = 0$ and $\theta_c = \pi/4$ for various values of α and β.

of the aerofoils we introduce the lift and drag coefficients and the lift-drag ratio

$$C_L = \frac{2\boldsymbol{F}\cdot\boldsymbol{j}}{\rho U^2 \ell}, \quad C_D = \frac{2\boldsymbol{F}\cdot\boldsymbol{i}}{\rho U^2 \ell}, \quad \frac{C_l}{C_d} = \frac{\mathbf{F}\cdot\boldsymbol{j}}{\mathbf{F}\cdot\boldsymbol{i}} \tag{5.3.1}$$

where $\boldsymbol{F}$ is the net fluid force acting upon the aerofoil. For an inviscid flow we have $\boldsymbol{F} = -\rho U\Gamma\boldsymbol{j}$, and so $C_L = -2\Gamma/U\ell = 2\gamma/\alpha$ and $C_D = 0$. Note however that the effects of viscosity are important in determining the aerodynamic properties of the aerofoil and will be considered in detail in Section 5.4.

Figure 5.3.1 shows the deformation of an elastic aerofoil in a static fluid with an internal support of length $L = 0.75$ for varying values of the corner angle θ_c, as well as the corresponding unsupported aerofoil shape for comparison. For $\theta_c = 3\pi/4$ and $\theta_c = \pi/2$ the support restricts the maximum

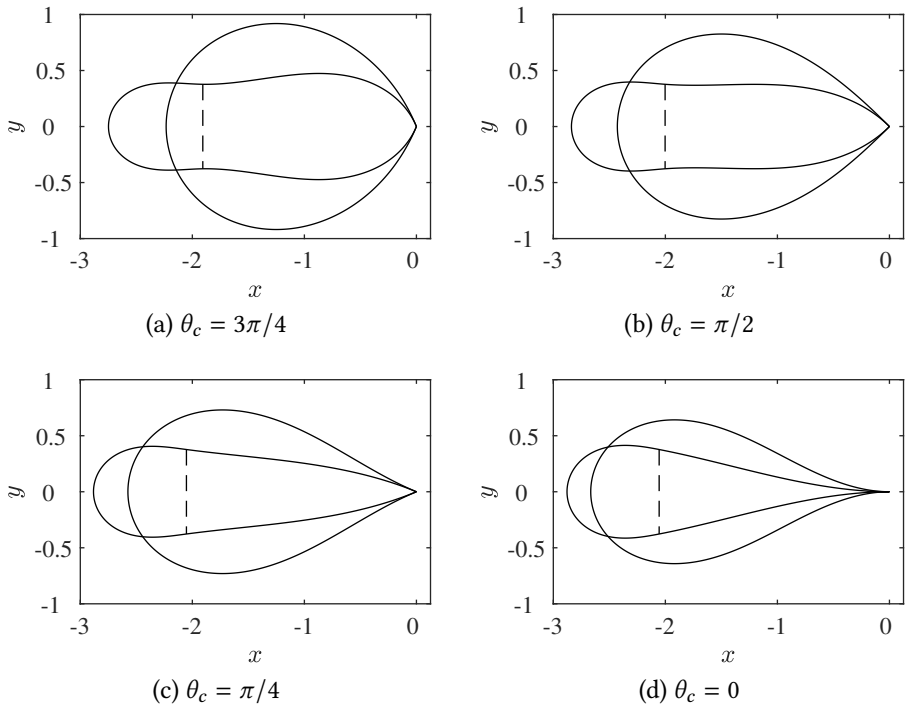

(a) $\theta_c = 3\pi/4$ (b) $\theta_c = \pi/2$

(c) $\theta_c = \pi/4$ (d) $\theta_c = 0$

Figure 5.3.1: Equilibrium shapes in a static fluid with $P = 0$ for varying trailing-edge corner angles θ_c. The supported aerofoil has a support of length $L = 0.75$ attached at $S_1 = 2\pi/3$ and $S_2 = 4\pi/3$, depicted as a broken line.

thickness of the aerofoil, although it bulges outwards either side of the support points and retains a fairly blunt shape. For $\theta_c = \pi/4$ and $\theta_c = 0$ however, a thin aerofoil shape is attained. This supported aerofoil has a much thinner profile than the corresponding unsupported aerofoil, and will therefore have significantly improved aerodynamic properties, as will be discussed in Section 5.4.

Figure 5.3.2 depicts the flow past the supported aerofoil as the flow speed parameter α is increased with a fixed angle of attack of 12 degrees. Recall that the angle of attack is defined as the angle the chord of the aerofoil makes to the horizontal, with the chord defined as the line between the trailing edge corner and the point furthest from the trailing edge. The angle of attack of 12 degrees is towards the upper limit of a typical aerofoil, and was chosen to show the most severe deformation; for lower angles of attack we found the aerofoil exhibits a similar but less severe deformation. The corner angle and the length and

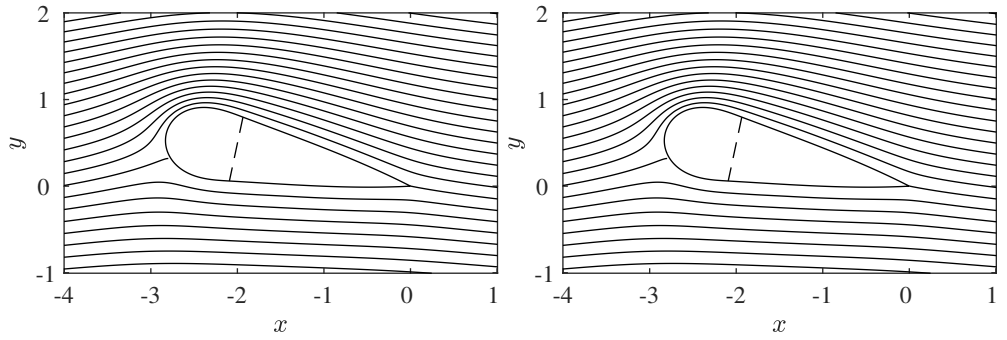

(a) $\alpha = 0$, $C_L = 4.59$ (b) $\alpha = 1/3$, $C_L = 4.21$

(c) $\alpha = 2/3$, $C_L = 2.89$ (d) $\alpha = 1$, $C_L = 0.19$

Figure 5.3.2: Aerofoil shapes and streamlines for an angle of attack of 12 degrees, a corner angle of $\theta_c = \pi/6$ and a pressure difference of $P = 0$. The internal support is depicted as a broken line of length $L = 0.75$ attached at the points $S_1 = 2\pi/3$ and $S_2 = 4\pi/3$. The streamlines are evenly spaced in the far-field, corresponding to evenly space values of the stream function in each panel, although the spacing of the stream function varies between panels as the far-field flow speed α is varied. (a) shows the limit as $\alpha \to 0$, corresponding to a rigid aerofoil.

position of the internal support have been chosen such that the aerofoil attains a shape resembling a traditional rigid aerofoil at $\alpha = 0$. Note that the case of $\alpha = 0$ can be considered as either the limit as the flow speed tends to zero, or the flow past a rigid aerofoil. As the flow speed α is increased the aerofoil starts to deform in response to the fluid flow. This deformation is most severe at the trailing edge, which becomes concave on the upper section, resulting in a region of relatively low flow speed and thus a higher fluid pressure. We also see an increase in the flow speed on the lower section towards the trailing edge, reducing the flow pressure in the region below the aerofoil. The aerofoil thus

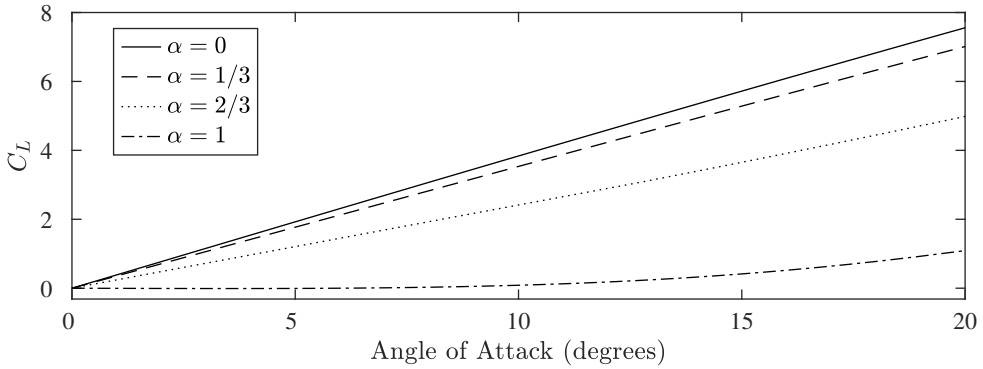

Figure 5.3.3: Lift coefficient C_L against the angle of attack of the aerofoil in degrees for various flow speeds α, with parameters $\theta_c = \pi/6$, $P = 0$, $L = 0.75$, $S = 2\pi/3$, $S_2 = 4\pi/3$. The corresponding aerofoil shapes are shown in Figure 5.3.2.

experiences a decrease in the lift coefficient C_L.

Figure 5.3.3 shows the inviscid lift coefficient C_L against the angle of attack of the supported aerofoil for various flow speeds. For low flow speed α, the elastic forces dominate over the fluid forces and the aerofoil acts rigidly as the angle of attack is increased, with the lift coefficient depending linearly on the angle of the trailing edge. As the flow speed α is increased, the aerofoil starts to deform in response to the fluid flow, as seen in Figure 5.3.2. This deformation results in a loss of lift; this loss in lift remains relatively small for low flow speeds α, while for $\alpha > 2/3$ a more severe loss of lift occurs, with the aerofoil achieving less than half of the lift of the corresponding rigid aerofoil.

The inflatable aerofoils used for small unmanned aircraft typically have a chord length of approximately 40 cm (Landis et al., 2003; Simpson, 2008), while the elastic aerofoils presented in this section typically have a dimensional chord length of approximately 2.9ℓ; we thus expect a typical length scale of $\ell = 0.14\,\mathrm{m}$. Taking the cruise speed of the aerofoil to be $U = 16\,\mathrm{m\,s^{-1}}$ (Simpson, 2008), we find that a value of $\alpha = 2/3$ corresponds to a bending modulus of $E_B = 2\,\mathrm{kg\,m^2\,s^{-2}}$. While this value is relatively high for a simple elastic material, the stiffness is increased for aerofoils constructed with composite materials (Lynch and Rogers, 1976) or inflatable panels (Bain et al., 1963).

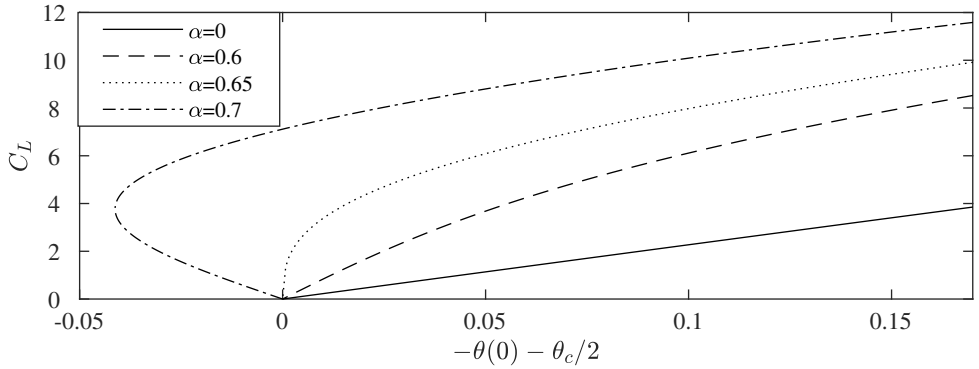

Figure 5.3.4: Lift coefficient against $-\theta(0) - \theta_c/2$ for various values of α, with parameters $\theta_c = \pi/6$, $L = 0.75$, $S_1 = 2\pi/3$, $S_2 = 4\pi/3$. The function $\theta(s)$ is the argument of the tangent vector defined in (5.1.14), and the value $-\theta(0) - \theta_c/2$ is the angle that the trailing edge is rotated clockwise from horizontal, with a value of $-\theta(0) - \theta_c/2 = 0$ corresponding to a corner which is top-bottom symmetric. The corresponding aerofoil shapes are shown in Figure 5.3.2.

Figure 5.3.4 shows the inviscid lift coefficient C_L against the value $-\theta(0) - \theta_c/2$, the angle that the trailing edge is rotated clockwise from horizontal. At $-\theta(0) - \theta_c/2 = 0$ there exist top-bottom symmetric aerofoils, for which no lift is generated. For low values of α the aerofoil behaves rigidly as the trailing edge is rotated, with a clockwise rotation of the trailing edge corresponding to a linear increase in the lift coefficient. For larger values of α however, a small rotation of the trailing edge results in a more severe aerofoil deformation, with a corresponding change in the lift generated. This sensitivity is most severe around $\alpha \approx 0.65$, where small deflections of the trailing edge drastically alter the equilibrium aerofoil shape. For $\alpha > 0.65$ the relation between the trailing edge and the lift coefficient is more complex; for an initially top-bottom symmetric aerofoil with $-\theta(0) - \theta_c/2 = 0$ an increase in the lift coefficient corresponds to an anticlockwise rotation of the trailing edge, until a turning point in the C_L curve, beyond which the lift is further increased by rotating the trailing edge clockwise as for a rigid aerofoil.

Figure 5.3.5 depicts flow past the deformed aerofoil shapes as P is decreased, with the other parameters equal to those in Figure 5.3.2d. Note that

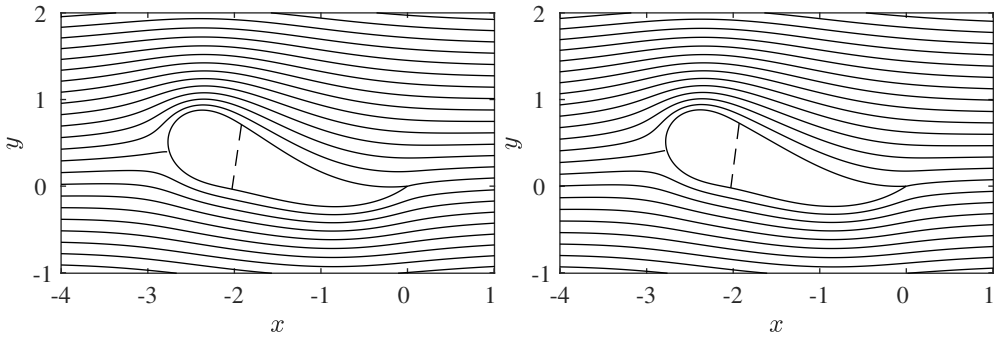

(a) $P = 0$, $C_L = 0.19$ (b) $P = -0.4$, $C_L = 0.63$

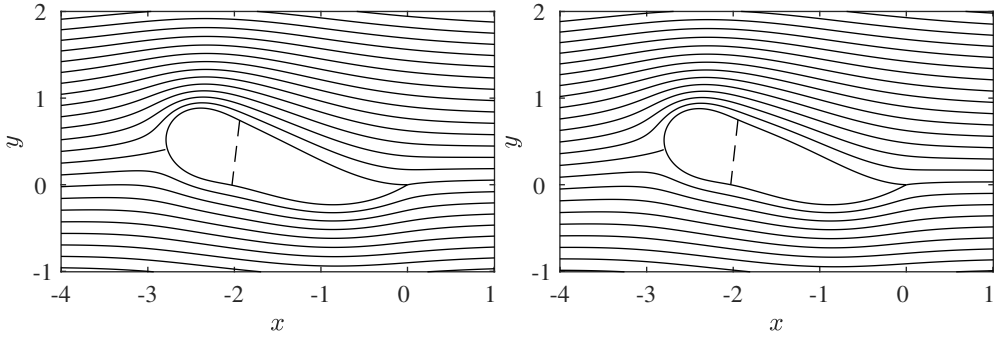

(c) $P = -0.8$, $C_L = 1.00$ (d) $P = -1.2$, $C_L = 1.38$

Figure 5.3.5: Aerofoil shapes and streamlines for an angle of attack of 12 degrees, a corner angle of $\theta_c = \pi/6$ and a far-field flow speed $\alpha = 1$. The internal support is depicted as a broken line of length $L = 0.75$ attached at the points $S_1 = 2\pi/3$ and $S_2 = 4\pi/3$. The streamlines are evenly spaced in the far-field, corresponding to evenly space values of the stream function.

a decrease of the parameter P corresponds to an increase in the interior pressure of the aerofoil. As the interior pressure is increased the aerofoil thickness increases towards the trailing edge and the upper section becomes less concave, resulting in a higher average flow speed along the upper section. This higher flow speed results in a lower pressure above the aerofoil, and thus a higher lift coefficient C_L. However, for $P \approx -1.2$ the aerofoil thickness is significantly increased, particularly towards the trailing edge, which we expect to result in a higher viscous drag. This thickness could be reduced by introducing a more complex internal support structure to the aerofoil, which would allow for a higher internal pressure and thus a higher lift coefficient while limiting the corresponding viscous drag. This will be discussed in more

detail in the summary. For an aerofoil with $\ell = 0.14\,\mathrm{m}$ and bending modulus $E_B = 2\,\mathrm{kg\,m^2\,s^{-2}}$, as considered previously, a value of $P = -1.2$ corresponds to a maximum inflation pressure $p_0 - p_\infty$ of approximately $0.9\,\mathrm{kPa}$. This suggests that the aerofoil attains an aerodynamic shape at relatively low internal pressures, which is desirable since a lower internal pressure reduces the risk of leaks, improving the reliability of the aerofoil (Jacob and Smith, 2009).

5.4 Viscous Effects

The deformed aerofoils presented in the previous sections were obtained by assuming that the fluid flow past the aerofoil is both inviscid and steady. While these assumptions significantly simplify the formulation of the problem, in a physical fluid the effects of viscosity cannot be neglected. For a high speed, low viscosity flow, the flow away from the aerofoil boundary can be treated as inviscid, with the viscous effects concentrated in a thin boundary layer along the aerofoil boundary. As the fluid in the boundary layer then passes the point of maximum flow speed along the aerofoil boundary it encounters a region of adverse pressure gradient which can cause the boundary layer to separate from the aerofoil boundary, producing a region of turbulent wake behind the aerofoil. The fluid pressure in this turbulent region will generally have a lower pressure than the potential flow, producing a significant drag force.

To analyse the effects of the viscous flow we treat the deformed aerofoil shapes obtained in the previous sections as rigid bodies, neglecting any further deformation that may be caused by the viscous flow. Such an approach is valid as a first approximation for streamlined aerofoils in high Reynolds number flows, where the boundary layer separation occurs close to the trailing edge of the aerofoil and the inviscid flow provides a good approximation to the viscous flow. We will confirm the validity of this

assumption further on.

5.4.1 Numerical Method

We compute the viscous flow past the aerofoil using the software package Gerris (Popinet, 2003, 2009), which solves the unsteady incompressible Navier-Stokes equations numerically using an adaptive mesh refinement method. The flow is computed in a channel bounded by solid walls with a slip boundary condition, with the channel width taken to be large enough that the flow near the aerofoil is unaffected by the walls. The flow is initialised at time $t = 0$ with a uniform horizontal flow of speed α. While this provides an accurate simulation of the unsteady viscous flow away from the aerofoil, the locally spatially isotropic mesh refinement used by Gerris is unsuitable for precisely resolving the boundary layer at the aerofoil boundary (Popinet, 2003); the viscous drag acting on the aerofoil must therefore be computed separately. Since the fluid pressure does not change throughout the boundary layer, an accurate value of the pressure drag acting on the aerofoil can still be obtained using the Gerris simulation.

To formulate the equations which govern the viscous boundary layer, we consider the Navier-Stokes equations

$$u\frac{\partial u}{\partial x} + v\frac{\partial u}{\partial y} = \frac{\alpha}{Re}\left(\frac{\partial^2 u}{\partial x^2} + \frac{\partial^2 u}{\partial y^2}\right) - \frac{\partial p}{\partial x}, \tag{5.4.1}$$

$$u\frac{\partial v}{\partial x} + v\frac{\partial v}{\partial y} = \frac{\alpha}{Re}\left(\frac{\partial^2 v}{\partial x^2} + \frac{\partial^2 v}{\partial y^2}\right) - \frac{\partial p}{\partial y}, \tag{5.4.2}$$

which along with the continuity condition

$$\frac{\partial u}{\partial x} + \frac{\partial v}{\partial y} = 0, \tag{5.4.3}$$

govern the steady two-dimensional incompressible viscous flow. Here $u(x, y)$

and $v(x, y)$ are the horizontal and vertical components of the fluid velocity, $p(x, y)$ is the fluid pressure, and $Re = U\ell/\nu$ is the Reynolds number where ν is the kinematic viscosity of the fluid. It is well known that for $Re \gg 1$ a viscous boundary layer of thickness $O\left(Re^{-1/2}\right)$ will form along the aerofoil boundary due to the viscous no-slip condition (Prandtl, 1905). To obtain the equations which govern the viscous flow in this thin boundary layer we introduce the boundary layer coordinates s and $\tilde{y}$, where s is the arc-length distance around the aerofoil and $\tilde{y}$ is the distance from the point $z = \eta(s)$ in the normal direction multiplied by $Re^{1/2}$ such that $\tilde{y} = 1$ is a distance of $Re^{-1/2}$ from the point $z = \eta(s)$. We denote as $\tilde{u}(s, \tilde{y})$ and $\tilde{v}(s, \tilde{y})$ the components of the flow velocity in the s and $\tilde{y}$ directions respectively, where

$$u = \mathrm{Re}(\eta_s)\tilde{u} + \frac{1}{\sqrt{Re}}\mathrm{Im}(\eta_s)\tilde{v}, \quad v = \mathrm{Im}(\eta_s)\tilde{u} - \frac{1}{\sqrt{Re}}\mathrm{Re}(\eta_s)\tilde{v}.$$

Note that the normal velocity $\tilde{v}$ has been rescaled to match the scale of $\tilde{y}$. The Cartesian derivatives are then given in terms of the boundary layer coordinates as

$$\frac{\partial}{\partial x} = \mathrm{Re}(\eta_s)\frac{\partial}{\partial s} + \sqrt{Re}\,\mathrm{Im}(\eta_s)\frac{\partial}{\partial \tilde{y}}, \quad \frac{\partial}{\partial y} = \mathrm{Im}(\eta_s)\frac{\partial}{\partial s} - \sqrt{Re}\,\mathrm{Re}(\eta_s)\frac{\partial}{\partial \tilde{y}}.$$

Substituting these expressions into (5.4.1)–(5.4.3) and taking the limit as $Re \to \infty$, we obtain

$$\tilde{u}\frac{\partial \tilde{u}}{\partial s} + \tilde{v}\frac{\partial \tilde{u}}{\partial \tilde{y}} = -\frac{\partial p}{\partial s} + \alpha\frac{\partial^2 u}{\partial \tilde{y}^2}, \tag{5.4.4}$$

$$0 = -\frac{\partial p}{\partial \tilde{y}}, \tag{5.4.5}$$

$$\frac{\partial \tilde{u}}{\partial s} + \frac{\partial \tilde{v}}{\partial \tilde{y}} = 0. \tag{5.4.6}$$

Equation (5.4.5) implies that the fluid pressure in the boundary layer is

independent of $\tilde{y}$, and so is equal to the fluid pressure in the potential flow evaluated at the aerofoil boundary. We thus have $\frac{\partial p}{\partial s} = -qq_s$, where $q(s)$ is the potential flow speed evaluated at the aerofoil boundary. Equation (5.4.4) is thus reduced to

$$\tilde{u}\frac{\partial \tilde{u}}{\partial s} + \tilde{v}\frac{\partial \tilde{u}}{\partial \tilde{y}} = qq_s + \alpha\frac{\partial^2 u}{\partial \tilde{y}^2}. \tag{5.4.7}$$

At the aerofoil boundary the viscous flow must satisfy the no-slip and no-penetration conditions

$$\tilde{u}(s,0) = 0, \quad \tilde{v}(s,0) = 0. \tag{5.4.8}$$

To match the flow velocity to that of the potential flow as $\tilde{y} \to \infty$ we require

$$\tilde{u}(s,\infty) = q(s)\,\mathrm{sgn}(s - s^*), \tag{5.4.9}$$

where s^* is the arc-length position of the leading-edge stagnation point and the sign $\mathrm{sgn}(s - s^*)$ has been taken since the potential flow is in the negative s direction for $s < s^*$.

To simplify the boundary layer equations, we use the method of Keller (1978) by introducing the rescaled variables

$$\zeta(s,\tilde{y}) \equiv \tilde{y}\sqrt{\frac{q(s)}{\alpha|s - s^*|}}, \quad f(s,\zeta(s,\tilde{y})) \equiv \mathrm{sgn}(s - s^*)\frac{\psi(s,\tilde{y})}{\sqrt{\alpha q(s)|s - s^*|}}, \tag{5.4.10}$$

where $s = s^*$ is the arc-length position of the leading-edge stagnation point, and $\psi(s,\tilde{y})$ is a stream function which satisfies

$$\tilde{u} = \frac{\partial \psi}{\partial \tilde{y}}, \quad \tilde{v} = -\frac{\partial \psi}{\partial s}.$$

Here ζ can be considered the normal distance from the aerofoil boundary in the boundary layer rescaled by the expected thickness of the boundary layer, and

$f(s,\zeta)$ is a rescaled stream function. The stream function automatically satisfies the continuity equation (5.4.6), and (5.4.7) becomes

$$f_{\zeta\zeta\zeta}+\frac{1}{2}\left((s-s^*)\frac{q_s}{q}+1\right)ff_{\zeta\zeta}+(s-s^*)\frac{q_s}{q}\left(1-f_\zeta^2\right)=(s-s^*)\left(f_\zeta f_{\zeta s}-f_{\zeta\zeta}f_s\right), \quad (5.4.11)$$

with boundary conditions

$$f(s,0)=0, \quad f_\zeta(s,0)=0, \quad f_\zeta(s,\infty)=1. \quad (5.4.12)$$

Note that near the leading edge we have $q(s)=(s-s^*)q_s(s^*)+O(s-s^*)^2$, and so

$$(s-s^*)\frac{q_s}{q}\to 1 \quad \text{as} \quad s\to s^*.$$

At $s=s^*$, (5.4.11) is reduced to

$$f_{\zeta\zeta\zeta}+ff_{\zeta\zeta}+1-f_\zeta^2=0, \quad (5.4.13)$$

with boundary conditions

$$f(0,0)=0, \quad f_\zeta(0,0)=0, \quad f_\zeta(0,\infty)=1. \quad (5.4.14)$$

This is a one-dimensional ODE which can easily be solved numerically to obtain the values of $f(0,\zeta)$, $f_\zeta(0,\zeta)$ and $f_{\zeta\zeta}(0,\zeta)$.

We solve (5.4.11) using the central difference method described by Keller (1978). We introducing a grid $s_i=s^*+i\Delta s$, $\zeta_j=j\Delta\zeta$ for $i=0,1,2\ldots$ and $j=0,1,2,\ldots,J$, where Δs and $\Delta\zeta$ are small constants and J is taken to be large enough for the variables to attain their far-field values at ζ_J. We rewrite (5.4.11)

as a system of three first order PDEs

$$\frac{\partial}{\partial\zeta}\begin{pmatrix} f \\ f_1 \\ f_2 \end{pmatrix} = \begin{pmatrix} f_1 \\ f_2 \\ (s-s^*)\frac{q_s}{q}\left(f_1^2 - \frac{1}{2}ff_2 - 1\right) - \frac{1}{2}ff_2 + (s-s^*)\left(f_1 f_{1_s} - f_2 f_s\right) \end{pmatrix}, \quad (5.4.15)$$

and then use a combination of central difference and two-point averages to evaluate the values of the unknowns f, f_1 and f_2 and their derivatives at the centre points $(s_{i+1/2}, \zeta_{i+1/2}) = \left(\frac{s_{i+1}+s_i}{2}, \frac{\zeta_{i+1}+\zeta_i}{2}\right)$, where their values are assumed to be known at s_i but unknown at s_{i+1}. For example, the centred values of f and its derivatives at $(s_{i+1/2}, \zeta_{i+1/2})$ are given by

$$\begin{aligned} f_{i+1/2,j+1/2} &= \frac{f_{i+1,j+1} + f_{i+1,j} + f_{i,j+1} + f_{i,j}}{4}, \\ \left(\frac{\partial f}{\partial s}\right)_{i+1/2,j+1/2} &= \frac{f_{i+1,j+1} - f_{i,j+1} + f_{i+1,j} - f_{i,j+1}}{2\Delta x}, \\ \left(\frac{\partial f}{\partial \zeta}\right)_{i+1/2,j+1/2} &= \frac{f_{i+1,j+1} + f_{i,j+1} - f_{i+1,j} - f_{i,j+1}}{2\Delta \zeta}. \end{aligned}$$

Starting at the leading edge $s = s^*$, where values of f, f_1 and f_2 can be obtained numerically by solving (5.4.13), we use Newton's method to solve (5.4.15), evaluating the derivatives using the central difference formulae, to obtain values of f, f_1 and f_2 at $s_1 = s^* + \Delta s$. We can then proceed in this way for each value s_i up until the boundary separates, at which point the system breaks down and no further solution can be obtained. The boundary layer on the upper section of the aerofoil is obtained by taking $\Delta s < 0$, and the boundary layer on the lower section is obtained by taking $\Delta s > 0$.

Noting that the normal derivative of the boundary layer flow speed is given in terms of the transformed variables as

$$\tilde{u}_{\tilde{y}} = \operatorname{sgn}(s-s^*) q \sqrt{\frac{q}{\alpha|s-s^*|}} f_{\zeta\zeta},$$

we find that the dimensional shear stress on the aerofoil boundary is given by

$$\frac{vU\rho}{\alpha\ell}\frac{\partial\tilde{u}}{\partial y}\bigg|_{y=0} = \frac{\rho U^2}{\alpha}\sqrt{\frac{1}{Re}}\frac{\partial\tilde{u}}{\partial\tilde{y}}\bigg|_{\tilde{y}=0} = \rho U^2\sqrt{\frac{1}{Re}}\left(\frac{q}{\alpha}\right)^{3/2}\frac{\operatorname{sgn}(s-s^*)}{\sqrt{|s-s^*|}}f_{\zeta\zeta}(s,0).$$

The net dimensional viscous force in the boundary layer acting upon the aerofoil is thus given by

$$\rho U^2\ell\sqrt{\frac{1}{Re}}\int_{s^-}^{s^+}\left(\frac{q}{\alpha}\right)^{3/2}\frac{\operatorname{sgn}(s-s^*)}{\sqrt{|s-s^*|}}f_{\zeta\zeta}(s,0)\hat{\boldsymbol{\tau}}(s)\mathrm{d}s, \tag{5.4.16}$$

where s^- and s^+ are the points at which the boundary layer separates on the top and bottom of the aerofoil respectively. The net dimensional force per unit span acting on the aerofoil can then be approximated as

$$\int_0^1 -p(s)\hat{\boldsymbol{n}}(s)\ell\mathrm{d}s + \rho\ell U^2\sqrt{\frac{1}{Re}}\int_{s^-}^{s^+}\frac{\operatorname{sgn}(s-s^*)}{\sqrt{|s-s^*|}}\left(\frac{q(s)}{\alpha}\right)^{3/2}f_{\zeta\zeta}(s,0)\,\hat{\boldsymbol{\tau}}(s)\mathrm{d}s, \tag{5.4.17}$$

where $p(s)$ is the dimensional pressure at the aerofoil boundary computed by the Gerris simulation. The first term in (5.4.17) is the net force due to the pressure acting on the aerofoil, and the second term is the viscous drag in the boundary layer. Note that this expression does not account for any viscous drag occurring past the boundary layer separation. However, for an aerodynamic aerofoil the separation will occur close to the trailing edge, so we expect any viscous drag past the separation point to be much smaller than the boundary layer drag and pressure forces.

5.4.2 Viscous Results

Figure 5.4.1 shows the viscous flow past an unsupported aerofoil with an angle of attack of 6 degrees, which is comparable to the angle of attack of a typical rigid aerofoil. The viscous flow is computed for both $Re = 5\times10^4$ and $Re = 10\times10^4$. For the flow of air past an aerofoil with perimeter $\ell = 0.14\,\mathrm{m}$, as

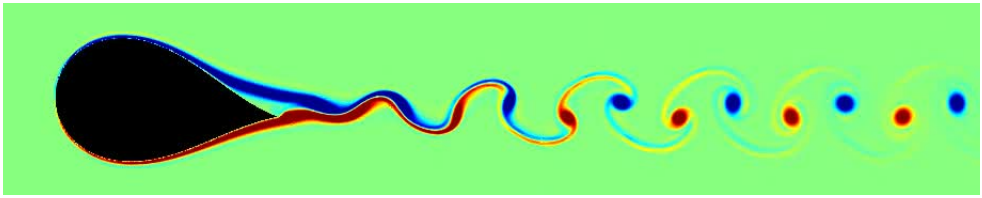

(a) Vorticity field for $Re = 5 \times 10^4$

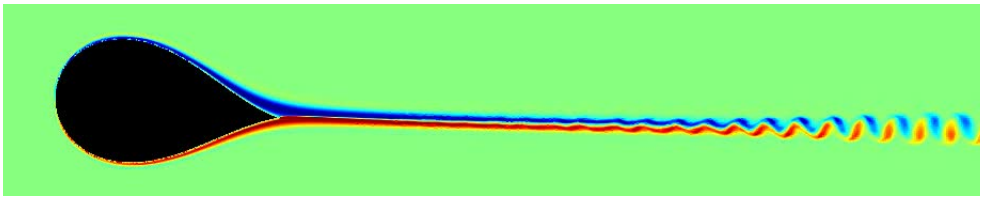

(b) Vorticity field for $Re = 10 \times 10^4$

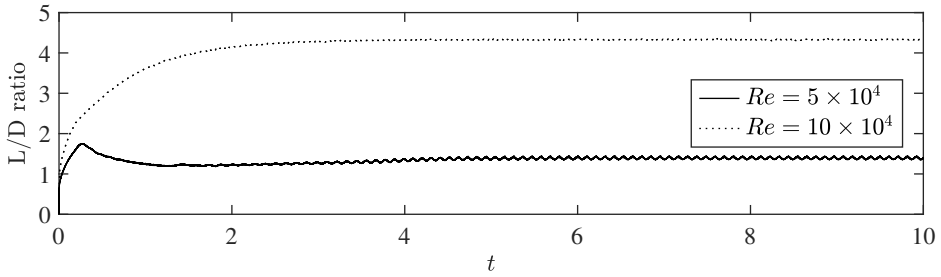

(c) Lift-to-drag ratios

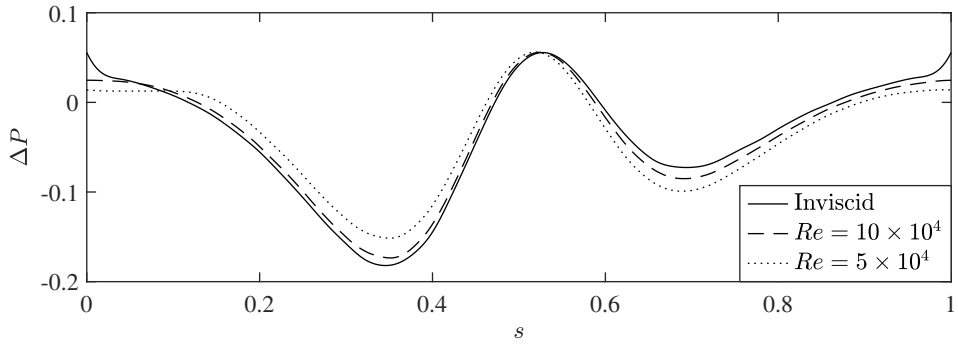

(d) Transmural fluid pressures

Figure 5.4.1: Simulations of the viscous flow past an unsupported aerofoil with parameters $\alpha = 1/3$, $\theta_c = \pi/6$, and an angle of attack of 6 degrees. (a) and (b) show a snapshot of the vorticity field at $t = 10$, with blue indicating negative vorticity, red indicating positive vorticity, and green indicating zero vorticity. (c) shows the lift-to-drag ratio of the aerofoil. (d) shows the dimensionless transmural fluid pressure $\Delta P \equiv (p - p_i)\ell^3/E_B$ at $t = 10$, with the inviscid pressure obtained using the boundary integral method.

considered in Section 5.3, these values of the Reynolds number correspond to far-field flow velocities of $U = 5\,\mathrm{m\,s^{-1}}$ and $U = 10\,\mathrm{m\,s^{-1}}$ respectively, where the kinematic viscosity of air is taken to be approximately $\nu = 1.46 \times 10^{-5}\,\mathrm{m^2\,s^{-1}}$. For $Re = 5 \times 10^4$, which corresponds to $U = 5\,\mathrm{m\,s^{-1}}$, the viscous boundary layer on the upper edge of the aerofoil separates relatively early due to the thickness of the aerofoil, causing a large viscous wake. Figure 5.4.1c shows the lift-to-drag ratio for this simulation, with the lift and drag forces computed using (5.4.17). The lift-to-drag ratio is volatile just after the flow is initiated, but by $t = 10$ the lift-to-drag ratio tends to a value of 1.4, although small regular oscillations remain due to the vortex shedding seen in panel (a). For $Re = 10 \times 10^4$, which corresponds to $U = 10\,\mathrm{m\,s^{-1}}$, the viscous boundary layer remains attached up to the trailing edge of the aerofoil, where it forms a thin, stable wake. The lift-to-drag ratio settles to a value of 4.3 which, while significantly better than the previous value of 1.4, is relatively poor compared to conventional aerofoils.

The dimensionless transmural pressures for the viscous simulations at $t = 10$ are compared to that of the inviscid flow in Figure 5.4.1d. Near the leading-edge stagnation point $s = 0.52$, the viscous fluid pressures agree well with the inviscid flow. However, towards the trailing edge at $s = 0$ and $s = 2\pi$ we observe a significant deviation between the pressures, with this deviation more severe for the lower value of Re. Along the upper section $0 \leq s \leq 0.52$ we observe that the fluid pressure generally increases for lower values of Re, while on the lower section $0.52 \leq s \leq 2\pi$ the fluid pressure decreases, resulting in a reduction of the lift force acting on the aerofoil. We also observe a decrease in the fluid pressure near the trailing edge, which corresponds to an increased form drag acting on the aerofoil.

Figure 5.4.2 shows the viscous flow past an aerofoil with internal support of length $L = 0.75$ connected to the aerofoil at $S_1 = 2\pi/3$ and $S_2 = 4\pi/3$. The flow parameters are the same as those in Figure 5.4.1. For $Re = 5 \times 10^4$, which

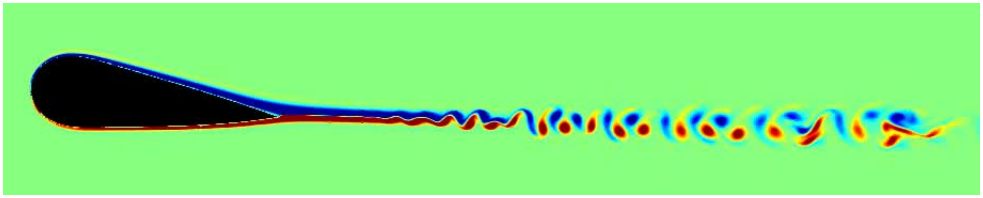

(a) Vorticity field for $Re = 5 \times 10^4$

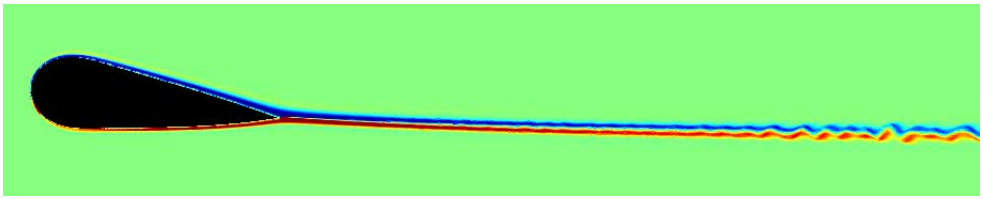

(b) Vorticity field for $Re = 10 \times 10^4$

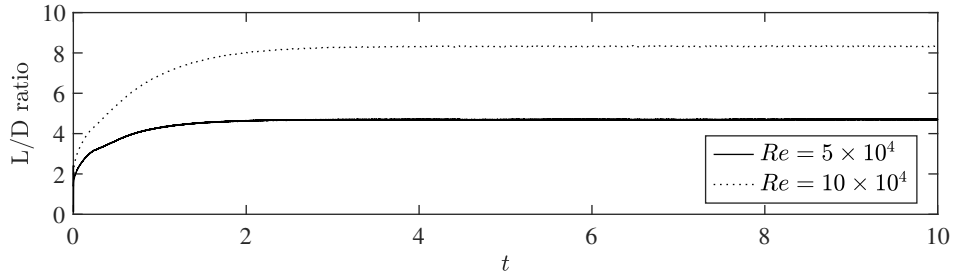

(c) lift-to-drag ratios

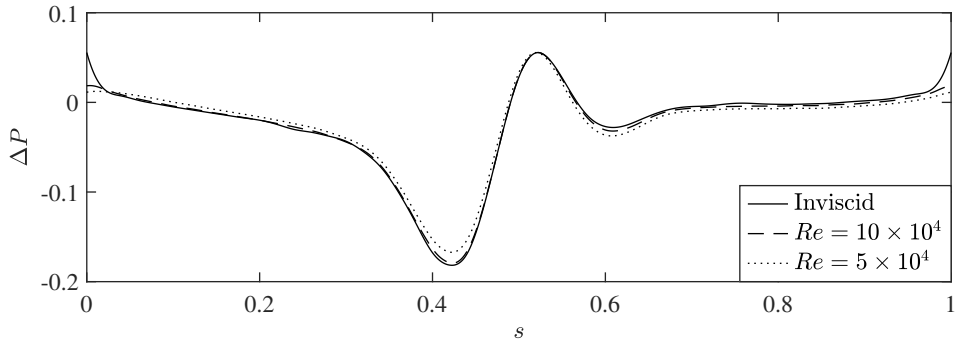

(d) Transmural fluid pressures

Figure 5.4.2: Simulations of the viscous flow past a supported aerofoil with parameters $\alpha = 1/3$, $\theta_c = \pi/6$, $L = 0.75$, $S_1 = 2\pi/3$, $S_2 = 4\pi/3$, and an angle of attack of 6 degrees. (a) and (b) show a snapshot of the vorticity field at $t = 10$, with black indicating negative vorticity, white indicating positive vorticity, and grey indicating zero vorticity. (c) shows the lift-to-drag ratio of the aerofoil. (d) shows the dimensionless transmural fluid pressure $\Delta P \equiv (p - p_i)\ell^3/E_B$ at $t = 10$, with the inviscid pressure obtained using the boundary integral method.

corresponds to $U = 5\,\mathrm{m\,s^{-1}}$, we find that, unlike the unsupported case, the boundary layer remains attached up to the trailing edge, reducing the oscillations in the lift-to-drag ratio. The lift-to-drag ratio attains a value of 4.7, which is significantly higher than that of the unsupported aerofoil. For $Re = 10 \times 10^4$, which corresponds to $U = 10\,\mathrm{m\,s^{-1}}$ the lift-to-drag ratio is increased further, reaching a value of 8.2, almost twice the value for the unsupported aerofoil.

The dimensionless transmural pressures for the viscous simulations at $t = 10$ are compared to that of the inviscid flow in Figure 5.4.2d. We find that the viscous pressures agree very well with the inviscid pressures for both $Re = 10 \times 10^4$ and $Re = 5 \times 10^4$. Since the numerical method used to obtain the aerofoil deformation is based on the inviscid model of the flow, the accuracy of the aerofoil shape will depend on the deviation of the transmural fluid pressure between the inviscid and viscous flows. We thus conclude that the inviscid flow used to obtain the deformed aerofoil shapes provides a good approximation for the flow speeds considered.

We have thus shown that with a simple internal support the aerofoil can maintain a good aerodynamic shape in realistic flow conditions, with significantly improved aerodynamic characteristics over an unsupported aerofoil.

5.5 Summary

We have studied the deformation and aerodynamics of an elastic aerofoil in a fluid flow. By modelling the aerofoil as a thin two-dimensional elastic cell we have formulated the equations which govern the aerofoil deformation in response to an inviscid fluid. We have presented a conformal mapping which is used to determine the inviscid flow past an aerofoil with no internal

support, and constructed an iterative numerical method based on a boundary integral equation for aerofoils with a simple internal support. Using the viscous boundary layer method by Keller (1978) along with unsteady viscous simulations using the software package Gerris (Popinet, 2003) we have analysed the aerodynamic properties of the deformed aerofoil shapes and confirmed the validity of the inviscid approximation.

We first considered the deformation of an elastic aerofoil with a fixed angle corner without any internal support. Guided by the smooth cell results from the previous chapters, we obtained a set of distinct solution branches for aerofoils in a static fluid and analysed the intricate development of these solution branches as a fluid flow is introduced. We observed that the aerofoil deformation in response to an increased flow speed α or pressure P varies significantly depending on the precise parameter values. Notably, we showed that the solution branch which passes through $P = 0$ contains aerofoils with good aerodynamic profiles for low flow speeds, for which an increase in the parameter P resulting in a more slender aerofoil. For larger flow speeds however, the aerofoil bulges out perpendicular to the flow, with higher transmural pressures resulting in a more severe deformation.

We then considered an aerofoil with an inextensible internal support which acts to constrain the deformation of the aerofoil and provide a realistic model of an inflatable aerofoil. We have focused on the case of an aerofoil with trailing edge angle $\theta_c = \pi/6$ and a single support of length $L = 0.75$, attached to the aerofoil at the points $S_1 = 2\pi/3$ and $S_2 = 4\pi/3$, which was found to provide a good aerodynamic shape. For inviscid flow the aerofoil does not significantly deform at low flow speeds and the lift depends almost linearly on the angle of attack as it would for a rigid aerofoil. At higher flow speeds a more substantial deformation occurs, particularly toward the trailing edge, and this results in a significant loss in lift. The loss in lift can be reduced by increasing the inflation

pressure, but at the expense of an increase in drag as the aerofoil bulges into a less aerodynamic shape. By computing the viscous flow past the deformed aerofoils we found that the presence of an internal support delays the boundary layer separation at the trailing edge, reducing the viscous wake and significantly improving the lift-to-drag ratio of the aerofoil.

6

Summary and Future Work

6.1 Summary

In this thesis we studied the deformation of a two-dimensional elastic cell in an inviscid stream.

In Chapter 2 we formulated the system of equations which governs the unsteady deformation of a two-dimensional elastic cell submerged in an inviscid fluid flow, and confirmed that these equations conserve the energy of the system. We presented a conformal mapping which is used to simplify the exterior flow problem, and reduced the steady form of the system to a single one-dimensional equation, providing a foundation for the following chapters.

In Chapter 3 we studied the case of a massless elastic cell in a uniform stream. Expanding on the results of Blyth and Părău (2013), we presented an asymptotic method to obtain equilibria solutions to arbitrary powers of the low flow speed parameter, and uncovered a series distinct solution branches which bifurcate at critical pressures corresponding to those obtained by Halphen (1888) for a buckled cell in a static fluid. Of particular note, we obtained steady cell shapes with left-right asymmetry and cells with top-bottom asymmetry. We used numerical methods to present a detailed analysis of the solution branches bifurcating from the first two critical pressures, and presented maps of the regions of parameter space in which these steady solutions are linearly stable. Using unsteady simulations, we

showed that unstable cells in certain regions of parameter space fall into a one of two distinct regular motions, either a flipping motion or a bulging motion, while for other parameter values the cell undergoes a fully chaotic unsteady motion.

In Chapter 4 we studied the equilibria of an elastic cell in flows with circulation. We used two different asymptotic expansions to obtain solutions which bifurcate from the unit circle at critical values of the transmural pressure and the circulation, and obtained the buckled mode-k symmetric equilibria cells first identified by Blyth and Părău (2013). We then studied the deformation of an elastic cell in a uniform stream with circulation, with the lift force balanced by the weight of the cell. We obtained asymptotic expansions for low flow speeds, and used numerical methods to expand upon the results obtained in Chapter 3, allowing for a detailed analysis of the more complex bifurcation structure which emerges when circulation is introduced to the flow.

In Chapter 5 we adapted the elastic cell formulation to allow for a fixed angle corner and an inextensible internal support, providing a simple model of an inflatable aerofoil. We used a combination of conformal mapping and boundary integral methods to analyse the deformed cell shapes for an unsupported cell in an inviscid fluid flow, and showed that while the cell takes an aerofoil-like shape for certain parameter values, the flow generally causes the cell to swell outwards perpendicular to the flow. We showed that by introducing an inextensible internal support we can constrain the deformation of the cell and maintain a good aerofoil-like shape for realistic flow parameters. We computed the viscous flow past the deformed cells by solving the viscous boundary layer equations along with unsteady viscous simulations using the software package Gerris, and showed that by including an internal support the viscous boundary layer separation can be delayed, significantly

improving the aerodynamic performance of the aerofoil.

6.2 Future Work

The general unsteady system of equations derived in Chapter 2 provided a framework for the two specific cases considered in the two following chapters: the unsteady motion of a massless cell in the absence of both lift and buoyancy considered in Chapter 3, and the equilibria of a cell with a heavy elastic boundary balanced by a lift force considered in Chapter 4. It would be informative to study the problem under more general conditions, allowing for buoyancy, a heavy cell boundary and a lift force, which would allow for a more complete understanding of the full system.

In Chapter 3 we considered the equilibria of a massless cell in a uniform stream. We showed that there exist an infinite number of distinct solution branches which bifurcate from the unit circle at a series of critical transmural pressures and performed a detailed analysis of the solutions which bifurcate at the lowest two values of these pressures. It would be informative to study the solution branches which bifurcate from the higher critical pressures and identify any general patterns which emerge.

The asymptotic expansions presented in Chapter 4 for cells in a circulatory flow with no uniform stream were based on perturbations of the circular rest state for low flow speeds. It would be informative to also take asymptotic expansions for weakly elastic cells about the exact solutions of Crowdy (2000) for a bubble in a circulatory flow.

The analysis of massive cells in a uniform stream with circulation in Chapter 4 was limited to finding equilibria states. It would be useful to adapt the linear stability method and the unsteady numerical method presented in Chapter 3 to incorporate the inertial terms of the elastic deformation

equations, allowing for a detailed analysis of the stability of the various solution branches in the same vein as in Chapter 3.

In Chapter 5 we presented results for an inflatable aerofoil, with a simple internal support chosen to demonstrate the improvement on the aerodynamic behaviour of the inflatable aerofoil under steady cruise conditions. Some inflatable aerofoils have a single support as considered here (e.g. Bain et al., 1963), but aerofoils with more complex internal structure are commonly used (e.g. Brown et al., 2001). It would therefore be useful to adapt the boundary integral method used in Chapter 5 to account for these more complex support structures, allowing for an analysis of a wider range of aerofoil designs. In either case the framework we have provided could be used as a basis to investigate how to optimise performance under different flight conditions depending on the intended application.

Bibliography

Bain, B. K., Thomas, B. J., Burger, E. M., Ross, R. S., Vorachek, J. J., and Wolcott, R. L. Inflatable aerofoil. US Patent US3106373A, 1963.

Batchelor, G. K. *An Introduction to Fluid Dynamics*. Cambridge Mathematical Library. Cambridge University Press, 2000.

Battles, Z. and Trefethen, L. N. An extension of MATLAB to continuous functions and operators. *SIAM J. Sci. Comput.*, 25(5):1743–1770, 2004.

Baumgarte, J. Stabilization of constraints and integrals of motion in dynamical systems. *Comput. Methods Appl. Mech. Eng.*, 1:1–16, 1972.

Blyth, M. G. and Pozrikidis, C. Buckling and collapse of heavy tubes resting on a horizontal or inclined plane. *Eur. J. Mech. A Solids*, 21:831–843, 2002.

Blyth, M. G. and Părău, E. I. Deformation of an elastic cell in a uniform stream and in a circulatory flow. *IMA J. Appl. Math.*, 78:665–684, 2013.

Brown, G., Haggard, R., and Norton, B. Inflatable structures for deployable wings. In *16th AIAA Aerodynamic Decelerator Systems Technology Conference and Seminar*. American Institute of Aeronautics and Astronautics, 2001.

Carrier, G. F. On the buckling of elastic rings. *J. Math. Phys.*, 26:94–103, 1947.

Carrier, G. F., Krook, M., and Pearson, C. E. *Functions of a complex variable: Theory and technique*. SIAM, 2005.

Chang, K. S. and Olbricht, W. L. Experimental studies of the deformation of a synthetic capsule in extensional flow. *J. Fluid Mech.*, 250:587–608, 1993.

Crowdy, D. G. Circulation-induced shape deformations of drops and bubbles: exact two-dimensional models. *Phys. Fluids*, 11(10):2836–2845, 1999.

Crowdy, D. G. A new approach to free surface Euler flows with capillarity. *Stud. Appl. Math.*, 105(1):35–58, 2000.

DeLillo, T. K. The accuracy of numerical conformal mapping methods: A survey of examples and results. *SIAM J. Numer. Anal.*, 31(3):788–812, 1994.

Djondjorov, P., Vassilev, V., and Mladenov, I. Analytic description and explicit parametrisation of the equilibrium shapes of elastic rings and tubes under uniform hydrostatic pressure. *Int. J. Mech. Sci.*, 53(5):355 – 364, 2011.

Driscoll, T. A. and Trefethen, L. N. *Schwarz-Christoffel Mapping*. Cambridge Monographs on Applied and Computational Mathematics. Cambridge University Press, 2002.

Elgindi, M., Yen, D., and Wang, C. Deformation of a thin-walled cylindrical tube submerged in a liquid. *J. Fluid Struct.*, 6(3):353 – 370, 1992.

Fedosov, D. A., Peltomäki, M., and Gompper, G. Deformation and dynamics of red blood cells in flow through cylindrical microchannels. *Soft Matter*, 10:4258–4267, 2014.

Flaherty, J. E., Keller, J. B., and Rubinow, S. I. Post buckling behavior of elastic tubes and rings with opposite sides in contact. *SIAM J. Appl. Math.*, 23:446–455, 1972.

Fung, Y. C. *Biomechanics*. Springer New York, 1997.

Goodyear Aircraft. Summary: Report of the development of a one place Inflatoplane. Technical Report GER 8146, Goodyear Aircraft, 1957.

Greenhill, A. The elastic curve, under uniform normal pressure. *Mathematische Annalen*, 52(4):465–500, 1899.

Halphen, G. H. *Traité des fonctions elliptiques et de leurs applications.* Gauthier-Villars, 1888.

Higley, M., Siegel, M., and Booty, M. R. Semi-analytical solutions for two-dimensional elastic capsules in stokes flow. *P. Roy. Soc. A - Math. Phys.*, 468(2146):2915–2938, 2012.

Jacob, J. and Smith, S. Design limitations of deployable wings for small low altitude UAVs. In *47th AIAA Aerospace Sciences Meeting including The New Horizons Forum and Aerospace Exposition.* American Institute of Aeronautics and Astronautics, 2009.

von Kármán, T. and Trefftz, E. Potential flow round aerofoil profiles. *Z. Flugtech. Motorluftschiffahrt*, 9:111, 1918.

Keller, H. B. Numerical Methods in Boundary-Layer Theory. *Annu. Rev. Fluid Mech.*, 10(1):417–433, 1978.

Landis, G. A., Colozza, A., and LaMarre, C. M. Atmospheric flight on venus: A conceptual design. *J. Spacecraft Rockets*, 40(5):672–677, 2003.

Lévy, M. Mémoire sur un nouveau cas intégrable du problème de l'élastique et l'une des ses applications. *J. Math. Pure Appl.*, 10:5–42, 1884.

Lynch, R. and Rogers, W. Aeroelastic tailoring of composite materials to improve performance. In *17th Structures, Structural Dynamics, and Materials Conference.* 1976.

Moreno, A. H., Katz, A. I., Gold, L. D., and Reddy, R. V. Mechanics of distension of dog veins and other very thin-walled tubular structures. *Circ. Res.*, 27:1069–1080, 1970.

Murray, J., Pahle, J., Thornton, S., Vogus, S., Frackowiak, T., Mello, J., and Norton, B. Ground and flight evaluation of a small-scale inflatable-winged aircraft. In *40th AIAA Aerospace Sciences Meeting & Exhibit*. American Institute of Aeronautics and Astronautics, 2002.

Nie, Q. and Tanveer, S. The stability of a two-dimensional rising bubble. *Phys. Fluids*, 7:1292–1306, 1995.

Peitgen, H.-O., Jürgens, H., and Saupe, D. *Chaos and Fractals*. Springer New York, 2004.

Popinet, S. Gerris: a tree-based adaptive solver for the incompressible Euler equations in complex geometries. *J. Comput. Phys.*, 190(2):572–600, 2003.

Popinet, S. An accurate adaptive solver for surface-tension-driven interfacial flows. *J. Comput. Phys.*, 228:5838 – 5866, 2009.

Pozrikidis, C. Buckling and collapse of open and closed cylindrical shells. *J. Eng. Math.*, 42:157–180, 2002a.

Pozrikidis, C. *A practical guide to boundary element methods with the software library BEMLIB*. Chapman & Hall/CRC, 2002b.

Pozrikidis, C. Numerical simulation of the flow-induced deformation of red blood cells. *Ann. Biomed. Eng.*, 31:1194–1205, 2003.

Pozrikidis, C. *Computational Hydrodynamics of Capsules and Biological Cells*. Chapman & Hall/CRC Mathematical and Computational Biology. CRC Press, 2010.

Prandtl, L. Über Flüssigkeitsbewegung bei sehr kleiner Reibung. In *Verh. III. Intern. Math. Kongr. Heidelberg*. B. G. Teubner, Leipzig, 1905.

Reasor, D., LeBeau, R., Smith, S., and Jacob, J. Flight testing and simulation of a Mars aircraft design using inflatable wings. In *45th AIAA Aerospace Sciences Meeting and Exhibit*. 2012.

Shankar, P. N. On the shape of a two-dimensional bubble in uniform motion. *J. Fluid Mech.*, 244:187–200, 1992.

Simpson, A. D. *Design and Evaluation of Inflatable Wings for UAVs*. Ph.D. thesis, University of Kentucky, 2008.

Smith, S., Hahn, A., Johnson, W., Kinney, D., Pollitt, J., and Reuther, J. The design of the canyon flyer, an airplane for Mars exploration. In *38th Aerospace Sciences Meeting and Exhibit*. 2000.

Sprott, J. C. *Chaos and Time-Series Analysis*. Oxford University Press, Oxford, 2003.

Tadjbakhsh, I. and Odeh, F. Equilibrium states of elastic rings. *J. Math. Anal. Appl.*, 18:59–74, 1967.

Tanveer, S. Some analytical properties of solutions to a two-dimensional steadily translating inviscid bubble. *Proc. R. Soc. Lond. A*, 452:1397–1410, 1996.

Vanden-Broeck, J.-M. and Keller, J. B. Deformation of a bubble or drop in a uniform flow. *J. Fluid Mech.*, 101:673–686, 1980.

Watson, L. and Wang, C. Hanging an elastic ring. *Int. J. Mech. Sci.*, 23(3):161 – 167, 1981.

Wegmann, R. and Crowdy, D. G. Shapes of two-dimensional bubbles deformed by circulation. *Nonlinearity*, 13(6):2131–2141, 2000.

Yorkston, A. A., Blyth, M. G., and Părău, E. I. The deformation and stability of an elastic cell in a uniform flow. *SIAM J. Appl. Math.*, 80(1):71–94, 2020a.

Yorkston, A. A., Blyth, M. G., and Părău, E. I. A model of an inflatable elastic aerofoil, 2020b. Manuscript prepared for submission.